Analysis of the Jahn-Teller Effect on the Spectrum and Structure of the NO_3 Radical

UNDERGRADUATE RESEARCH THESIS

Presented in Partial Fulfillment of the Requirements for graduation "with Honors Research Distinction in Chemistry" in the College of Arts and Sciences of The Ohio State University

By

Henry Khoa Tran,

Undergraduate Program in Chemistry

The Ohio State University

2016

Thesis Committee:

Professor Terry A. Miller, Department of Chemistry and Biochemistry, Advisor

Professor Thaliyil Rajanbabu, Department of Chemistry and Biochemistry

Professor Alexander Leibman, Department of Mathematics

Abstract

The magnitude of the Jahn-Teller effect in NO_3 has been a large topic of research worldwide. The rotational structure of the perpendicular bands in the $\widetilde{A}^2E'' \leftarrow \widetilde{X}^2A_2'$ electronic spectrum of NO_3 has been previously suggested to exhibit asymmetric top behavior. A rovibronic Hamiltonian has been developed to describe an oblate symmetric top under the influence of Jahn-Teller distortions, coriolis coupling, spin-rotation coupling, and spin-orbit coupling. The rotationally resolved, perpendicular transitions in the $\widetilde{A}^2E'' \leftarrow \widetilde{X}^2A_2'$ spectrum have been fit using this model and the results indicate that negligible to no Jahn-Teller distortions are observed in the rotational structure, inconsistent with the *ab-initio* analysis. The previous vibronic fit was also inconsistent with *ab-initio* results. In that analysis, the fit Hamiltonian includes up to second order Jahn-Teller coupling, whereas the *ab-initio* analysis considers up to quartic Jahn-Teller coupling. To pursue the vibronic discrepancy further, hypothetical spectra calculated from the *ab-initio* Hamiltonian have been fit using the quadratic Hamiltonian to determine the effects of higher order coupling terms in the fit parameters of the lower order model. The potentials of NO_3 and Li_3 were analyzed using this method. Extending upon this analysis, the effect of experimental error on fit parameters was analyzed by varying a set of computed levels in a way that mimics experimental error and fitting these levels. The distribution of fit parameters was studied.

For my mom, Dr. Tuyet Thi Bach To, and grandma, Dr. Ngoc Thi My Nguyen. And for my late grandpa, Dr. Nghien Van To, who drove me everyday to elementary school so that I could succeed in my academic pursuits, but left before I finished high school.

Acknowledgments

I deeply thank my supportive family and my friends, without whom these past years would not have been nearly as enjoyable. Of course, I would not be where I am today without my mom, Tuyet To, and grandma, Ngoc Nguyen. There was a time in my life when I thought they would not support my endeavors and am glad that I was completely wrong.

Before I even entered college, my love of chemistry began in the AP Chemistry class of Bonnie Bloom at Hilliard Davidson High School. Throughout my college years, my english teacher, Dan Owens, provides continuous life advice and is one of the reasons I chose to go into graduate school. My math teacher, Bill Kuch, has been wonderful support for me during these past years and I look forward to scaring his Calculus BC students again before I potentially embark from Ohio forever.

I have to thank all my group mates who have made my development as a scientist possible. First a warm thanks to the McCoy group for housing me in the McCoy-Foster-Group-For-Students-Of-Emeritus-Advisors. They say college is the time in your life where you learn to become an independently functional human being and I am glad that Becky exists so that I can avoid that process. Thanks to Mourad for laying out the experimental groundwork to my projects. His advice for my work had always been helpful, as well as his advice in life. Dmitry was one of the first people in the group I worked with and helped me get my first project started. Thanks to Dmitry for imposing the fear of equations onto the group, which has helped give me guidance when I was stuck multiple times. I am greatly appreciative of Ming-Wei, who gives me far too much credit each year at MolSpec for continuing his excellent analysis on NO_3, but I truly appreciate his interest in my work. A huge thanks goes to Terrance, my first mentor in the group and the guy that had to

come to all my weekly meetings with Prof. Miller. Terrance helped teach me a lot of the early material when I joined the group, and then he went on to teach me working skills in the group, and then he went on to teach me how to start my first project. And then he graduated and left behind a vast body of knowledge without which my projects would still be in their infant stages. He would oversee my work, set up weekly meetings with me and even to this day he provides support for my project whenever he has time. A great deal of what I know and what I have accomplished is thanks to Terrance. Scott is always around to liven up the office. I am constantly impressed at how quickly he progresses through his project and the depth of questions that he asks me every day, it really keeps me on my toes. He is very talented and I wish him the best of luck! And finally, thanks to the senior member of the Miller group, Meng. I have always been able to approach Meng about any question I had about literally anything, and he has always surprised me with his vast knowledge of literally everything (not always productive). Meng is the person I turn to everyday in the office to rejuvenate my energy, as well as complain about my lack of energy. I have been told that I am a bit of a drama queen, and I extend a sincere thanks to Meng who is always there to console me. Whether it is science or life advice, Meng is always there to give me support. I'm going to miss talking to him everyday.

My time at THE Ohio State University has changed my life and it would not have been possible without the support of my wonderful mentors from all around the university. First, a thanks to my advisors, Joanna Spanos and Mary Bailey in particular, for making sure I graduated. I am also thankful to Dana Kuchem and Erin Odor from the Fellowship Office for introducing me to and helping attain these once-in-a-lifetime opportunities. I am deeply grateful that whenever I needed assistance with these fellowships or graduate schools, Prof. Thaliyil Rajanbabu (Babu) has always been ready to help and I thank him for my successes in these endeavors. My favorite classes have been with Prof. Sherwin Singer. The afternoons I spent in his office bouncing (endless) questions off of him are some of my fondest memories as a student. Prof. Anne McCoy was my advisor on paper, but she has done much more than that for me. I know I can always turn to Anne with advice regarding any concern on my mind. She also invites me to her group meetings to expose me to theoretical research,

which I cannot stress how generous this is considering I'm not even her student. I know of few people so enthusiastic and supportive, and I am glad to have had the chance to learn from her. I am honored every time I get to work with Prof. John Stanton. His interest in my projects rejuvenates my own passion. The chance to work with John has helped me develop a mind for asking interesting questions and approaching these questions. Beyond this, I am truly thankful for John's support on all of my applications. I do not think I would have nearly as many opportunities as I do now without his help. I am lucky to be able to work with a theorist for whom I have so much respect, someone who consistently tackles problems no one else in this world would dare take on and with an unwavering dedication. Like being a Michigan fan. Seriously, when is the last time Michigan beat OSU?

My greatest thanks goes to Prof. Terry Miller. I sent him an email as a clueless freshman that to this day I am far too embarrassed of to even acknowledge its existence. We set up a meeting anyways. He asked me what classes I had taken, what working skills I could contribute, and how much free time I had each week. Believe me when I say I gave him no reason to take me on as a student, but we decided to meet again next week somehow and so far, that offer has not been retracted. Prof. Miller sat with me one-on-one each week to answer my questions about papers I had read and monitor my research progress, a commitment I doubt any other advisor would give to an undergraduate. I began contributing real research results the following year and Prof. Miller would careful scrutinize my work throughout the week. I was initially very eager to throw results out as soon as possible, but Prof. Miller's high standard for our work has kept me honest and taught me to think deeply about my results. Being around the group showed me how questions and projects are started, and how one begins to solve these questions. In general, I learned what it means to conduct proper science. As I go on in life, I owe a great deal of my scientific development to Prof. Miller. Beyond just the research, Prof. Miller has always been available for research advice, or even life advice in general. He has been so generous as to afford me multiple opportunities to present at conferences, help me apply for fellowships, and even paying me a salary every break. My research has truly shaped both my undergraduate experience and life trajectory and there are no words to express my gratitude.

Vita

1994	Born—Fountain Valley, CA, USA
2012	High School Dipolma Hilliard Davidson High School Hilliard, OH, USA
2012 – Present	Morrill Excellence Scholar The Ohio State University Columbus, OH, USA
2013 – Present	Student Research Assistant The Ohio State University Columbus, OH, USA
2014 – Present	Gary Booth Scholar, College of Arts and Sciences Undergraduate Research Scholar, Bareis and Goldstein Memorial Scholar The Ohio State University Columbus, OH, USA
2015 – Present	Barry M. Goldwater Scholar The Ohio State University Columbus, OH, USA

Fields of Study

Major Field: Chemistry and Mathematics
with Honors Research Distinction and Honors

Table of Contents

List of Figures

List of Tables

Chapter 1
Introduction

1.1 The Chemistry of NO_3

The nitrate radical (NO_3) is a key intermediate in atmospheric chemistry, appearing in the stratosphere and troposphere. NO_3 is formed in the atmosphere by the oxidation of NO_2 with ozone.

$$NO_2 + O_3 \longrightarrow NO_3 + O_2 \tag{1.1}$$

NO_3 is also formed by the dissociation of dinitrogen pentoxide

$$N_2O_5 + M \longleftrightarrow NO_3 + NO_2 \tag{1.2}$$

NO_3 is best known for being the primary oxidant in the night sky and is known to react with organic pollutants to form toxic organic compounds and peroxyacylnitrates.[5] OH is considered one of the fastest oxidizers, but NO_3 is present in concentrations two orders of magnitude higher than OH at night, making NO_3 responsible for most of nighttime oxidations.[5] It has been discovered that NO_3 can form a stable organic nitrate complex with alkenes, allowing it to travel from urban to pristine areas.[6,5]

$$NO_3 + R_2C{=}CR_2 \longrightarrow R_2C(ONO_2)CR_2 \tag{1.3}$$

NO_3 is also known known for its role in nitric acid formation, which is the only identified source of atmospheric acidification in the night sky.[7] Nitric acid is formed from the reaction

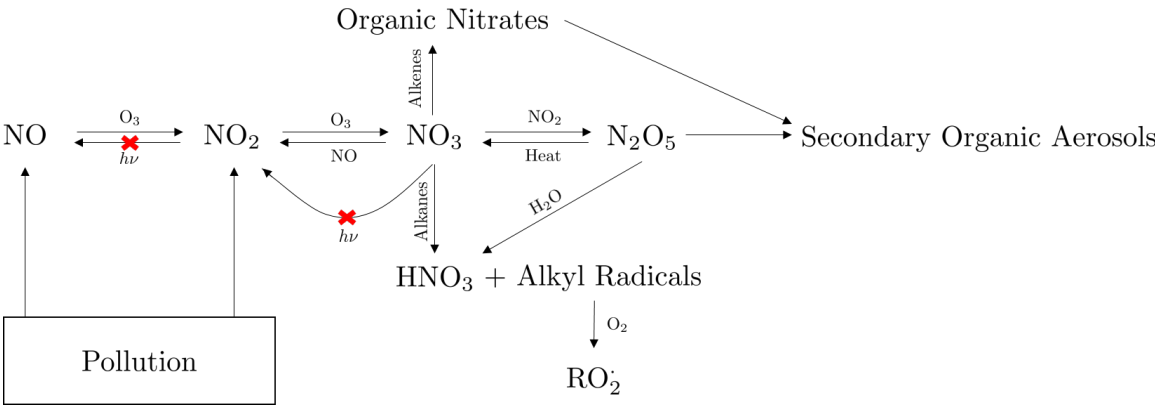

Figure 1.1: Diagram highlighting features of the chemistry of NO_3.

between NO_3 and NO_2 and subsequent hydrolysis.[5]

$$\begin{aligned} NO_3 + NO_2 &\longrightarrow N_2O_5 \\ N_2O_5 + H_2O &\longrightarrow 2\,HNO_3 \end{aligned} \tag{1.4}$$

HNO_3 can also form when NO_3 abstracts a hydrogen from alkyl molecules and volatile organic compounds (VOC), forming an alkyl radical that further reacts with oxygen to form peroxy radicals.

$$\begin{aligned} NO_3 + RH &\longrightarrow R\cdot + HNO_3 \\ R\cdot + O_2 &\longrightarrow RO_2\cdot \end{aligned} \tag{1.5}$$

Peroxy radicals in particular are beneficial in oxidizing and reducing ozone pollution.[5] Some of these peroxy radicals decompose quickly to form HO_2 radicals, which react with NO to form OH at night, potential further oxidizing compounds that usually do not react with NO_3.[5] Many of these products also end up forming reactive organic aerosols that are known to cause lung and heart problems, among other health effects.[8] The chemistry of NO_3 is summarized in Figure 1.1

1.2 The Spectroscopy of NO_3

Beyond its atmospheric importance, NO_3 has a surprisingly complex electronic structure and proves to be a challenge for spectroscopic analyses. Walsh found that the dominant

Table 1.1: Normal modes of NO_3 Radical

Mode	Symmetry	Description	Vibronic Symmetry[a]	Band Type
ν_1	a_1'	sym. stretch	e''	$\mu_m(\perp)$
ν_2	a_2''	umbrella bend	e'	$\mu_e(\perp)$
ν_3	e'	asym. stretch	$a_1''+ a_2''+ e''$	$\mu_e(\parallel), -, \mu_m(\perp)$
ν_4	e'	asym. bend	$a_1''+ a_2''+ e''$	$\mu_e(\parallel), -, \mu_m(\perp)$

a. Fundamental in $\widetilde{A}^2E''$ state in D_{3h}

configuration of the frontier orbitals of NO_3 in the $\widetilde{X}^2A_2'$ state to be $(e')^4(e'')^4(a_2')^1$ and predicted the geometry of NO_3 in the $\widetilde{X}^2A_2'$ state to be D_{3h}.[9] Promotion of an electron in the e'' orbital to the a_2' orbital gives the $\widetilde{A}^2E''$ state configuration and promotion of an electron in the e' to the a_2' orbital gives the $\widetilde{B}^2E'$ state configuration. The $\widetilde{B}^2E' \leftarrow \widetilde{X}^2A_2'$ transition is electric dipole allowed and has been the subject of many studies.[10,11,12] The $\widetilde{A}^2E'' \leftarrow \widetilde{X}^2A_2'$ transition is electric dipole forbidden, but some vibronic transitions are allowed through Herzberg-Teller coupling and others are magnetic dipole allowed.

The electronic structure of NO_3 is especially complex because of Jahn-Teller (JT) coupling. In particular, the $\widetilde{A}^2E''$ state and $\widetilde{B}^2E'$ are Jahn-Teller active and there are pseudo-Jahn-Teller (PJT) effects between all three of the lower lying electronic states. There is significant PJT coupling between the $\widetilde{X}^2A_2'$ and $\widetilde{B}^2E'$ state through the degenerate stretch and bend, leading to a great deal of literature regarding the assignment of these vibrational mode from both experimental[13,14,15,16,17,18,19,20] and theoretical[21,22,23] analyses. Above 17,000 cm^{-1}, NO_3 dissociates into NO and O_2 and recent experiments and electronic structure analysis have supported a roaming mechanism for this reaction.[24]

In the D_{3h} geometry, NO_3 has 4 normal modes which are listed in Table 1.1. The $\widetilde{A}^2E''$ state is electronically degenerate and NO_3 has degenerate vibrations in ν_3 and ν_4. By the Jahn-Teller Theorem, NO_3 exhibits Jahn-Teller coupling along ν_3 and ν_4. Jahn-Teller coupling will split the components of the fundamentals of these modes into three vibronic components, each having symmetries of a_1'',a_2'', and e''. Overtones and combinations of these bands split into increasing numbers of components, each having one of these symmetries. The parallel electric-dipole transition moment has a_1'' symmetry and

the perpendicular electric-dipole transition moment has e' symmetry. The perpendicular magnetic-dipole transition moment has e'' symmetry. In order for a vibronic transition between the vibrationaless level in the $\widetilde{X}^2A_2'$ state and the ν' level in the $\widetilde{A}^2E''$ state to be dipole allowed, either of the products

$$\begin{gathered}\Gamma^{\nu'} \otimes e' \\ \Gamma^{\nu'} \otimes (a_1' \oplus a_2' \oplus e') \\ \Gamma^{\nu'} \otimes ({a_1}'' \oplus {a_2}'' \oplus e'')\end{gathered} \tag{1.6}$$

must contain the totally symmetric representation of the D_{3h} point group, A_1'. Transitions corresponding to the first product are the parallel electric-dipole transitions and to the second product are the perpendicular electric-dipole transitions. Transitions corresponding to the third product are the perpendicular magnetic-dipole transitions. Odd quanta of ν_2 are allowed by parallel electric-dipole selection rules. The ν_1 mode and even quanta of ν_2 are vibronically forbidden and can only be observed as combination bands. ν_1 combination bands will maintain the same symmetry of the bands which they add. In the case of nobilinear coupling, this will appear as anharmonic progressions of the vibronically allowed components of other bands observed in the spectrum. Combinations of odd quanta of ν_2 with ν_3, ν_4 or their combination bands with one another will have e' symmetry. These bands arise from the addition of ν_2 to an e'' component of these bands' vibronic manifolds. The lower lying vibronic states are pictured schematically in Figure 1.2. Red arrows correspond to parallel electric-dipole allowed transitions. Blue arrows correspond to perpendicular electric-dipole allowed transitions. Green arrows correspond to magnetic-dipole allowed transitions. The labels to the left of the energy levels specify the vibrational mode. The labels to the right of the energy levels correspond to vibronic symmetries.

1.3 Previous Studies

An outstanding issue regarding the $\widetilde{A}^2E''$ electronic state is the strength of the Jahn-Teller coupling. In the presence of strong Jahn-Teller coupling, NO_3 distorts from the higher symmetry D_{3h} configuration to the lower symmetry C_{2v} configuration. To this end, there

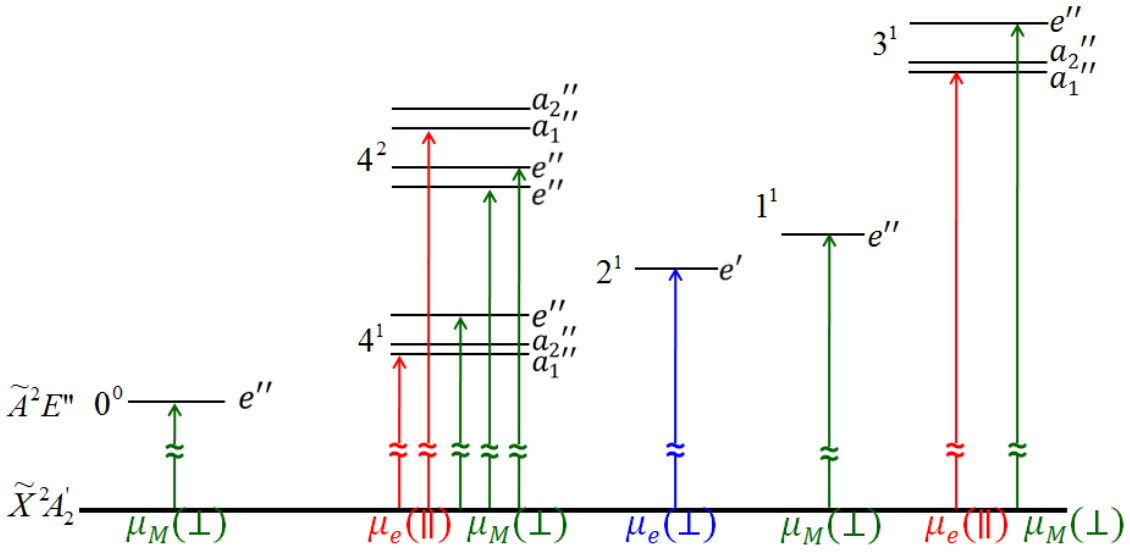

Figure 1.2: Allowed vibronic transitions in the $\widetilde{A}^2E'' \leftarrow \widetilde{X}^2A_2'$ spectrum.

have been multiple contradictory results from both experimental and theoretical studies.

Weaver *et al.* first detected the $\widetilde{A}^2E''$ state by electron photodetachment.[25] They obtained a dense spectrum from which they assigned the origin to 7000 $cm^{-1}$and the ν_1 and ν_4 fundamental to 750 cm^{-1} and 524 cm^{-1} respectively. They predicted that ν_1 and ν_4 were vibronically coupled. Later, Hirota and coworkers observed and assigned the rotationally resolved spectrum of 4_0^1 and were able to describe many of its features by using an oblate symmetric top Hamiltonian.[26] This lead them to suggest that the $\widetilde{A}^2E''$ is weakly Jahn-Teller coupled and is effectively in the D_{3h} configuration. Further experiments using FTIR by Kawaguchi assigned the 2_0^1 band, but did not analyze its rotational structure.[18]

The first broad range absorption spectrum of the $\widetilde{A}^2E''$ state was reported by Deev *et al.* using ambient temperature, cavity ringdown spectroscopy. They were able to assign a progression of the ν_4 fundamental and give a tentative assignment of the ν_3 fundamental.[27] They found that the 4_0^1 hot-band and the 2_0^1 band could only be simulated by using an asymmetric top Hamiltonian. This suggested that the equilibrium geometry of NO_3 was statically distorted to C_{2v} geometry. However, the contour of the ν_4 progression was fit using an oblate symmetric top Hamiltonian, lending support to Hirota's original study. An

irregular progression of ν_4 was attributed to Jahn-Teller coupling in ν_4 and two $\nu_1 + n\nu_4$ combination bands were assigned and found to give different values for the frequency of ν_1, supporting bilinear coupling between these modes. The 3_0^1 band was assigned in this experiment to 8287 cm^{-1}, but this disagrees by hundreds of wavenumbers from electronic structure calculations. The origin of the $\widetilde{A}^2E'' \leftarrow \widetilde{X}^2A_2'$ transition was estimated to be 7064 cm^{-1} based on the frequency of the 4_1^0 hot-band. The high temperature of the experiment allows for the possibility of other hot bands that would interfere with the analysis. Also, the vibronic bands were not rotationally resolved.

Later matrix experiments were conducted on the $\widetilde{X}^2A_2'$ and $\widetilde{A}^2E''$ by Jacox and Thompson.[28] These experiments greatly increased the range of observation of the $\widetilde{A}^2E''$ and allowed for more key transitions to be assigned. Jacox's analysis supported weak Jahn-Teller coupling in ν_4, however, the interaction between NO_3 and the neon matrix significantly increased the noise making it difficult to assign weaker features. The matrix also shifted the bands from their gas phase frequencies. Jacox and Thompson later reassigned the feature assigned to 3_0^1 by Deev[27] to $2_0^1 4_0^1$.[29] They suggested that ν_3 may have a frequency of 800 cm^{-1}, which differs even more drastically from theory and no satisfactory explanation for this discrepancy has been found.

Takematsu *et al.* directly observed a magnetic dipole transition to the $\widetilde{A}^2E''$ origin band and several hot bands.[30] A doublet was observed that was suspected to be a result of spin-orbit coupling, or from an a_2'' vibronic component of a degenerate mode, which would be both electric and magnetic dipole forbidden. If the cause was spin-orbit coupling, other doublets would be expected in the spectrum unless spin-orbit coupling is completely quenched by Jahn-Teller coupling. These other doublets are not observed. Moreover, the 4_1^0 band shows no splitting, even though it terminates on the same level. They also reported the separation of the e'' and a_1'' components of the ν_4 fundamental based on 4_1^1 and the earlier 4_0^1 frequencies. The separation reported is 1.6(1.9) cm^{-1} that they claim is characteristic of relatively weak Jahn-Teller coupling in ν_4. Alternatively, it is also possible that the low energy levels are being pushed to three-fold degeneracy by strong Jahn-Teller coupling in ν_3. Further analysis of the overtones of ν_3 and ν_4 are necessary to distinguish between these

two cases.

In the most recent vibronic analysis, Codd *et al.*[1] observed the $\widetilde{A}^2E'' \leftarrow \widetilde{X}^2A_2'$ transition in a jet-cooled sample eliminating the interference of hot bands and significantly narrowing the rotational contour. This spectrum was fit using a quadratic Jahn-Teller Hamiltonian model. The frequency of ν_3 was determined to be 1433.6 cm^{-1}, in closer agreement with theoretical predictions. Moreover, the analysis predicted strong and moderate Jahn-Teller coupling in ν_3 and ν_4 respectively, supporting theoretical predictions. The frequency of e' combination bands were also inferred and included in the fit. Although both the experiment and theory predict qualitatively the same Jahn-Teller coupling, the Jahn-Teller coupling in ν_3 determined by Codd is significantly stronger than theoretical predictions, and may be attributed to the different analytical forms of the potential used in both analyses.

Chapter 2
The Jahn-Teller Effect

The Jahn-Teller theorem was first proved by Hermann Arthur Jahn and Edward Teller using group theory and states that any non-linear molecule with spatially degenerate orbitals cannot be stable. Any molecule with an electronic degeneracy will distort its molecular geometry to attain a structure of lower energy.[31] This geometric distortion creates a conical intersection in the electronic potential energy surface, leading to the break down of the Born-Oppenheimer approximation.[32] Discussed in this Chapter are the theorem, then the problems arising from the Jahn-Teller effect, and finally the Jahn-Teller effect in the context of NO_3.

2.1 The Eigenvalue Problem

In quantum mechanics, the state of a system is completely specified by its wavefunction Ψ contained in a Hilbert Space. Every observable corresponds to an linear operator over a Hilbert Space. The observation of an observable quantity corresponds to the eigenvalues of the corresponding operator. As a convention, operators will be written with a hat ($\hat{}$). These eigenfunctions form a complete set over the Hilbert Space.

For a molecule, the molecular Hamiltonian is

$$\hat{\mathcal{H}} = \hat{T}_e + \hat{T}_N + \hat{V}_{ee} + \hat{V}_{NN} + \hat{V}_{eN} + \hat{\mathcal{H}}_{so} \tag{2.1}$$

$$
\begin{aligned}
\hat{T}_e &= -\sum_i \frac{\hbar^2}{2m_e}\nabla_i^2 \\
\hat{T}_N &= -\sum_I \frac{\hbar^2}{2M_I}\nabla_I^2 \\
\hat{V}_{ee} &= \sum_i \sum_{j>i} \frac{e^2}{4\pi\epsilon_0|\mathbf{r}_i - \mathbf{r}_j|} \\
\hat{V}_{NN} &= \sum_I \sum_{J>I} \frac{Z_I Z_J e^2}{4\pi\epsilon_0|\mathbf{R}_I - \mathbf{R}_J|} \\
\hat{V}_{eN} &= -\sum_I \sum_i \frac{Z_I e^2}{4\pi\epsilon_0|\mathbf{R}_I - \mathbf{r}_i|}
\end{aligned}
\tag{2.2}
$$

where n is the number of electrons, N is the number of nuclei, lowercase indices run over electrons, capital indices run over nuclei, m_e is the electron mass, M_I is the mass of the I^{th} nuclei, e is the electron charge, ϵ_0 is the permittivity of free space, $\hbar$ is the reduced Planck Constant, Z_I is the atomic number of the I^{th} nucleus, $\mathbf{r}_i$ is the position vector of the i^{th} electron, $\mathbf{R}_I$ is the position vector of the I^{th} nucleus, ∇_i^2 is the Laplacian in electron coordinates $\mathbf{r}_i$, and ∇_I^2 is the Laplacian in nuclear coordinates $\mathbf{R}_I$. The set of all electron coordinates will be denoted as $\mathbf{r} = (\mathbf{r}_1, \ldots, \mathbf{r}_n)$ and the set of all nuclear coordinates will be denoted as $\mathbf{R} = (\mathbf{R}_1, \ldots, \mathbf{R}_N)$.

$\hat{\mathcal{H}}$ corresponds to total energy and obtaining the eigenvalues and eigenfunctions of this operator is the goal of molecular quantum mechanics.

$$
\hat{\mathcal{H}}\Psi(\mathbf{r}, \mathbf{R}) = E\Psi(\mathbf{r}, \mathbf{R}) \tag{2.3}
$$

2.2 The Jahn-Teller Theorem

The original theorem presented by Jahn and Teller[31] relied on generating all possible molecular point groups and exhaustively proving the theorem. The D_{3h} case will be briefly considered.

Suppose $\hat{\mathcal{H}}$ has eigenvalue E and belonging to degenerate eigenfunction $\phi_1, \ldots, \phi_k$ for a molecule in the high symmetry limit, such as D_{3h}. Suppose there is a small displacement along non-totally symmetric mode coordinate Q_d labeled δQ_d. The new Hamiltonian can

be expanded by perturbation theory as

$$\hat{\mathcal{H}}' = \hat{\mathcal{H}} + \hat{\mathcal{H}}^{(1)} \tag{2.4}$$

where $\hat{\mathcal{H}}^{(1)} = \dfrac{\partial \hat{\mathcal{H}}}{\partial Q_d}\delta Q_d$. The corresponding energy is

$$E' = E + E^{(1)} \tag{2.5}$$

where $E^{(1)}$ are the eigenvalues of $\hat{\mathcal{H}}^{(1)}$. Finally, it is known that $\dfrac{\partial \hat{\mathcal{H}}}{\partial Q_d}\delta Q_d$ transforms as the same representation of Q_d. The matrix elements of $\hat{\mathcal{H}}^{(1)}$ in the basis of eigenstates of $\hat{\mathcal{H}}$ are

$$\hat{\mathcal{H}}^{(1)}_{ij} = \langle \phi_i | \, \hat{\mathcal{H}}^{(1)} \, | \phi_j \rangle \tag{2.6}$$

and are thus non-zero when (note that ϕ_i and ϕ_j have the same symmetry as ϕ_1 because these states are degenerate)

$$\Gamma(\phi_1) \otimes \Gamma(\phi_1) \otimes \Gamma(Q_d) \supseteq A_1 \tag{2.7}$$

If this expression contains the totally symmetric representation, then all cross terms are non-zero. Since the unperturbed Hamiltonian, $\hat{\mathcal{H}}$, is diagonal in this basis, $\hat{\mathcal{H}}'$ contains non-diagonal elements in this basis. The energy eigenvalues of $\hat{\mathcal{H}}'$ are shifted from the diagonal elements of $\hat{\mathcal{H}}$ and the electronic degeneracy is lifted. One of these energy eigenvalues will be lower than the eigenvalues of $\hat{\mathcal{H}}$. Once again, $\hat{\mathcal{H}}'$ describes the energetics of the molecule distorted along Q_d. Since a lower energy configuration is obtained, the molecule will remain distorted along Q_d. It can be shown that Equation 2.7 is equivalent to the existence of mode Q_d such that $\Gamma(Q_d) \subset \Gamma(\phi_1) \otimes \Gamma(\phi_1)$.

The Jahn-Teller Theorem: *In all molecular point groups except* $C_{\infty v}$ *and* $D_{\infty h}$, *there are non-totally symmetric modes that are contained in the direct product of any degenerate irreducible representation.*

Special Cases: It should be noted that the vibrational normal modes can be determined from any point group representation.

1. $C_{\infty v}$ and $D_{\infty h}$ — All degenerate irreducible representations are $E_1, E_2, E_3, \ldots$. The

product of any of these is

$$E_k \otimes E_k = A_1 \oplus E_{2k} \tag{2.8}$$

There is one vibrational mode (symmetric stretch) that transforms as E_1.

$$E_1 \not\subset A_1 \oplus E_{2k} \tag{2.9}$$

so linear molecules do not exhibit the Jahn-Teller effect.

2. D_{3h} — There are two degenerate irreducible representations.

$$E' \otimes E' = E'' \otimes E'' = A_1' \oplus A_2' \oplus E' \tag{2.10}$$

There are two vibrational normal modes that transform as E' and these are illustrated in Figure 2.1 and

$$E' \subset A_1' \oplus A_2' \oplus E' \tag{2.11}$$

□

2.3 Break-Down of the Born Oppenheimer Approximation

As a molecule distorts along a nuclear coordinate, there remains a point of degeneracy when the change in nuclear coordinate is zero. This point is called the conical intersection. Conical intersections created by the Jahn-Teller effect or other effects lead to the break-down of the popular Born-Oppenheimer approximation.

In order to solve Equation 2.1, all numerical methods depend on the Born-Oppenheimer approximation. In the Born-Oppenheimer approximation, one assumes that nuclear and electronic degrees of freedom are uncorrelated and the electronic Hamiltonian $\hat{\mathcal{H}}_e = \hat{T}_e + \hat{V}_{NN} + \hat{V}_{eN} + \hat{V}_{ee}$ can be solved first at a fixed $\mathbf{R}$ to obtain $E_e(\mathbf{R})$ for each nuclear coordinate $\mathbf{R}$. The solutions to this Hamiltonian are denoted $\psi(\mathbf{r};\mathbf{R})$ where the parametric dependent on $\mathbf{R}$ is emphasized.

$$\hat{\mathcal{H}}_e \psi_j(\mathbf{r};\mathbf{R}) = E_{e,j}(\mathbf{R}) \psi_j(\mathbf{r};\mathbf{R}) \tag{2.12}$$

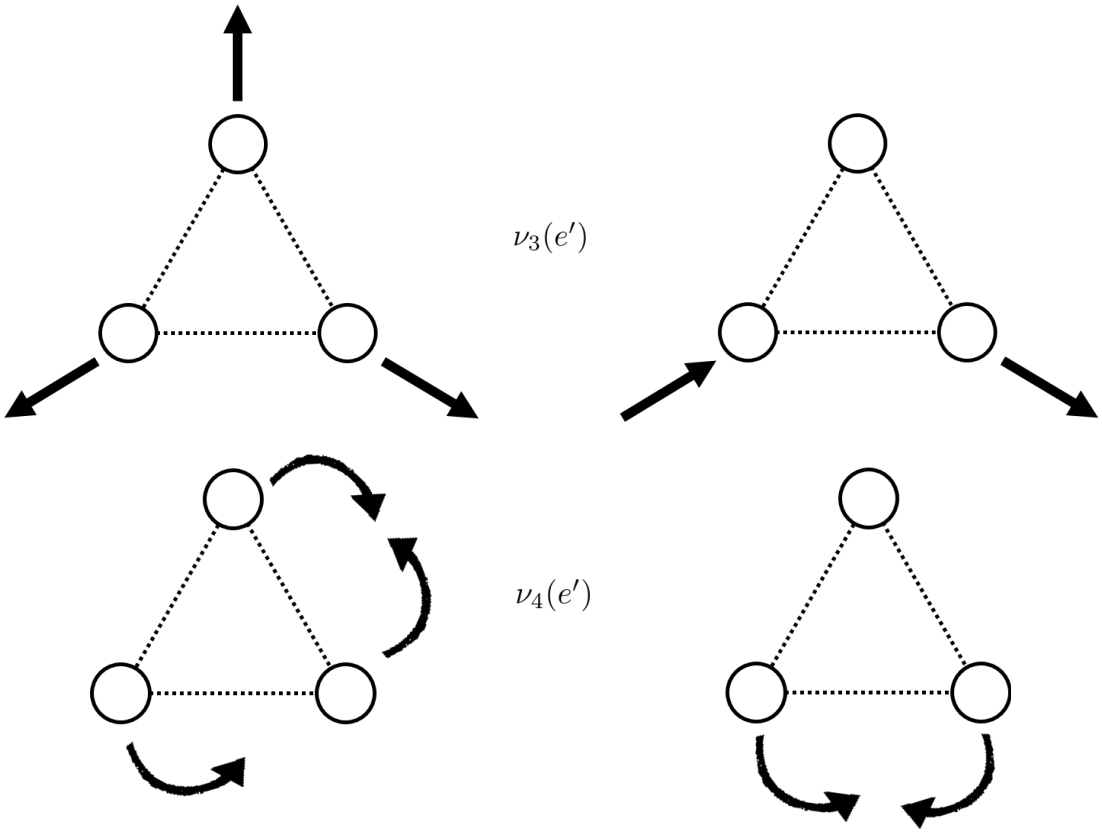

Figure 2.1: The degenerate vibrational modes in the D_{3h} point group.

At each step, the total wavefunction Ψ can be expanded in the complete basis

$$\Psi(\mathbf{r}, \mathbf{R}) = \sum_j c_j \psi(\mathbf{r}; \mathbf{R}) \tag{2.13}$$

At each different $\mathbf{R}$, the expansion coefficients c_j change and one can think of c_j as a function that depends on $\mathbf{R}$. Call $c_j \equiv \chi_j(\mathbf{R})$. Then the total wavefunction is

$$\Psi(\mathbf{r}, \mathbf{R}) = \sum_j \chi_j(\mathbf{R}) \psi_j(\mathbf{r}; \mathbf{R}) \tag{2.14}$$

This is called the Born-Huang expansion. Substituting Equation 2.14 into Equation 2.3 yields

$$\begin{aligned} \hat{\mathcal{H}} \sum_j \psi_j(\mathbf{r}; \mathbf{R}) \chi_j(\mathbf{R}) &= \sum_j (\hat{T}_N + E_{e,j}(\mathbf{R})) \psi_j(\mathbf{r}; \mathbf{R}) \chi_j(\mathbf{R}) \\ &= \sum_j \left(\sum_I -\frac{\hbar^2}{2M_I} \left(\psi_j \nabla_I^2 \chi_j + 2 \nabla_I \psi_j \cdot \nabla_I \chi_j + \chi_j \nabla_I^2 \psi_j \right) + E_{e,j} \psi_j \chi_j \right) \end{aligned} \tag{2.15}$$

where all derivatives are with respect to nuclear coordinates. Taking the overlap integral over electron coordinates with some electronic eigenfunction (ψ_l) gives

$$\langle \psi_l | \hat{\mathcal{H}} | \Psi \rangle = \sum_j \left(\left[\hat{K}_{lj}^{(2)} - \sum_I \frac{\hbar^2}{M_I} \hat{K}_{lj,I}^{(1)} \cdot \nabla_I \right] \chi_j \right) + \left(\sum_I \frac{-\hbar^2}{2M_I} \nabla_I^2 + E_{e,l} \right) \chi_l \tag{2.16}$$

where

$$\begin{aligned} \hat{K}_{lj,I}^{(1)} &= \langle \psi_l | \nabla_I | \psi_j \rangle \\ \hat{K}_{lj}^{(2)} &= -\sum_I \frac{\hbar^2}{2M_I} \langle \psi_l | \nabla_I^2 | \psi_j \rangle \end{aligned} \tag{2.17}$$

Let $\hat{\mathbf{K}}_I^{(1)}$ denote the matrix with matrix elements (i, j) as $\hat{K}_{lj,I}^{(1)}$. Then, taking the same overlap integral with the right-hand side of Equation 2.3 yields

$$\langle \psi_l | \hat{\mathcal{H}} | \Psi \rangle = E \chi_l \tag{2.18}$$

Rearrangement yields

$$\left(\mathbf{E}_e - \sum_I \frac{\hbar^2}{2M_I} \left(\nabla_I + \hat{\mathbf{K}}_I^{(1)} \right)^2 - E \right) \vec{\chi} = 0 \tag{2.19}$$

where $\mathbf{E}_e$ and $\vec{\chi}$ are vectors with components $E_{e,j}$ and χ_j respectively, j indexing electronic eigenvalues. Taking a nuclear gradient (∇_L) of Equation 2.12 yields

$$\left(\nabla_L \hat{\mathcal{H}}_e\right) \psi_j + \hat{\mathcal{H}}_e \nabla_L \psi_j = E_{e,j} \nabla_L \psi_j \tag{2.20}$$

The overlap integral gives

$$\langle \psi_l | \nabla_L \hat{\mathcal{H}}_e | \psi_j \rangle + E_{e,l} \langle \psi_l | \nabla_L | \psi_j \rangle = E_{e,j} \langle \psi_l | \nabla_L | \psi_j \rangle \tag{2.21}$$

and since

$$\hat{K}^{(1)}_{lj,L} = \langle \psi_l | \nabla_L | \psi_j \rangle = \frac{\langle \psi_l | \nabla_L \hat{\mathcal{H}}_e | \psi_j \rangle}{E_{e,j} - E_{e,l}} \tag{2.22}$$

Equation 2.19 becomes undefined for $E_{e,j} = E_{e,l}$, or an electronic degeneracy.

A point where $E_{e,j} = E_{e,l}$ is called the conical intersection. From a qualitative standpoint, it makes sense that the nuclear derivative of the wavefunction would be undefined here by looking at Figure 2.2, which shows the potential energy surfaces for two electronic states with a conical intersection. At a conical intersection, there is a radiation-less transition between two electronic states, leading to a discontinuous change in the wavefunction along nuclear coordinations. It will be shown later than the Jahn-Teller effect leads to a conical intersection, which is a point of electronic degeneracy. Hence, the Born-Oppenheimer approximation fails for molecules exhibiting the Jahn-Teller effect.

2.4 The Jahn-Teller Hamiltonian

Recall the total molecular Hamiltonian described in Equation 2.1.

$\hat{V}$ is Taylor Expanded in the vibrational normal mode coordinates Q_i about the equilibrium of these modes in the highly symmetric geometry, R_0.[33,34] When the Jahn-Teller effect is absent, the first derivative of electronic potential with respect to nuclear coordinates should be zero as discussed in Section 2.2. However, in the general case

$$\hat{V} = \sum_{k=0}^{\infty} \frac{1}{k!} \sum_{i=1}^{3N-6} \left(\frac{\partial^k \hat{V}}{(\partial Q_i)^k} \right) \Bigg|_{R_0} Q_i^k \tag{2.23}$$

where N is the number of nuclei. In practice, this expansion is truncated at second order.

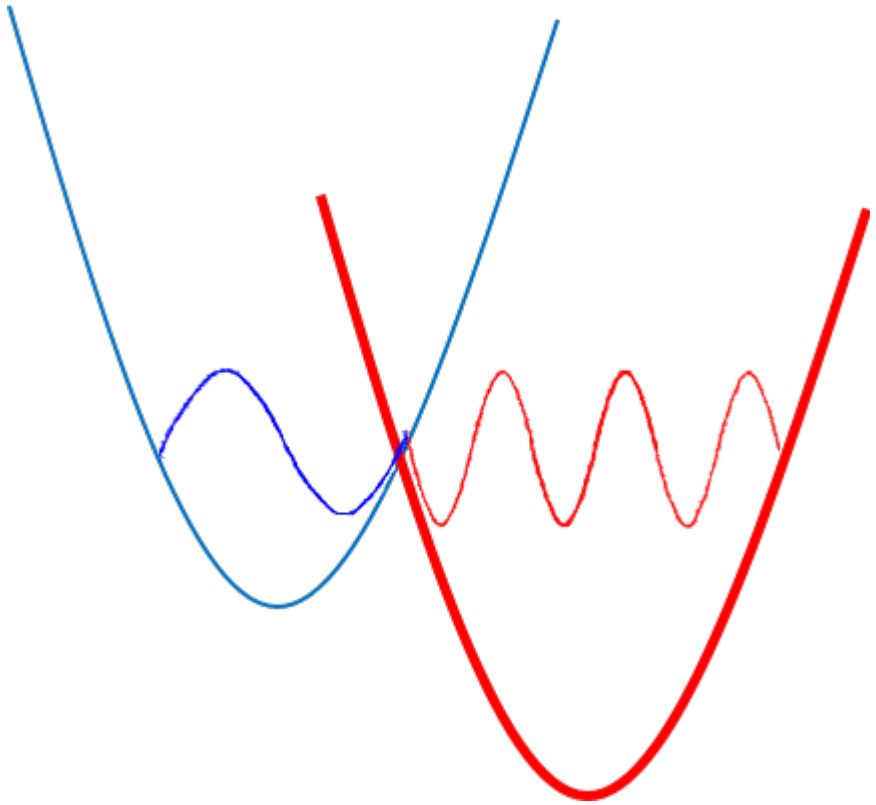

Figure 2.2: Pictorial representation of the breakdown of the Born-Oppenheimer approximation. The two Born-Oppenheimer potential energy surfaces are shown here and characteristic wavefunction is drawn at the conical intersection along both surfaces. There is a discontinuous change at the conical intersection when the surfaces are viewed as adiabatic Born-Oppenheimer potential energy surfaces.

Table 2.1: Coupling constants in the Jahn-Teller Hamiltonian.

Symbol	Description	Definition
d_i	Gradient along symmetric mode	$\frac{\partial}{\partial Q_i}(\langle\Lambda_\pm\|\hat{\mathcal{H}}_e\|\Lambda_\pm\rangle)_0$
k_i	Linear JT coupling constant	$\frac{\partial}{\partial Q_{i,\pm}}(\langle\Lambda_\pm\|\hat{\mathcal{H}}_e\|\Lambda_\mp\rangle)_0$
λ_i	Harmonic force constant for JT active mode	$\frac{\partial^2}{\partial Q_{i,+}\partial Q_{i,-}}(\langle\Lambda_\pm\|\hat{\mathcal{H}}_e\|\Lambda_\pm\rangle)_0$
λ'_i	Harmonic force constant for JT inactive mode	$\frac{\partial^2}{\partial Q_i^2}(\langle\Lambda_\pm\|\hat{\mathcal{H}}_e\|\Lambda_\pm\rangle)_0$
g_{ii}	Quadratic JT coupling constant	$\frac{\partial^2}{\partial Q_{i,\pm}^2}(\langle\Lambda_\pm\|\hat{\mathcal{H}}_e\|\Lambda_\mp\rangle)_0$
g_{ij}	Cross-quadratic JT coupling constant	$\frac{\partial^2}{\partial Q_{i,\pm}Q_{j,\pm}}(\langle\Lambda_\pm\|\hat{\mathcal{H}}_e\|\Lambda_\mp\rangle)_0$
b_{ij}	Bilinear JT coupling constant	$\frac{\partial^2}{\partial Q_{i,\pm}\partial Q_j}(\langle\Lambda_\pm\|\hat{\mathcal{H}}_e\|\Lambda_\mp\rangle)_0$

In experimental spectra, there is typically only enough data to accurately determine up to second order terms. The effect of this truncation is explored in detail in Chapter 6. By truncating the expansion at $k = 2$ the potential may be expressed as shown in Equation 2.24.

$$\hat{V} = \hat{\mathcal{H}}_e(R_0) + \sum_{i=1}^{3N-6-2p} \frac{1}{2}\lambda'_i|Q_i|^2 + \sum_{i=1}^{p}\sum_{r=+,-} \frac{1}{2}\lambda_i|Q_{i,r}|^2 + \sum_{i=1}^{3N-6-2p} d_iQ_i + \sum_{i=1}^{p}\sum_{r=+,-} k_iQ_{i,r} + \sum_{i=1}^{p}\sum_{r=+,-} \frac{1}{2}g_{ii}(Q_{i,r})^2 + \sum_{i=1}^{p}\sum_{j=1}^{p,j\neq i}\sum_{r=+,-} \frac{1}{2}g_{ij}(Q_{i,r}Q_{j,r}) + \sum_{j=1}^{3N-6-2p}\sum_{i=1}^{p}\sum_{r=+,-} \frac{1}{2}b_{ij(}Q_{i,r}Q_j) \tag{2.24}$$

where $\hat{\mathcal{H}}_e(R_0)$ is the electric potential at the symmetric configuration, p is the number of degenerate normal modes, Q_i are the normal coordinates of the nondegenerate modes, and $Q_{i,r}$ are the normal coordinates of the degenerate modes expressed as a complex linear combination of the normal coordinates in Cartesian coordinates.

$$Q_{i,\pm} = Q_{i,x} \pm iQ_{i,y} \tag{2.25}$$

The coefficients of the expansion are the parameters that will be fit. Their definitions and names are listed in Table 2.1.

2.4.1 Basis Set

A direct product basis set is used containing the vibrational, electronic and spin components.

$$\prod_{j}^{m} |\nu_j\rangle \prod_{i}^{p} |\nu_i l_i\rangle |\Lambda\rangle |\Sigma\rangle \tag{2.26}$$

where $m = 3N - 6 - 2p$ is the number of nondegenerate modes. Λ is the projection of the electronic angular momentum onto the principle axis. Σ is the projection of the total spin of molecule, S, onto the principle axis, ν_j and ν_i are vibrational quantum numbers of the non-degenerate and degenerate vibrations respectively, and l_i is the vibrational angular momentum of degenerate mode i. Σ varies from $-S$ to S by increments of 1. Vibrational angular momentum is unique to degenerate modes and l_i ranges from $-\nu_i$ to $+\nu_i$ in increments of 2. It will be seen that Jahn-Teller coupling exists between states of different ν, l, and Λ, so none of these are good quantum numbers. Instead, a new quantum number j is defined that remains a good quantum number in the limit of linear Jahn-Teller coupling.

$$j = \sum_{i}^{p} l_i + \frac{1}{2}\Lambda \tag{2.27}$$

In the case of only linear Jahn-Teller coupling, levels arising from states with $j = \pm\frac{3}{2}$ mod 3 will be a_1 or a_2 symmetry while levels arising from all other values of j will have e symmetry.[33] The positive and negative j-blocks with the same $|j|$ are degenerate so only the positive values of j need be considered.

When quadratic JT coupling is present levels of j differing by $\pm 3n$, where n is any integer, are coupled and both the positive and negative j-blocks must be included. In this case, only the vibronic symmetry of the eigenfunctions remains a good quantum number. The Hamiltonian can be block diagonalized into three blocks, two of which are degenerate. The three blocks involve basis states with $j = \frac{1}{2}$ mod 3, $j = \frac{5}{2}$ mod 3, and $j = \frac{3}{2}$ mod 3. The first two of these blocks are degenerate and give rise to eigenfunctions of e symmetry. The third of these blocks give rise to eigenfunctions of a_1 and a_2 symmetry.

In this case only the vibronic symmetry of the eigenfunctions is preserved and the

Hamiltonian is reduced to three noninteracting blocks, two of which are degenerate. The block with values $j = \frac{1}{2} \pm 3n$ and $j = \frac{5}{2} \pm 3n$ are degenerate and have e symmetry while those with $j = \frac{3}{2} \pm 3n$ have a_1 or a_2 symmetry. In the limit of relatively weak coupling ν may be a useful label to describe the dominant character of a given eigenfunction. Where coupling is strong there may be several basis functions with different values of ν with roughly equal contribution.

2.4.2 Coupling Constants

The strength of the JT effect in spectroscopic studies has typically been reported in terms of the unitless constants D_i and K_i for linear and quadratic JT coupling respectively.[33,35] These terms are related to the linear and quadratic coupling constants defined in Table 2.1 by a mass weighted transformation.

$$D_i = \frac{k_i^2}{2\hbar} \left(\frac{M_i}{\lambda_i^3} \right)^{\frac{1}{2}} \tag{2.28}$$

$$K_i = \frac{g_{ii}}{\lambda_i} \tag{2.29}$$

M_i is the reduced mass of mode i. As is conventional is spectroscopic studies, the terms D_i and K_i will be used will be used in our analyses The bilinear (B_{ij}) and cross quadratic (C_{ij}) terms are transformed in a similar way and defined to be a constant with units of cm^{-1}.

$$B_{ij} = b_{ij} \frac{1}{4c} \left(\frac{1}{M_i \lambda_i} \right)^{1/4} \left(\frac{1}{M_j \lambda_j} \right)^{1/4} \tag{2.30}$$

$$C_{ij} = g_{ij} \frac{1}{4c} \left(\frac{1}{M_i \lambda_i} \right)^{1/4} \left(\frac{1}{M_j \lambda_j} \right)^{1/4} \tag{2.31}$$

D_i may only be positive while K_i, B_{ij}, and C_{ij} may be either positive or negative.

2.5 Potential Energy Surface of Jahn-Teller Active Molecules

As was mentioned in the Section 2.3, the electronic problem can be solved for fixed nuclear configurations to yield $E_{e,j}(\mathbf{R})$. Comparing Equation 2.12 and Equation 2.19, it is seen that

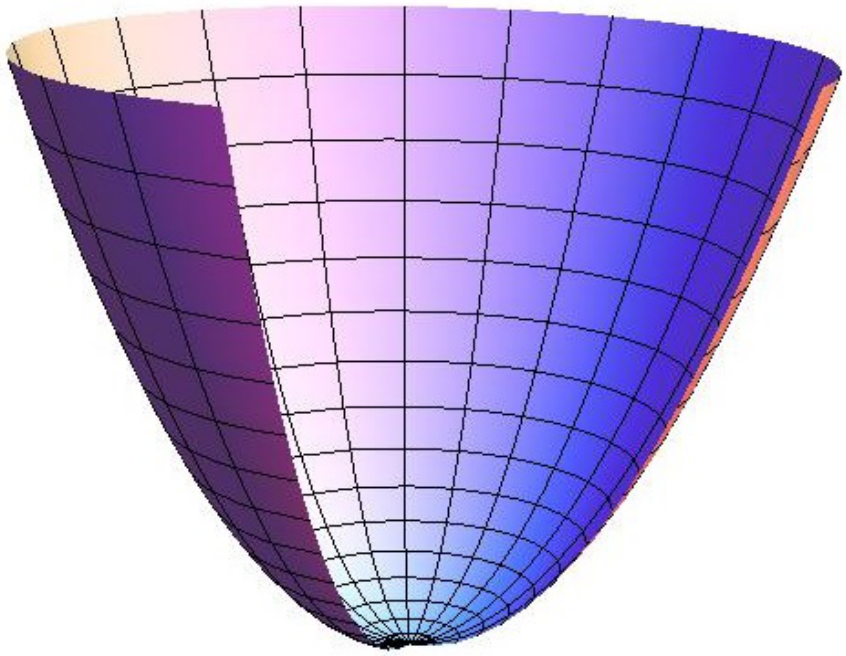

Figure 2.3: Potential energy surface for a two dimensional harmonic oscillator.

$E_{e,j}(\mathbf{R})$ plays the role of a potential energy term to the contracted kinetic energy operator $\sum_I \frac{\hbar^2}{2M_I}\left(\nabla_I + \hat{\mathbf{K}}_I^{(1)}\right)^2$ for χ, or the nuclear part of Ψ. $E_{e,j}(\mathbf{R})$ serves as an effective potential for the nuclear problem and is referred to as the potential energy surface (PES).

The well known approximation for the PES is the harmonic oscillator approximation in which the PES is described by a function that is quadratic in nuclear coordinates.

$$E_{e,j}(\mathbf{R}) = k_j|\mathbf{R}|^2 \tag{2.32}$$

where k_j is the harmonic constant of the j^{th} surface. This surface in two dimensions is shown in Figure 2.3. The lowest energy of the molecule on this PES is at the origin, which corresponds to no nuclear displacement along any vibrational degrees of freedom, or no geometric molecular distortion and the Jahn-Teller effect is not observed.

Since the Jahn-Teller effect arises from the coupling of degenerate electronic states and normal coordinates, there may be one or more points where the two adiabatic surfaces cross one another. In terms of the Jahn-Teller effect, it is illustrative to change to cylindrical coordinates where the two degenerate normal mode coordiantes $Q_{i,+}$ and $Q_{i,-}$ are

parametrized in terms of the polar coordinates ρ and ϕ. Energy remains the z coordinate.

$$Q_{i,\pm} = \rho_i e^{\pm \mathrm{i}\phi_i} \tag{2.33}$$

The origin is the point on the PES where the two electronic states are degenerate with one another is called the conical intersection. As with the harmonic PES this corresponds to the non-distorted configuration of the molecule, which is also used as the reference geometry R_0 about which the potential is expanded in the Taylor series expansion in Eq. 2.24. Following the development presented by Barckholtz and Miller the PES for an electronic state with weak linear and quadratic JT coupling and no SO coupling may be expanded in the diabatic electronic basis as:[33]

$$\hat{V} = \begin{bmatrix} \frac{\lambda_i}{2}\rho_i^2 & \rho_i k_i e^{-i\phi_i} + \rho^2 g_{ii} e^{-2i\phi_i} \\ \rho_i k_i e^{-i\phi_i} + \rho^2 g_{ii} e^{-2i\phi_1} & \frac{\lambda_i}{2}\rho_i^2 \end{bmatrix} \begin{bmatrix} |\Lambda_+\rangle|\Sigma\rangle \\ |\Lambda_-\rangle|\Sigma\rangle \end{bmatrix} \tag{2.34}$$

This matrix can readily be diagonalized to give the eigenvalues, U, as functions of ρ and ϕ. ϕ is referred to as the pseudo-rotation angle.

$$U_{i,\pm} = \frac{1}{2}\lambda_i \rho_i^2 \pm \rho_i k_i \left(1 + \frac{2 g_{ii}\rho_i}{k_i} cos(3\phi) + \frac{g_{ii}^2 \rho_i^2}{k_i^2}\right)^{\frac{1}{2}} \tag{2.35}$$

$U_{i,\pm}$ are the adiabatic PES. Expanding the radical to second order in ρ gives

$$U_{i,\pm} \approx \frac{1}{2}\lambda_i \rho_i^2 \pm [k_i \rho_i + g_{ii}\rho_i^2 cos(3\phi_i)] \tag{2.36}$$

The lower adiabatic PES for linear Jahn-Teller coupling and no quadratic Jahn-Teller coupling is shown in Figure 2.4. It is referred to as the Mexican hat potential. The lower adiabatic PES including quadratic Jahn-Teller coupling is shown in Figure 2.5. In the case where bilinear coupling is included the above formulas are the same with the modification that k_i should be replaced with $(k_i + b_{i,j}Q_j)$ where Q_j is the mode coupled via bilinear coupling to mode i.[36] In these surfaces, we see that there is a minimum away from the reference geometry. This minimum corresponds to some movement along the normal mode coordinates and if the molecule spends more time at this minimum, which it should if the

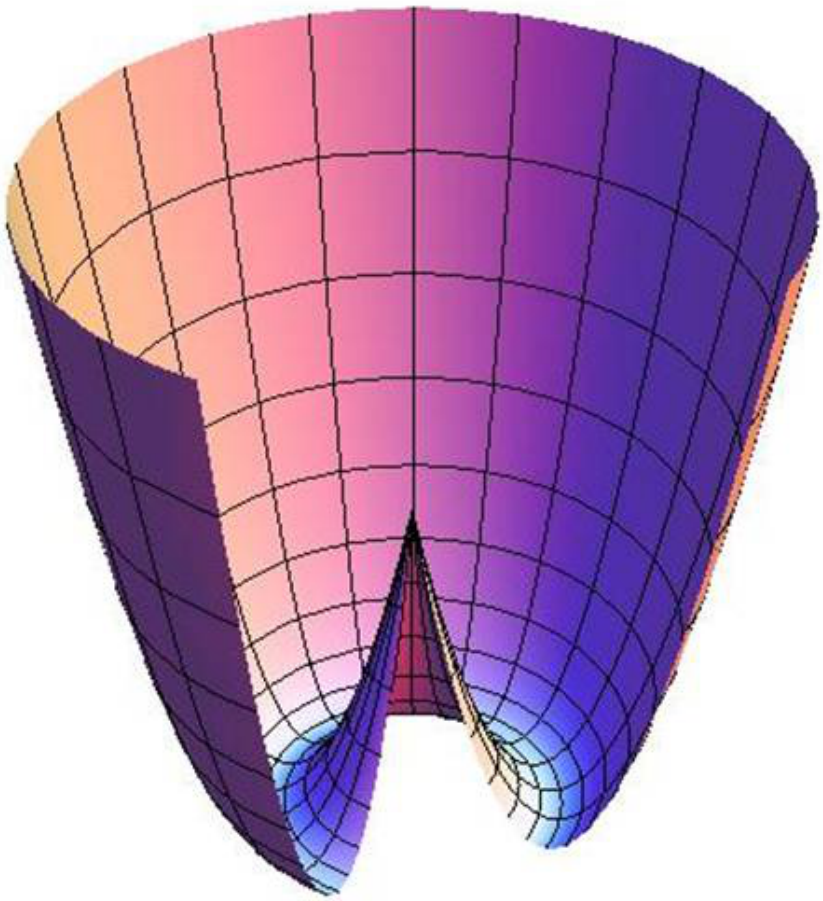

Figure 2.4: Lower adiabatic PES with linear Jahn-Teller coupling.

conical intersection is higher in energy, the effect is a geometric distortion along a normal mode coordinate. The difference in energy between the bottom of the well and the conical intersection of the PES along one normal mode i is the stabilization energy, ϵ_i.

$$\epsilon_i = D_i \omega_i \tag{2.37}$$

In the case where multiple modes exhibit the Jahn-Teller effect, the total stabilization energy is the sum of the contributions of all individual modes.

$$\sum_{i}^{p} D_i \omega_i \tag{2.38}$$

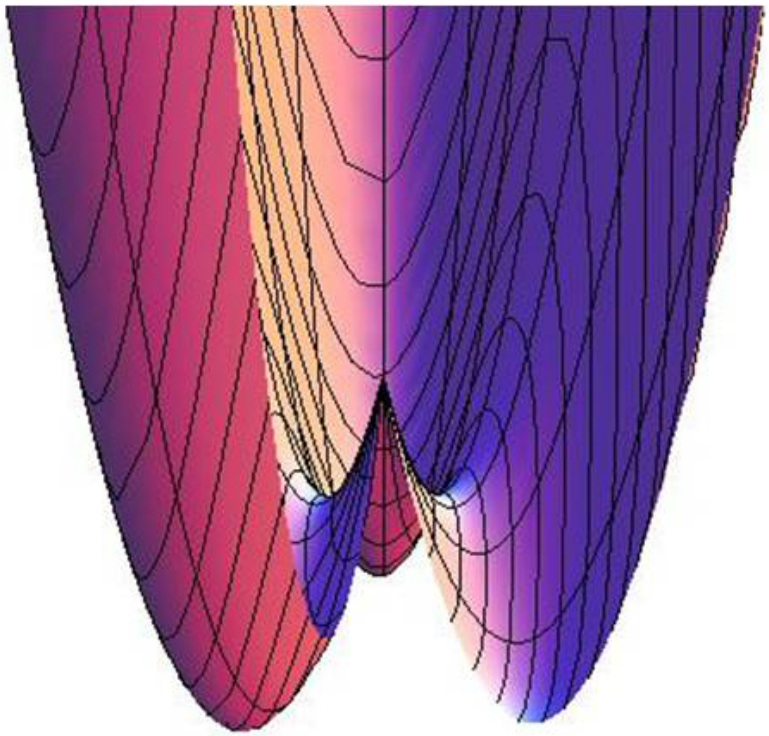

Figure 2.5: Lower adiabatic PES with linear and quadratic Jahn-Teller coupling.

When there is quadratic and linear Jahn-Teller coupling then the PES changes as a function of ϕ leading to, in the case of a threefold axis of symmetry, three equivalent wells separated by barriers. This is shown in Figure 2.6. The highlighted black trace corresponds to movement along the pseudo-rotation angle ϕ, or a pseudo-rotation. The minimum along this trace is referred to as wells or just minimums and the maximums are referred to as pseudo-rotational barriers. The sign of g_{ii} alternates which points on the PES are the minima and which are the barriers. As the linear and quadratic coupling become very strong these three wells become deep and effectively isolated from one another. The energy of the barrier and minimum with respect to the energy at the conical intersection can be casted in terms of D_i and K_i.[33]

$$E_{\text{minimum}} \approx -D_i\omega_i(1 + K_i) \tag{2.39}$$

$$E_{\text{barrier}} \approx -D_i\omega_i(1 - K_i) \tag{2.40}$$

The height of the pseudo-rotational barrier relative to E_{min} is the difference between Equations 2.39 and 2.40.

$$E_{\text{barrier}} - E_{\text{minimum}} = 2D_i\omega_i K_i \tag{2.41}$$

A pictorial representation of these energies are shown in Figure 2.7.

We observe in the PES for both linear and quadratic Jahn-Teller a conical intersection at the origin. As discussed in Section 2.3, this causes a break down of the Jahn-Teller effect. Jahn-Teller effect proves to be a tremendous complication in electronic structure theory.

2.6 Matrix Elements

The Hamiltonian in Equation 2.1 can be divided into

$$\hat{\mathcal{H}} = \hat{\mathcal{H}}_T + \hat{\mathcal{H}}_{har} + \hat{\mathcal{H}}_{gra} + \hat{\mathcal{H}}_{SO} + \hat{\mathcal{H}}^{JT}_{lin} + \hat{\mathcal{H}}^{JT}_{quad} + \hat{\mathcal{H}}^{JT}_{cross} + \hat{\mathcal{H}}^{JT}_{bi} \tag{2.42}$$

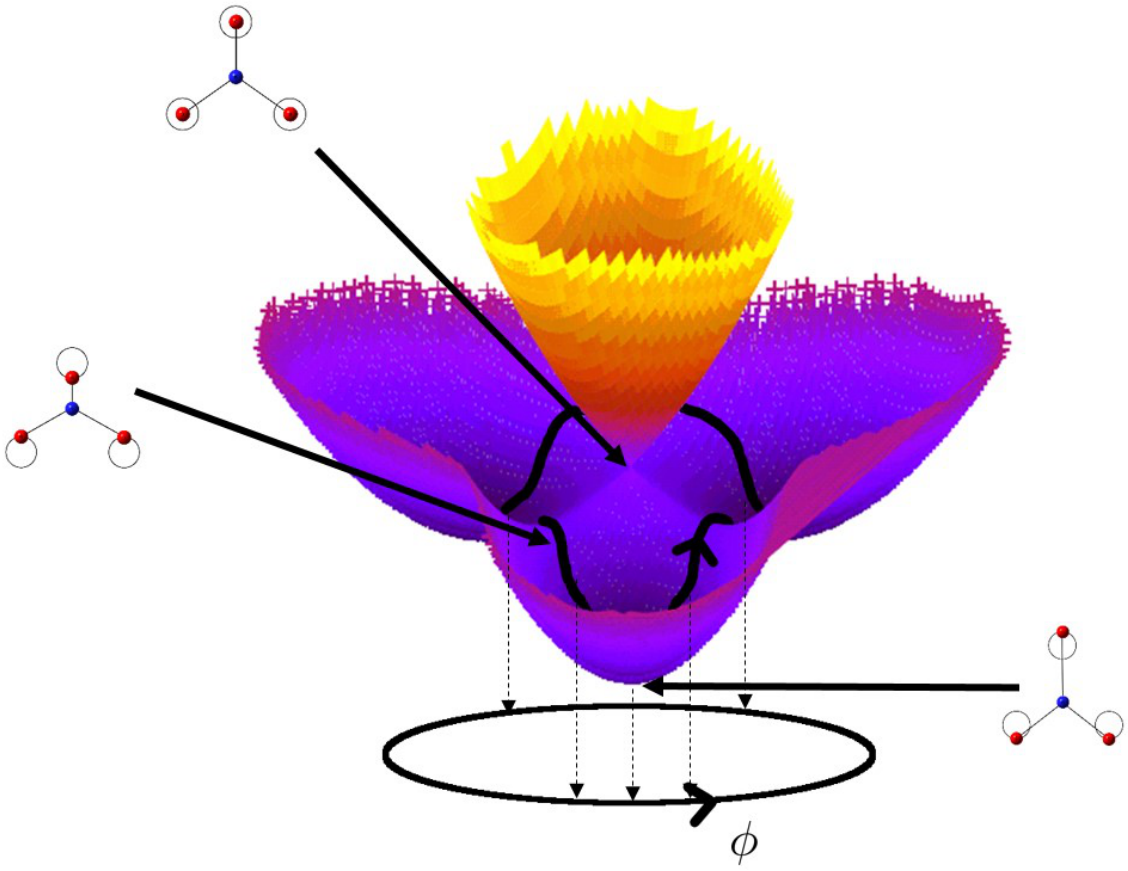

Figure 2.6: Diagram highlighting the pseudo-rotation coordinate on the lower adiabatic PES.

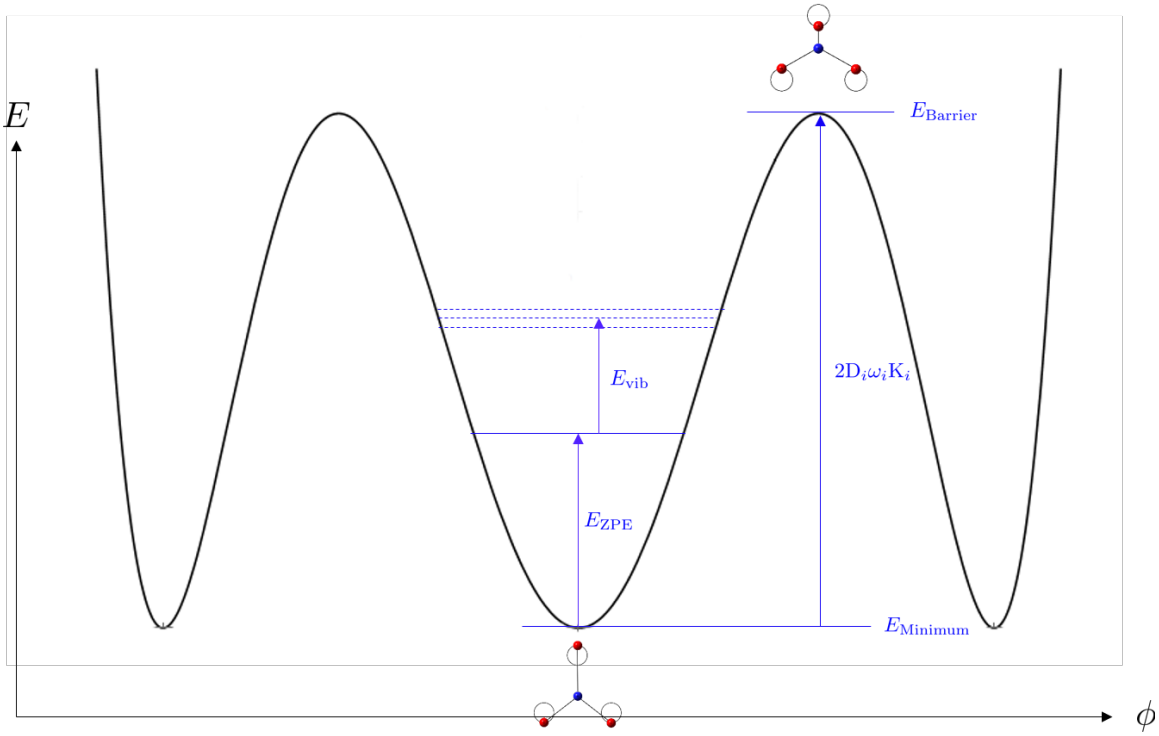

Figure 2.7: Diagram highlighting the energy of the minimum, barrier, and height of the barrier on a quadratic PES along the pseudo-rotation coordinate. The zero point energy and vibrational levels are also included.

where the electronic Hamiltonian is ignored and the electronic energy at the reference geometry, $E(R_0)$ is set equal to 0. The terms of this equation are

$$\begin{aligned}
\hat{\mathcal{H}}_T + \hat{\mathcal{H}}_{har} &= \hat{T}_N + \sum_{i=1}^{3N-6-2p} \frac{1}{2}\lambda_i' |Q_i|^2 + \sum_{i=1}^{p} \sum_{r=+,-} \frac{1}{2}\lambda_i |Q_{i,r}|^2 \\
\hat{\mathcal{H}}_{gra} &= \sum_{i=1}^{3N-6-2p} d_i Q_i \\
\hat{\mathcal{H}}_{lin}^{JT} &= \sum_{i=1}^{p} \sum_{r=+,-} k_i Q_{i,r} \\
\hat{\mathcal{H}}_{quad}^{JT} &= \sum_{i=1}^{p} \sum_{r=+,-} \frac{1}{2} g_{ii} (Q_{i,r})^2 \\
\hat{\mathcal{H}}_{cross}^{JT} &= \sum_{i=1}^{p} \sum_{j=1}^{p,j\neq i} \sum_{r=+,-} \frac{1}{2} g_{ij} (Q_{i,r} Q_{j,r}) \\
\hat{\mathcal{H}}_{bi}^{JT} &= \sum_{j=1}^{3N-6-2p} \sum_{i=1}^{p} \sum_{r=+,-} \frac{1}{2} b_{ij(} Q_{i,r} Q_j)
\end{aligned} \tag{2.43}$$

The matrix elements of these portions of the Hamiltonian will be given separately. For a detailed discussion of the effect of the matrix elements, the reader is referred to Terrance Codd's dissertation.[37]

$$\begin{aligned}
&\langle\Sigma| \prod_{i=1}^{p} \langle\nu_i, l_i| \prod_{j=1}^{m} \langle\nu_j| \langle\Lambda_\pm| \hat{\mathcal{H}}_T + \hat{\mathcal{H}}_{har} |\Lambda_\pm\rangle \prod_{j=1}^{m} |\nu_j'\rangle \prod_{i=1}^{p} |\nu_i', l_i'\rangle |\Sigma\rangle = \\
&\sum_{i=1}^{p} \omega_i(\nu_i + 1) - \omega_i \chi_i (\nu_i + 1)^2 + \sum_{j=1}^{m} \omega_j \left(\nu_j + \frac{1}{2}\right) - \omega_j \chi_j \left(\nu_j + \frac{1}{2}\right)^2
\end{aligned} \tag{2.44}$$

$$\langle\Sigma| \prod_{i=1}^{p} \langle\nu_i, l_i| \prod_{j=1}^{m} \langle\nu_j| \langle\Lambda_\pm| \hat{\mathcal{H}}_{SO} |\Lambda_\pm\rangle \prod_{j=1}^{m} |\nu_j'\rangle \prod_{i=1}^{p} |\nu_i', l_i'\rangle |\Sigma\rangle = a\zeta_e \Lambda\Sigma \tag{2.45}$$

$$\begin{aligned}
&\langle\Sigma| \prod_{i=1}^{p} \langle\nu_i, l_i| \prod_{j=1}^{m} \langle\nu_j| \langle\Lambda_\pm| \hat{\mathcal{H}}_{lin}^{JT} |\Lambda_\mp\rangle \prod_{j=1}^{m} |\nu_j'\rangle \prod_{i=1}^{p} |\nu_i', l_i'\rangle |\Sigma\rangle = \\
&\sum_i \omega_i [D_i(\nu_i \mp (-1)^{s_1} l_i + 2)]^{1/2} \times \left[\delta_{\nu_{i+1}, \nu_i'} \delta_{l_i \mp (-1)^{s_1}, l_i'} \left(\prod_{h\neq i} \delta_{\nu_h, \nu_h'} \delta_{l_h, l_h'} \right) \right] \\
&+ \sum_i \omega_i [D_i(\nu_i \pm (-1)^{s_1} l_i)]^{1/2} \times \left[\delta_{\nu_{i-1}, \nu_i'} \delta_{l_i \mp (-1)^{s_1}, l_i'} \left(\prod_{h\neq i} \delta_{\nu_h, \nu_h'} \delta_{l_h, l_h'} \right) \right]
\end{aligned} \tag{2.46}$$

$$\langle\Sigma|\prod_{i=1}^{p}\langle\nu_i,l_i|\prod_{j=1}^{m}\langle\nu_j|\langle\Lambda_{\pm}|\hat{\mathcal{H}}^{JT}_{quad}|\Lambda_{\mp}\rangle\prod_{j=1}^{m}|\nu'_j\rangle\prod_{i=1}^{p}|\nu'_i,l'_i\rangle|\Sigma\rangle =$$

$$\sum_i \omega_i\frac{K_i}{4}[(\nu_i\mp(-1)^{s_2}l_i)(\nu_i\mp(-1)^{s^2}l_i-2)]^{\frac{1}{2}}\times\left(\delta_{v_i-2,\nu'_i}\delta_{l_i\pm2(-1)^{s_2},l'_i}\left[\prod_{j\neq i}\delta_{\nu_j,\nu'_j}\delta_{l_j,l'_j}\right]\right)$$

$$+\sum_i \omega_i\frac{K_i}{2}[(\nu_i\pm(-1)^{s_2}l_i+2)(\nu_i\mp(-1)^{s^2}l_i+2)]^{\frac{1}{2}}\times\left(\delta_{v_i,\nu'_i}\delta_{l_i\pm2(-1)^{s_2},l'_i}\left[\prod_{j\neq i}\delta_{\nu_j,\nu'_j}\delta_{l_j,l'_j}\right]\right)$$

$$+\sum_i \omega_i\frac{K_i}{4}[(\nu_i\pm(-1)^{s_2}l_i+4)(\nu_i\pm(-1)^{s^2}l_i+2)]^{\frac{1}{2}}\times\left(\delta_{v_i+2,\nu'_i}\delta_{l_i\pm2(-1)^{s_2},l'_i}\left[\prod_{j\neq i}\delta_{\nu_j,\nu'_j}\delta_{l_j,l'_j}\right]\right) \tag{2.47}$$

Chapter 3
The Rotational Model

To date, the only complete rotational analysis of the $\widetilde{A}^2E'' \leftarrow \widetilde{X}^2A_2'$ vibronic bands is of 4_0^1 by Hirota.[26] As discussed in Chapter 2, the rotational structure has potential to reveal key characteristics about the molecular structure of NO_3, and thus the magnitude of Jahn-Teller coupling. Deev *et al.*[27] were only able to reproduce the contour of 2_0^1 using an asymmetric top Hamiltonian and Chen[38] reported that the perpendicular bands could not be analyzed satisfactorily using an oblate symmetric top Hamiltonian. Our group has collected rotationally resolved spectra of a handful of the $\widetilde{A}^2E'' \leftarrow \widetilde{X}^2A_2'$ vibronic transitions. In order to analyzed these bands in the context of Jahn-Teller coupling, a modified rotational Hamiltonian taking into account vibronic coupling must be utilized.

3.1 Rotational Hamiltonian for Vibronically Coupled Systems

The general rotational Hamiltonian as described by Mayer and Cederbaum[2] neglects the effect of spin, but includes the effect of vibronic angular momentum $\vec{\pi}$.

$$\hat{\mathcal{H}}_r = U(\mathbf{q}) + \sum_{\alpha\beta} B_{\alpha\beta}(\hat{J} - \hat{\pi})_\alpha(\hat{J} - \hat{\pi})_\beta. \tag{3.1}$$

$$= U(q) + \sum_{\alpha\beta} B_{\alpha\beta}\hat{\pi}_\alpha\hat{\pi}_\beta \tag{3.2}$$

$$+ \sum_{\alpha\beta} -B_{\alpha\beta}[\hat{J}_\alpha, \hat{\pi}_\beta]_+ \tag{3.3}$$

$$+ \sum_{\alpha\beta} B_{\alpha\beta}\hat{J}_\alpha\hat{J}_\beta \tag{3.4}$$

Greek indices run over spacial coordinates a, b, and c. These coordinates will be aligned with the three principle axes of rotation for NO_3, with c lining up with the axis of three-fold rotational symmetry. $U(\mathbf{q}) = -\frac{\hbar^2}{8}\sum_{\alpha} B_{\alpha\alpha}$ is an additional energy term. $\hat{J}$ is the total angular momentum operator. $\hat{\pi}$ is the vibronic angular momentum operator. B is the tensor of rotational constants defined by $B_{\alpha\beta} = \frac{h}{8\pi^2 c I_{\alpha\beta}}$ where c is the speed of light and $I_{\alpha\beta}$ are the components of the moment of inertia tensor. In the principle axis frame, B is diagonal. As is customary, the diagonal values of $B_{\alpha\alpha}$ will be labeled A, B, and C where $C \leq B \leq A$. The following derivations will start from the D_{3h} geometry of NO_3 where $C < B = A$. The first two terms in the sum are independent of rotational angular momentum and can be ignored. The second term is the coupling between vibronic and rotational angular momentum and will be called the coriolis Hamiltonian, $\hat{\mathcal{H}}_{cor}$. The fourth term is the rotational Hamiltonian, $\hat{\mathcal{H}}_{rot}$.

$$\hat{\mathcal{H}}_{rot} = \sum_{\alpha\beta} B_{\alpha\beta}\hat{J}_{\alpha}\hat{J}_{\beta} \tag{3.5}$$

$$\hat{\mathcal{H}}_{cor} = \sum_{\alpha\beta} -B_{\alpha\beta}[\hat{J}_{\alpha}, \hat{\pi}_{\beta}]_{+} \tag{3.6}$$

This model is based off of the oblate symmetric top symmetry in which NO_3 has a D_{3h} geometry, so only the D_{3h} representation will be considered. For now, single and double prime representations will not be distinguished. A product basis of vibronic eigenfunctions $|\psi\rangle$ and Hund's Case (b) rotational basis functions $|J, N, K\rangle$ is used. Here, $\vec{N}$ is the rotational angular momentum, K is the projection of N onto the c axis, and $\mathbf{J}$ is the total angular momentum, $\mathbf{J} = \mathbf{N} + \mathbf{S}$ where $\mathbf{S}$ is the spin angular momentum. S is not explicitly stated because it can be inferred from J and N. The basis is represented as

$$|\psi\rangle\,|J, N, K\rangle \tag{3.7}$$

Let $|\psi_a\rangle$ and $|\psi_b\rangle$ be the two degenerate components of $|\psi_E\rangle$. The more convenient complex representation basis $|\psi_+\rangle$ and $|\psi_-\rangle$ in the $|\psi_E\rangle$ manifold will be used instead. The states

and operators have the form

$$|\psi_\pm\rangle = |\psi_a\rangle \pm i\,|\psi_b\rangle \tag{3.8}$$

$$\hat{O}_\pm = \hat{O}_a \pm i\hat{O}_b \tag{3.9}$$

The rotational constant matrix in the new basis $a+ib, a-ib, c$ is

$$B = \begin{pmatrix} \frac{1}{4}(B_{aa}+B_{bb}+2iB_{ab}) & \frac{1}{4}(B_{aa}+B_{bb}) & 0 \\ \frac{1}{4}(B_{aa}+B_{bb}) & \frac{1}{4}(B_{aa}+B_{bb}-2iB_{ab}) & 0 \\ 0 & 0 & B_{cc} \end{pmatrix} \tag{3.10}$$

3.1.1 The E Manifold

In this section, only the matrix elements for vibronic states of E' symmetry will be considered, which is what will be used for the analysis of the degenerate vibronic bands. In the next section, the Hamiltonian will be generalized to the full vibronic manifold.

The form of $\hat{\mathcal{H}}_{cor}$ is first determined. Expanding out Equation 3.6,

$$\begin{aligned} \hat{\mathcal{H}}_{cor} = &-2\hat{J}_c(B_{cc}\hat{\pi}_c + B_{c-}\hat{\pi}_+ + B_{c+}\hat{\pi}_-) \\ &-2\hat{J}_+(B_{+-}\hat{\pi}_- + B_{--}\hat{\pi}_+ + B_{c-}\hat{\pi}_c) \\ &-2\hat{J}_-(B_{+-}\hat{\pi}_+ + B_{++}\hat{\pi}_- + B_{c+}\hat{\pi}_c) \end{aligned} \tag{3.11}$$

Utilizing the fact that the Hamiltonian must belong to the totally symmetric representation (A_1'), Equation 3.11 can be reduced using the symmetry representations of π_α. The D_{3h} symmetry representations of angular momentum operators are given by Mayer and Cederbaum[2] and are summarized in Table 3.1.

In the vibronic basis, the terms $\langle\psi_1|\,\hat{\mathcal{H}}_{cor}\,|\psi_2\rangle$ are nonzero for all operators where the product

$$\Gamma_{\psi_1} \otimes \Gamma_{\hat{O}} \otimes \Gamma_{\psi_2} \tag{3.12}$$

contains the totally symmetric representation (A_1'). Here, $\hat{O}$ refers to $\hat{\pi}_\alpha$ since this is the only operator that is diagonal in the vibronic eigenfunctions and in the E manifold, the

Table 3.1: D_{3h} Representations of Angular Momentum Operators $\hat{\pi}$.[2]

Operator	Representation (D_{3h})
$\hat{\pi}_c$	A_2'
$\hat{\pi}_\pm$	E''
$\hat{\pi}_c^2$	A_1'
$\hat{\pi}_c\hat{\pi}_\pm$	E''
$\hat{\pi}_+\hat{\pi}_- + \hat{\pi}_-\hat{\pi}_+$	A_1'
$\hat{\pi}_+\hat{\pi}_- - \hat{\pi}_-\hat{\pi}_+$	A_2'
$\hat{\pi}_\pm^2$	E'

terms which survive are the terms proportional to $\hat{\pi}_\alpha$ such that

$$A_1' \subseteq E' \otimes \Gamma_{\hat{\pi}_\alpha} \otimes E' \tag{3.13}$$

Equation 3.11 reduces to

$$\hat{\mathcal{H}}_{cor} = -2C\hat{J}_c\hat{\pi}_c \tag{3.14}$$

$\hat{\pi}_c$ operates only on the vibronic eigenfunctions and gives

$$\begin{aligned} \langle\psi_\pm|\,\hat{\pi}_c\,|\psi_\pm\rangle &= \pm\zeta_t \\ \langle\psi_\pm|\,\hat{\pi}_c\,|\psi_\mp\rangle &= 0 \end{aligned} \tag{3.15}$$

where ζ_t is the vibronic angular momentum. $\hat{J}_c = \hat{N}_c + \hat{S}_c$ but only $\hat{N}_c$ will be considered as $\hat{S}_c$ will be considered in the spin-orbit Hamiltonian. $\hat{N}_c$ operates on the rotational basis functions and has the form

$$\langle J,N,K|\,\hat{N}_c\,|J,N,K\rangle = K \tag{3.16}$$

$\hat{\mathcal{H}}_{cor}$ in total has the form

$$\langle\psi_\pm|\,\langle J,N,K|\,\hat{\mathcal{H}}_{cor}\,|J,N,K\rangle\,|\psi_\pm\rangle = \mp 2CK\zeta_t \tag{3.17}$$

Equation 3.5 has the expanded form

$$\hat{\mathcal{H}}_{rot} = B_{cc}\hat{J}_c^2 + B_{+-}[\hat{J}_+,\hat{J}_-]_+ + B_{--}\hat{J}_+^2 + B_{++}\hat{J}_-^2 \tag{3.18}$$

Denote the first two terms as $\hat{\mathcal{H}}^{(1)}_{rot}$ and the last two terms as $\hat{\mathcal{H}}^{(2)}_{rot}$.

$$\hat{\mathcal{H}}^{(1)}_{rot} = B_{cc}\hat{J}_c^2 + B_{+-}[\hat{J}_+, \hat{J}_-]_+ \tag{3.19}$$

$$\hat{\mathcal{H}}^{(2)}_{rot} = B_{--}\hat{J}_+^2 + B_{++}\hat{J}_-^2 \tag{3.20}$$

$\hat{\mathcal{H}}^{(1)}_{rot}$ transforms as A_1' and is vibronically diagonal. $B_{+-} = \frac{1}{2}B_{bb}$ and $[\hat{J}_+, \hat{J}_-]_+ = 2(\hat{J}_a^2 + \hat{J}_b^2)$ so $\hat{\mathcal{H}}^{(1)}_{rot}$ can be written as

$$\begin{aligned}\hat{\mathcal{H}}^{(1)}_{rot} &= B_{cc}\hat{J}_c^2 + B_{bb}\hat{J}_b^2 + B_{aa}\hat{J}_b^2 \\ &= B_{cc}(\hat{N}_c{}^2 + 2\hat{N}_c\hat{S}_c + \hat{S}_c{}^2) + B_{bb}(\hat{N}_b{}^2 + 2\hat{N}_b\hat{S}_b + \hat{S}_b{}^2) + B_{aa}(\hat{N}_a{}^2 + 2\hat{N}_a\hat{S}_a + \hat{S}_a{}^2)\end{aligned} \tag{3.21}$$

which is the form of the typical rotational Hamiltonian. The terms in $\hat{N}_\alpha^2$ form the pure rotational Hamiltonian that will be taken as a rigid rotor with linear centrifugal distortion: $\hat{\mathcal{H}}_{rr} + \hat{\mathcal{H}}_{cd}$. The terms involving $\hat{N}_\alpha\hat{S}_\alpha$ form the spin-rotation Hamiltonian that couples spin and rotational angular momentum: $\hat{\mathcal{H}}_{sr}$. The terms in $\hat{S}_\alpha^2$ form the total spin angular momentum operator, but since it does not depend on rotational angular momentum, this term will be ignored.

$$\hat{\mathcal{H}}_{rr} + \hat{\mathcal{H}}_{cd} = \sum_\alpha B_{\alpha\alpha}\hat{N}_\alpha^2 \tag{3.22}$$

$$\hat{\mathcal{H}}_{sr} = 2\sum_\alpha B_{\alpha\alpha}\hat{N}_\alpha\hat{S}_\alpha \tag{3.23}$$

Starting from the D_{3h} symmetry of NO_3, Equation 3.22 describes an oblate symmetric top where $C < B = A$. $\hat{\mathcal{H}}_{rr}$ and $\hat{\mathcal{H}}_{cd}$ for an oblate symmetric top is well known and in the Hund's Case (b) basis, has the form

$$\langle\psi_\pm|\langle J, N, K|\,\hat{\mathcal{H}}_{rr}\,|J, N, K\rangle|\psi_\pm\rangle = B^\Gamma N(N+1) + (C-B)K^2 \tag{3.24}$$

$$\langle\psi_\pm|\langle J, N, K|\,\hat{\mathcal{H}}_{cd}\,|J, N, K\rangle|\psi_\pm\rangle = -D_N N^2(N+1)^2 - D_K K^2 - D_{NK}N(N+1)K^2 \tag{3.25}$$

D_N, D_K, and D_{NK} are the centrifugal distortion constants. These arise from a perturbation treatment of the rigid rotor, where the perturbation is taken as a small change in bond length

because of distortions away from rigidity as a result of centrifugal force. In this work, these will be free parameters.

$\hat{\mathcal{H}}_{sr}$ was included in Hirota's analysis of the 4_0^1 band[26] and the same form as presented in that work will be used in this work.

$$\begin{aligned}\langle\psi_\pm|\langle J,N,K|\,\hat{\mathcal{H}}_{sr}\,|J,N,K\rangle\,|\psi_\pm\rangle &= \left[\frac{J(J+1)-N(N+1)-S(S+1)}{2}\right]\left[\frac{\varepsilon_{bb}-(\varepsilon_{bb}-\varepsilon_{cc})K^2}{N(N+1)}\right]\\ \langle\psi_\pm|\langle J,N-1,K|\,\hat{\mathcal{H}}_{sr}\,|J,N,K\rangle\,|\psi_\pm\rangle &= \frac{1}{2}(\varepsilon_{bb}-\varepsilon_{cc})\left[\frac{K}{2N}\right]\sqrt{N^2-K^2}\end{aligned} \tag{3.26}$$

where $\varepsilon_{\alpha\alpha}$ are the diagonal elements of the spin-rotation tensor.

$\hat{\mathcal{H}}_{rot}^{(2)}$ transforms as E' and thus couples only $\psi_\pm$ with $\psi_\mp$. The matrix elements are vibronically off diagonal. Define

$$h_1 = \langle\psi_\pm|\,B_{\pm\pm}\,|\psi_\pm\rangle \tag{3.27}$$

These are the Watson terms defined by Watson.[39] They are rigorously the expectation of the derivative of the rotational constants and are the terms that quantify the JT coupling. The rest of $\hat{\mathcal{H}}_{rot}^{(2)}$ operate on the rotational basis functions. Moreover, the $\hat{S}_\pm$ operators are related only to spin and will be ignored.

$$\hat{\mathcal{H}}_{rot}^{(2)} = B_{--}\hat{N}_+^2 + B_{++}\hat{N}_-^2 \tag{3.28}$$

$\hat{N}_+$ and $\hat{N}_-$ are the lowering and raising operators respectively in the molecule fixed coordinate system. These operate as

$$\begin{aligned}\hat{N}_+\,|J,N,K\rangle &= \sqrt{N(N+1)-K(K-1)}\,|J,N,K-1\rangle\\ \hat{N}_-\,|J,N,K\rangle &= \sqrt{N(N+1)-K(K+1)}\,|J,N,K+1\rangle\end{aligned} \tag{3.29}$$

Let $\mathcal{F}_+(N,K) = \sqrt{N(N+1)-K(K-1)}$ and $\mathcal{F}_-(N,K) = \sqrt{N(N+1)-K(K+1)}$. Then $\hat{\mathcal{H}}_{rot}^{(2)}$ has the form

$$\begin{aligned}\langle\psi_+|\langle J,N,K+2|\,\hat{\mathcal{H}}_{rot}^{(2)}\,|J,N,K\rangle\,|\psi_-\rangle &= h_1\mathcal{F}_-(N,K)\mathcal{F}_-(N,K+1)\\ \langle\psi_-|\langle J,N,K-2|\,\hat{\mathcal{H}}_{rot}^{(2)}\,|J,N,K\rangle\,|\psi_+\rangle &= h_1\mathcal{F}_+(N,K)\mathcal{F}_+(N,K-1)\end{aligned} \tag{3.30}$$

Finally, the spin-orbit Hamiltonian is included as a perturbation.

$$\hat{\mathcal{H}}_{so} = a\sum_{\alpha}\hat{L}_{\alpha}\hat{S}_{\alpha} = a\hat{L}_c\hat{S}_c + a\hat{L}_+\hat{S}_- + a\hat{L}_-\hat{S}_+ \tag{3.31}$$

where $\hat{L}$ is electronic angular momentum and a is a perturbation constant. The last two terms are treated in the spin-rotational term, so only the first term needs attention. $\hat{L}_z$ operates only on the vibronic part and its action is $\hat{L}_c\left|\psi_{\pm}\right\rangle = \pm\zeta_e d\left|\psi_{\pm}\right\rangle$ where $\zeta_e d$ is the projection of electronic angular momentum on the principle axis. This matrix is thus vibronically diagonal. Turning to $\hat{S}_c$, for a state with $S = \dfrac{1}{2}$, its expansion into the full spin-rotational basis is[40]

$$\begin{aligned}\left|J = N \pm S, N, K\right\rangle = &\left(\frac{J + K + \frac{1}{2}}{2J+1}\right)^{\frac{1}{2}}\left|J, P = K \pm S\right\rangle\left|S, \Sigma = \pm S\right\rangle \\ &\pm\left(\frac{J - K + \frac{1}{2}}{2J+1}\right)^{\frac{1}{2}}\left|J, P = K \mp S\right\rangle\left|S, \Sigma = \mp S\right\rangle\end{aligned} \tag{3.32}$$

where Σ is the projection of S onto the principle axis and P is the projection of J onto the principle axis, or $K + \Sigma$. $\hat{S}_c$ operates on these basis functions to yield

$$\hat{S}_c\left|J = N + \Sigma, N, K\right\rangle = \Sigma\left(\frac{2K}{2J+1}\right)\left|J = N + \Sigma, N, K\right\rangle \tag{3.33}$$

and $\hat{\mathcal{H}}_{so}$ has the form

$$\left\langle\psi_{\pm}\right|\left\langle J = N + \Sigma, N, K\right|\hat{\mathcal{H}}_{so}\left|J = N + \Sigma, N, K\right\rangle\left|\psi_{\pm}\right\rangle = \pm a\zeta_e d\Sigma\left(\frac{2K}{2J+1}\right) \tag{3.34}$$

This completes the discussion of the matrix elements. One final consideration is that it is more efficient to transform the basis functions into a new basis that better approximates the eigenfunctions. A Wang-Type symmetrized basis is such a basis.[41]

$$\left|\psi_E, J, N, K, \wp\right\rangle = \frac{1}{\sqrt{2}}\left(\left|\psi_+\right\rangle\left|J, N, K\right\rangle + (-1)^{N-K+\wp}\left|\psi_-\right\rangle\left|J, N, -K\right\rangle\right) \tag{3.35}$$

where $\wp$ is a parity value that takes on 0 and 1. Conducting this change of basis, the final rotational matrix elements are obtained.

$$\hat{\mathcal{H}}_r = \hat{\mathcal{H}}_{rot}^{(1)} + \hat{\mathcal{H}}_{rot}^{(2)} + \hat{\mathcal{H}}_{cor} + \hat{\mathcal{H}}_{so} \tag{3.36}$$

$$\begin{aligned}\langle \psi_E, J, N, K, \wp | \hat{\mathcal{H}}^{(1)}_{rot} | \wp, J, N, K, \psi_E \rangle =& BN(N+1) + (C-B)K^2 \\ & - D_N[N(N+1)]^2 - D_K K^4 - D_{NK} N(N+1) K^2 \\ & + \left[\frac{J(J+1) - N(N+1) - S(S+1)}{2} \right] \\ & \times \left[\frac{\epsilon_{bb} - (\epsilon_{bb} - \epsilon_{cc}) K^2}{N(N+1)} \right]\end{aligned} \tag{3.37a}$$

$$\langle \psi_E, J, N-1, K, \wp | \, \hat{\mathcal{H}}^{(1)}_{rot} \, | \wp, J, N, K, \psi_E \rangle = \frac{1}{2}(\varepsilon_b - \varepsilon_c) \left[\frac{K}{2N} \right] \sqrt{N^2 - K^2} \tag{3.37b}$$

$$\langle \psi_E, J, N, K, \wp | \hat{\mathcal{H}}_{cor} + \hat{\mathcal{H}}_{so} | \wp, J, N, K, \psi_E \rangle = - \left(2C\zeta_t \mp \frac{a_z^0 \zeta_e d_z}{2J+1} \right) K \tag{3.37c}$$

$$\langle \psi_E, J, N-1, K, \wp | \mathcal{H}^E_{so} | \wp, J, N, K, \psi_E \rangle = - \frac{a_z^0 \zeta_e d_z \sqrt{N^2 - K^2}}{2J+1} \tag{3.37d}$$

$$\begin{aligned}\langle \psi_E, J, N, -K+2, \wp | \mathcal{H}^E_{JT} | \wp, J, N, K, \psi_E \rangle =& h_1 (-1)^{N-K+\wp} \sqrt{N(N+1) - K(K-1)} \\ & \times \sqrt{N(N+1) - (K-1)(K-2)}\end{aligned} \tag{3.37e}$$

3.1.2 The Complete Rovibronic Hamiltonian

For completeness, the full rovibronic Hamiltonian in the entire A_1, A_2, E manifold will be presented.

$$\mathcal{H}_{rve} = \begin{pmatrix} \mathcal{H}_d(A_1^\kappa) & \mathcal{H}(A_1^\kappa, A_2^\kappa) & \mathcal{H}(A_1^\kappa, E^\kappa(1)) & \mathcal{H}(A_1^\kappa, E^\kappa(2)) \\ \mathcal{H}(A_2^\kappa, A_1^\kappa) & \Delta E_{A_2^\kappa, A_1^\kappa} \hat{I} + \mathcal{H}(A_2^\kappa) & \mathcal{H}(A_2^\kappa, E^\kappa(1)) & \mathcal{H}(A_2^\kappa, E^\kappa(2)) \\ \mathcal{H}(E^\kappa(1), A_1^\kappa) & \mathcal{H}(E^\kappa(1), A_2^\kappa) & \Delta E_{E^\kappa(1), A_1^\kappa} \hat{I} + \mathcal{H}(E^\kappa) & \mathcal{H}(E^\kappa(1), E^\kappa(2)) \\ \mathcal{H}(E^\kappa(2), A_1^\kappa) & \mathcal{H}(E^\kappa(2), A_2^\kappa) & \mathcal{H}(E^\kappa(2), E^\kappa(1)) & \Delta E_{E^\kappa(2), A_1^\kappa} \hat{I} + \mathcal{H}(E^\kappa) \end{pmatrix} \tag{3.38}$$

$\kappa = 0(1)$ for single (double) prime. The basis used for A_j^κ states are the same as in Equation 3.7 and the basis used for E^κ states are the same as in Equation 3.35. The matrix elements

are listed explicitly below. First are the diagonal elements.

$$\begin{aligned}\langle\psi_{E^\kappa},J,N,K,\wp|\,\mathcal{H}(E^\kappa)\,|\wp,J,N,K,\psi_{E^\kappa}\rangle = B_z z^{E^\kappa}K^2\\ +\frac{1}{2}(B_{xx}^{E^\kappa}+B_{yy}^{E^\kappa})(N(N+1)-K^2)-\left(2B_{zz}^{E^\kappa}\zeta_t^{E^\kappa}\mp\frac{a_z^0\zeta_e d_z^{E^\kappa}}{2J+1}\right)K\end{aligned} \tag{3.39a}$$

$$\langle\psi_{E^\kappa},J,N-1,K,\wp|\mathcal{H}(E^\kappa)|\wp,J,N,K,\psi_{E^\kappa}\rangle = -\frac{a_z^0\zeta_e d_z\sqrt{N^2-K^2}}{2J+1} \tag{3.39b}$$

$$\begin{aligned}\langle\psi_{E^\kappa},J,N,-K+2,\wp|\mathcal{H}(E^\kappa)|\wp,J,N,K,\psi_{E^\kappa}\rangle = h_1^{E^\kappa}(-1)^{N-K+\kappa+\wp}\\ \times\mathcal{F}_+(N,K-1)+\mathcal{F}_+(N,K-2)\end{aligned} \tag{3.39c}$$

$$\left\langle\psi_{A_j^\kappa},J,N,K,\wp\right|\mathcal{H}(A_j^\kappa)\left|\wp,J,N,K,\psi_{A_j^\kappa}\right\rangle = B_z z^{A_j^\kappa}K^2+\frac{1}{2}(B_{xx}^{A_j^\kappa}+B_{yy}^{A_j^\kappa})(N(N+1)-K^2) \tag{3.40}$$

Next, the elements coupling A_1^κ and A_2^κ with each other and with E^κ are considered.

$$\left\langle\psi_{A_2^\kappa},J,N,K\right|\mathcal{H}(A_2^\kappa,A_1^\kappa)\left|J,N,K,\psi_{A_1^\kappa}\right\rangle = -2B_{zz}^{A_2^\kappa A_1^\kappa}\zeta_t^{A_2^\kappa A_1^\kappa}K\mp a_z\zeta_e d_z^{A_2^\kappa A_1^\kappa}\frac{K}{2J+1} \tag{3.41a}$$

$$\left\langle\psi_{A_2^\kappa},J,N\pm1,K\right|\mathcal{H}(A_2^\kappa,A_1^\kappa)\left|J,N,K,\psi_{A_1^\kappa}\right\rangle = a_z\zeta_e d_z^{A_2^\kappa A_1^\kappa}\frac{\sqrt{(J+1/2)^2-K^2}}{2J+1} \tag{3.41b}$$

$$\left\langle\psi_{A_j^\kappa},J,N,K+2\right|\mathcal{H}(A_j^\kappa,E^\kappa)\,|E^\kappa,J,N,K,\wp\rangle = \frac{1}{\sqrt{2}}h_{1+}^{A_j^\kappa,E^\kappa}\mathcal{F}_+(N,K)\mathcal{F}_+(N,K+1) \tag{3.42a}$$

$$\left\langle\psi_{A_j^\kappa},J,N,-K-2\right|\mathcal{H}(A_j^\kappa,E^\kappa)\,|E^\kappa,J,N,K,\wp\rangle = \frac{(-1)^{N-K+\kappa+\wp}}{\sqrt{2}}h_{1-}^{A_j^\kappa,E^\kappa}\mathcal{F}_+(N,K)\mathcal{F}_+(N,K+1) \tag{3.42b}$$

$$\langle\psi_{E^\kappa},J,N,K-2,\wp|\,\mathcal{H}(A_j^\kappa,E^\kappa)\left|A_j^\kappa,J,N,K\right\rangle = \frac{1}{\sqrt{2}}h_{1+}^{A_j^\kappa,E^\kappa}\mathcal{F}_+(N,K-1)\mathcal{F}_+(N,K-2) \tag{3.42c}$$

$$\langle \psi_{E^\kappa}, J, N, -K-2, \wp | \, \mathcal{H}(A_j^\kappa, E^\kappa) \, | A_j^\kappa, J, N, K \rangle = \frac{(-1)^{N+K+\kappa+\wp}}{\sqrt{2}} h_{1-}^{A_j^\kappa, E^\kappa} \mathcal{F}_+(N,K)\mathcal{F}_+(N,K+1) \tag{3.42d}$$

Finally, the elements coupling the different components of E^κ are considered.

$$\begin{aligned} \left\langle \psi_{E^\kappa(n)}, J, N, K, \wp \right| \mathcal{H}(E^\kappa(n), E^\kappa(m)) \left| \wp, J, N, K, \psi_{E^\kappa(m)} \right\rangle = B_{zz}^{E^\kappa(n)E^\kappa(m)} K^2 \\ + \frac{1}{2}(B_{xx}^{E^\kappa(n)E^\kappa(m)} + B_{yy}^{E^\kappa(n)E^\kappa(m)})(N(N+1) - K^2) \\ - \left(2B_{zz}^{E^\kappa(n)E^\kappa(m)} \zeta_t^{E^\kappa(n)E^\kappa(m)} \mp \frac{a_z^0 \zeta_e d_z^{E^\kappa(n)E^\kappa(m)}}{2J+1} \right) K \end{aligned} \tag{3.43a}$$

$$\langle \psi_{E^\kappa(n)}, J, N-1, K, \wp | \mathcal{H}(E^\kappa(n), E^\kappa(m)) | \wp, J, N, K, \psi_{E^\kappa(m)} \rangle = -\frac{a_z^0 \zeta_e d_z^{E^\kappa(n)E^\kappa(m)} \sqrt{N^2 - K^2}}{2J+1} \tag{3.43b}$$

$$\begin{aligned} \langle \psi_{E^\kappa(n)}, J, N, -K+2, \wp | \mathcal{H}(E^\kappa(n), E^\kappa(m)) | \wp, J, N, K, \psi_{E^\kappa(m)} \rangle = h_1^{E^\kappa(n), E^\kappa(m)} (-1)^{N-K+\kappa+\wp} \\ \times \mathcal{F}_+(N, K-1) + \mathcal{F}_+(N, K-2) \end{aligned} \tag{3.43c}$$

The definitions for new parameters are listed below. Essentially, all parameters play the same role, but since the expectation is taken over different vibronic states, the actual values for the parameters are different between different expectations.

$$B_{zz}^{\Gamma,\Gamma'} \zeta_t^{\Gamma,\Gamma'} = \langle \psi_\Gamma | \left(B_{zz} \hat{\pi}_z + B_{z-} \hat{\pi}_+ + B_{z+} \hat{\pi}_- \right) | \psi_{\Gamma'} \rangle \tag{3.44}$$

$$a_z \zeta_e d_z^{\Gamma,\Gamma'} = \langle \psi_\Gamma | \, a_z \hat{L}_z \, | \psi_{\Gamma'} \rangle \tag{3.45}$$

$$h_{1\pm}^{\Gamma,\Gamma'} = \frac{1}{\sqrt{2}} \langle \psi_\Gamma | \, B_{\pm\pm} \, | \psi_{\Gamma'} \rangle \tag{3.46}$$

Table 3.2: Character table of D_{3h} point group for taken from Bunker and Jensen[3]

D_{3h}	E	$2C_3$	$3C_2$	σ_h	$2S_3$	$3\sigma_v$	
$D_{3h}(M)$	E	(123)	(23)	E^*	$(123)^*$	$(23)^*$	
A_1'	1	1	1	1	1	1	α_{zz}, $\alpha_{xx}+\alpha_{yy}$
A_1''	1	1	1	-1	-1	-1	
A_2'	1	1	-1	1	1	-1	$\hat{J}_z$
A_2''	1	1	-1	-1	-1	1	T_z
E'	2	-1	0	2	-1	0	(T_x,T_y),$(\alpha_{xx}$-$\alpha_{yy},\alpha_{xy})$
E''	2	-1	0	-2	1	0	$(\hat{J}_x,\hat{J}_y)$,$(\alpha_{xz},\alpha yz)$

3.2 Intensity

3.2.1 Nuclear Spin Statistics

$N^{16}O_3$ is the main isotopologue of NO_3. The ground state of the oxygen nucleus has nuclear spin $I = 0$. By the Spin-Statistics Theorem,[3] oxygen is a boson and the state of the system must be totally symmetric with respect to exchange of any two oxygen atoms.

The symmetry of the symmetry of the total wavefunction is a direct product of the rotational, vibronic, and nuclear symmetries.

$$\Gamma_{tot} = \Gamma_r \otimes \Gamma_{ve} \otimes \Gamma_n \ni \Gamma_{ts} \tag{3.47}$$

This product must contain the totally symmetric representation for bosons. The terms in order are the symmetry of the total, rotational, vibronic, and nuclear wavefunction and Γ_{ts} is the totally symmetric representation. In order to enforce this condition, all possible states for each component of this product will be analyzed. The molecular symmetry group of NO_3 is $D_{3h}(M)$, which is isomorphic to the D_{3h} point group. The character table of $D_{3h}(M)$ and the D_{3h} point group is shown as Table 3.2. Table 3.2 shows all operations of this point group. E is the identity operator. $(i, j, \ldots, k)$ is the permutation operator on the three oxygen. For example, (23) switches two of the oxygen atoms. E^* is the inversion operator through the nitrogen. Greater detail regarding the analysis of the nuclear spins can be found in Ming-Wei Chen's dissertation.[38]

Table 3.3: Characters of the rotational basis functions under the D_{3h} point group.[3]

	E	(123)	(23)	E*	(123)*	(23)*
$\|J, N, K \neq 0\rangle$	2	$2\cos\left(\frac{2\pi K}{3}\right)$	0	$2(-1)^K$	$2\cos\left(-\frac{\pi K}{3}\right)$	0
$\|J, N, 0\rangle$	1	1	$(-1)^N$	1	1	$(-1)^N$

In the ground nuclear state of NO_3, nitrogen has spin $I = 1$ and oxygen has spin $I = 0$. The character of each nuclear spin wavefunction under the operations of the D_{3h} point group are given by[3]

$$\chi_n[\hat{O}] = \prod_i (2I_i + 1) \tag{3.48}$$

where I_i indicates the nuclear spin of all the nuclei grouped together by the operator, and i runs over all such groups. For example, the (23) operator switches two oxygen atoms and groups those together. The last oxygen and the nitrogen are untouched and both constitute a term in the product. So $\chi_n[(23)] = 1 \times 1 \times 3$. The characters of the nuclear wavefunction under each operator are

$$\begin{aligned}
\chi_n[E] &= 1 \times 1 \times 1 \times 3 = 3 \\
\chi_n[(123)] &= 1 \times 3 = 3 \\
\chi_n[(23)] &= 1 \times 1 \times 3 = 3 \\
\chi_n[E^*] &= 1 \times 1 \times 1 \times 3 = 3 \\
\chi_n[(123)^*] &= 1 \times 3 = 3 \\
\chi_n[(23)^*] &= 1 \times 1 \times 3 = 3
\end{aligned} \tag{3.49}$$

Γ_n can thus be reduced to $\Gamma_n = 3A_1'$.

First, the $\widetilde{X}^2A_2'$ state of $NO_3$is considered. Transitions in the spectra occur from the ground vibrationaless level, so Γ_{ve} is just the representation of the electronic state. $\Gamma_{ve} = A_2'$. The representation of the rotational basis functions can be determined from the character table in Table 3.3 and Table 3.4. The results are representations listed in Table 3.4.

By applying Equation 3.47, the only rotational levels that produce a Γ_{tot} containing the

Table 3.4: Full character table of the rotational basis functions under the D_{3h} point group.[3]

K	E	(123)	(23)	E^*	$(123)^*$	$(23)^*$	Γ_r
0 (N Even)	1	1	1	1	1	1	A_1'
0 (N Odd)	1	1	-1	1	1	-1	A_2'
$6n+1$	2	-1	0	-2	1	0	E''
$6n+2$	2	-1	0	2	-1	0	E'
$6n+3$	2	2	0	-2	-2	0	$A_1'' \oplus A_2''$
$6n+4$	2	-1	0	2	-1	0	E'
$6n+5$	2	-1	0	-2	1	0	E''
$6n$	2	2	0	2	2	0	$A_1' \oplus A_2'$

totally symmetric representation are levels with, for all integers n,

$$K'' = 0(N \text{ odd}), 6n, 6n+3 \tag{3.50}$$

For the $\widetilde{A}^2E''$ state, the perpendicular transitions terminate on levels with vibronic symmetry $\Gamma_{ev} = E'$. Again, using Table 3.4, the only rotational levels which give a totally symmetric representation in Equation 3.47 are levels with

$$K' = 6n+1, 6n+2, 6n+4, 6n+5 \tag{3.51}$$

These results are summarized in Figure 3.1

3.2.2 Rotational Transition Intensities

The relative transition intensity I of the rotational transition in a given rovibronic band is calculated from the population of the ground state level (Boltzmann distribution) and square of the dipole overlap integral (Fermi's Golden Rule) or line strength S.[3]

$$I(\tau' J'; \tau'' J'') = g_J g_I e^{\frac{-E_{\eta''}}{k_B T}} \mathbf{S}(\tau' J'; \tau'' J'') \tag{3.52}$$

$$\mathbf{S}(\tau' J'; \tau'' J'') = \left| \sum_{\alpha} \left\langle \psi_{E'}, J', N', K', 1-\wp \right| \mu_\alpha \left| \wp, J', N', K', \psi_{A_2'} \right\rangle \right|^2 \tag{3.53}$$

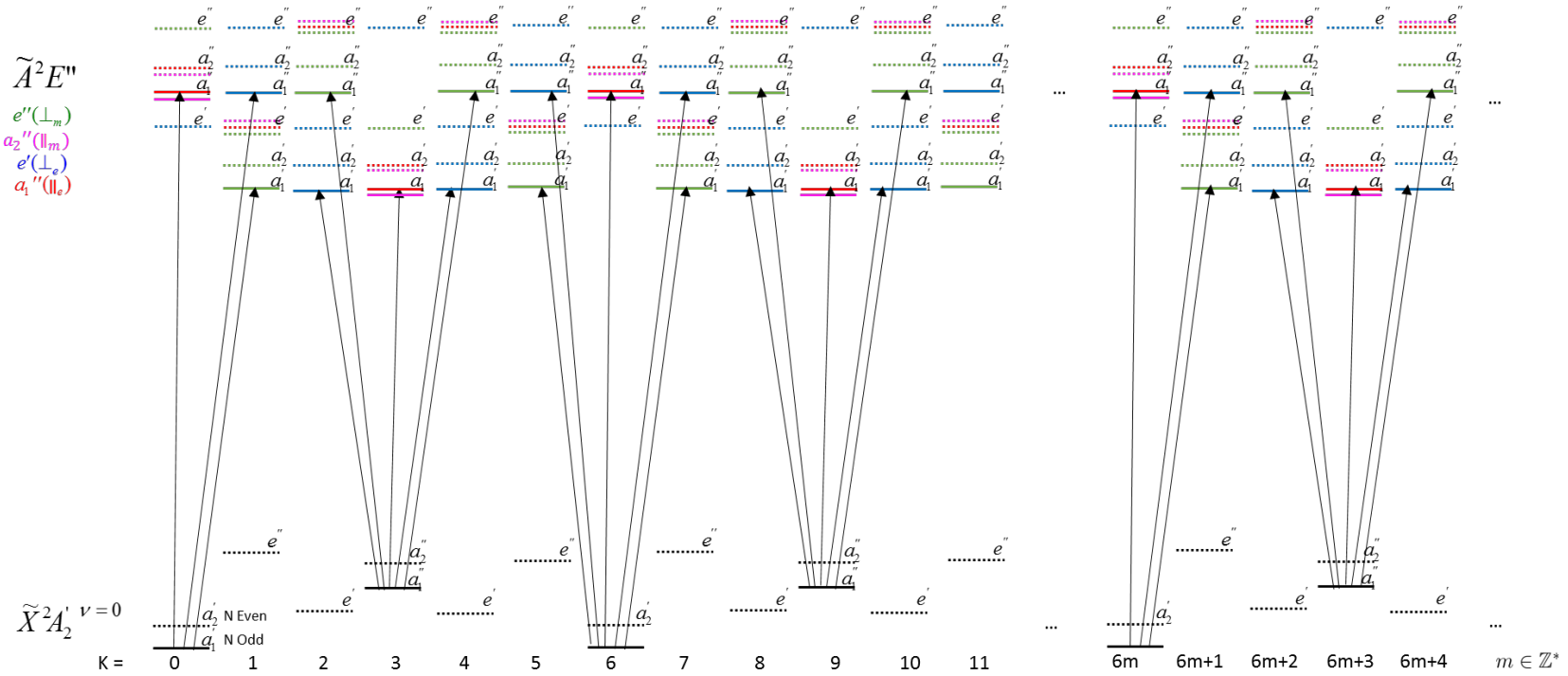

Figure 3.1: Schematic diagram of the allowed rovibronic transitions in NO_3, taking into account nuclear spin statistics. Each line represents a vibronic level of a different symmetry. The columns are separated by K values. The label by each line corresponds to the level's rovibronic symmetry. The color of each line corresponds to the type of transition: Red for parallel electric dipole, blue for perpendicular electric dipole, magenta for parallel magnetic dipole, green for perpendicular magnetic dipole. Dotted levels indicate levels to and from which no rovibronic transitions are allowed, by nuclear spin statistics. Note that the levels are not ordered by energy and no N dependence is shown.

τ' refers to the excited state and τ'' refers to the ground state. $E_{\eta''}$ is the energy of the ground state level and the upper and lower indices refers to the intensity or line strength between upper and lower states. T is the temperature and k_B is Boltzmann's constant. μ_α are the components of the dipole moment operator. $g_J = 2J + 1$ is the degeneracy of the rotational levels and g_I (equals 1 or 0) is the degeneracy of the nuclear spin states that was discussed in Section 3.2.1.

The form of $\mathbf{S}$ was derived by Zare.[42] In this case, the ground vibronic eigenfunction has the symmetry of the vibrationaless level of the $\widetilde{X}^2A_2'$ state, which is A_2', and the excited vibronic eigenfunction has symmetry E' for the perpendicular electric dipole bands and $A_1{}''$ for the parallel electric dipole bands.

Perpendicular Band Intensities

The simplified form for the perpendicular transition line strength in a Wang-Type basis is

$$\begin{aligned}\mathbf{S}(\tau' J'; \tau'' J'') =& \sqrt{(2J''+1)\,(2J'+1)\,(2N''+1)(2N'+1)}\left\langle \psi_{E'_\pm}\right| \mu_\pm \left|\psi_{A_2'}\right\rangle^2 \\ &\times \frac{(-1)^{J'+S+K'}}{\sqrt{2}} \begin{Bmatrix} J'' & J' & 1 \\ N' & N'' & S \end{Bmatrix} \\ &\times \left[\begin{pmatrix} N' & 1 & N'' \\ -K' & 1 & K'' \end{pmatrix} + (-1)^{N''-K''+\wp} \begin{pmatrix} N' & 1 & N'' \\ -K' & 1 & K'' \end{pmatrix} \right]\end{aligned}$$

$\left\langle \psi_{E'_\pm}\right| \mu_\pm \left|\psi_{A_2'}\right\rangle$ is the transition dipole moment. $(\cdots)$ and $\{\cdots\}$ are the Wigner 3j and 6j symbols respectively whose values are known.[3] Moreover, these Wigner symbols tell us the rotational selection rules. For a perpendicular dipole transition in the Wang-type basis, the selection rules are

$$\begin{aligned} J' - J'' &= 0, \pm 1 \\ K' - K'' &= 1 \\ K' + K'' &= 1 \end{aligned} \tag{3.54}$$

Parallel Band Intensity

For the parallel bands,

$$\begin{aligned}\mathbf{S}(\tau' J'; \tau'' J'') =& (-1)^{K'+J\prime+S+1} \\ & \times \sqrt{(2J''+1)\,(2J'+1)\,(2N''+1)(2N'+1)}\left\langle \psi_{A^{1-\kappa}_{1-j}} \right| \mu_z \left| \psi_{A'_2} \right\rangle^2 \\ & \times \begin{Bmatrix} J'' & J' & 1 \\ N' & N'' & S \end{Bmatrix} \begin{pmatrix} N' & 1 & N'' \\ -K & 0 & K \end{pmatrix}\end{aligned}$$

The selection rules for a parallel transition are:

When $K = 0$

$$\begin{gathered}\Delta J = 0 \ (J'' \neq J' \neq 0) \\ \Delta J = \pm 1 \\ \Delta K = 0\end{gathered} \tag{3.55}$$

and when $K \neq 0$

$$\begin{gathered}\Delta J = \pm 1 \\ \Delta K = 0\end{gathered} \tag{3.56}$$

3.3 Implementation

The Hamiltonian and intensity functions were implemented as a dynamic link library compatible with group software SPECVIEW. Subroutines which generated the Hamiltonian matrix and calculated intensity of transitions, weighing nuclear spin statistics, were written in C++ and compiled into a *.dll. SPECVIEW calls these subroutines to diagonalize the Hamiltonian matrix and calculate the intensities of transitions. SPECVIEW is equipped with a GUI to display the simulated spectrum and allows for assignments of transitions to experimental frequencies. A least-squares routine is included to vary the parameters defined in the Hamiltonian and optimize agreement between calculated frequencies and assigned frequencies.

Chapter 4
Rovibronic Analysis of the Degenerate Vibronic Bands

The rotationally resolved spectra of the vibronic bands in the $\widetilde{A}^2E'' \leftarrow \widetilde{X}^2A_2'$ transition were collected previously in our group using a jet-cooled sample of NO_3 with a cavity ring-down apparatus.[37] The allowed vibronic transitions in NO_3 are dictate by the dipole moment operator and the details are discussed in Section 1.2. The list of allowed transitions along with the band type are listed in Table 1.1. The parallel electric dipole vibronic transitions terminate on levels of a_1'' vibronic symmetry and the perpendicular electric dipole vibronic bands terminate on levels of degenerate e' symmetry. Of these bands, the rotationally resolved spectra of the 2_0^1, $2_0^1 4_0^2$, and $2_0^1 4_0^2$ bands have been collected.

The structure of the $\widetilde{X}^2A_2'$ state has been well-studied by Kawaguchi *et al.* and analyzed using an oblate symmetric top Hamiltonian discussed in Section 3.1. The rotational constants, centrifugal constants, and spin-rotational constants from this analysis are presented in Table 4.1 and will be the parameters used for the $\widetilde{X}^2A_2'$ state in the proceeding analysis of the $\widetilde{A}^2E'' \leftarrow \widetilde{X}^2A_2'$transition.[4]

Previously, a handful of the parallel vibronic transitions of a_1'' symmetry were satisfactorily analyzed in our group.[37] In particular, the 3_0^1, $3_0^1 4_0^1$, 4_0^1, 4_0^2, and 4_0^3 bands were able to be characterized. The simulation of the first three are presented in Figure 4.1. The oblate symmetric top model was used to describe both the $\widetilde{X}^2A_2'$ state and the $\widetilde{A}^2E''$ state for the parallel transitions to levels of a_1'' vibronic symmetry. However, this model was not capable of simulating the perpendicular vibronic transitions to levels of e' vibronic symmetry,

Table 4.1: Oblate symmetric top parameters as determined by Kawaguchi *et al.*[4] These are the parameters used in the proceeding simulations.

Constant (cm^{-1})	$\widetilde{X}^2A_2'(\nu = 0)$
B	0.4585445(61)
C	0.2286274(57)
D_N (10^{-6})	1.0880(94)
D_{NK} (10^{-6})	-2.062(19)
D_K (10^{-6})	1.047(14)
ϵ_{bb}	-0.01642(14)
ϵ_{cc}	0.00074(14)

producing fewer lines than observed in the experimental spectra.

Since then, the spectra of the 2_0^1 and $2_0^1 4_0^2$perpendicular vibronic bands have been successfully analyzed. The oblate symmetric top model discussed in Section 3.1 was used to describe the ground state levels and the modified rotational Hamiltonian also described in Section 3.1 was used to describe the rovibronic levels of the vibronic levels of the $\widetilde{A}^2E''$ electronic state. In the proceeding section, the analysis of the two perpendicular bands collected in our group are discussed. In general, a significant contribution from coriolis and spin-orbit coupling was found, but only negligible JT distortions was found. Moreover, there is evidence of perturbations from high energy rovibrational levels in the $\widetilde{X}^2A_2'$ state.

4.1 SPECVIEW and Procedure of Analysis

The rovibronic analysis was done on our group's spectral simulation software, SPECVIEW. The SPECVIEW software calls subroutines created outside of the program that generate the Hamiltonian matrix and transition intensities. SPECVIEW uses this to produce a visual spectral simulation with an artificial bandwidth. Any frequency can be assigned to each transition. SPECVIEW performs a least-squares optimization on the parameters defined in the Hamiltonian to best match transitions to assigned frequencies. The optimization is done by taking a numerical Jacobian and Hessian in all of the parameters. Since J is a good quantum number in this case, the Hamiltonian matrix subroutine generates separate

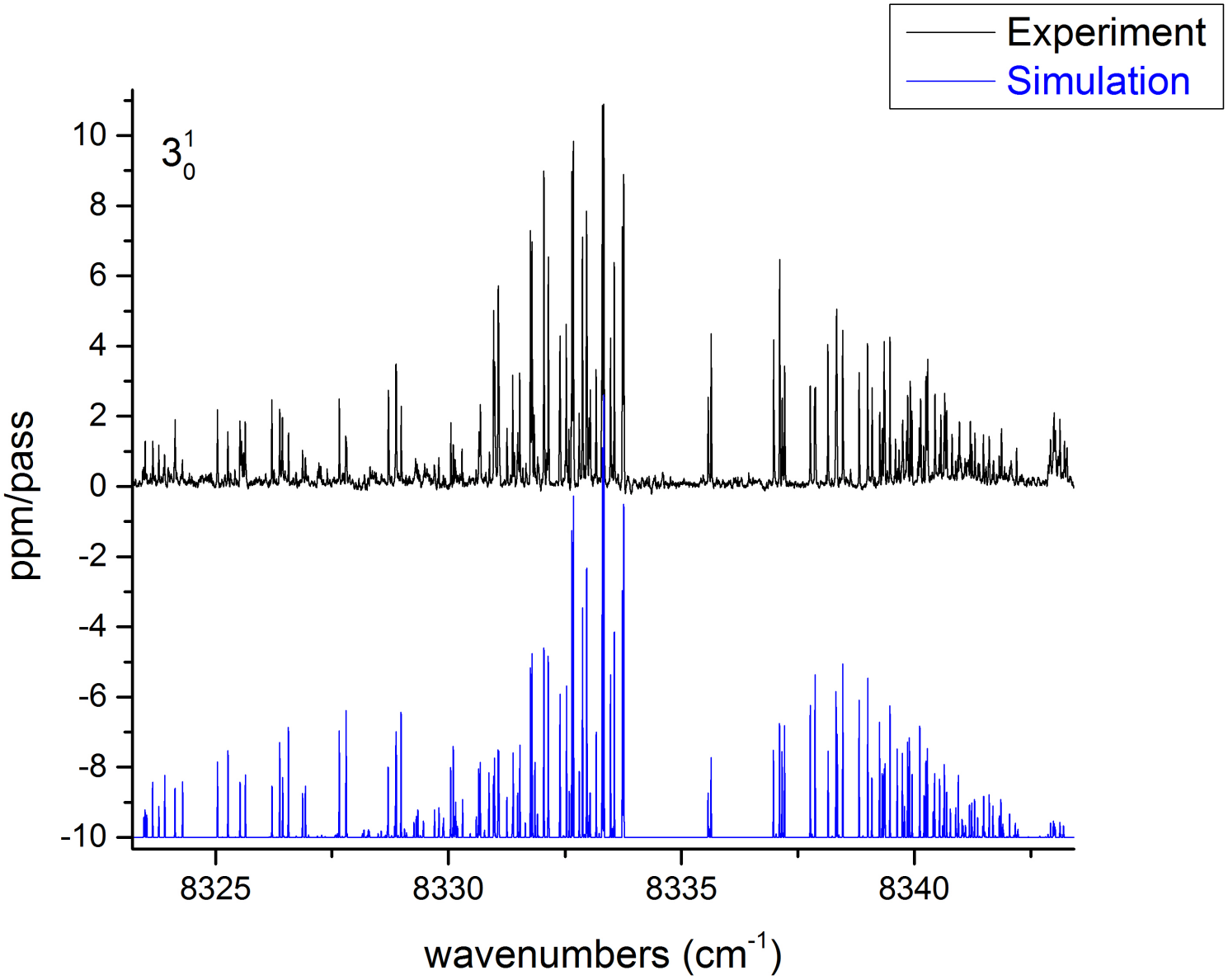

(a) Simulation of the 3_0^1 band.

Figure 4.1: Rovibronic simulation of the parallel $\widetilde{A}^2E'' \leftarrow \widetilde{X}^2A_2'$ vibronic bands

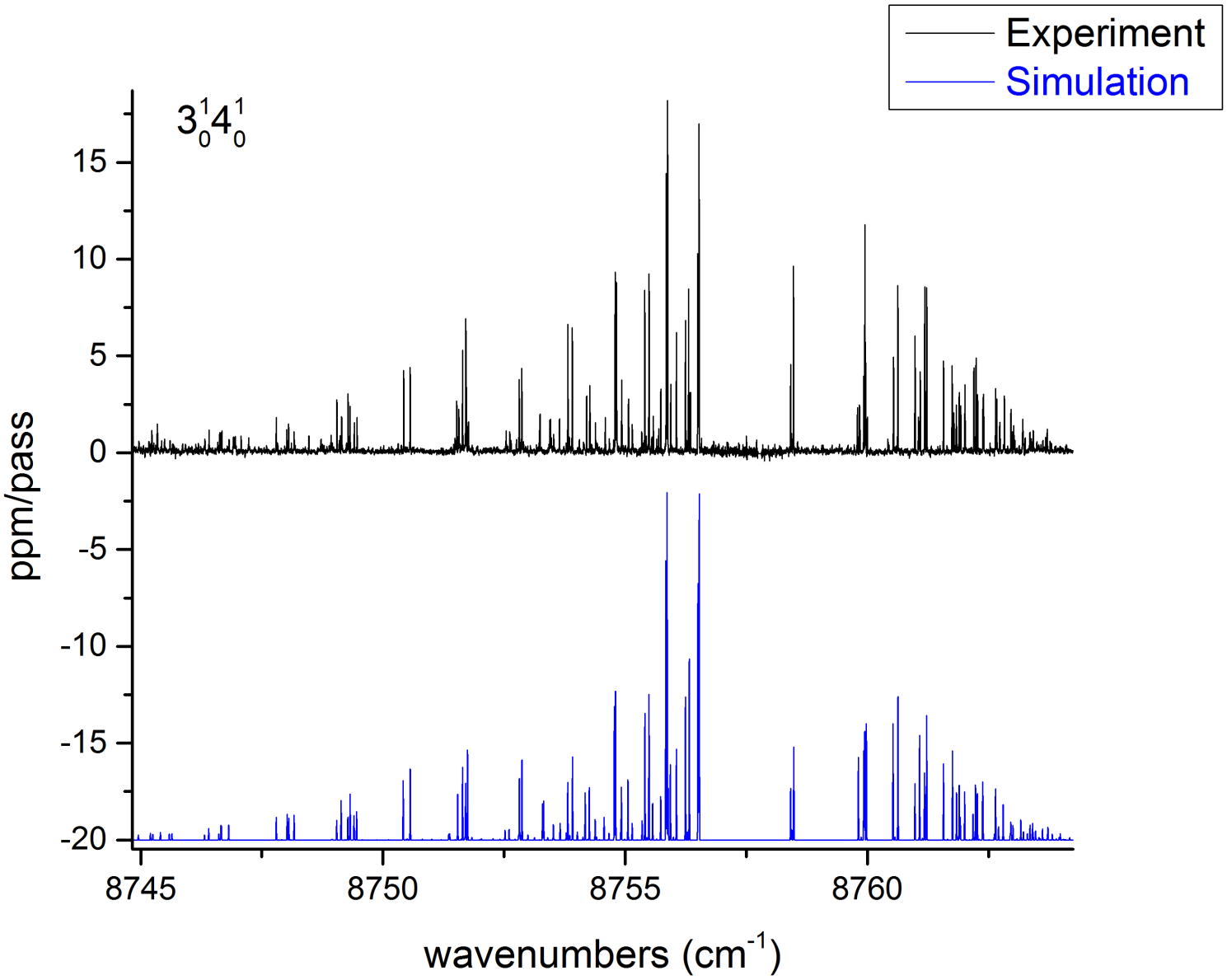

(b) Simulation of the $3_0^1 4_0^1$ band.

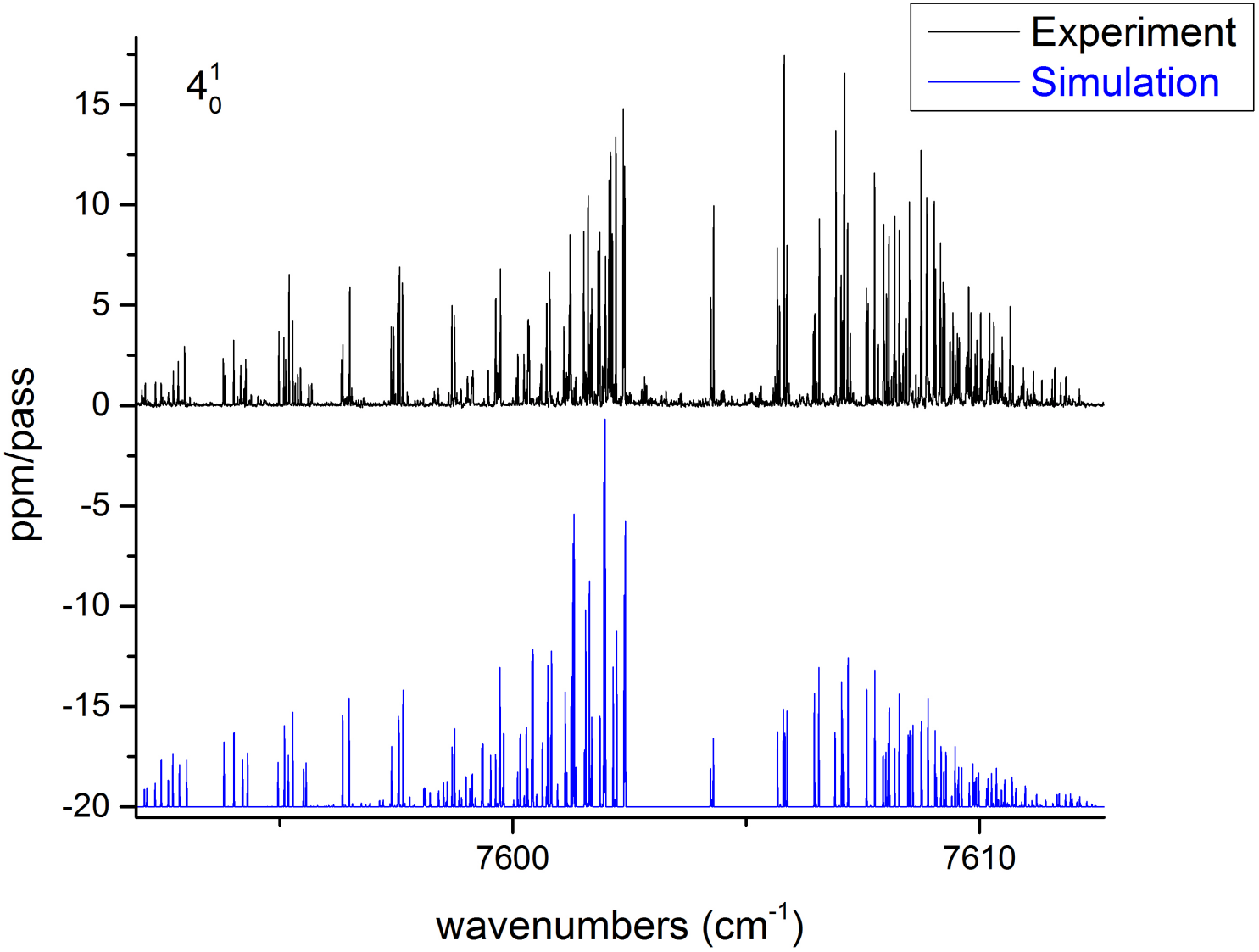

(c) Simulation of the 4_0^1 band.

J blocks in the total Hamiltonian that are then treated separately in SPECVIEW. Further details regarding SPECVIEW can be found in the SPECVIEW manual.[37]

The following analyses are performed in SPECVIEW using the model described in Chapter 3. This $\widetilde{X}^2A_2'$ state levels are calculated from an oblate symmetric top Hamiltonian described in Section 3.1 and the $\widetilde{A}^2E''$ levels are calculated from the full model described in Section 3.1. The parameters for the $\widetilde{X}^2A_2'$ state model were fixed to the values determined by Kawaguchi *et al.*[4] The parameters in the $\widetilde{A}^2E''$ state model were varied as free parameters for the least-squares fit. In all of the presented simulations, J levels up to $J = \frac{21}{2}$ are included, and this was found to be adequately converged for the spectra.

The fitting was done in the expected manner of assigning unambiguous transitions, running a fit on the parameters and producing a new simulated spectrum, and repeat by assigning more transitions that better match experiment with the newly determined parameters. The transitions are assigned by checking a combination difference criterion. From the selection rules in Equation 3.54, transitions to an $\widetilde{A}^2E''$ state level with $J = J'$ should be observed from all $\widetilde{X}^2A_2'$ state levels with $J = J'' = J' - 1, J', J' + 1$, with the appropriate K selection rule. The rotational basis functions are further defined in terms of N where $J = N + S$. Here, $\Delta S = 0$ always so $N'' = N' - 1, N', N' + 1$ as well. Since the energy structure of the $\widetilde{X}^2A_2'$ is well-known, the differences between $\widetilde{X}^2A_2'$ state levels with these quantum numbers should also be known and readily available from the energies of the oblate symmetric top Hamiltonian used for the $\widetilde{X}^2A_2'$ state using the parameters in Table 4.1, which replicate other independent experimental measurements of the $\widetilde{X}^2A_2'$ state. Given any one of the

$$\begin{aligned}
\left|\tilde{A}, J, S, N.K'\right\rangle &\leftarrow \left|\tilde{X}, J+1, S, N+1, K''\right\rangle \\
\left|\tilde{A}, J, S, N, K'\right\rangle &\leftarrow \left|\tilde{X}, J, S, N, K''\right\rangle \\
\left|\tilde{A}, J, S, N, K'\right\rangle &\leftarrow \left|\tilde{X}, J-1, S, N-1, K''\right\rangle
\end{aligned} \tag{4.1}$$

transition frequencies, it is possible to infer the frequency of the other two. This is illustrated in Figure 4.2. If an assignment is correct, then the two other frequencies should also be observed in the experimental spectrum. The failure of the criterion was used for rejecting

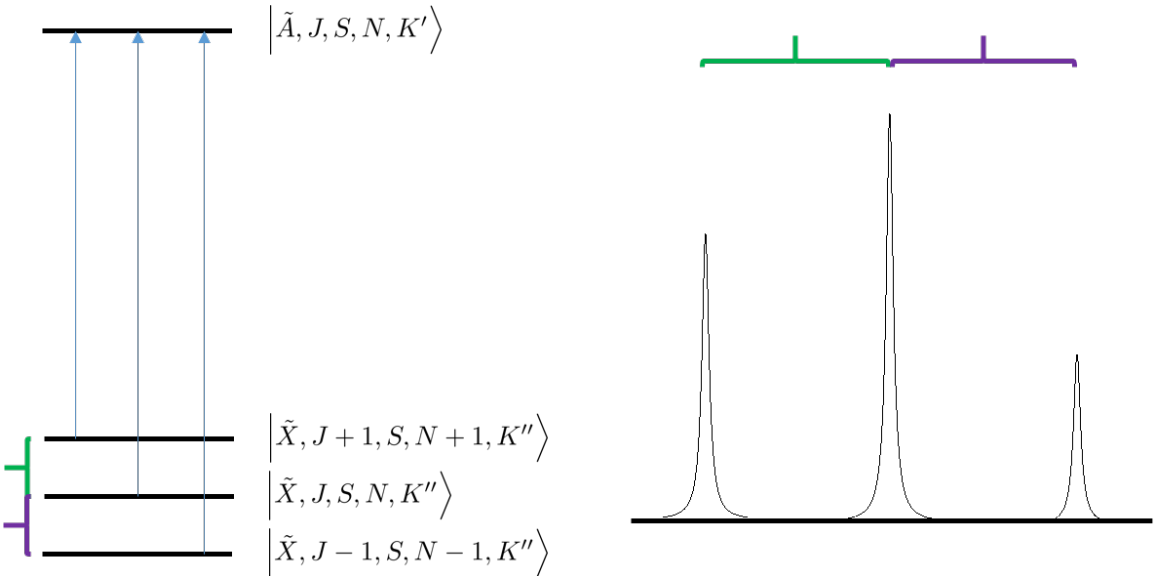

Figure 4.2: Diagram of the J selection rule used for combination differences. The spacing of the $\widetilde{X}^2A_2'$ state levels are known and thus, the other two transitions can be inferred from one observed transition.

assignments. This also allows for more assignments to be made from a single assignment. In circumstances where the intensity of inferred transitions are predicted to be too small to be observed, this criterion is ignored.

A compilation of combination differences, coded by N', for the 2_0^1 band assignments is pictured in Figure 4.3

4.2 The 2_0^1 Band

The fundamental of ν_2 is interesting in that it functions to illuminate the vibrationaless level. If there is a strong Jahn-Teller distortion, the effect is most strongly felt at the bottom of the electronic potential energy surface as discussed in Section 2.5. The Jahn-Teller effect in particular is present only along ν_3 and ν_4, and there is no coupling between ν_2 with any of these modes. This means that an excitation in ν_2 does not contribute to the relative of energy as one moves along the pseudo-rotational cut of the Jahn-Teller potential energy surface along a Jahn-Teller active mode, illustrated in Figure 2.7. 2_0^1 is the simplest band of

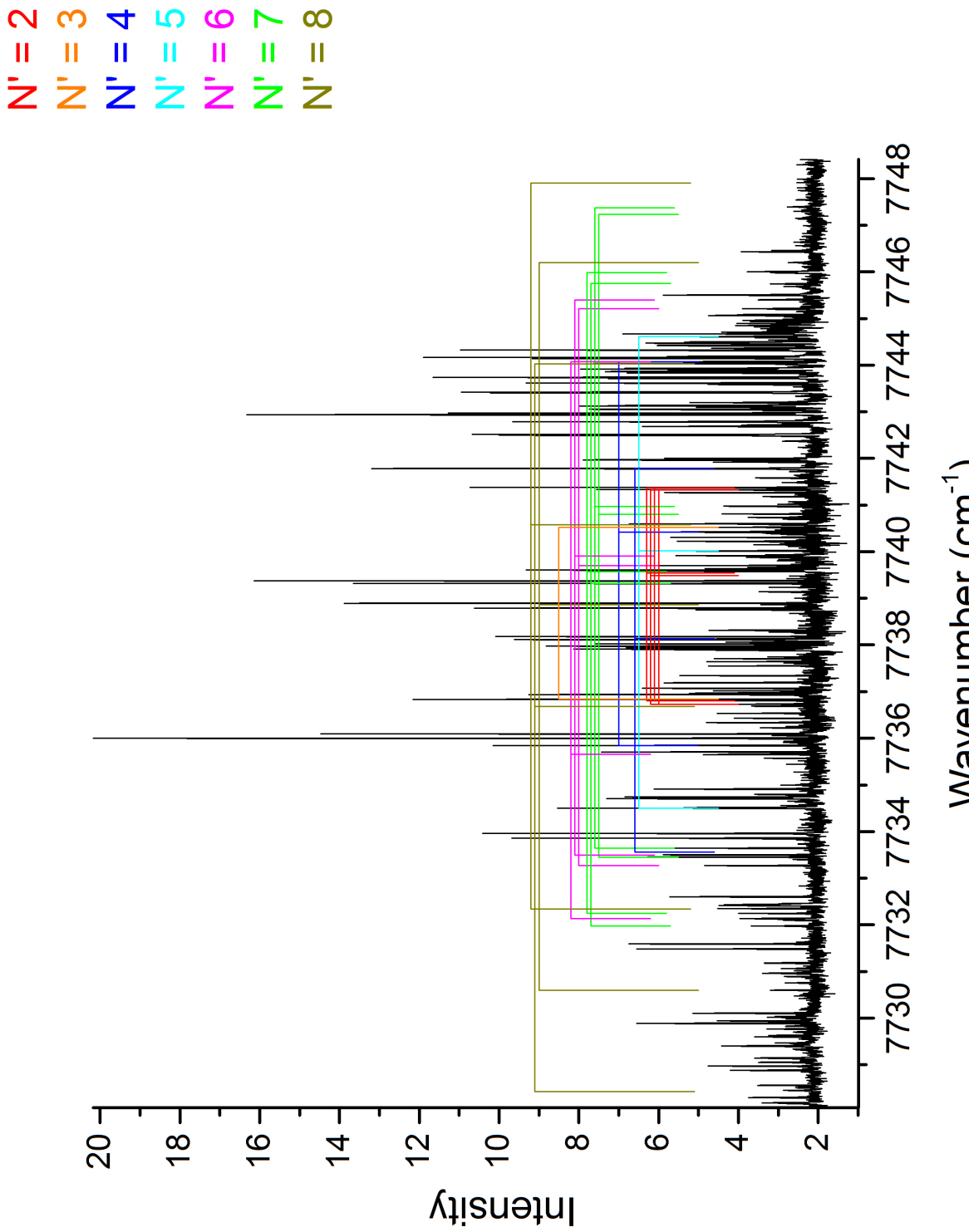

Figure 4.3: Experimental trace of the 2_0^1 band with combination difference triples labeled by N'.

Table 4.2: 2_0^1 band simulation parameters.

Constant (cm^{-1})	2_0^1	$\widetilde{X}^2A_2'(\nu=0)^4$
B	0.432933(37)	0.4585445(61)
C	0.215931(15)	0.2286274(57)
h_1	0.002187(31)	–
C·ζ_t	-0.033902(44)	–
$a_0\zeta_e d_z$	-0.0833(12)	–
D_N (10^{-6})	4.6[a]	1.0880(94)
D_{NK} (10^{-6})	-8.5[a]	-2.062(19)
D_K (10^{-6})	3.9[a]	1.047(14)
ϵ_{bb}	0.01799(16)	-0.01642(14)
ϵ_{cc}	0.0008[a]	0.00074(14)
T_{ev}	7739.816(4)	0.0
Lines Fit	84	
Temp (K)	17	
Std. Dev. of Fit (MHz)	194	

[a]Fixed during the fit.

this kind, which motivates a rotational analysis. For comparison, the previous simulation of 2_0^1 using an oblate symmetric top is presented in Figure 4.4, which shows that the old simulation does a poor job of simulating the experimental spectrum.

The simulation of the 2_0^1 band is presented in Figure 4.5. The parameters determined from the least-squares fit are presented in Table 4.2. The assignments used to obtain this fit are listed in Appendix A. The simulation is presented at a temperature of 17 K. In general, the simulation agrees quite well with the experimental spectrum. The P and Q branches of the spectrum agree very well as seen in Figure 4.6a and 4.6c respectively. It is interesting to note that while the lines on the blue end of Figure 4.6a seem to be poorly simulated, an alternative, independent experimental scan was taken of the 2_0^1 band and the P branch agrees more closely with the simulation in intensity as shown in Figure 4.6b. This highlights the experimentally variability in intensity. Some of the simulation discrepancies may be due to experimental error. The R branch pictured in Figure 4.6d however, is very dense. The higher J levels in the R branch are more sensitive to centrifugal distortion. Because of the difficulty of assigning levels in this region however, the centrifugal constants have not yet

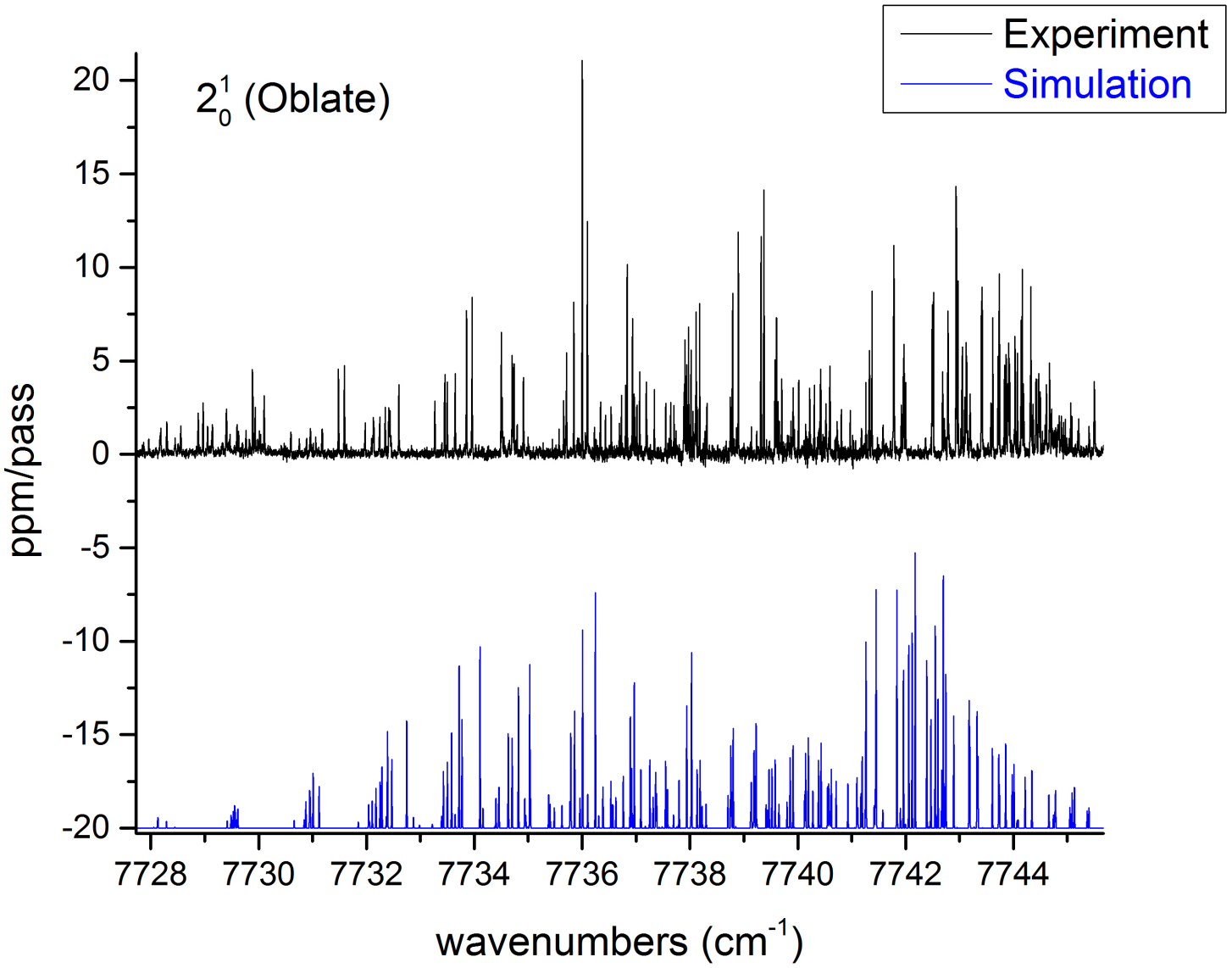

Figure 4.4: Previous simulation of the 2_0^1 band using an oblate symmetric top Hamiltonian. The simulation is poor.

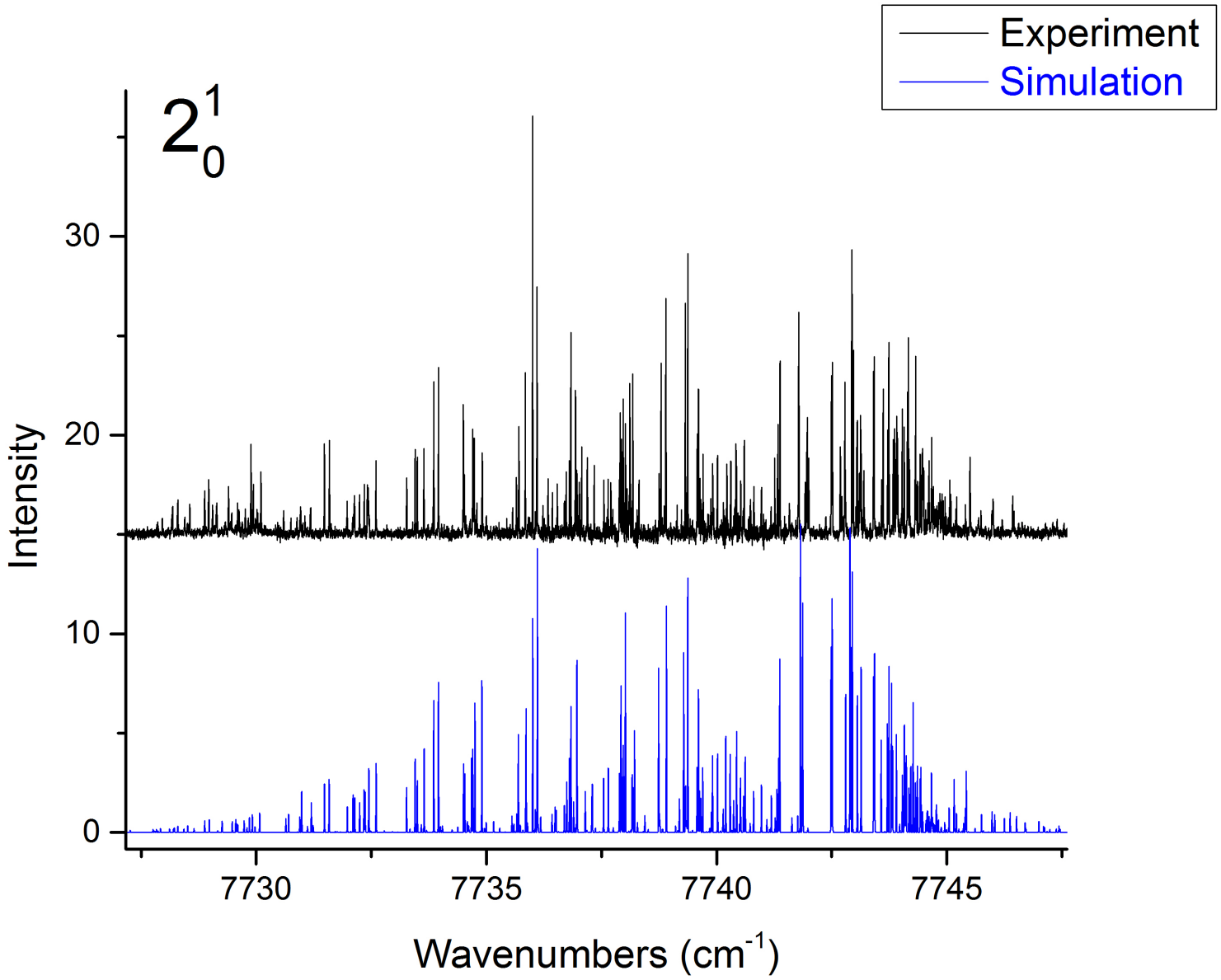

Figure 4.5: The rovibronic simulation of the 2_0^1 band. The upper trace is the experimental spectrum. The lower trace is the simulated spectrum.

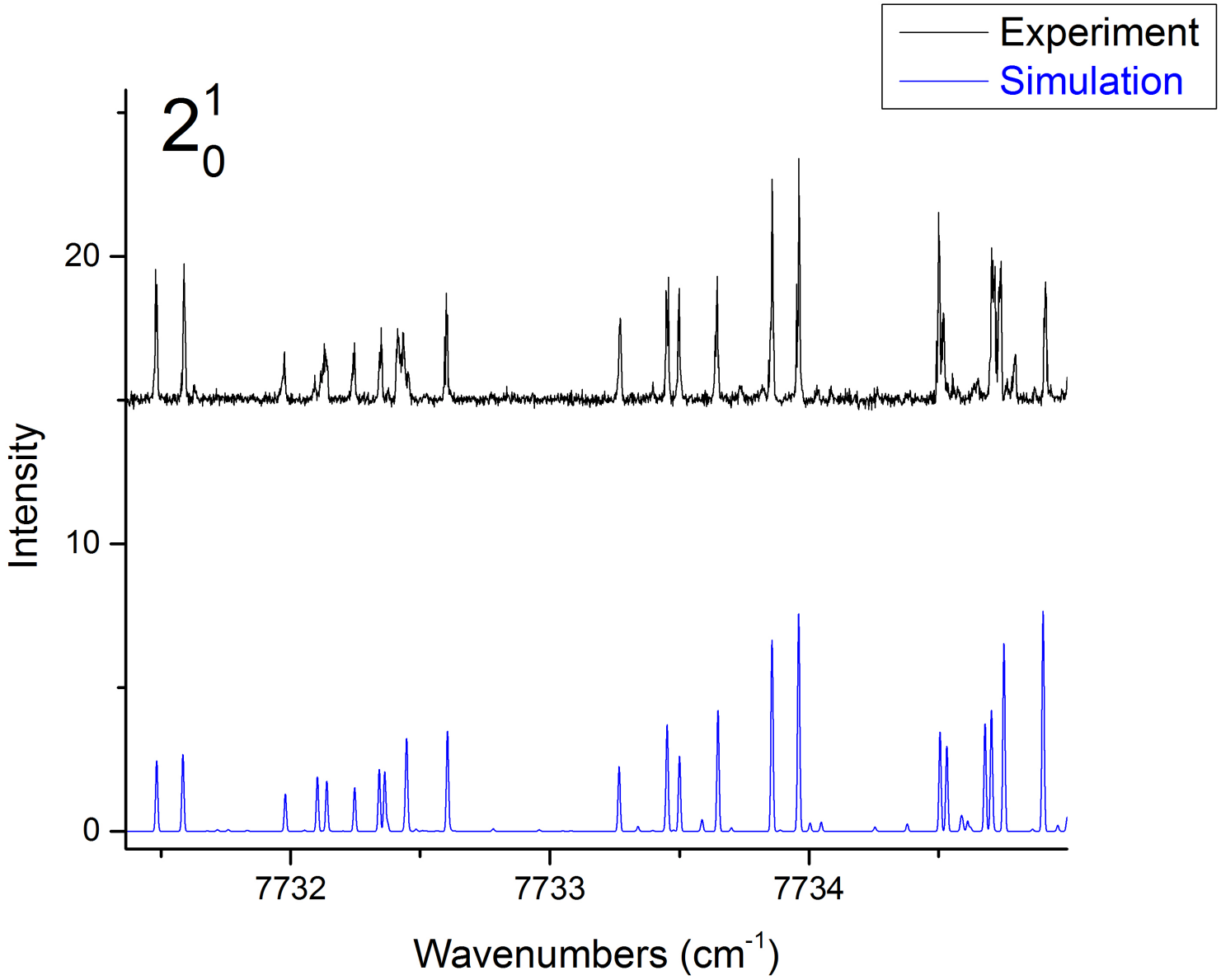

(a) 2_0^1 P-Branch Region

Figure 4.6: Closer view of the 2_0^1 band simulation in the P, Q, and R branches.

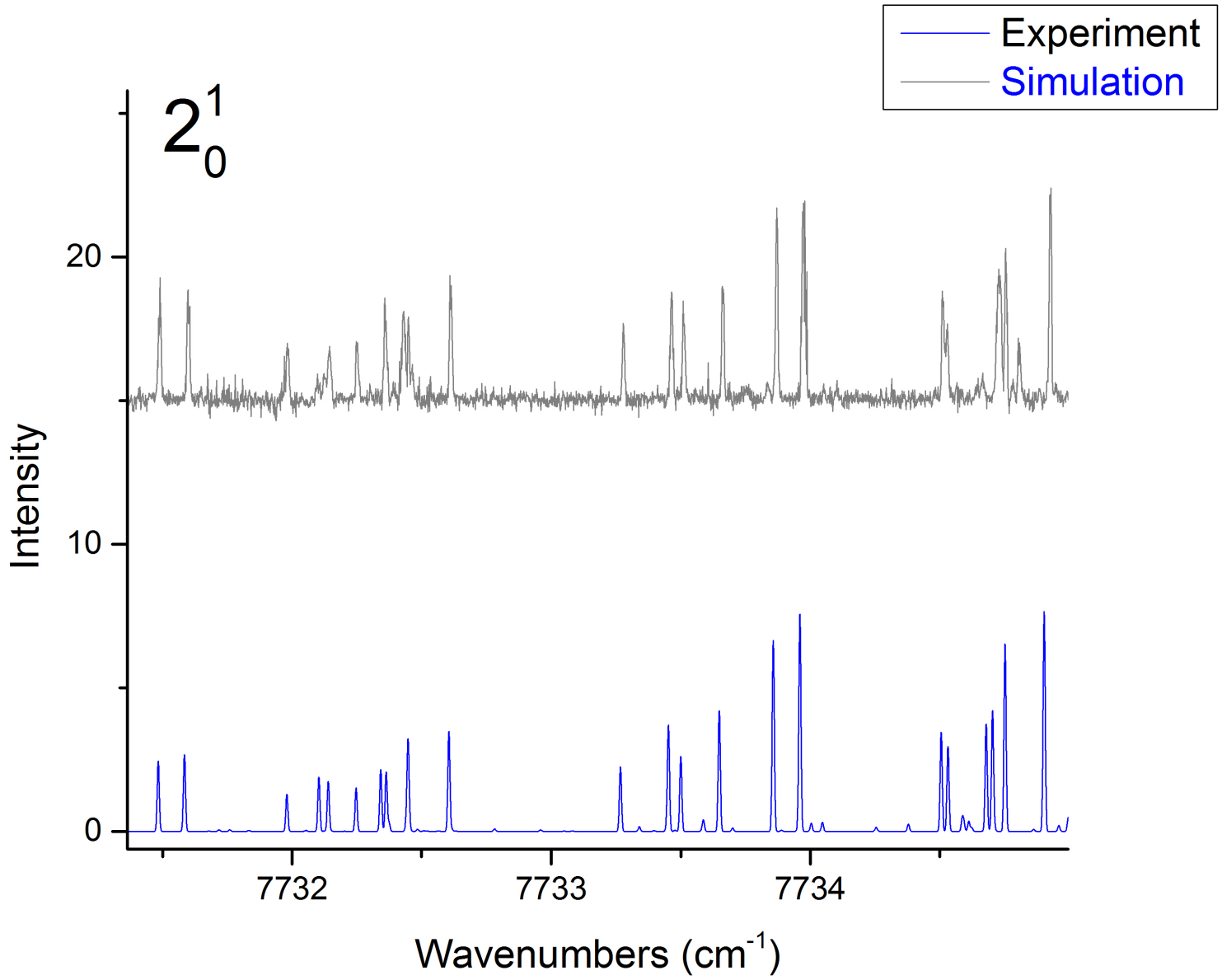

(b) 2_0^1 P-Branch Region (Alternative Experimental Trace). The difference in intensities between two different traces highlights the variability in intensity because of experimental error.

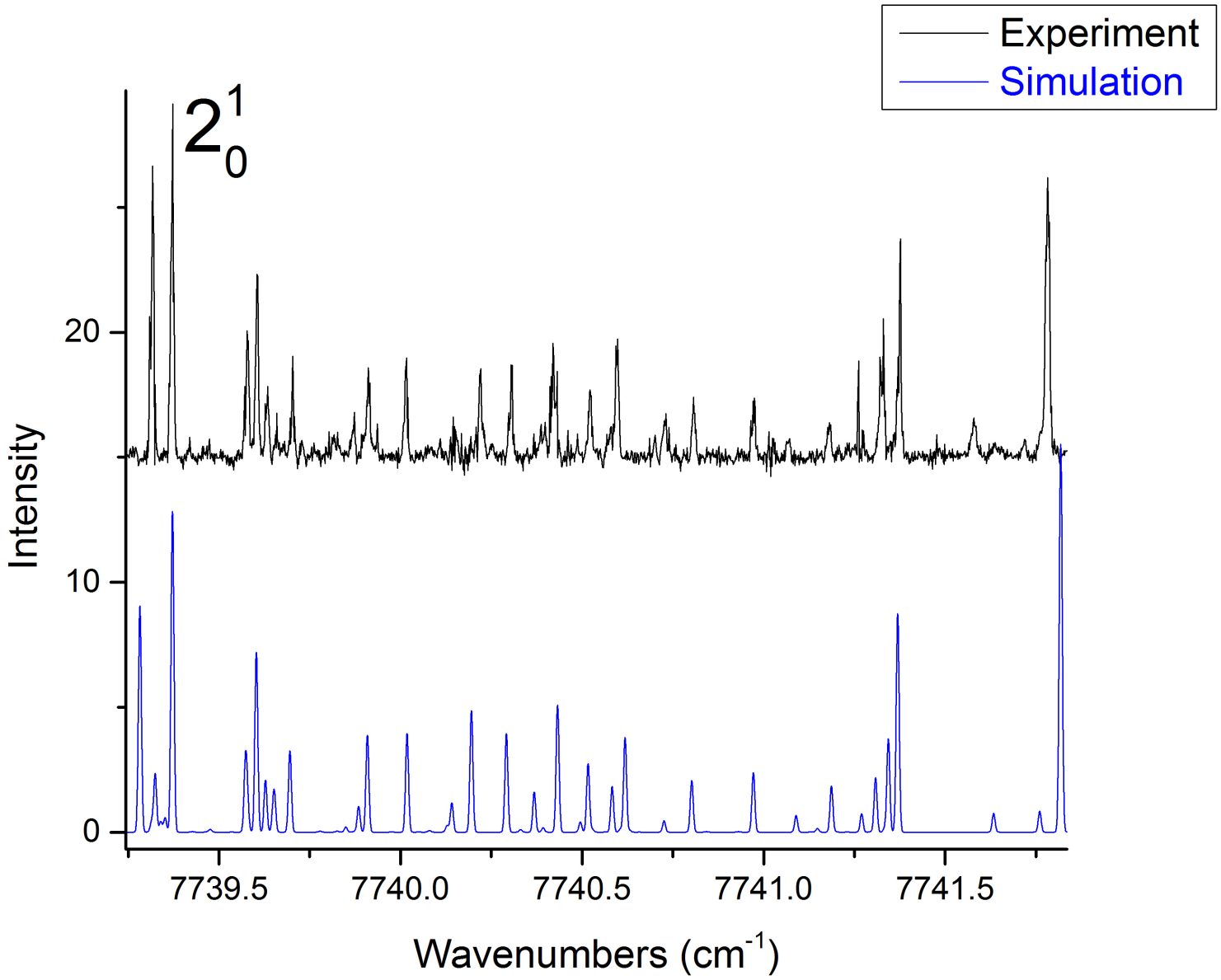

(c) 2_0^1 Q-Branch Region

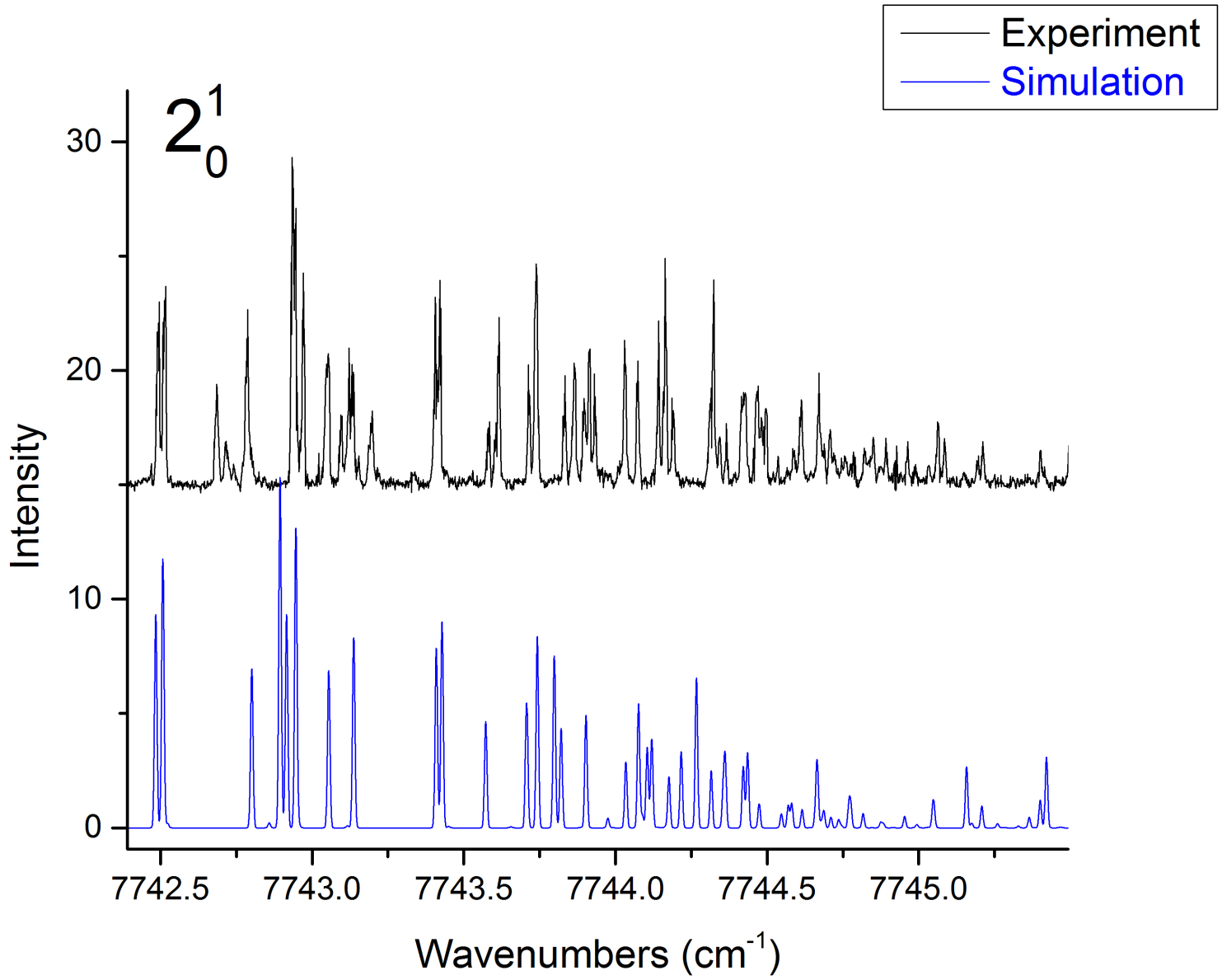

(d) 2_0^1 R-Branch Region

been well-determined from fitting, and thus have been fit in the $\widetilde{A}^2E''$ model. Regardless, the contour of the R branch is still simulated very well.

The experimental spectrum has an estimated experimental error of 250 MHz. The RMS of the fit is below this at 194 MHz, indicating that a good fit was obtained. 84 lines constitute roughly half of the total lines with reasonable intensity. However, in Section 4.5, an explanation for many of the lines not assigned will be given. With the results of that section in mind, it is fair to say that $\frac{3}{4}$ of the observed experimental lines have been confidently assigned, and considering most of the R branch region cannot be confidently assigned because of the density of lines, this is quite good.

4.3 The $2_0^1 4_0^2$ Band

The simulation of the $2_0^1 4_0^2$ band is presented in Figure 4.7. The parameters determined from the least-squares fit are presented in Table 4.3. The assignments used to produce the fit are listed in Appendix B. The simulation is presented at a temperature of 17 K. Like the 2_0^1 simulation, there is excellent agreement in the P and Q branches as indicated in Figures 4.8a and 4.8b. Same problems plague the analysis of the $2_0^1 4_0^2$ band as the 2_0^1 band. The centrifugal constants are not able to be well-determined and the R branch as pictured in Figure 4.8c is too dense to make proper assignments. However, although specific assignments are difficult, the contour of the R branch is generally well-reproduced.

84 lines were assigned, which constitutes about half of the experimental lines with significant intensities. However, as for the analysis of the 2_0^1 band, there is reason, presented in Section 4.5, to believe that in actuality, $\frac{3}{4}$ of the experimental lines have been assigned. Considering that the R branch region cannot be confidently assigned, this is quite good. The experimental spectrum has an estimated error of 250 MHz and the RMS of the fit is again below this at 209 MHz.

The average bond length and inertial defect were also calculated for the $2_0^1 4_0^2$ band using Equations 4.20 and 4.21. The results are posted in Table 4.7.

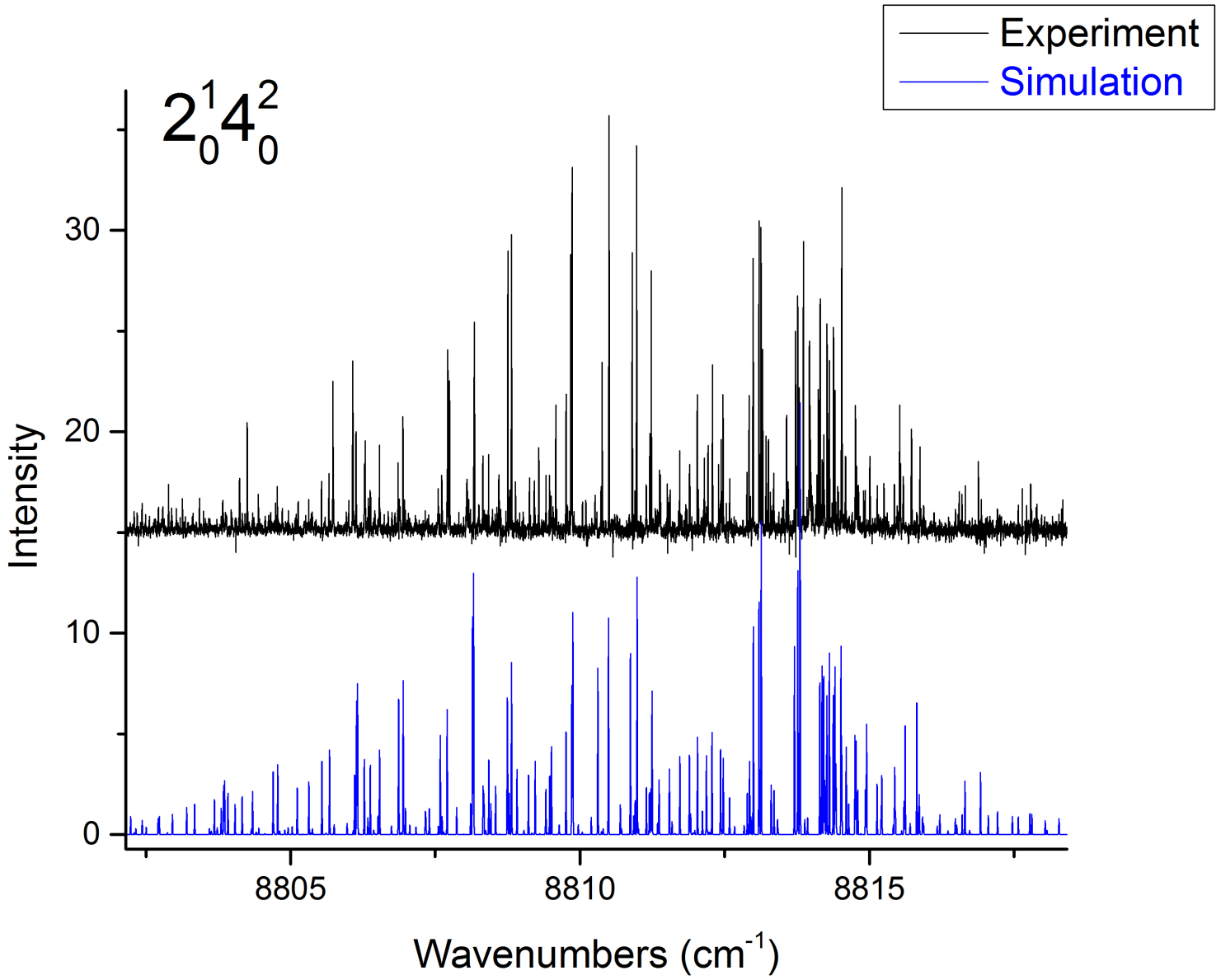

Figure 4.7: The rovibronic simulation of the $2_0^1 4_0^2$ band. The upper trace is the experimental spectrum. The lower trace is the simulated spectrum.

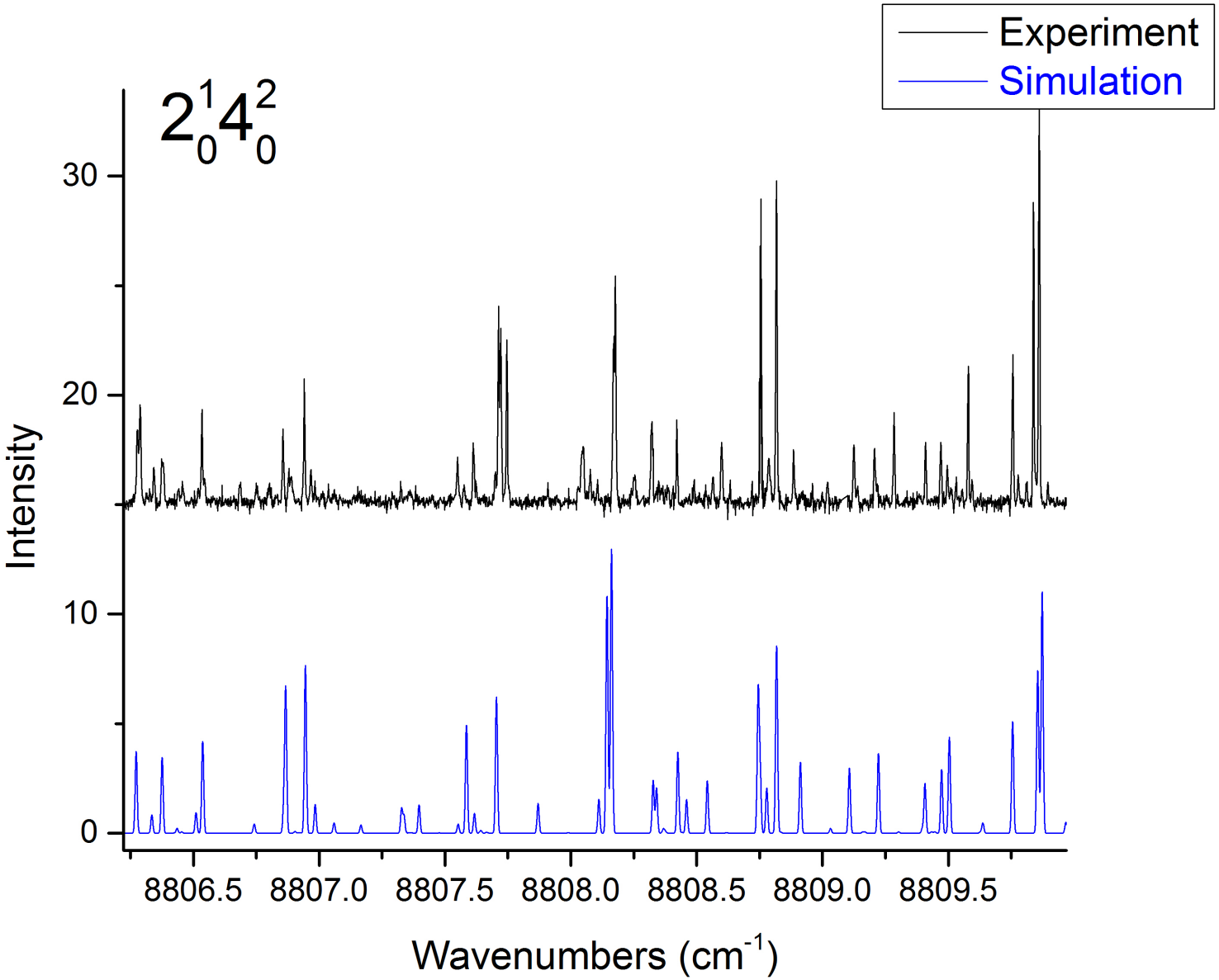

(a) $2_0^1 4_0^2$ P-Branch Region

Figure 4.8: Closer view of the $2_0^1 4_0^2$ band simulation in the P, Q, and R branches.

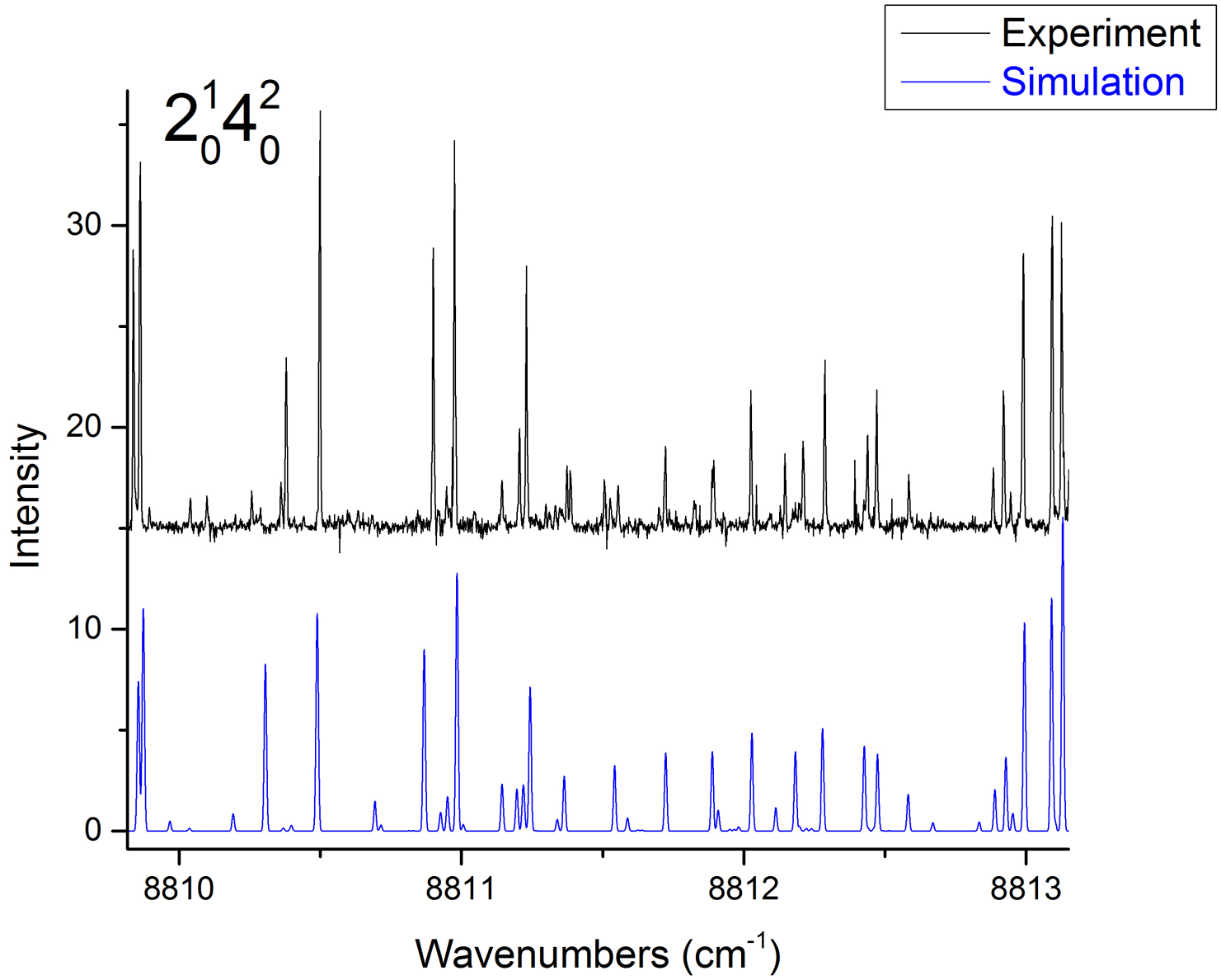

(b) $2_0^1 4_0^2$ Q-Branch Region

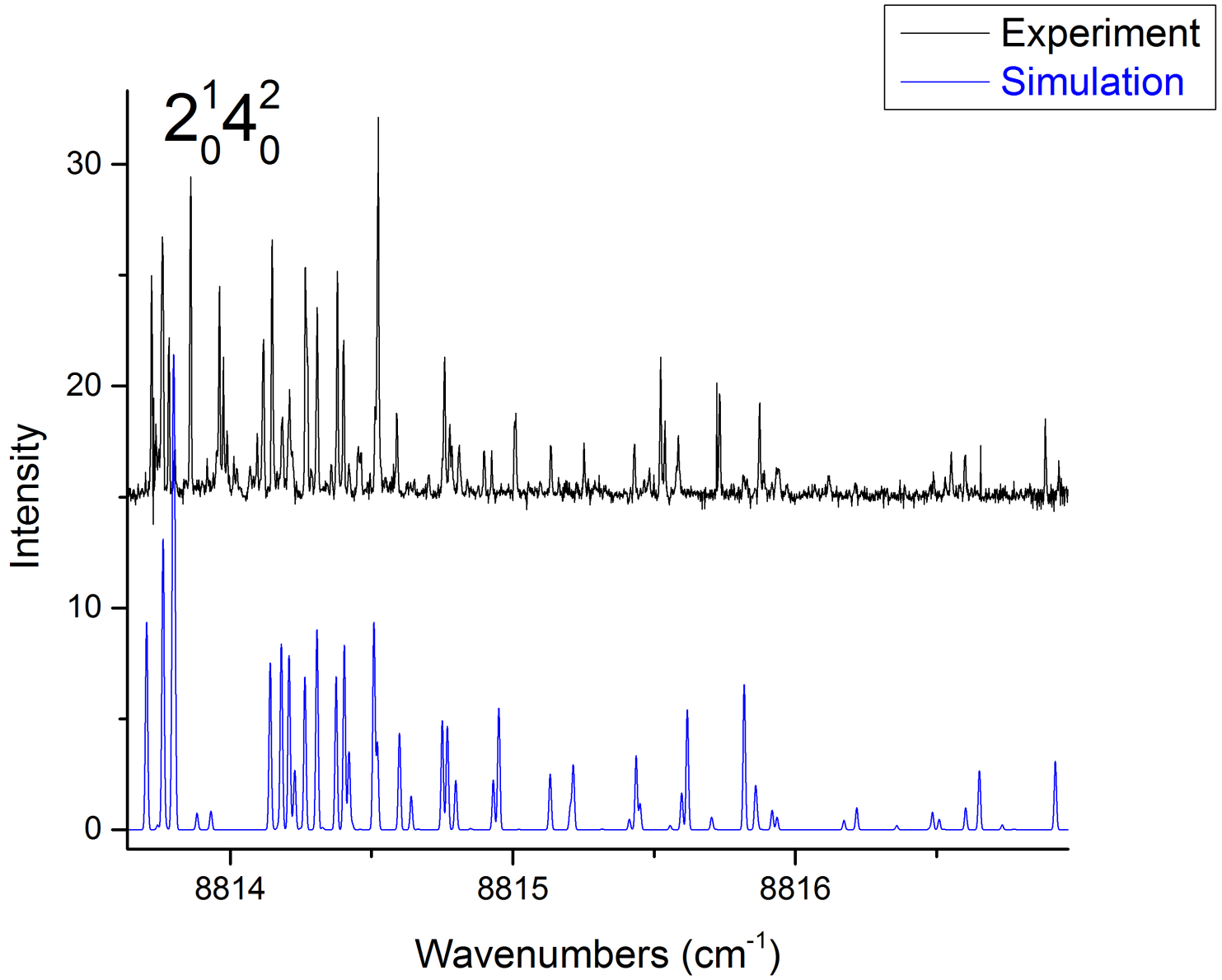

(c) $2_0^1 4_0^2$ R-Branch Region

Table 4.3: $2_0^1 4_0^2$ band simulation parameters.

Constant (cm^{-1})	$2_0^1 4_0^2$	$\widetilde{X}^2 A_2'(\nu = 0)^4$
B	0.431368(44)	0.4585445(61)
C	0.212371(30)	0.2286274(57)
h_1	0.002054(32)	–
C·ζ_t	0.013644(74)	–
$a_0\zeta_e d_z$	0.0113(15)	–
D_N (10^{-6})	4.6[a]	1.0880(94)
D_{NK} (10^{-6})	-8.5[a]	-2.062(19)
D_K (10^{-6})	3.9[a]	1.047(14)
ϵ_{bb}	0.01723(18)	-0.01642(14)
ϵ_{cc}	0.0008[a]	0.00074(14)
T_{ev}	8811.532(9)	0.0
Lines Fit	84	
Temp (K)	17	
Std. Dev. of Fit (MHz)	209	

[a]Fixed during the fit.

4.4 The $2_0^1 4_0^1$ Band

The experimental trace of the $2_0^1 4_0^1$ band has been collected and is presented in Figure 4.9. However, this band has not been analyzed. The contour of the band departs from the contour of the 2_0^1 and $2_0^1 4_0^2$ bands significantly, making a continued analysis difficult. Moreover, many weaker lines appear in the spectrum than has been predicted by any simulation thus far. This may be indicative of significant perturbation. Work on this band is still continuing.

4.5 Split Lines Analysis

Hirota[26] reported that many lines in his 4_0^1 experimental band were not reproduced by the oblate symmetric top Hamiltonian. Chen confirms this finding in his analysis of the 4_0^1 and 4_0^2 band.[38] The same effect was observed in the rovibronically analyzed bands. In certain parts of the spectrum, two experimental lines appear where the simulation predicts one line. This is seen in Figure 4.10. A pattern for this line splitting was never discerned, however,

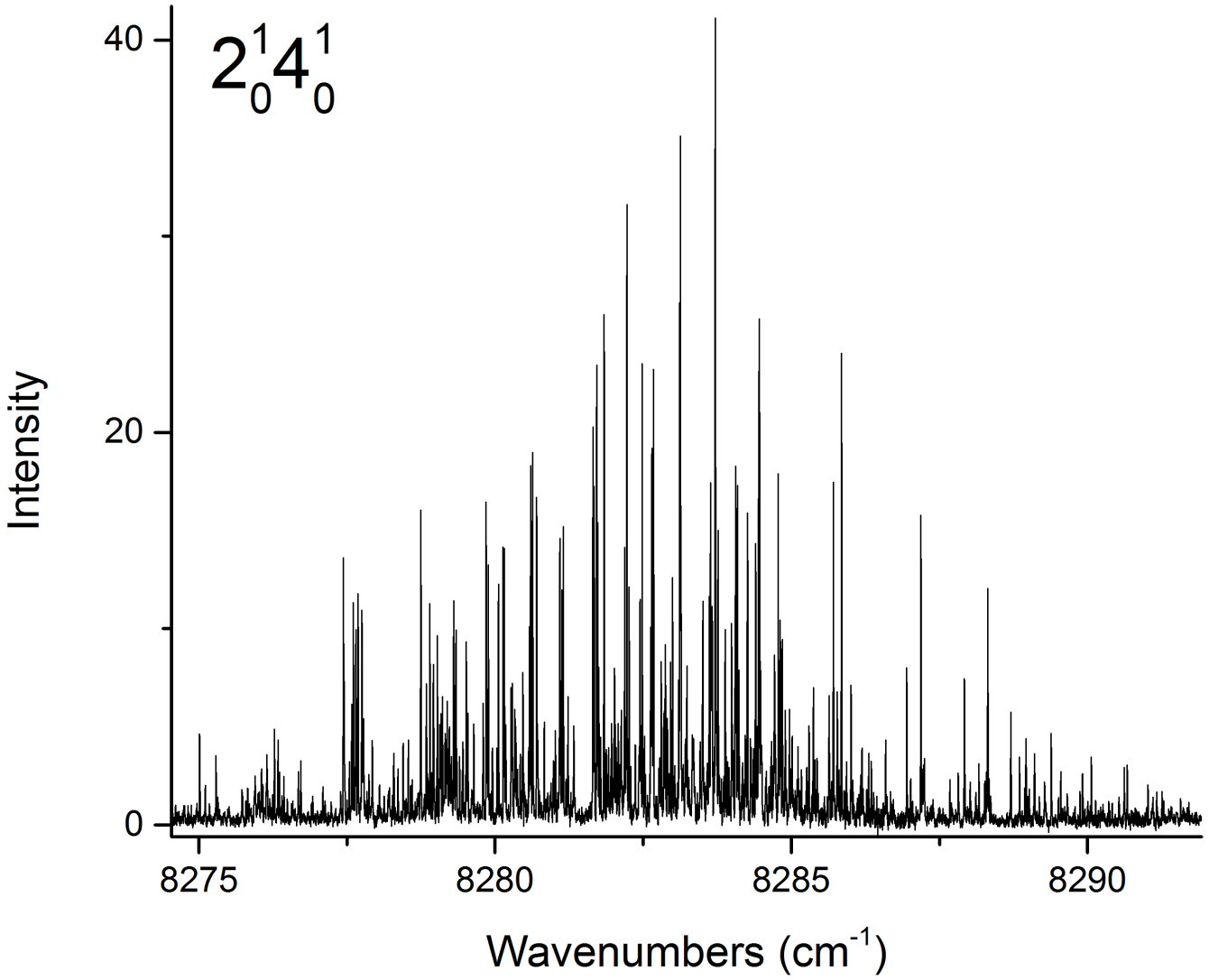

Figure 4.9: The experimental trace of the $2_0^1 4_0^1$ band.

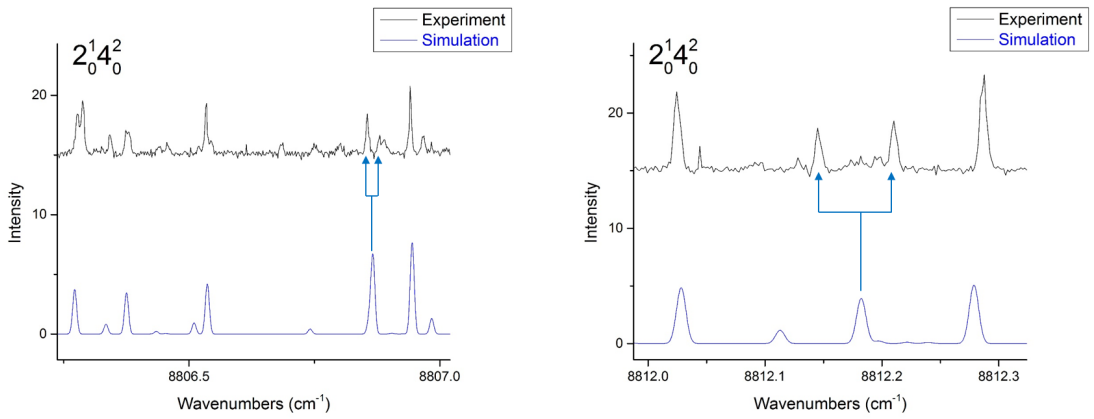

Figure 4.10: Split line phenomenon as seen in the $2_0^1 4_0^2$ band. The top black trace is the experiment and the bottom blue trace is the simulation. Blue arrows indicate transitions where the split lines are observed.

splittings in one branch of the spectrum, e.g. Q, are seen for the corresponding lines in the other two branches, e.g. R and P. These pairs will be referred to as split lines.

This effect is suspected to be a result of accidental degeneracy between a dark state and a bright state, where the dark state comes from rotational levels of high vibrational levels in the $\widetilde{X}^2 A_2'$ state. The two levels perturb each other and results in two shifted levels that share intensity. A schematic diagram for this effect is shown in Figure 4.11. ψ_1 is a bright state and ψ_2 is a dark state that is accidentally degenerate with ψ_1. ψ_0 is a lower lying state with nonzero transition intensity to ψ_1, but zero transition intensity to ψ_2. Only ψ_1 has intensity, but coupling produces two new levels that are a linear combination of both ψ_1 and ψ_2. These two new levels both share the intensity originally only present in the transition to the bright state, ψ_1.

The Hamiltonian matrix $\mathcal{H}$ and overlap matrix $\mathbf{S}$ for these two levels are

$$\mathcal{H} = \begin{pmatrix} E_1 & \frac{h}{2} \\ \frac{h}{2} & E_2 \end{pmatrix} \tag{4.2}$$

$$\mathbf{S} = \begin{pmatrix} 1 & 0 \\ 0 & 1 \end{pmatrix} \tag{4.3}$$

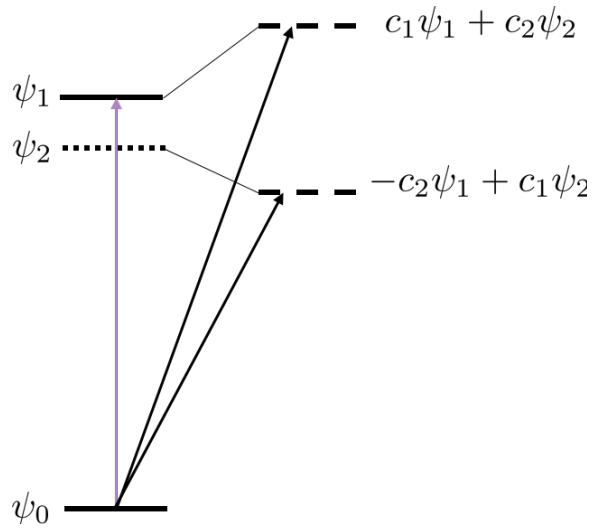

Figure 4.11: A schematic diagram of the split lines phenomenon. ψ_1 is a bright state and ψ_2 is a dark state. Two levels on the right are the resulting levels from coupling and both have intensity.

where E_i is the unperturbed energy of ψ_i and h is a coupling constant. Solving the secular equation gives us two energy eigenvalues E_+ and E_-.

$$E_\pm = \frac{E_1 + E_2 \pm \sqrt{(E_1 - E_2)^2 + h^2}}{2} \tag{4.4}$$

The difference between these two levels is

$$\begin{aligned}
\Delta E &= E_+ - E_- \\
&= (E_1 - E_2)\sqrt{1 + \frac{h^2}{(E_1 - E_2)^2}} \\
&= (E_1 - E_2)\left(1 + \frac{1}{2}\frac{h^2}{(E_1 - E_2)^2} + \mathcal{O}(h^4)\right) \\
&\approx (E_1 - E_2)\left(1 + \frac{1}{2}\frac{h^2}{(E_1 - E_2)^2}\right)
\end{aligned} \tag{4.5}$$

The new eigenstates can be calculated.

$$\begin{aligned}
(\mathbf{H} - E_\pm \mathbf{S}) \begin{pmatrix} a_1^\pm \\ a_2^\pm \end{pmatrix} &= 0 \\
\frac{(E_1 - E_2) \mp \sqrt{(E_1 - E_2)^2 + h^2}}{2} a_1^\pm + \frac{h}{2} a_2^\pm &= 0
\end{aligned} \tag{4.6}$$

$$\begin{aligned}
\frac{a_1^{\pm}}{a_2^{\pm}} &= -\frac{h}{(E_1-E_2) \mp \sqrt{(E_1-E_2)^2+h^2}} \\
&= -\frac{h(E_1-E_2 \pm \sqrt{(E_1-E_2)^2+h^2})}{(E_1-E_2)^2-[(E_1-E_2)^2+h^2]} \\
&= -\frac{E_1-E_2 \pm (E_1-E_2)\sqrt{1+\frac{h^2}{(E_1-E_2)^2}}}{h} \\
&= -\frac{E_1-E_2 \pm (E_1-E_2)(1+\frac{1}{2}\frac{h^2}{(E_1-E_2)^2}+\mathcal{O}(h^4))}{h}
\end{aligned} \tag{4.7}$$

The two solutions are

$$\begin{aligned}
\frac{a_1^{+}}{a_2^{+}} &= -\frac{2(E_1-E_2)+\mathcal{O}(h^2)}{h} \\
&\approx -\frac{2(E_1-E_2)}{h}
\end{aligned} \tag{4.8}$$

$$\begin{aligned}
\frac{a_1^{-}}{a_2^{-}} &= -\frac{-\frac{1}{2}\frac{h^2}{(E_1-E_2)^2}+\mathcal{O}(h^4)}{h} \\
&\approx \frac{h}{2(E_1-E_2)}
\end{aligned} \tag{4.9}$$

By letting $c_1 = -a_1^+$ and $c_2 = a_2^+$, the final eigenstates are

$$\begin{aligned}
\psi_+ &= c_1\psi_1 + c_2\psi_2 \\
\psi_- &= -c_2\psi_1 + c_1\psi_2
\end{aligned} \tag{4.10}$$

where

$$\frac{c_1}{c_2} = \frac{2(E_1-E_2)}{h} \tag{4.11}$$

To see how this relates to intensity, suppose I_1 is the intensity of the transition between ground state ψ_0 and ψ_1. Fermi's Golden Rule gives

$$\langle\psi_0|\,\mu\,|\psi_1\rangle \propto \sqrt{I_1} \tag{4.12}$$

where μ is the dipole moment operator. Since ψ_2 is a dark state,

$$\langle\psi_0|\,\mu\,|\psi_2\rangle = 0 \tag{4.13}$$

The intensities of ψ_g to $\psi_\pm$ can be derived from the form of Equation 4.10 combined with Equation 4.12 and 4.13.

$$\begin{aligned}\sqrt{I_+} &\propto \langle\psi_0|\,\mu\,|\psi_+\rangle \propto c_1\sqrt{I_1}\\ \sqrt{I_-} &\propto \langle\psi_0|\,\mu\,|\psi_-\rangle \propto c_2\sqrt{I_1}\end{aligned} \tag{4.14}$$

Define R as the ratio of intensities between the two split lines.

$$R = \frac{I_+}{I_-} = \left(\frac{c_1}{c_2}\right)^2 = \frac{4(E_1-E_2)^2}{h^2} \tag{4.15}$$

Then

$$\begin{aligned}\frac{R-1}{R+1} &= \left(1-\frac{h^2}{4(E_1-E_2)^2}\right)\left(\frac{1}{1+\frac{h^2}{4(E_1-E_2)^2}}\right)\\ &= \left(1-\frac{h^2}{4(E_1-E_2)^2}\right)\left(1-\frac{h^2}{4(E_1-E_2)^2}+\cdots\right)\\ &= \left(1-\frac{h^2}{4(E_1-E_2)^2}\right)^2+\cdots\\ &= 1-\frac{h^2}{2(E_1-E_2)^2}+\mathcal{O}(h^4)\\ &\approx 1-\frac{h^2}{2(E_1-E_2)^2}\end{aligned} \tag{4.16}$$

Solving for $E_1 - E_2$ in Equation 4.5 and combining with Equation 4.16 yields

$$\begin{aligned}(E_1-E_2) &= \Delta E\left(1+\frac{h^2}{2(E_1-E_2)^2}\right)^{-1}\\ &= \Delta E\left(1-\frac{h^2}{2(E_1-E_2)^2}+\mathcal{O}(h^4)\right)\\ &\approx \Delta E\left(1-\frac{h^2}{2(E_1-E_2)^2}\right)\\ &\approx \Delta E\left(\frac{R-1}{R+1}\right)\end{aligned} \tag{4.17}$$

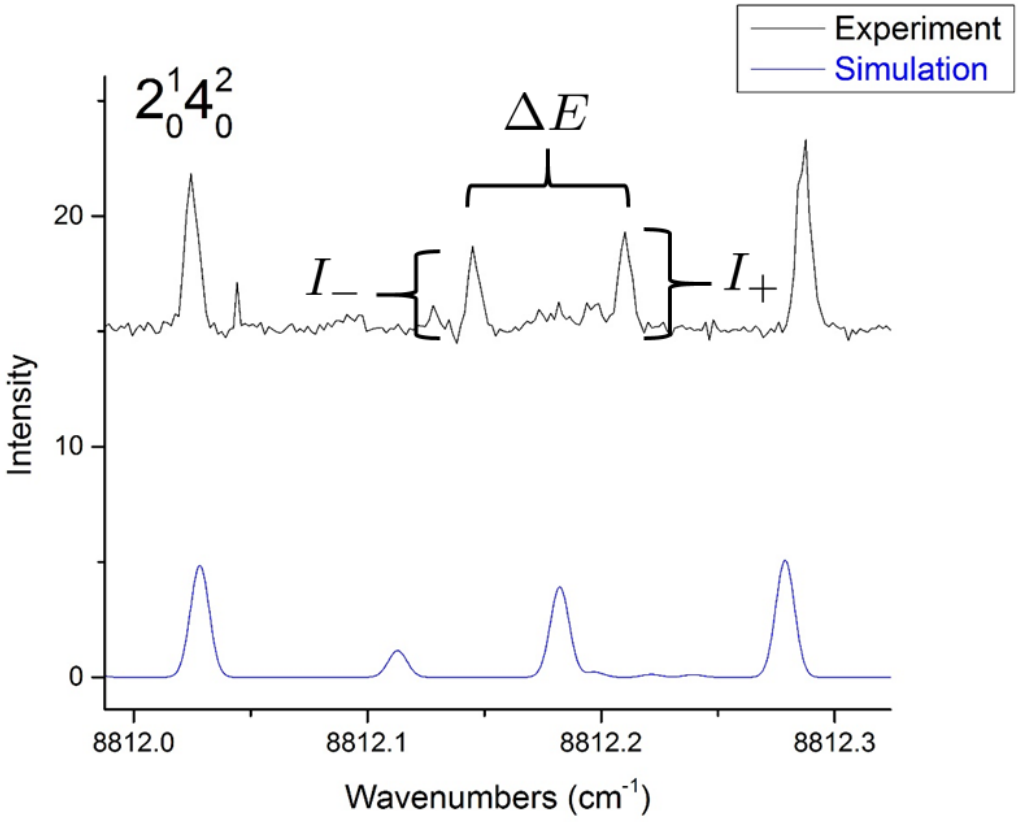

Figure 4.12: ΔE and R as observed from an experimental spectrum.

h can be obtained as well by rearranging Equation 4.5 and using Equation 4.17

$$\begin{aligned} h^2 &= 2\Delta E(E_1 - E_2) - 2(E_1 - E_2)^2 \\ &= 2\Delta E^2 \left(\frac{R-1}{R+1}\right) - 2\Delta E^2 \left(\frac{R-1}{R+1}\right)^2 \\ &= 2\Delta E^2 \left(\frac{2R}{(R+1)^2}\right) \\ h &= \Delta E \left(\frac{2\sqrt{R}}{R+1}\right) \end{aligned} \tag{4.18}$$

ΔE and R are both observed parameters in the experiment as shown in Figure 4.12. These can be used to calculate the unperturbed energies of each level in a doublet. We assumed the coupling is symmetric in both directions. The total energy difference is $\Delta E - (E_1 - E_2)$. This means that E_1 shifts up by half of this difference, and E_2 shifts down by

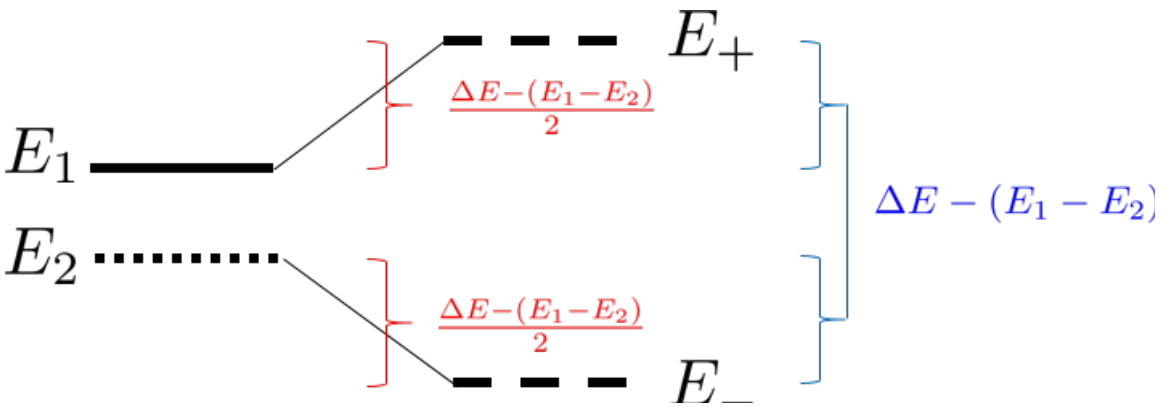

Figure 4.13: Schematic representation of the energies of the split lines unperturbed levels in terms of measured parameters.

half of this difference as well, as pictured in Figure 4.13. Hence, E_i can be calculated by

$$E_1 = E_+ - \frac{\Delta E - \Delta E\left(\frac{R-1}{R+1}\right)}{2}$$
$$E_2 = E_- + \frac{\Delta E - \Delta E\left(\frac{R-1}{R+1}\right)}{2} \tag{4.19}$$

If this two state perturbation model is correct, then one of E_1 or E_2 should match the predicted energy from the simulation. This analysis has been done previously for 4_0^1, 3_0^1, and $3_0^1 4_0^2$. We have now conducted the same analysis for 2_0^1 and $2_0^1 4_0^2$. The results are listed in Tables 4.4 and 4.5. Support of the hypothesis is seen as for each splitting, there is a corresponding splitting in a different branch of the spectrum, which h coupling values that are equal within experimental error. Branches where the corresponding splitting is not listed are cases where either the intensity is too small for a reasonable analysis, or there is overlap that makes the analysis impossible. It is interesting to note that compared to the parallel bands, many fewer split lines were identified for the perpendicular bands.

Table 4.4: Listings of all split lines found in the 2_0^1 band.

	Freq	Int	E_{unp}	E_{pre}	E_{pre}-E_{unp} (MHz)	$\lvert h\rvert$	Splitting
P branch							
Doublet 1	7735.65469	2.13988	7735.69213	7735.694489	-70.8074	-0.04696	-0.05216
	7735.70685	5.44088	7735.66941	–	-751.509	–	–
Assignment	$\lvert 7/2, 4, -2\rangle \leftarrow \lvert 9/2, 5, 3\rangle$						
Q branch							
Doublet 1	7740.25388	0.54753	7740.29799	7740.29166	189.782	-0.03391	-0.05063

	7740.30451	3.70579	7740.2604	–	-936.934	–	–
Assignment	$\|7/2,4,-2\rangle \leftarrow \|7/2,4,3\rangle$						
R branch							
Doublet 1	Intensity too weak						
Assignment	$\|7/2,4,-2\rangle \leftarrow \|5/2,3,3\rangle$						
P branch							
Doublet 2	7736.93127	7.25825	7736.95341	7736.961958	-256.141	-0.0735	-0.08314
	7737.01441	2.63462	7736.99227	–	908.4077	–	–
Assignment	$\|7/2,3,-3\rangle \leftarrow \|9/2,4,3\rangle$						
Q branch							
Doublet 2	7740.59782	4.73962	7740.61014	7740.6181	-238.66	-0.0611	-0.08809
	7740.68591	0.77041	7740.67359	–	1663.134	–	–
Assignment	$\|7/2,3,-3\rangle \leftarrow \|7/2,3,3\rangle$						
R branch							
Doublet 3	No R branch transition.						
Assignment							
P branch							
Doublet 3	Intensity too weak						
Assignment	$\|13/2,6,-2\rangle \leftarrow \|15/2,7,3\rangle$						
Q branch							
Doublet 3	7739.87269	1.79808	7739.89795	7739.908714	-322.724	-0.03582	-0.03796
	7739.91065	3.57455	18.57455	–	-2.3E+08	–	–
Assignment	$\|13/2,6,-2\rangle \leftarrow \|13/2,6,3\rangle$						
R branch							
Doublet 3	7745.4012	1.50733	7745.39474	7745.40049	-172.359	0.027213	0.03525
	7745.3659	0.33579	7745.37233	–	-843.864	–	–
Assignment	$\|13/2,6,-2\rangle \leftarrow \|11/2,5,3\rangle$						
P branch							
Doublet 4	7734.74054	4.84111	7734.75063	7734.751904	-38.1891	-0.03971	-0.04916
	7734.7897	1.2502	7734.77961	–	830.3561	–	–
Assignment	$\|11/2,6,-5\rangle \leftarrow \|13/2,7,6\rangle$						
Q branch							
Doublet 4	7741.18099	1.39109	7741.19076	7741.186747	120.2712	-0.04025	-0.05122
	7741.23221	0.32789	7741.22244	–	1069.718	–	–
Assignment	$\|11/2,6,-5\rangle \leftarrow \|11/2,6,6\rangle$						
R branch							
Doublet 4	No R branch transition.						
Assignment							
P branch							
Doublet 5	7732.09274	0.87138	7732.10545	7732.103415	61.03618	-0.02354	-0.02361
	7732.11635	1.01635	7732.10364	–	6.696015	–	–
Assignment	$\|15/2,8,-5\rangle \leftarrow \|17/2,9,6\rangle$						
Q branch							
Doublet 5	7740.36686	0.93922	7740.37835	7740.3679	313.3023	-0.01946	-0.01973
	7740.38659	1.31072	7740.3751	–	215.6682	–	–
Assignment	$\|15/2,8,-5\rangle \leftarrow \|15/2,8,6\rangle$						
R branch							
Doublet 5	Intensity too weak.						
Assignment	$\|15/2,8,-5\rangle \leftarrow \|13/2,7,6\rangle$						
P branch							

Doublet 6	7730.88947	0.85219	7730.92406	7730.946647	-676.852	-0.0871	-0.08942
	7730.97889	0.53768	7730.9443	–	-70.4203	–	–
Assignment	$\|17/2, 8, -2\rangle \leftarrow \|19/2, 9, 3\rangle$						
Q branch							
Doublet 6	7739.13749	1.48493	7739.18163	7739.188547	-207.296	-0.09665	-0.09705
	7739.23454	1.23881	7739.1904	–	55.52751	–	–
Assignment	$\|17/2, 8, -2\rangle \leftarrow \|17/2, 8, 3\rangle$						
R branch							
Doublet 6	7746.4642	0.56534	7746.50978	7746.51405	-127.874	-0.09705	-0.09724
	7746.5614	0.49951	7746.5158	–	52.28964	–	–
Assignment	$\|17/2, 8, -2\rangle \leftarrow \|15/2, 7, 3\rangle$						

4.6 The Effect of New Parameters

The advantage of this analysis over previous analyses is the inclusion of parameters corresponding the spin-orbit coupling ($a\zeta_e d$), coriolis coupling ($C\zeta_t$), and the Watson term (h_1). These parameters are defined in Equations 3.44, 3.45, and 3.46 respectively where $\Gamma = \Gamma' = E'$ were omitted from the notation used in this chapter.

4.6.1 Spin-Orbit Coupling

Spin-orbit coupling serves to increase the separation between levels in the $\widetilde{A}^2E''$ of the same N' and K', but different Σ. Figure 4.14 highlights all these pairs with $K'' = 3$, coded by their N'' quantum number. Figure 4.15 demonstrates the effect of spin-orbit coupling in a region of the 2_0^1 simulation where spin-orbit coupling greatly improves the simulation. The remaining splittings are a result of spin-rotational coupling. In Figure 4.15, spin-orbit coupling provides the essential splitting between multiple lines in the spectrum.

4.6.2 Coriolis Coupling

While the effect is difficult to quantify, Figure 4.16 demonstrates the improvement in the spectrum from the addition of this term. The value of vibronic angular momentum, ζ_t, for both analyzed bands can be computed by dividing $C\zeta_t$ by C. The numbers are listed in Table 4.6. Previous studies have determined a very weak electronic angular momentum in the $\widetilde{A}^2E''$ state, so it is expected this significant vibronic angular momentum to be a result of significant vibrational angular momentum in the $\widetilde{A}^2E''$ state.

Table 4.5: Listings of all split lines found in the $2_0^1 4_0^2$ band.

	Freq	Int	E_{unp}	E_{pre}	E_{pre}-E_{unp} (MHz)	$\|h\|$	Splitting
P branch							
Doublet 1	8807.550	2.171	8807.585	8807.585	7.4	0.061	0.061
	8807.611	2.830	8807.577	–	-234.8	–	–
Assignment	$\|7/2,4,-2\rangle \leftarrow \|9/2,5,3\rangle$						
Q branch							
Doublet 1	8812.144	3.698	8812.180	8812.182	-65.7	0.065	0.065
	8812.210	4.319	8812.175	–	-217.2	–	–
Assignment	$\|7/2,4,-2\rangle \leftarrow \|7/2,4,3\rangle$						
R branch							
Doublet 1	8815.827	0.820	8815.864	8815.865	19.7	0.061	0.062
	8815.889	1.194	8815.853	–	-366.2	–	–
Assignment	$\|7/2,4,-2\rangle \leftarrow \|5/2,3,3\rangle$						
P branch							
Doublet 2	8806.855	3.464	8806.863	8806.866	-89.171	-0.023	-0.0251
	8806.880	1.668	8806.872	–	173.8	–	–
Assignment	$\|11/2,6,-5\rangle \leftarrow \|13/2,7,6\rangle$						
Q branch							
Doublet 2	8813.289	1.998	8813.298	8813.301	-109.093	-0.024	-0.025
	8813.314	1.071	8813.305	–	118.9	–	–
Assignment	$\|11/2,6,-5\rangle \leftarrow \|11/2,6,6\rangle$						
R branch							
Doublet 3	No R branch transition.						
Assignment							
P branch							
Doublet 3	8805.099	0.905	8805.118	8805.114	130.261	-0.029	-0.030
	8805.12911	1.52936	8805.110144	–	-101.7895364	–	–
Assignment	$\|11/2,6,-2\rangle \leftarrow \|13/2,7,3\rangle$						
Q branch							
Doublet 3	8811.527	1.489	8811.542	8811.542	11.8	-0.026	-0.027
	8811.553	2.112	8811.538	–	-125.6	–	–
Assignment	$\|11/2,6,-2\rangle \leftarrow \|11/2,6,3\rangle$						
R branch							
Doublet 3	8817.039	0.772	8817.053	8817.055	-50.868	-0.032	-0.033
	8817.071	0.570	8817.058	–	96.96185445	–	–
Assignment	$\|11/2,6,-2\rangle \leftarrow \|9/2,5,3\rangle$						

Table 4.6: Vibronic angular momentum for the degenerate vibronic bands.

	2_0^1	$2_0^1 4_0^2$
ζ_t (cm^{-1})	0.157	0.0642

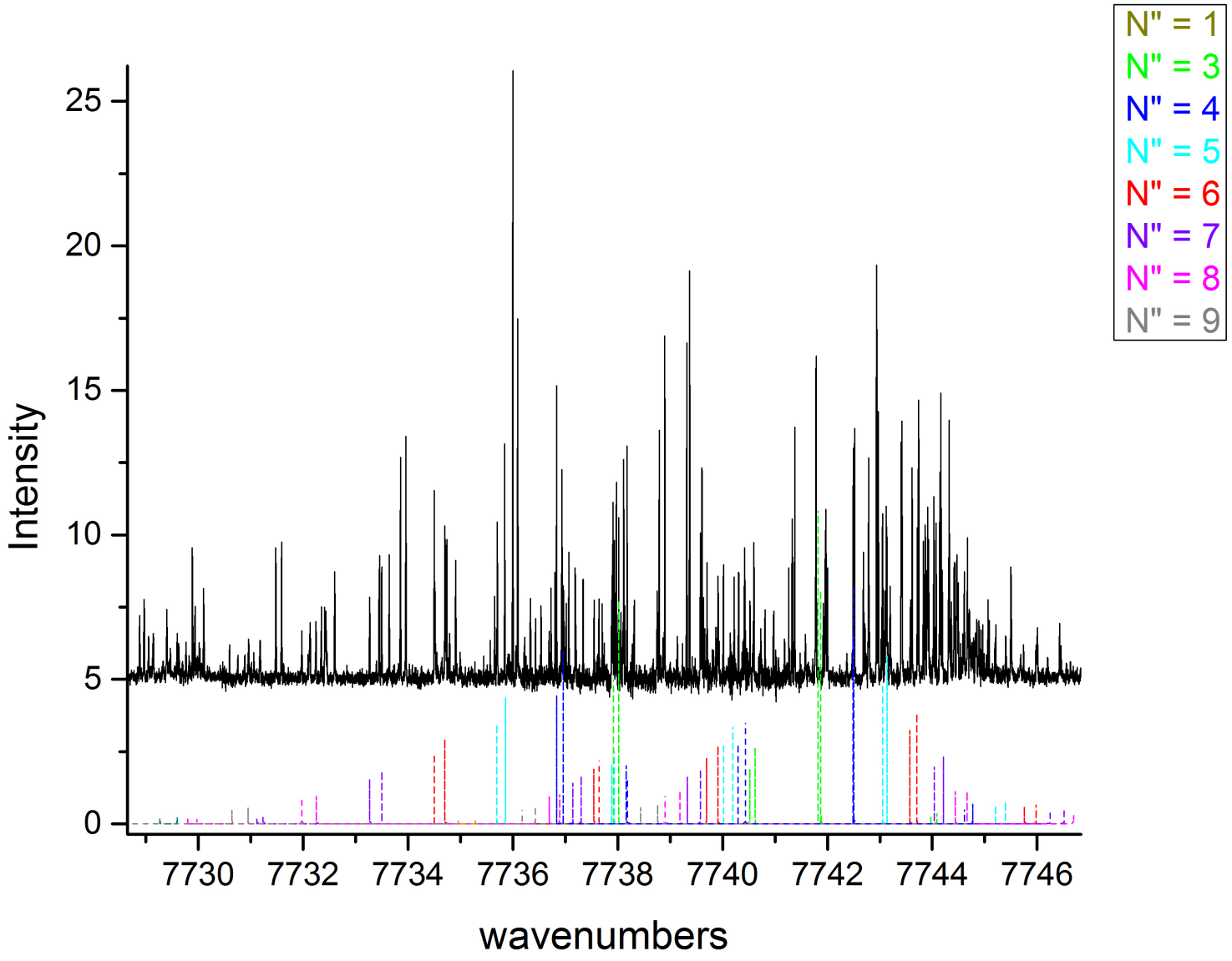

Figure 4.14: Pairs of transitions from levels with $K'' = 3$ and N'' as labeled in the 2_0^1 band. The difference between levels sharing K'' and N'' are in Σ.

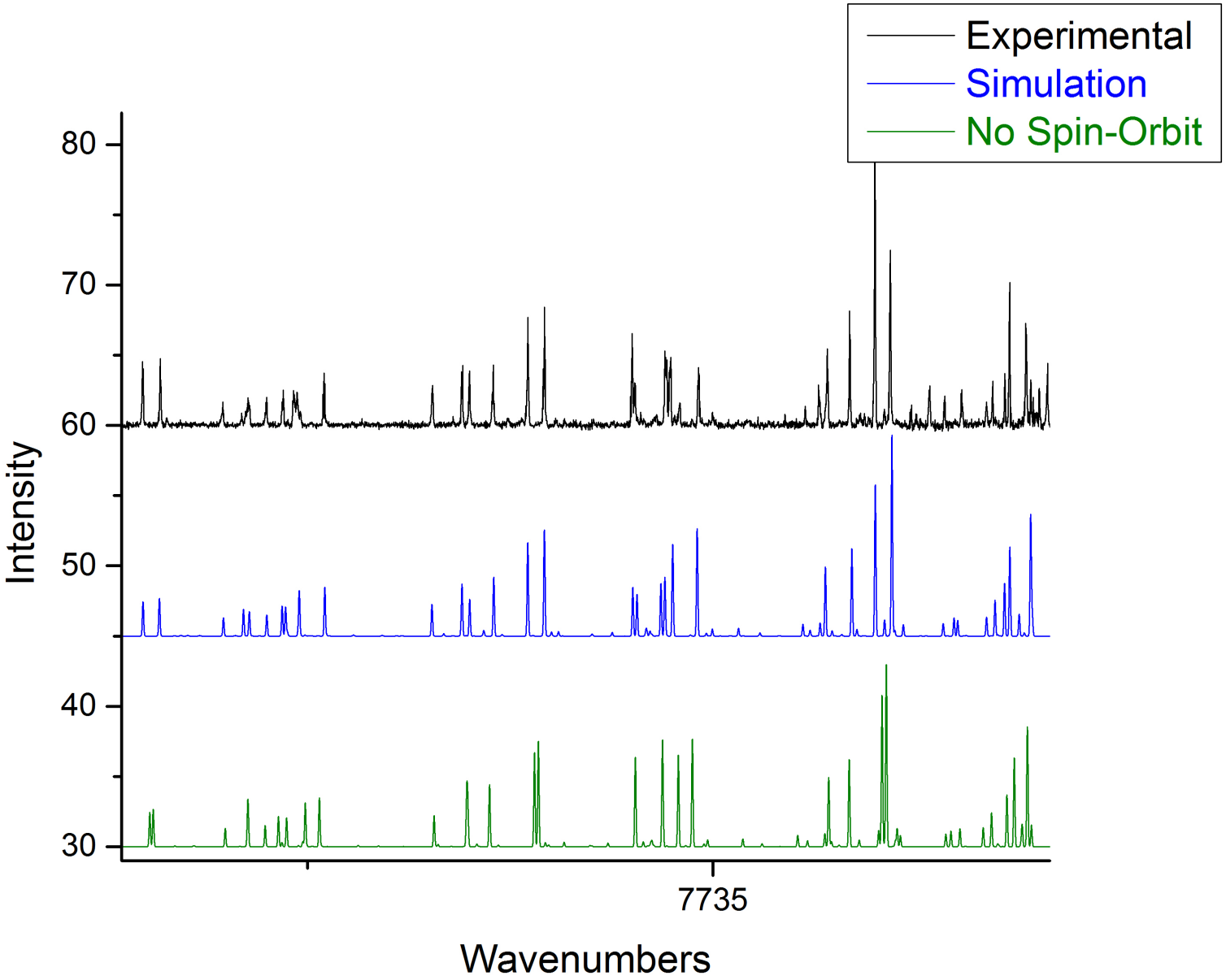

Figure 4.15: A demonstration of the effect of spin-orbit coupling in the 2_0^1 band simulation. The top black trace is the experimental trace. The middle blue trace is the final simulation. The bottom green trace uses the same parameters as the final simulation, except for zero spin-orbit coupling.

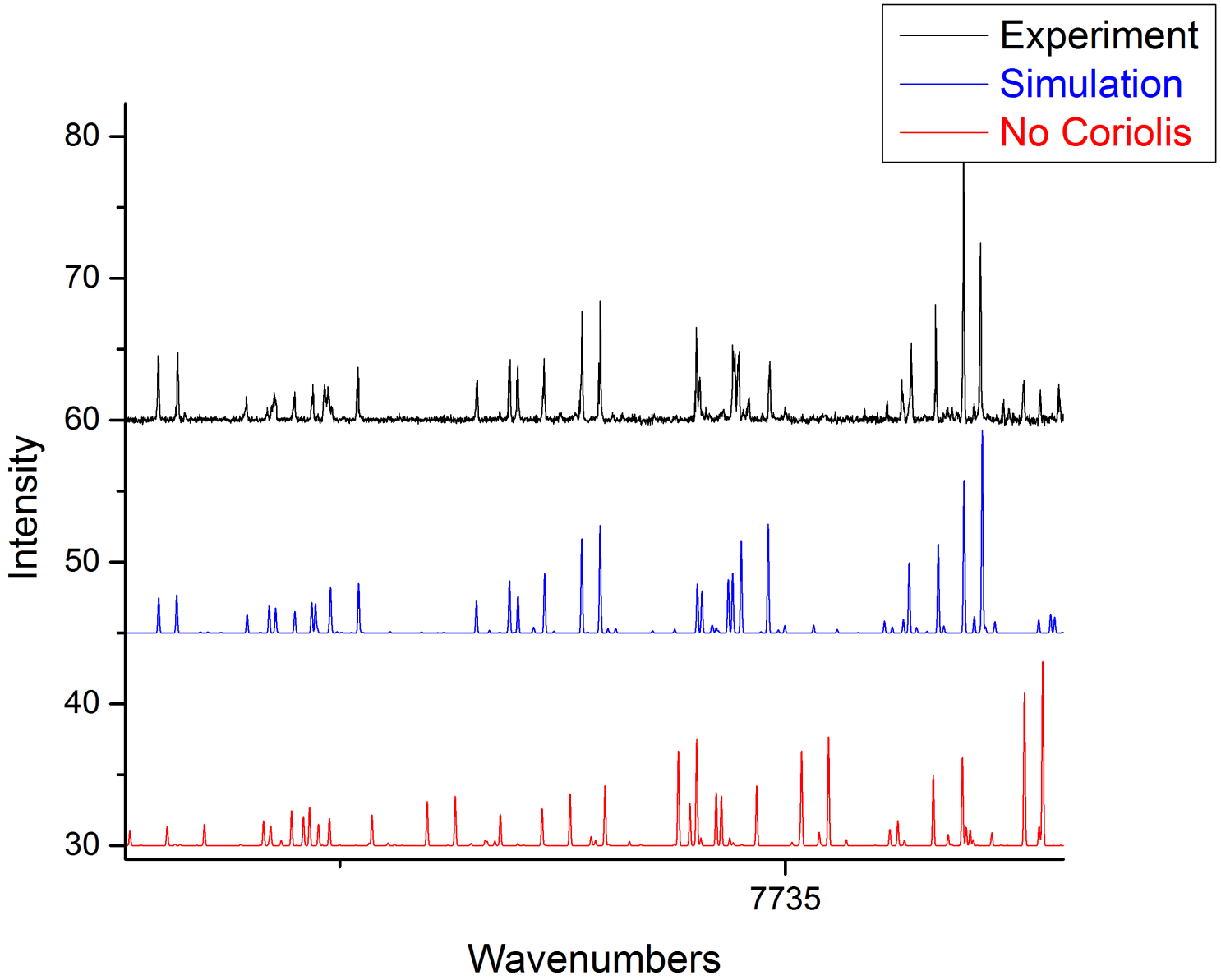

Figure 4.16: A demonstration of the effect of coriolis coupling in the 2_0^1 band simulation. The top black trace is the experimental trace. The middle blue trace is the final simulation. The bottom red trace uses the same parameters as the final simulation, except for zero coriolis coupling.

Table 4.7: Comparison of rovibronic simulations of parallel and perpendicular vibronic bands in the $\widetilde{A}^2E'' \leftarrow \widetilde{X}^2A_2'$ transition.

Constant (cm^{-1})	2_0^1 (e')	$2_0^1 4_0^2$ (e')	3_0^1 (a_1'')	$3_0^1 4_0^1$ (a_1'')	4_0^1 (a_1'')	$\widetilde{X}^2A_2'(\nu=0)^4$
B	0.432933(37)	0.431368(44)	0.43027(3)	0.42985(5)	0.43240(5)	0.4585445(61)
C	0.215931(15)	0.212371(30)	0.21593(2)	0.20737(8)	0.21527(6)	0.2286274(57)
h_1	0.002187(31)	0.002054(32)	–	–	–	–
C·ζ_t	-0.033902(44)	0.013644(74)	–	–	–	–
$a_0\zeta_e d_z$	-0.0833(12)	0.0113(15)	–	–	–	–
D_N (10^{-6})	4.6[a]	4.6[a]	4.6(3)	2.0(3)	-2.54(24)	1.0880(94)
D_{NK} (10^{-6})	-8.5[a]	-8.5[a]	-8.5(6)	-6.4(1)	–	-2.062(19)
D_K (10^{-6})	3.9[a]	3.9[a]	3.9(3)	8.8(8)	–	1.047(14)
ϵ_{bb}	0.01799(16)	0.01723(18)	0.0163(1)	0.0164(1)	0.0148(3)	-0.01642(14)
ϵ_{cc}	0.0008[a]	0.0008[a]	0.0008(1)	-0.0001(2)	–	0.00074(14)
T_{ev}	7739.816(4)	8811.532(9)	8333.946(1)	8756.792 (1)	7602.5923(23)	0.0
N-O Bond Length (Å)	1.271	1.281	1.271	1.297	1.273	1.235
Δ (u·Å^2) = I_C - $2I_B$	0.193	1.219	-0.286	2.837	0.334	0.206

[a]Fixed in the fit.

4.6.3 Watson Term

The h_1 parameter defined by Watson[39] is related to the magnitude of linear Jahn-Teller distortion and serves to couple $+K$ states with $-K$ states. Its effect on the spectrum at lower values is negligible. In Figure 4.17, it is seen that two simulations using different values of h_1 are not very different, on the order of magnitude found in these fits. In fact, it seems that only very few lines are sensitive to this parameter and this is highlighted in Figure 4.18. As such, even for well-determined fits of this parameter, it may be that h_1 is deceptively well fit because it is determined from only a few assignments. As such, the validity of the h_1 value obtained from the fit is in question.

4.7 Discussion of Results

The complete set of parameters determined from the fits, as well as average bond N—O bond length and inertial defect, for the perpendicular and parallel bands is listed in Table 4.7

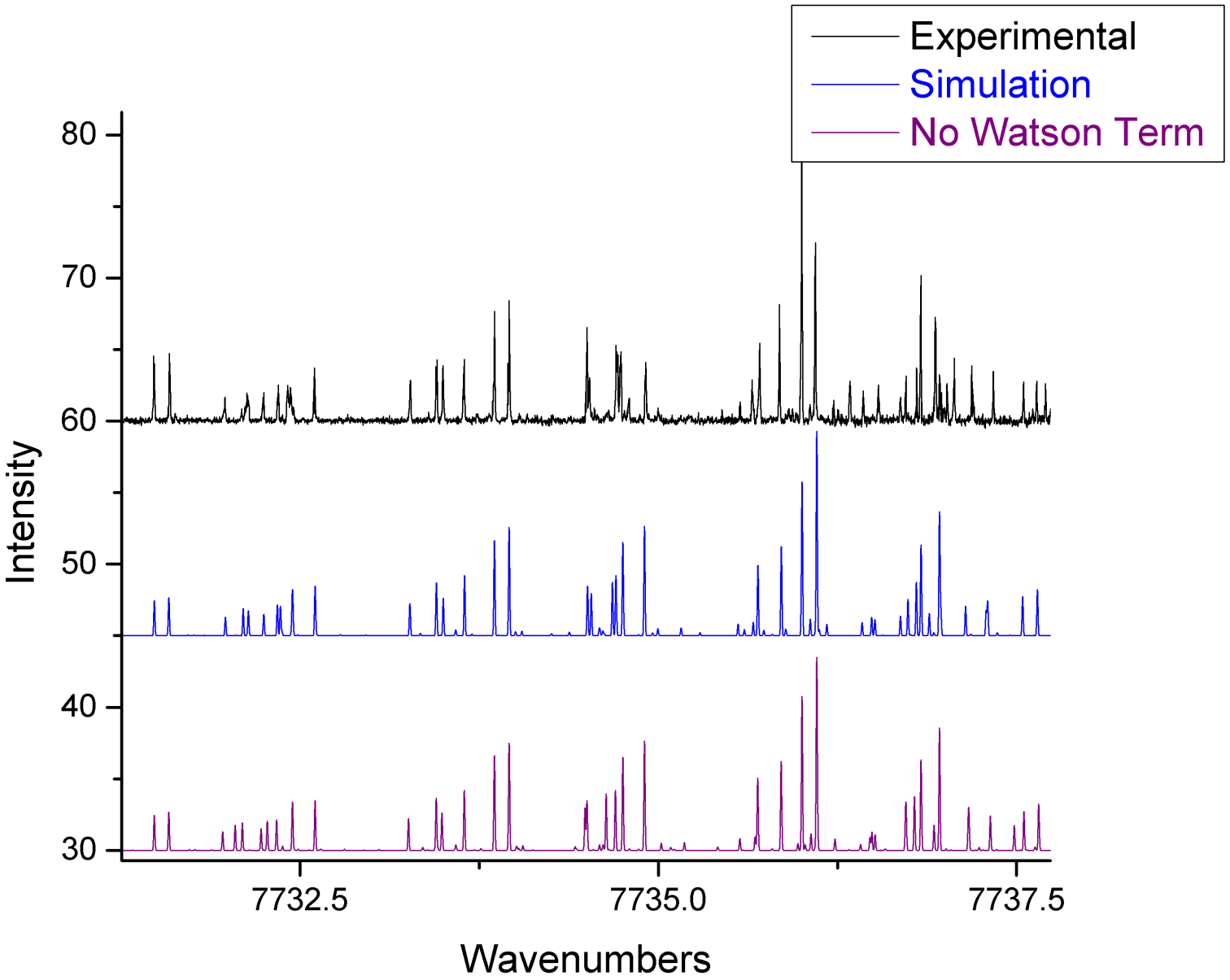

Figure 4.17: A demonstration of the effect of the Watson term in the 2_0^1 band simulation. The top black trace is the experimental trace. The middle blue trace is the final simulation. The bottom purple trace uses the same parameters as the final simulation, except with $h_1 = 0$.

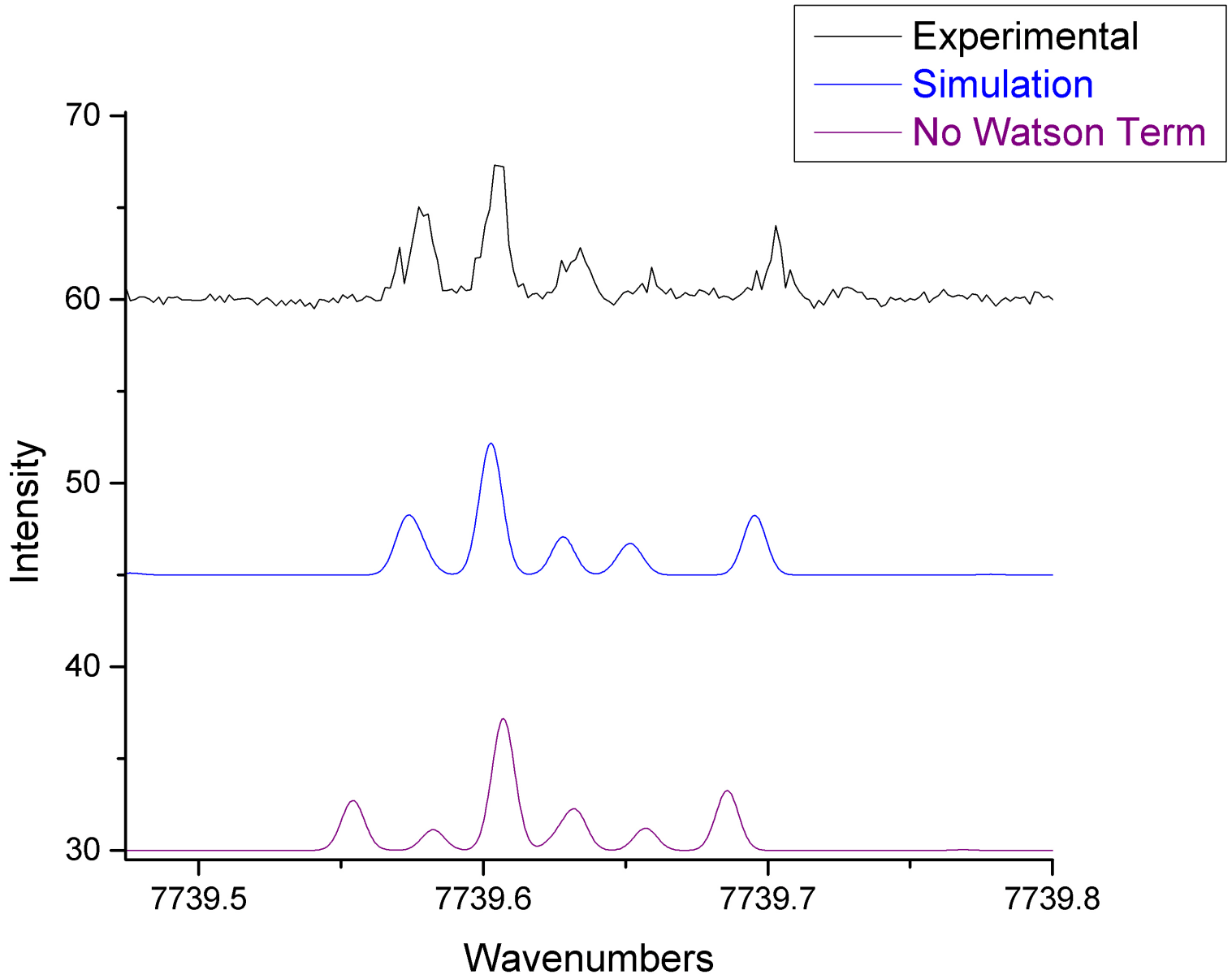

Figure 4.18: A portion of the 2_0^1 band highlighted to show one of few lines affected by the Watson term. The top black trace is the experimental trace. The middle blue trace is the final simulation. The bottom purple trace uses the same parameters as the final simulation, except with $h_1 = 0$.

4.7.1 Average N—O Bond Length

The average N—O bond length, $\bar{r}$, was calculated using a classical rotor model and the moment of inertial around the principle axis, $I_c = \dfrac{h}{8\pi^2 cC}$ where c is the speed of light.

$$I_c = 3m_{\mathrm{O}}\bar{r}^2 \tag{4.20}$$

The results are listed in Table 4.7. Additionally, the inertial defect Δ measures the non-planarity of NO_3 and can be calculated from

$$\Delta = I_c - 2I_b \tag{4.21}$$

A planar molecule should have $\Delta = 0$. The results are also listed in Table 4.7

4.7.2 *Ab-Initio* Determination of h_1

The new rotational constant matrix for an oblate symmetric top under the influence of non-zero h_1 is[39]

$$\begin{pmatrix} B - h_1\cos(3\phi) & h_1\sin(3\phi) & 0 \\ h_1\sin(3\phi) & B + h_1\cos(3\phi) & 0 \\ 0 & 0 & C \end{pmatrix} \tag{4.22}$$

where ϕ is the pseudo-rotation angle that was defined in Section 2.5. The eigenvalues of this matrix are the principle rotational constants, or the inverse of moment of inertia. From this, it is possible to determine the moment of inertia of NO_3 at the bottom in a minimum and on the pseudo-rotation barrier on the electronic potential energy surface. The bond lengths of NO_3 at both these positions was calculated using *ab-initio* methods by Stanton.[1] These numbers are used to calculate the moment of inertia at these positions. In the minimum, two N—O bonds are equal and the remaining bond is longer than the others. At the barrier, two N—O bonds are equal and the remaining bond is shorter than the others.

The eigenvalues of Equation 4.22 are independent of ϕ and take the values

$$\begin{aligned} A' &= B + h_1 \\ B' &= B - h_1 \\ C' &= C \end{aligned} \tag{4.23}$$

with eigenvectors (principle axes) in frame of the principle axes at the first minimum

$$\begin{cases} \begin{pmatrix} -\cot 3\phi - \csc 3\phi \\ 1 \\ 0 \end{pmatrix}, \begin{pmatrix} -\cot 3\phi + \csc 3\phi \\ 1 \\ 0 \end{pmatrix}, \begin{pmatrix} 0 \\ 0 \\ 1 \end{pmatrix} & 3\phi \neq n\pi \\ \begin{pmatrix} n+1 \mod 2 \\ n \mod 2 \\ 0 \end{pmatrix}, \begin{pmatrix} n \mod 2 \\ n+1 \mod 2 \\ 0 \end{pmatrix}, \begin{pmatrix} 0 \\ 0 \\ 1 \end{pmatrix} & 3\phi = n\pi \end{cases} \tag{4.24}$$

The following calculations are conducted in the eigenvector frame. Equation 4.24 describes how the principal axes change with pseudo-rotation angle. The bond lengths and angles calculated by Stanton are listed in Table 4.8.

$$I_\alpha = m_{\mathrm{O}} \sum_i |\mathbf{r}_i \times \mathbf{u}_\alpha|^2 \tag{4.25}$$

where α refers to a principle axis, i sums over all oxygen atoms, m_{O} corresponds to the mass of oxygen, $\mathbf{r}_i$ is the radial vector from nitrogen to oxygen and u_α is the unit vector along the α principle axis. Figure 4.19 illustrates how Equation 4.26 and 4.27 are derived.

$$\begin{aligned} 2m_{\mathrm{O}} \left(\sin\left(\frac{\theta^m}{2} \right) r_s^m \right)^2 &= \frac{h}{8\pi^2 c A'^m} \\ m_{\mathrm{O}} \left(r_l^m \right)^2 + 2m_{\mathrm{O}} \left(\cos\left(\frac{\theta^m}{2} \right) r_s^m \right)^2 &= \frac{h}{8\pi^2 c B'^m} \end{aligned} \tag{4.26}$$

$$\begin{aligned} 2m_{\mathrm{O}} \left(\sin\left(\frac{\theta^b}{2} \right) r_l^b \right)^2 &= \frac{h}{8\pi^2 c A'^b} \\ m_{\mathrm{O}} \left(r_s^b \right)^2 + 2m_{\mathrm{O}} \left(\cos\left(\frac{\theta^b}{2} \right) r_l^b \right)^2 &= \frac{h}{8\pi^2 c B'^b} \end{aligned} \tag{4.27}$$

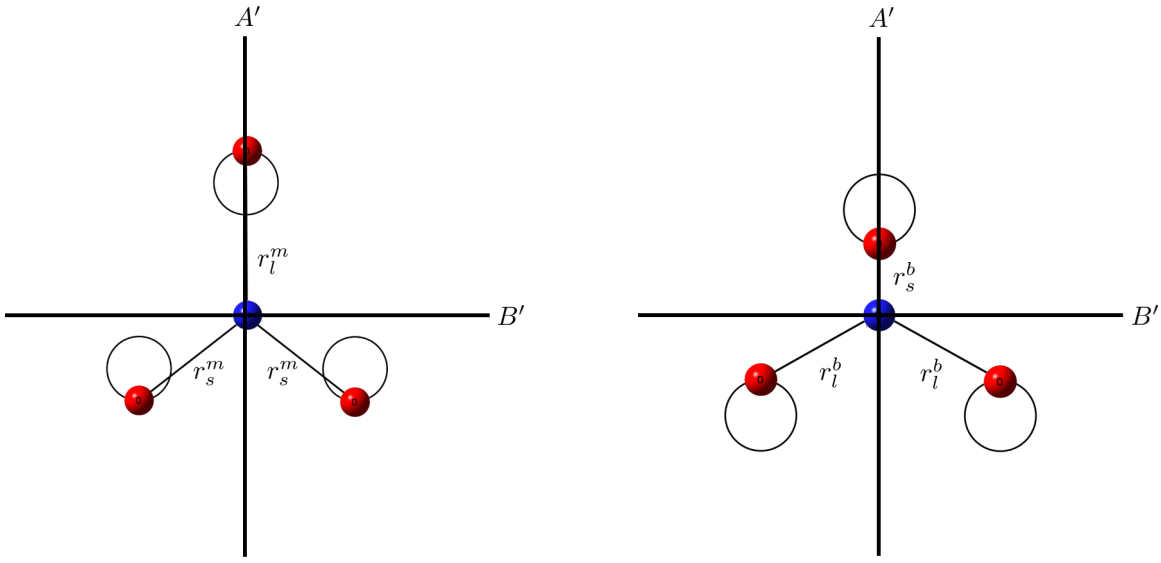

(a) Minimum (b) Barrier

Figure 4.19: The geometry of NO_3 at the pseudo-rotation minimum and barrier. Labels on axes indicate the moment of inertia around that axis.

Here, superscripts ^{m} and ^{b} stand for the values calculated at the minimum and barrier respectively. Subscripts $_s$ and $_l$ indicate whether the long or short bond length is used. At the minimum, there is one unique long bond and at the minimum, there is one unique short bond. θ is taken as the angle between the two non-unique oxygens. The difference in A' and B' is $2h_1$ and thus, an h_1 value can be obtained at both minimum and barrier.

$$h_1 = \frac{A' - B'}{2} \tag{4.28}$$

These are also listed in Table 4.8. The averaged value is $h_1 = 0.0177$ cm^{-1}. This is an order of magnitude higher than both fit values of h_1. The fits indicate a lower Jahn-Teller distortion compared to the *ab-initio* analysis.

4.7.3 *Ab-initio* Determination of Spin-Rotation Coupling

The spin-rotation coupling term, ε_{bb}, is rigorously

$$\varepsilon_{bb} = -2 \sum_{i \neq j} \frac{\langle i| B\hat{L}_x |j\rangle \langle j| a\hat{L}_x |i\rangle + \langle j| B\hat{L}_x |i\rangle \langle i| a\hat{L}_x |j\rangle}{E_i - E_j} \tag{4.29}$$

Table 4.8: *Ab-initio* bond lengths and bond angles and h_1 values at the minimum and barrier of the electronic potential energy surface. The bond angle is between the two oxygens with the same bond length.[1]

	Minimum	Barrier
Short Bond (Å)	1.207	1.220
Long Bond (Å)	1.462	1.306
Bond Angle	131.3°	112.3°
h_1 (cm^{-1})	0.0184	0.0170
Average h_1 (cm^{-1})	0.0177	

where i and j run over electronic states, E_i is the energy of the i^{th} electronic state, and the rest of the terms are defined in Section 3.1. A few approximations can be made. The spin-orbit coupling to the $\widetilde{B}^2E'$ state has been found to be small, so only the term involving the $\widetilde{A}^2E''$ and $\widetilde{X}^2A_2'$ states is included. If B and a are pulled out of the expectation,

$$\varepsilon_{bb} \approx \frac{4|aB||\left\langle \tilde{A}\right| \hat{L}_x \left|\tilde{B}\right\rangle|^2}{\Delta E(\tilde{A} \leftarrow \tilde{X})} \tag{4.30}$$

By approximating $|\left\langle \tilde{A}\right| \hat{L}_x \left|\tilde{B}\right\rangle|$ to unity, this equation can be used to find the value of a. For 2_0^1, $a \approx 73$ cm^{-1}, and for $2_0^1 4_0^2$, $a \approx 70$ cm^{-1}. Through discussions with Lan Cheng, an *ab-initio* value of $\sim$50 cm^{-1} has been determined for a. Because of these rough approximations, any value within a factor of 2 should be considered a good match.

4.7.4 The Lack of Jahn-Teller Distortion

The most recent *an-intio* analysis predicts a stronger Jahn-Teller coupling. Our group's vibronic analysis predicts an even greater Jahn-Teller distortion. There is yet another discrepancy in the rotational analysis, which predicts negligible Jahn-Teller distortion. At the present, there is no explanation for this large discrepancy.

The parameter h_1 determines the magnitude of linear Jahn-Teller distortion and should always be present in a molecule exhibiting linear Jahn-Teller distortions. As will be referenced in Chapter 5, both *ab-initio* and experimental vibronic fits agree on a large linear Jahn-Teller distortion and this is seen as a higher h_1 inferred from *ab-initio* calculations.

One consideration is the discrepancy between rotational and vibrational timescales. It is typically believed that rotational motion occurs on larger timescales than vibrations, and the Jahn-Teller effect is in essence, a vibrational effect. It may be that the Jahn-Teller effect is not observed on the rotational timescale. Figure 2.6 shows the quadratic Jahn-Teller potential energy surface and the cut along the psuedo-rotation coordinate. Figure 2.7 shows a schematic representation of the vibronic energy level structure along this cut. The potential energy surface along ν_3 and ν_4 exhibits a Jahn-Teller distortion that gives rise to the the pseudo-rotational barrier. Figure 2.7 is a one-dimensional simplification. NO_3 can lie far from the conical axis in Figure 2.6, corresponding to strong Jahn-Teller distortion, but if the energy state $E_{\mathrm{ZPE}} + E_{\mathrm{vib}}$ of NO_3 shown in Figure 2.7 lies close to the barrier height, ΔE, NO_3 converts between different forms or moves along the cut so quickly that the structure of NO_3 averages out and appears to be at the conical axis. This means that NO_3 is delocalized on the potential energy surface and averages to a symmetric top. Only ν_3 and ν_4 contribute to E_{ZPE} and E_{vib} in Figure 2.7. Moreover, since ν_3 exhibits strong Jahn-Teller coupling and ν_4 exhibits weak Jahn-Teller coupling, contributions from ν_3 should be more heavily weighted. From the bottom of the minimum at E_{Minimum}, there is a zero-point energy contribution, E_{ZPE}, from ν_3 (and ν_4 to a lesser extent). The frequency of ν_3 in the $\widetilde{A}^2E''$ state is agreed to be around $\nu_3 = 1400$–1600 cm^{-1}. The zero-point energy of a degenerate mode is $h\nu = 1400$–1600 cm^{-1}. The *ab-initio* analysis determines ΔE to be 1906 cm^{-1} from the minimum. Adding in a minor contribution from the zero-point energy of ν_4, the *ab-initio* barrier height is close to the energy of the zero-point energy. However, our group's vibronic fit indicates that the pseudo-rotation barrier is 3441 cm^{-1}, with a consequence of perhaps stronger localization in a distorted geometry. This also raises a question that will be pursued in Chapter 6, regarding the accuracy of the experimental fit and potential to overestimate the Jahn-Teller effect. The Watson term however, should rigorously be nonzero, even in the case of large delocalization, making it difficult to reach a conclusion with this information.

Another qualitative determination that can be made about this result is based on the fact that h_1 for 2_0^1 and $2_0^1 4_0^2$ are very similar. Since ν_4 contributes to E_{ZPE} and E_{vib} in

Figure 2.7, one might except two quanta of ν_4 to eliminate any Jahn-Teller distortion that was seen in 2_0^1. This turns out not to be the case and the most likely explanation is that ν_4 is very weakly Jahn-Teller coupled, and contributes weakly to the energy structure in Figure 2.7. This has been backed by other vibronic analyses of the $\widetilde{A}^2E''$ state.[37,27]

In summary, while there are some potential explanations to believe that a rotational analysis cannot study Jahn-Teller distortions, there are rigorous reasons to believe that a nonzero Watson term should have been observed regardless, and potential explanations for this discrepancy are merely conjectures at this point. An explanation will be the subject of further work.

Chapter 5
The Vibronic Problem

5.1 SOCJT 2

Another way to study the Jahn-Teller effect is to study the vibronic structure directly, which our group has done recently.[1] Before we discuss the results, we will first briefly discuss the software used for the analysis and emphasize changes since the vibronic analysis.

Our group has developed the software SOCJT 2 which builds, diagonalizes, and fits the Hamiltonian described in Chapter 2. SOCJT 2 is capable of calculating the vibronic structure of any $E \otimes e$ Jahn-Teller system except for systems with a four-fold symmetric axis of rotation. Further details on SOCJT 2 can be found in the dissertation work of Terrance Codd.[37]

SOCTJ 2 generates the vibronic matrix using a hashtable. A hashtable is a data structure that assigns to each matrix element a unique string called a *key* and an integer called a *value* that is the position of that basis function in the basis vector. Selection rules are used to determine the position of nonzero matrix elements and then the matrix elements are inserted from the hashtable. This routine scales as $O(n)$.[37]

The diagonalization routine in SOCJT 2 utilizes the Lanczos Algorithm which will be discussed in greater detail in Section 5.1.1

The parameters are fit using a Levenberg-Marquardt nonlinear least squares optimization algorithm.[43] SOCJT 2 uses the algorithm published on the ALGLIB library written by Sergey Bochkanov.[44] Briefly, the Levenberg-Marquardt algorithm works by minimizing the sums of squares of the difference between calculated eigenvalues and experimental frequen-

cies. In this case the function is defined as the difference between the calculated eigenvalues and the experimental frequencies.

$$f(\omega_i, \omega_{exe\ i}, D_i, K_i, B_{ij}...) = \sum_i [(\text{calculated frequency})_i - (\text{experimental frequency})_i]^2 \tag{5.1}$$

SOCJT 2 has demonstrated linear scaling with respect to basis size.[37]

5.1.1 The Lanczos Algorithm

In problems such as rotational energies, a large number of eigenvalues are required because of the high population of rotational levels. In the vibronic problem however, only the lowest eigenvalues are necessary. The Lanczos Algorithm is a technique that calculates the lowest few eigenvalues of a matrix.

Suppose we begin with a Hermitian matrix H. It is desirable to reduce H to a matrix T that is tridiagonal because $\mathcal{O}(n)$ algorithms exist to diagonalize T.

$$T = \begin{bmatrix} \alpha_1 & \beta_2 & & & \\ \beta_2 & \alpha_2 & \ddots & & \\ & \ddots & \ddots & \ddots & \\ & & \ddots & \ddots & \beta_n \\ & & & \beta_n & \alpha_n \end{bmatrix} \tag{5.2}$$

where α_i and β_i are scalars. If we have a change of basis matrix $Q = (q_1, \ldots, q_n)$ such that

$$HQ = QT \tag{5.3}$$

From this equation, one obtains the relationships

$$\begin{aligned} &\beta_{i+1} v_{i+1} = H v_i - \alpha_i v_i - \beta_i v_{i-1} \\ &\alpha_i = v_i^T H v_i \\ &\beta_{i+1} = v_{i+1}^T H v_i \\ &\beta_1 \equiv 0, v_0 \equiv 0, v_1 \equiv [\text{Normalized Random Vector}] \end{aligned} \tag{5.4}$$

The Lanczos Algorithm can be thought of as a Gram-Schmidt procedure, but different

in that it only projects out the last two vectors obtained in the algorithm. However, in the case of a Hermitian matrix, this is enough.

Theorem: *The vectors q_i obtained through the recursion defined in Equation 5.4 are orthogonal. Assume the zero vector does not show up*

Proof: We know that $q_{i+1}^\dagger q_i = 0$ and $q_{i+1}^\dagger q_{i-1} = 0$. For $i = 3$, we are done. Suppose $q_k^\dagger q_n = 0$ for $k < n-1$. We will show that $q_k \dagger q_{n+1} = 0$ for all $k < n$.

$$\begin{aligned} q_k^\dagger H q_n &= (q_k^\dagger H^\dagger) q_n = (H q_k)^\dagger q_n \\ &= (\beta_{k-1} q_{k-1} + \alpha_k q_k + \beta_k q_{k+1})^\dagger q_n \\ &= \beta_{k-1} q_{k-1}^\dagger q_n + \alpha_k q_k^\dagger q_n + \beta q_{k+1}^\dagger q_n = 0 \end{aligned} \tag{5.5}$$

And

$$q_k^\dagger H q_n = \beta_{n-1} q_k^\dagger q_{n-1} + \alpha_n q_k^\dagger q_n + \beta_{n-1} q_k^\dagger q_{n+1} \tag{5.6}$$

Rearrange to obtain

$$\beta_{n-1} q_k^\dagger q_{n+1} = q_k^\dagger H q_n - \beta_{n-1} q_k^\dagger q_{n-1} - \alpha_n q_k^\dagger q_n = 0 \tag{5.7}$$

□

Hence, the Lanczos Algorithm produces a complete basis $\{q_1, \ldots, q_n\}$. In practice however, the Lanczos vectors end up not being orthogonal due to round off error. The order-r Krylov Subspace (K_r) is defined as

$$K_r = \text{Span}(v_0, H v_0, \ldots, H^{r-1} v_0) \tag{5.8}$$

For a finite number of steps

5.1.2 The Seed Vector

A key feature of the Lanczos Algorithm is that the set of Lanczos vectors obtained from the algorithm are generated through repeated application of the matrix of interest. Given that we are diagonalzing the Hamiltonian, it becomes possible to take advantage of some important features of the Hamiltonian, such as the fact that the Hamiltonian must be a

totally symmetric operator.

In the product basis discussed in Chapter 2, the doubly degenerate eigenvalues have $j = \pm\frac{1}{2} \mod 3$. However, the a_1 and the a_2 levels both have $j = \frac{3}{2} \mod 3$. This makes distinction between non-degenerate levels difficult in our basis set. One way to solve this problem is to directly test the symmetry of the eigenfunction, by observing how coefficients change under symmetry operations. SOCTJ 2 is capable of doing this,[37] but the method is undesirable because it comes with a large memory bottleneck. The true eigenvalues of the Hamiltonian matrix are required in order to perform this test. If the Lanczos routine is ran K times and a basis size of M is used, then the algorithm gives us K Lanczos vectors in M components. These vectors must be stored because the eigenvalues of the tridiagonal matrix must be converted back to the real eigenvalues. This requires $K \times M$ bytes of data. Although K is relatively small, M grows to be quite large making this method unfeasible for medium to large bases. A second disadvantage is the time cost of transforming the basis of Lanczos vectors to the original product basis.

The new method named the "Seed Vector" is an alternative way to obtain only eigenvalues of the exact desired symmetry, and it avoids the M term in the memory requirement. Consider the symmetry of the Lanczos vector q_{i+1}. Based on Equation 5.4

$$\Gamma(q_{i+1}) = \Big(\Gamma(\hat{\mathcal{H}}) \otimes \Gamma(q_i)\Big) \oplus \Gamma(q_i) \oplus \Gamma(q_{i-1}) \tag{5.9}$$

However, since the Hamiltonian is totally symmetric, $\Gamma(\hat{\mathcal{H}}) \otimes \Gamma(q_i) = \Gamma(q_i)$. Since Lanczos vectors are obtained from repeated application of the Hamiltonian to the initial vector, the symmetry of the initial vector will be the symmetry of all the Lanczos vectors. In exact form, if the starting vector has symmetry a_1, then all Lanczos vectors have symmetry a_1 and thus only a_1 eigenvectors can be obtained from the tridiagonal matrix. In practice however, there is round off error and all eigenvectors are still obtained. However, the first eigenvector is of true a_1 symmetry and numerically, we check that the dot product

$$q_1 \cdot v = q_1 \cdot \sum_i a_i q_i \tag{5.10}$$

between the first Lanczos vector and the eigenvector is greater than a tolerance. If so, we

trust that the eigenvector is a_1 and keep it. Otherwise, we discard the eigenvector and its eigenvalue.

The advantage to this method is that it does not reference the eigenvectors in the original basis. This means that the Q transformation matrix does not have to be saved. The method only requires knowledge of the eigenvectors of T, which is a $K \times K$ matrix. For K eigenvectors with K components, only $K \times K$ bytes is required, which is a relatively small number. Moreover, to maintain accuracy, basis size must increase relatively quickly with the system complexity. However, the number of Lanczos iterations remains consistent.

There is a problem that must be addressed involving "accidental orthogonality." It was assumed that eigenvectors have zero overlap with the first Lanczos vector for only symmetry reasons. This is not true, and there are cases where there could be zero overlap with the same symmetry. One such example we have encountered is that the symmetry of a vector depends on the linear combination of different l states in the degenerate mode. However, additional quanta in a totally symmetric mode does not affect this symmetry, but will create a situation with a zero dot product. In order to circumvent this, we have added contributions from different quanta of the totally symmetric mode into the seed vector. This is a problem that must be handled as it arises.

5.2 Previous Vibronic Analysis

Our group has collected a jet-cooled, cavity ringdown spectrum of the $\widetilde{A}^2E'' \leftarrow \widetilde{X}^2A_2'$electronic transition of the NO_3 radical from 7550 cm^{-1} to 9750 cm^{-1} as seen in Figure 5.1. An excellent fit of the spectrum was produced using SOCJT 2. The results of the fit are listed in Table 5.1. The assignments used in the fit are listed in Table 5.2 There are two different fits. The "Weak JT" fit starts from weak Jahn-Teller coupling in ν_3, whereas the "Strong JT" starts from strong Jahn-Teller coupling in ν_3. Two different set of assignments were made for the Strong JT fit. The Low E fit makes fewer assignments on higher energy levels compared to the High E fit. As shown in Table 5.2, the fits agree well with experiment. The calculated spectrum is plotted along with the experimental spectrum in Figure 5.2.[1]

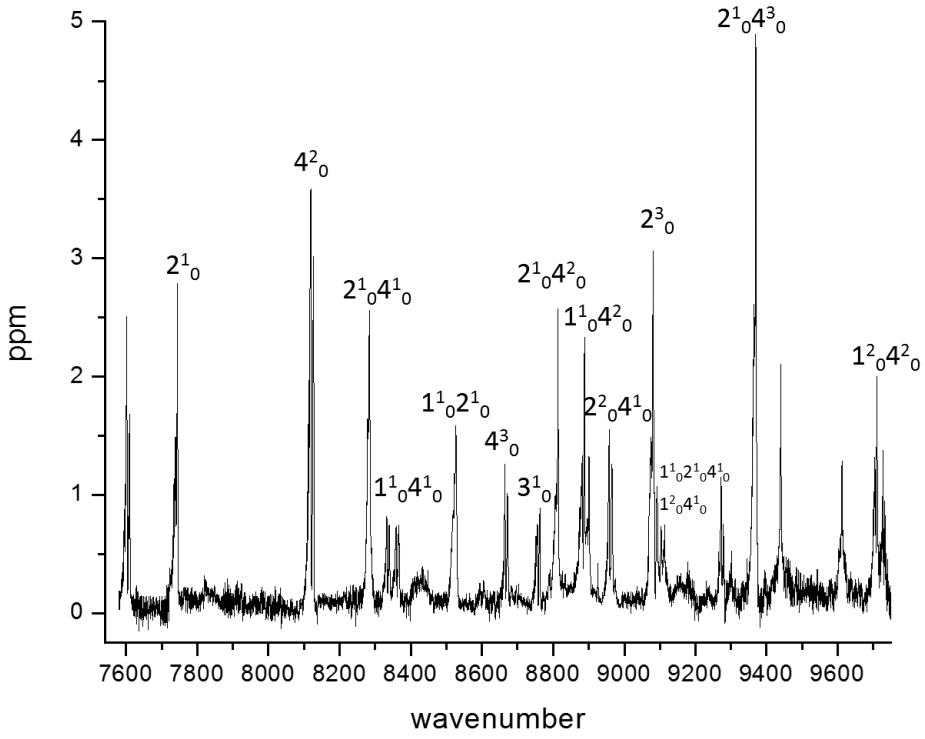

Figure 5.1: The vibronic bands in $\widetilde{A}^2E'' \leftarrow \widetilde{X}^2A_2'$ electronic transition obtained by jet-cooled cavity ringdown spectroscopy.[1]

Table 5.1: Best parameters and errors obtained from the $\widetilde{A}^2E'' \leftarrow \widetilde{X}^2A_2'$ spectral fit.[1]

Mode		Weak JT		Strong JT: Low E		Strong JT: High E	
ν_3	ω	1560.8 cm^{-1}	0.6 cm^{-1}	1435.6 cm^{-1}	1.5 cm^{-1}	1434.7 cm^{-1}	1.1 cm^{-1}
	D	0.0605	0.0005	3.21	0.02	3.20	0.01
	K	0.1979	0.0007	0.244	0.001	0.244	0.000
ν_4	ω	525.7 cm^{-1}	0.2 cm^{-1}	528.2 cm^{-1}	0.6 cm^{-1}	530.7 cm^{-1}	0.2 cm^{-1}
	D	0.0050	0.0003	0.00	0.03	0.00	0.01
	K	0.0325	0.0008	0.0219	0.0040	0.0206	0.0008

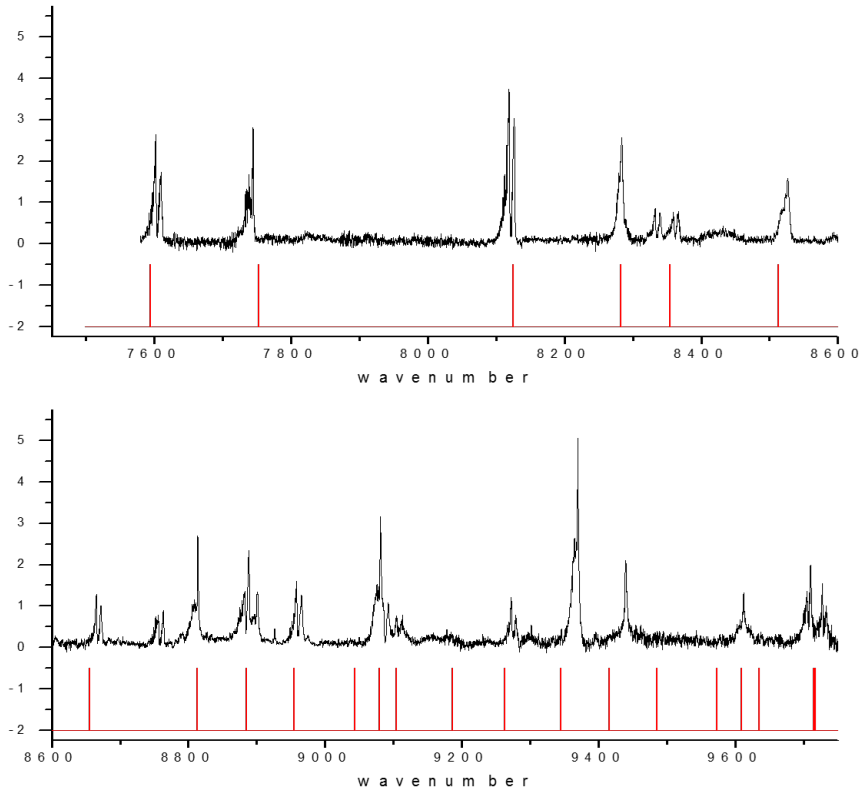

Figure 5.2: Calculated $\widetilde{A}^2E'' \leftarrow \widetilde{X}^2A_2'$ spectrum. The top trace is the experimental trace. The bottom trace is are the calculated levels using the fit parameters.[1]

Table 5.2: Jahn-Teller Fits (All Units in cm^{-1})[1]

Assignment	Experimental	Weak Coupling	Error	Low Energy	Error	High Energy	Error
Origin	7062.3[30]	–		–		–	
$3_0^1\ a_2''$	7070.3	–		7070.5	-0.2	7070.5	-0.2
$4_0^1\ e''\ (2_0^1 4_0^1)$	7601.6	7591.5	10.1	7601.6	0.0	7603.8	-2.2
$4_0^1\ a_1''$	7601.8	7598.7	3.1	7596.2	5.6	7598.3	3.4
$4_0^2\ a_1''$	8118.9	8120.8	-1.9	8118.6	0.3	8123.5	-4.7
$4_0^2\ e''(2_0^1 4_0^1)$	8131.7	8130.5	1.2	8133.2	-1.5	8137.7	-6.0
$3_0^1\ e''\ (2_0^1 3_0^1)$	8218.6	–		8220.3	-1.7	8219.0	-0.4
$3_0^1\ a_1''$	8332.8	–		8333.0	-0.2	8332.8	0.0
$3_0^2\ e''\ (2_0^1 3_0^2)$	8409.7	–		8409.4	0.2	8409.7	0.0
$4_0^3\ a_1''$	8665.1	8664.1	1.0	8666.6	-1.5	8673.2	-8.1
$3_0^1 4_0^1\ a_1''$	8755.7	8755.4 (3_0^1)	0.3	8754.0	1.7	8754.9	0.8
$4_0^1\ e''\ (2_0^3 4_0^1)$	7593.6	–		–		7590.2	3.3
$4_0^3\ e''\ (2_0^1 4_0^3)$	8687.6	8687.0	0.6	–		8674.2	13.3
$3_0^1 4_0^1\ e''\ (2_0^1 3_0^1 4_0^1)$	8757.4	8758.5 (3_0^1)	-1.1	–		8749.3	8.1
$3_0^1 4_0^2\ a_1''$	9271.9	9270.7 ($3_0^1 4_0^1$)	1.2	–		9280.2	-8.4
$4_0^5\ a_1''$	9704.2	9705.4	-1.2	–		9703.9	0.3
$4_0^5\ a_1''$	9726.9	9728.9	-2.0	–		9722.1	4.7
RMS Error =			3.37		2.05		5.52

However, an issue arose from this analysis comparing the experimental fit to *ab-initio* calculations. While the results agree qualitatively in that both predict strong coupling in ν_3, the magnitude of this coupling is significantly higher in the experimental fit than determined in the *ab-initio* calculation. The comparisons of D and K are shown in Table 5.3.[1]

5.2.1 Computational Details and Quartic Jahn-Teller Hamiltonian

A potential suspect for this discrepancy is the inclusion of cubic and quartic terms in the Jahn-Teller potential. It is possible that the lack of these terms in the fitting potential has caused the linear and quadratic coupling to deceptively increase, compensating for effects that cannot be produced in the Hamiltonian. The computational model developed by Stanton is briefly summarized.

The potential energy surface of the $\widetilde{A}^2E''$ state was computed using Equation of Motion Ionized Potential (EOMIP) level of theory and a coupled-cluster basis set with single, double, and triple excitations (CCSDT). The nitrate anion was used as the reference state and

Table 5.3: Characteristics of the Jahn-Teller potential energy surface determined from the experimentally fit parameters versus electronic structure calculations.

	Exp. Fit	Calc.
JTSE (cm^{-1})	5738	2999
Pseudo-rotation Barrier (cm^{-1})	2295	1093
D_3	3.21	1.15
K_3	0.244	0.136
D_4	≤ 0.01	0.18
K_4	0.022	0.12

calculations were done in the vicinity of the nitrate anion geometry, D_{3h}. These calculations were used to parametrize the following Hamiltonian in the Cartesian diabatic basis.

$$\hat{\mathcal{H}} = \hat{T}_N + \begin{pmatrix} V_{11} & V_{12} \\ V_{12} & V_{22} \end{pmatrix} \tag{5.11}$$

where

$$\begin{aligned} V_{xy} = &\sum_i F_i^{xy} q_i + \frac{1}{2} \sum_{ij} F_{ij}^{xy} q_i q_j \\ &+ \frac{1}{6} \sum_{ijk} F_{ijk}^{xy} q_i q_j q_k + \frac{1}{24} \sum_{ijkl} F_{ijkl}^{xy} q_i q_j q_k q_l \end{aligned} \tag{5.12}$$

Here, the summation indexes run over normal mode coordinates. $F_{i\ldots j}^{xy}$ are the gradients along the normal mode coordinates $q_i, \ldots, q_j$ in the (x, y) electronic block. For degenerate modes, the two degenerate components will be distinguished by a and b. For example, the gradient along the q_{ia} and q_{jb} coordinates of the degenerate i and j normal modes will be denoted F_{iajb}^{xy}. In the adiabatic basis, these gradients are transformed into $f_{i\ldots j}^{X}$, which are the gradients along normal modes $q_i, \ldots, q_j$ on the $^2A_2$ ($X = A$) or $^2B_1$ ($X = B$) adiabatic surfaces. The transformation will not be discussed, and all quartic parameters will be presented in terms of the diabatic parameters. However, the quadratic terms can be

converted to the convention discussed in Section 2.4.2.

$$
\begin{aligned}
D_i &= \frac{1}{2}\left(\frac{f_i^A}{\omega_i}\right)^2 \\
K_i &= \frac{\frac{1}{2}(f_{ii}^A - f_{ii}^B)}{\omega_i} \\
B_{ij} \text{ or } C_{ij} &= \frac{1}{2}(f_{ij}^A - f_{ij}^B)
\end{aligned}
\tag{5.13}
$$

Chapter 6
Fits of the Quartic Jahn-Teller Hamiltonian

As discussed in Chapter 2, the vibronic analysis thus far has been conducting by truncating the potential in Equation 2.24 to second order. This truncation is done because the parameters that can be fit are limited by the amount of spectral lines observed in the experimental data. Any terms higher than second order cannot be well-determined from usual vibronic spectra. The error introduced by this truncation may be very large. The model using only up to second order terms may not be able to reproduce the effects produced by higher order terms. Even if the spectrum is reproduced well, it is possible that significant contributions from higher order terms can be manifested in the lower order terms, producing a deceptively good fit with inaccurate parameters. As was seen in the previous vibronic analysis, a comparison of a second order Hamiltonian fit and fourth order *ab-initio* Hamiltonian have shown that while both demonstrate good agreement with experimental data, significantly different parameters and properties about the spectrum can still result from the different models.[1]

While this possibility is difficult to quantify in an experimental analysis, there is much more room for exploration in a controlled environment with artificial spectra of known linear to quartic terms. We have compared the model Hamiltonian discussed in Chapter 2 that utilizes a second order expansion and an equivalent Hamiltonian extended to fourth order terms developed by Stanton.[21] By calculating artificial spectra of known parameter values from the fourth order model, these artificial spectra can be fit with the second order model

and the fit parameters can be compared quantitatively with actual values. In particular, we are interested in how the parameters of the second order model changes with increasing cubic and quartic terms that are not present in the fit Hamiltonian, but may be present in real systems. This problem extends beyond NO_3, as similar quadratic models are generally used to fit experimental data. The same issues encountered in the analysis of NO_3 can occur for these molecules as well. The *ab-initio* potentials for NO_3 and Li_3 serve as the starting point.

6.1 Procedure of Fits

We are interested in how the parameters of a fit may change with increasing cubic and quadratic contributions. For each of the potentials to be analyzed in the following chapter, the quartic model calculates a set of vibronic eigenvalues. Each set uses the same quadratic terms that are present in the quadratic model, but different values of the cubic and quadratic coupling terms. The cubic and quartic terms are determined from an *ab-initio* analysis and in each set, are multiplied by a different scaling factor ranging from zero to unity.

Each of these sets are treated as artificial spectra and are fit using the quadratic Hamiltonian. The first set with zero cubic and quadratic coupling is fit perfectly, and the fit begins to deviate from perfection. The optimum parameters obtained from each fit as well as the RMS of the fit are collected and plotted against the scaling factor. This provides insight on how second order parameters change in order to account for a fourth order effect.

For levels based off of the NO_3 potential, vibronic levels of a_1'' and e'' are fit. This is to emulate the previous vibronic analysis[1] where the observable a_1'' levels were fit and implied e'' levels from combination differences were added to the fit. For levels based off of the Li_3 potential, levels of a_1'', a_2'', and e'' vibronic symmetry were fit.

6.2 The NO_3 Potential

The *ab-initio* coupling values for NO_3 in the $\widetilde{A}^2E''$ state was determined previously.[1] In our analysis, we consider two different set of parameters: a potential with only cubic coupling

Table 6.1: Parameters in the potential: Realistic Coupling (Cubic Only)

ω_1	750 cm^{-1}
ω_3	1417.68 cm^{-1}
D_3	1.0586
K_3	0.2143
ω_4	513.9 cm^{-1}
D_4	0.3151
K_4	0.2
C_{34}	-100 cm^{-1}

set to realistic values and no quartic coupling and a potential with the true *ab-initio* cubic and quartic coupling.

6.2.1 Realistic Coupling — Cubic Only

While a cubic potential would generally not be considered physically accurate, it is still meaningful to isolate the effect of cubic terms on the quadratic potential.

The quadratic parameters used in the Hamiltonian are listed in Table 6.1. The cubic term is scaled from 0 to 1 in steps of 0.1 and each of these sets are fit, except for C_{34} which is fixed to 100 cm^{-1}. The results of the fit for each parameter are plotted in 6.1.

An interesting result lies in the plot of D_3 in Figure 6.1c. As the scaling increases, D_3 increases quite rapidly, especially at higher cubic coupling. One manifestation of the cubic term is seen as a large increase in the quadratic D_3 term. This leads to an overestimation of the Jahn-Teller effect. This overestimation is one such possibility for the discrepancy in the previous vibronic analysis, and it shows up in this example.

There is a general trend of decreasing ω_1 and increasing ω_3. ω_4 seems stable except for a sudden change in at a scaling factor of 1.0.

The other Jahn-Teller coupling parameters K_3, D_4, and K_4 are quite small in this example. Hence, a small variance can appear to be very large and this leads to large fluctuations in the plots for these parameters.

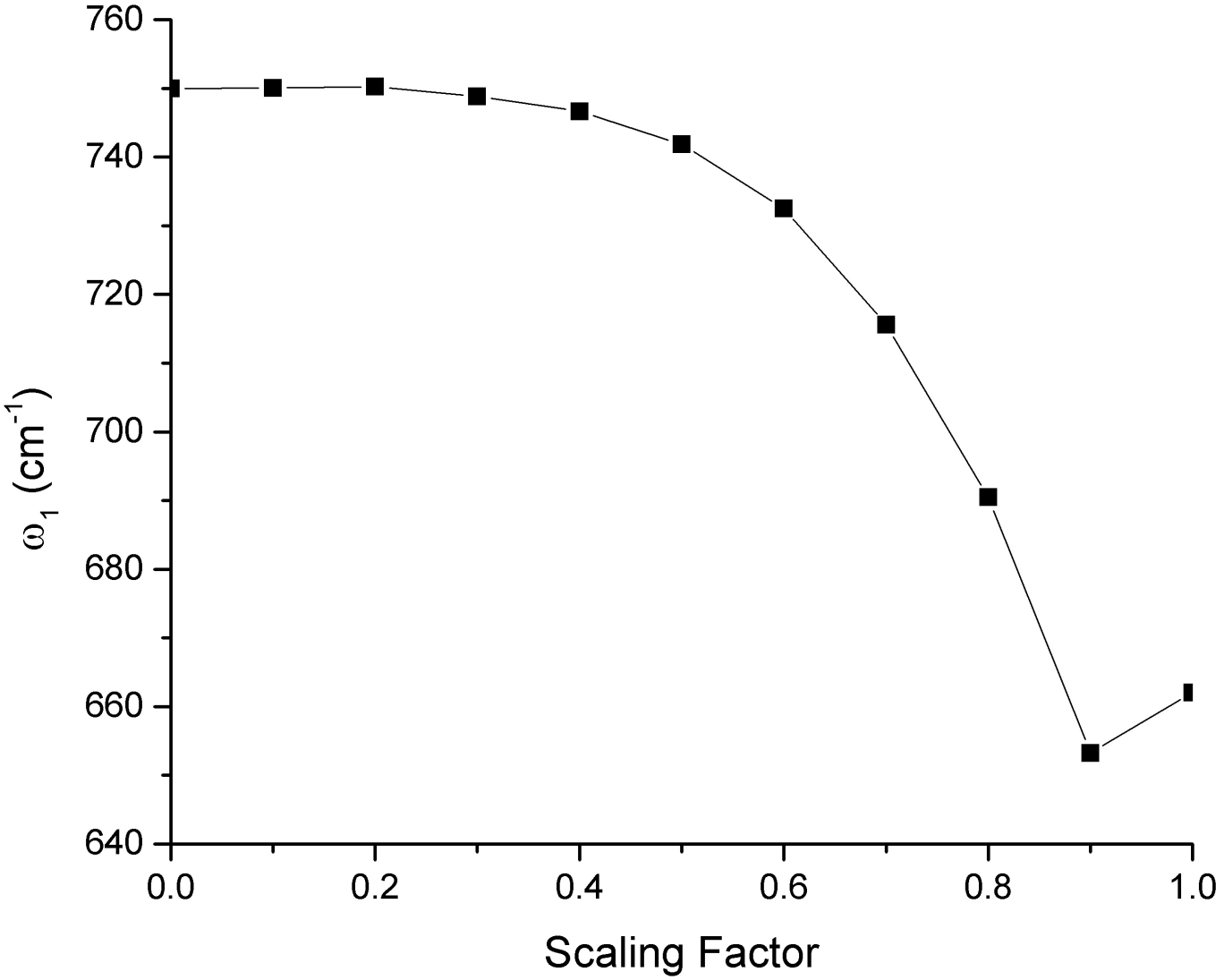

(a) Fit values for ω_1.

Figure 6.1: Scaling fits for the NO_3 Realistic Coupling (Cubic Only) potential.

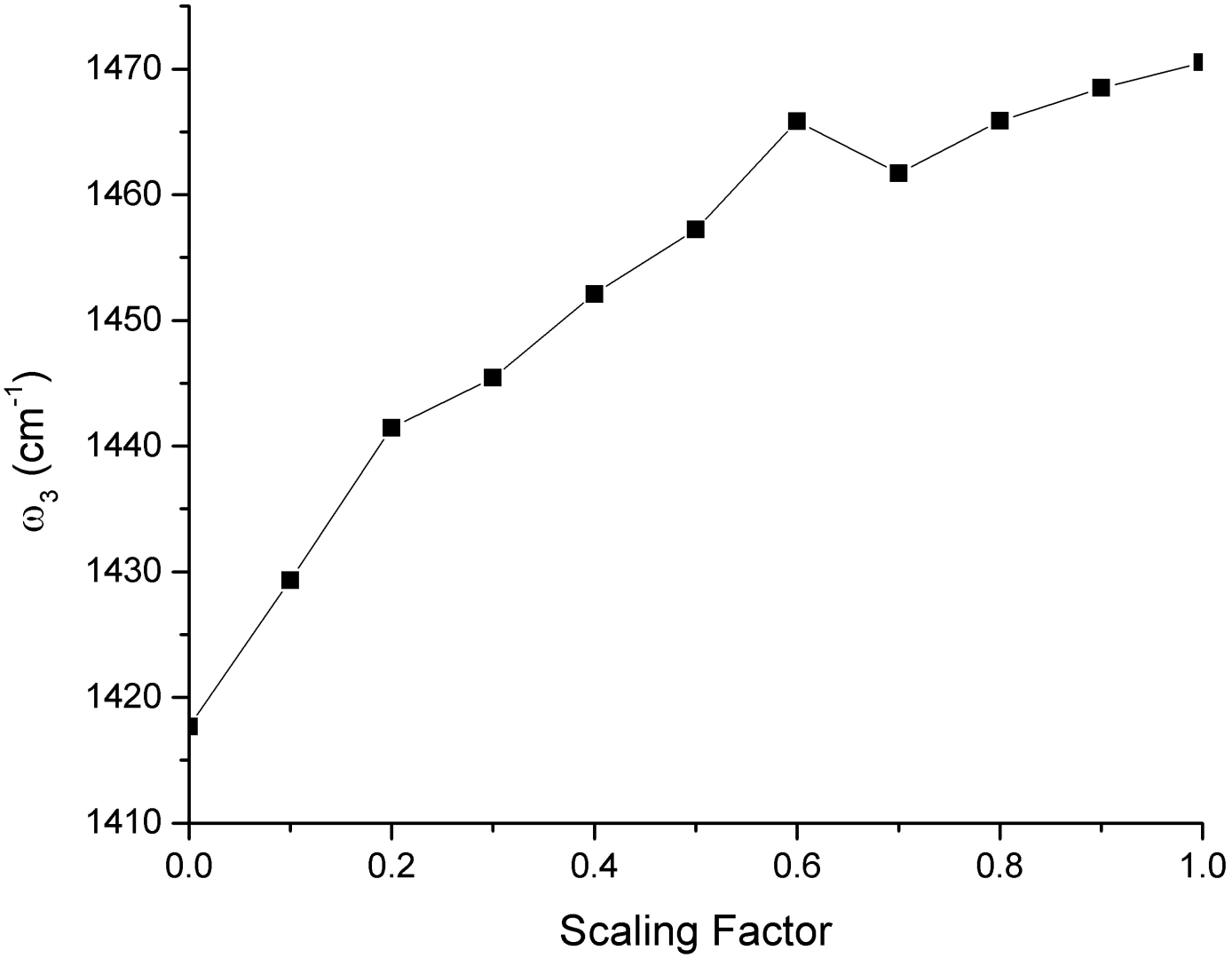

(b) Fit values for ω_3.

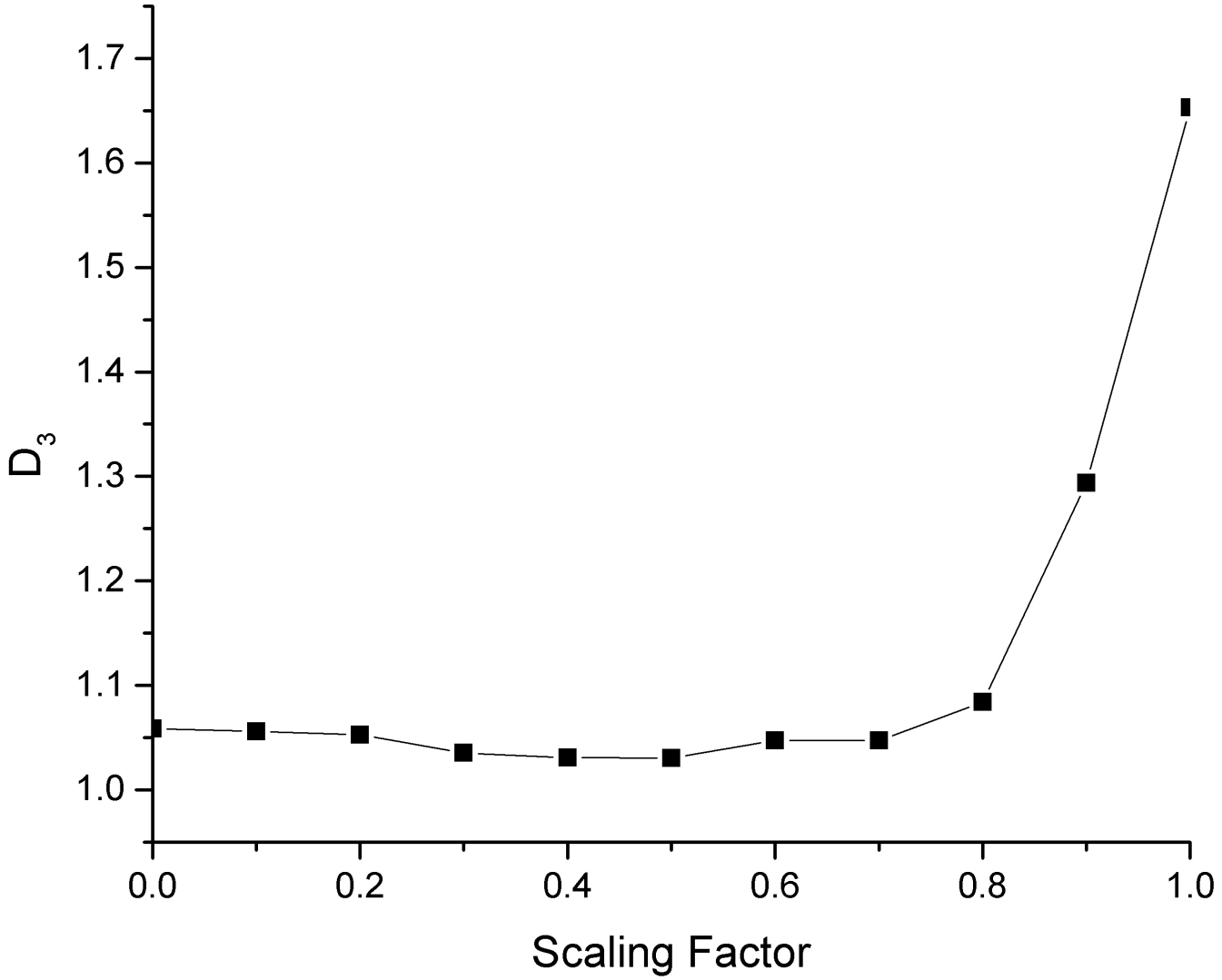

(c) Fit values for D_3.

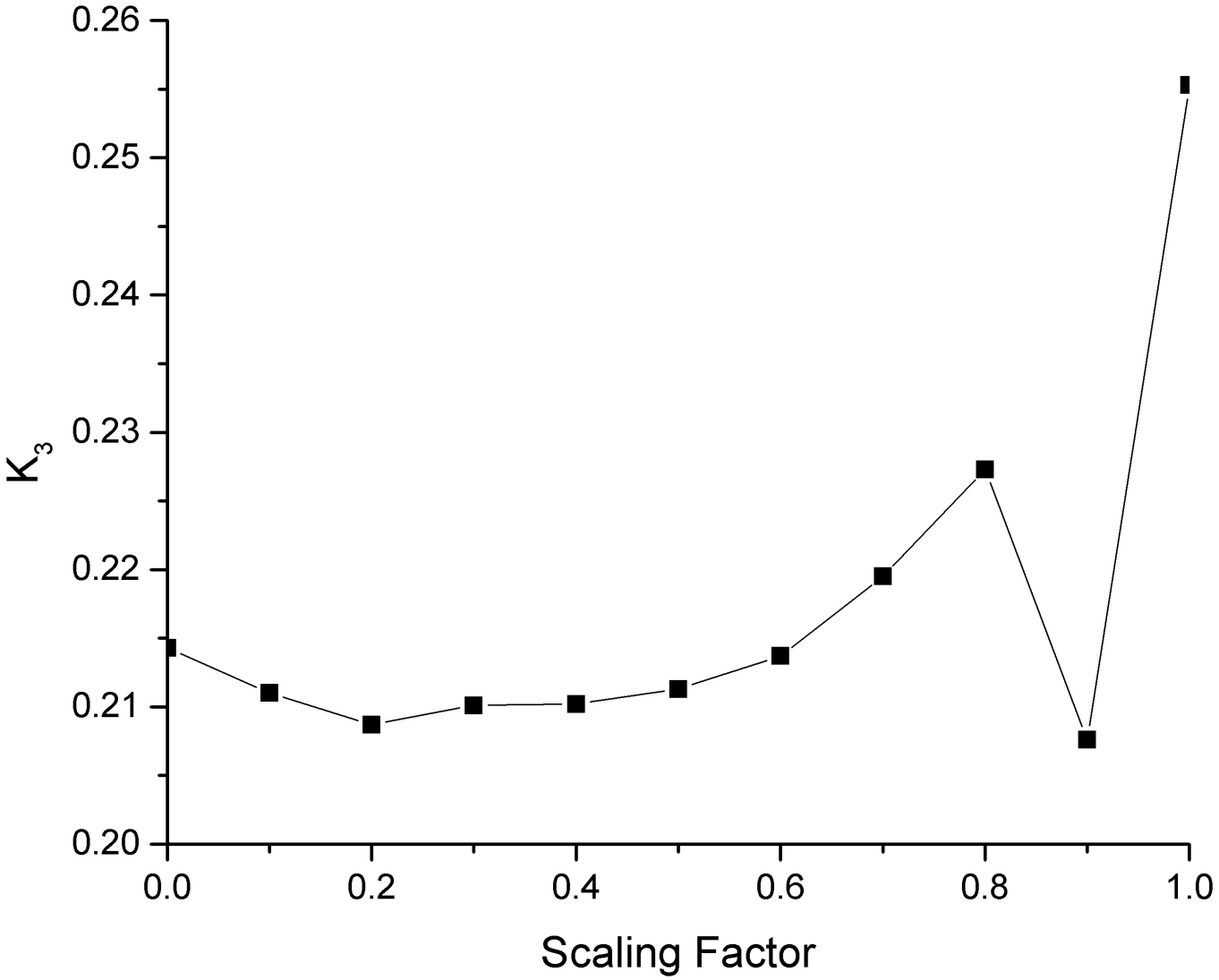

(d) Fit values for K_3.

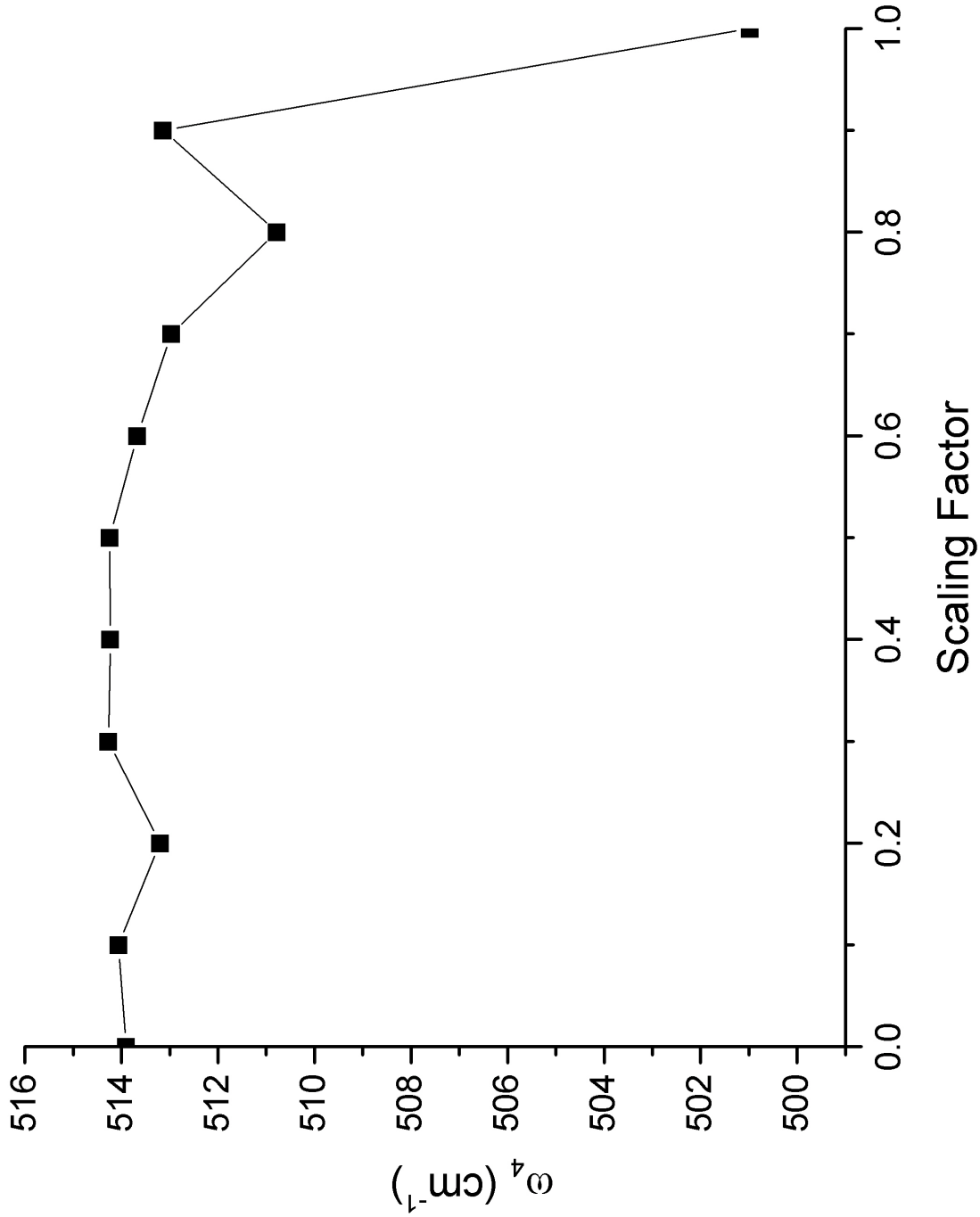

(e) Fit values for ω_4.

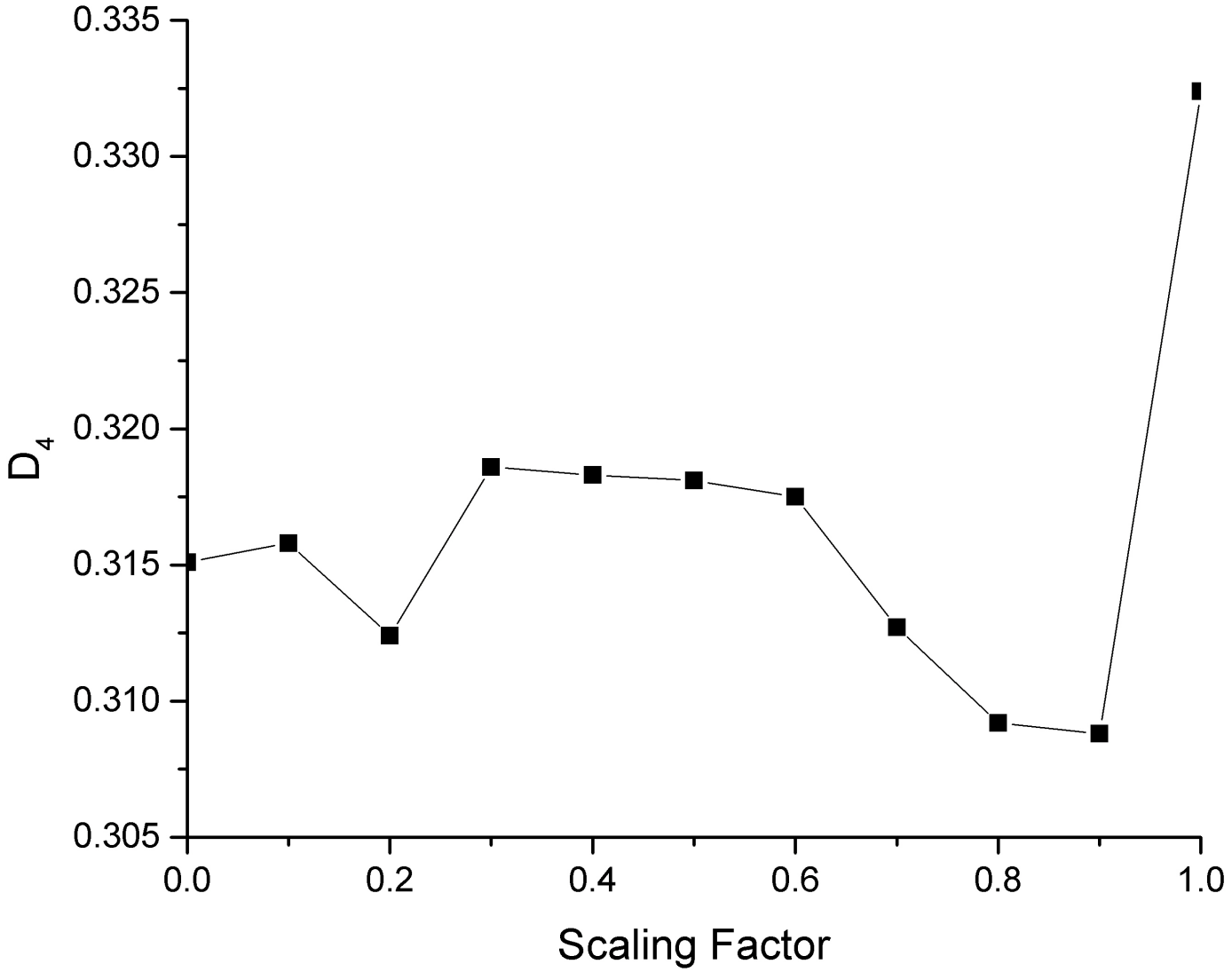

(f) Fit values for D_4.

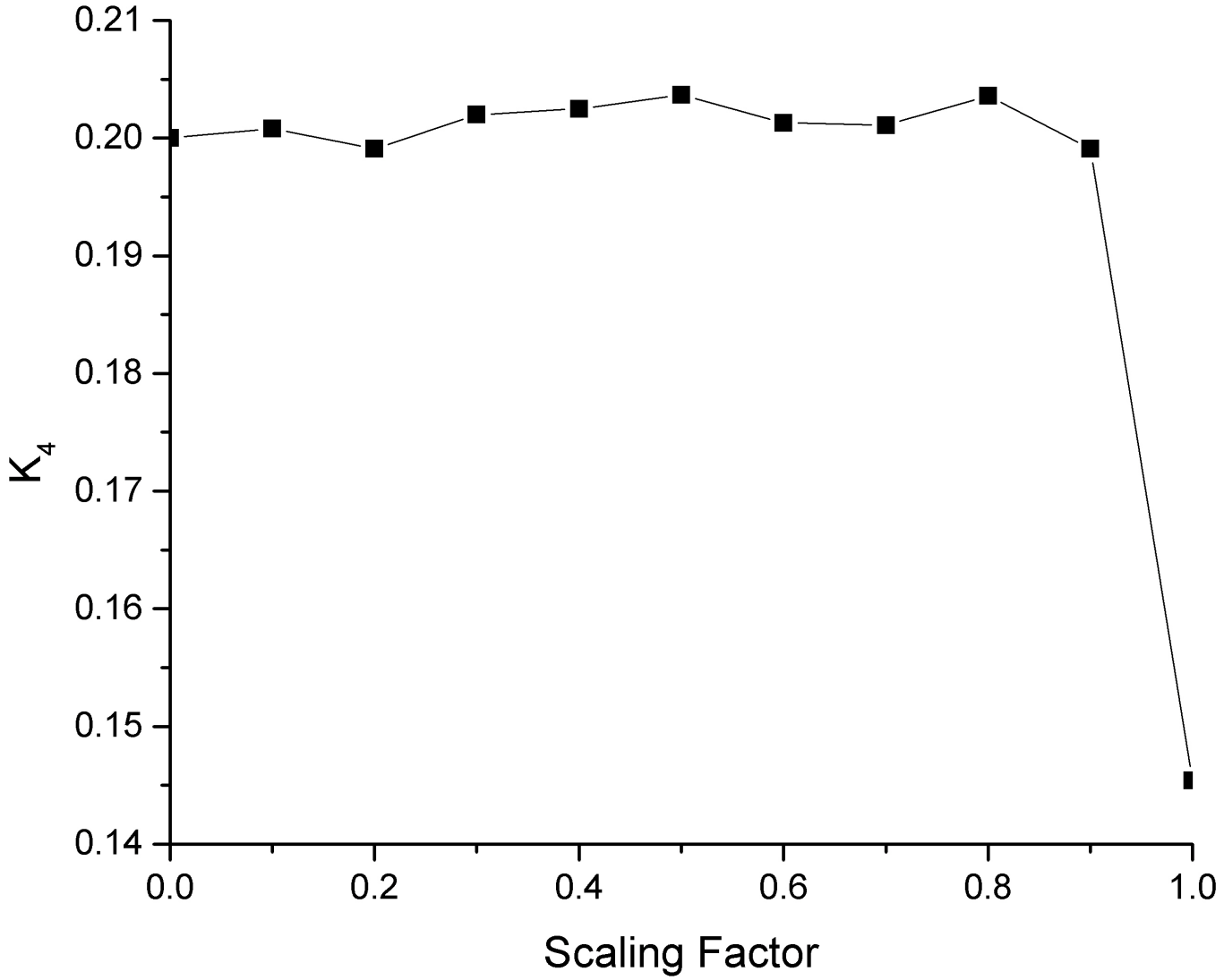

(g) Fit values for K_4.

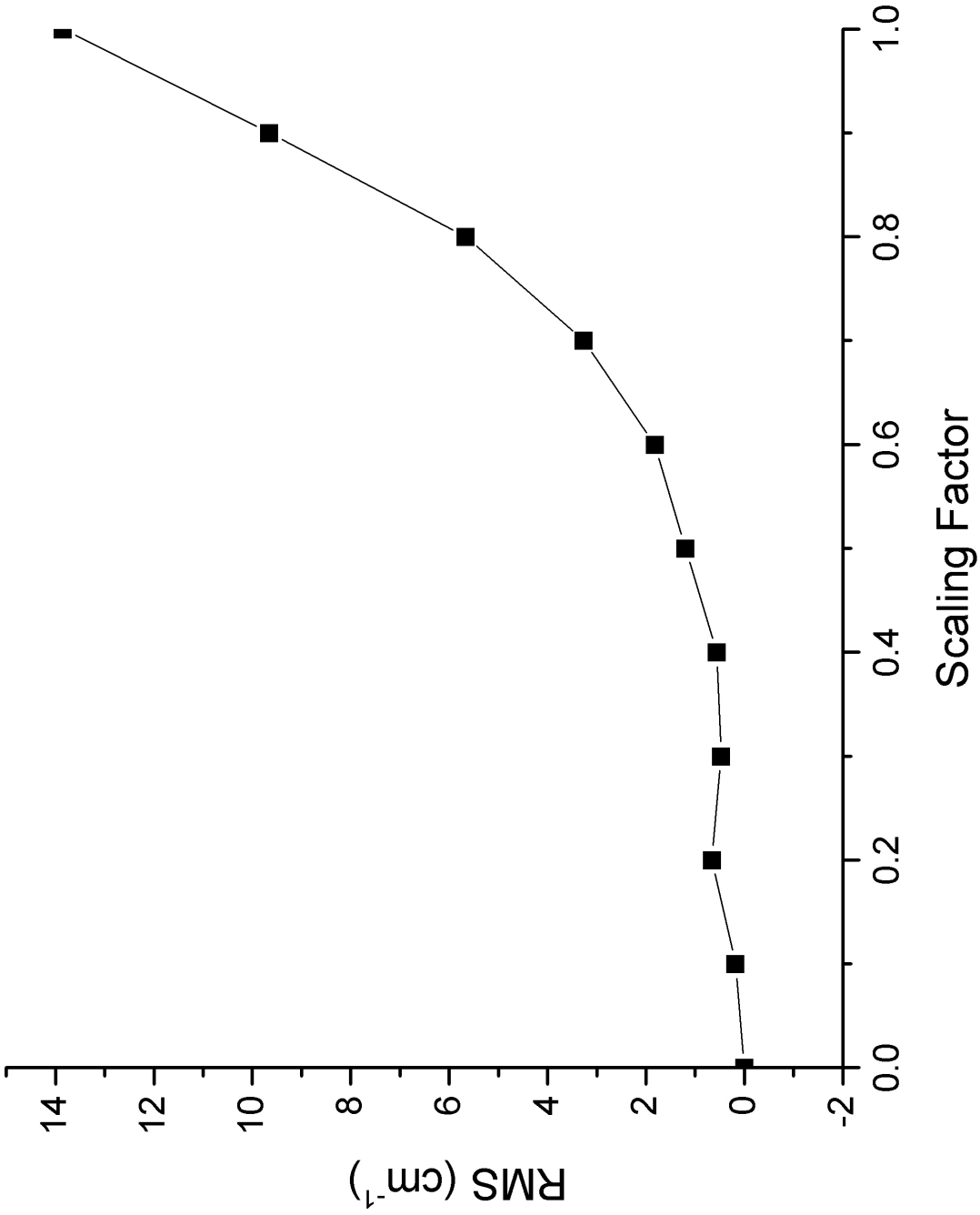

(h) Fit values for RMS.

6.2.2 True Coupling

In this set, the values of coupling determined using EOMIP/CCSDT are used. This directly studies how the potential determined by Codd[1] may have been effected by lack of terms up to fourth order.

The parameters of the quadratic Hamiltonian are the same as mentioned in Section 5.2.1 and are reproduced in Table 6.2. In Table 6.2, the parameters in the quadratic fit Hamiltonian are first presented, and then the parameters of the *ab-initio* quartic Hamiltonian in the diabatic basis are presented. The plots of the best fit parameters versus scaling factor are pictured in Figure 6.2

Table 6.2: Parameters in the potential: True Coupling. All units are cm^{-1} unless otherwise specified.

ω_1	1005.89
ω_3	1212.69
D_3 (unitless)	1.782
K_3 (unitless)	0.2794
ω_4	664.91
D_4 (unitless)	0.2605
K_4 (unitless)	-0.1282
B_{13}	132.675
B_{14}	57.6295
C_{34}	-22.5206
ω_1	1032.5988
ω_3	1252.8356
ω_4	674.1107
F_1^{11}	262.3966
F_{3a}^{11}	-2296.6115
F_{4a}^{11}	-390.9784

Continued

Table 6.2: Continued

F_{3b}^{12}	-2296.6115
F_{4b}^{12}	-390.9784
F_{1}^{22}	262.3966
F_{3a}^{22}	2296.6115
F_{4a}^{22}	390.9784
F_{13a}^{11}	-131.2731
F_{14a}^{11}	-52.3437
F_{3a3a}^{11}	1584.6468
F_{3a4a}^{11}	-96.7478
F_{4a4a}^{11}	590.8067
F_{3b3b}^{11}	921.0242
F_{3b4b}^{11}	-18.0785
F_{4b4b}^{11}	757.4147
F_{13b}^{12}	-131.2731
F_{14b}^{12}	-52.3437
F_{3a3b}^{12}	-331.8112
F_{3a4b}^{12}	39.3346
F_{4a3b}^{12}	39.3346
F_{4a4b}^{12}	83.3039
F_{13a}^{22}	131.2731
F_{14a}^{22}	52.3437
F_{3a3a}^{22}	921.0242
F_{3a4a}^{22}	-18.0785
F_{4a4a}^{22}	757.4147
F_{3b3b}^{22}	1584.6468
F_{3b4b}^{22}	-96.7478
F_{4b4b}^{22}	590.8067

Continued

Table 6.2: Continued

F^{11}_{111}	206.8187
F^{11}_{113a}	-4.0393
F^{11}_{114a}	-5.9598
F^{11}_{13a3a}	333.5362
F^{11}_{13a4a}	-88.0238
F^{11}_{14a4a}	57.786
F^{11}_{13b3b}	293.1042
F^{11}_{13b4b}	-80.4695
F^{11}_{14b4b}	71.8621
F^{11}_{3a3a3a}	317.3563
F^{11}_{3a3a4a}	-61.1236
F^{11}_{3a4a4a}	30.1075
F^{11}_{3a3b3b}	-187.4373
F^{11}_{3a3b4b}	67.0726
F^{11}_{3a4b4b}	-8.7954
F^{11}_{4a4a4a}	45.5645
F^{11}_{4a3b3b}	65.0896
F^{11}_{4a3b4b}	1.8605
F^{11}_{4a4b4b}	-50.7968
F^{12}_{113b}	-4.0393
F^{12}_{114b}	-5.9598
F^{12}_{13a3b}	-20.216
F^{12}_{13a4b}	3.7771
F^{12}_{14a3b}	3.7771
F^{12}_{14a4b}	7.038
F^{12}_{3a3a3b}	32.4797
F^{12}_{3a4a3b}	1.983

Continued

Table 6.2: Continued

F^{12}_{3a4a4b}	10.656
F^{12}_{4a4a4b}	-1.308
F^{12}_{3b3b3b}	97.4392
F^{12}_{3b3b4b}	3.966
F^{12}_{3b4b4b}	21.312
F^{12}_{4b4b4b}	-3.9242
F^{22}_{111}	206.8187
F^{22}_{113a}	4.0393
F^{22}_{114a}	5.9598
F^{22}_{13a3a}	293.1042
F^{22}_{13a4a}	-80.4695
F^{22}_{14a4a}	71.8621
F^{22}_{13b3b}	333.5362
F^{22}_{13b4b}	-88.0238
F^{22}_{14b4b}	57.786
F^{22}_{3a3a3a}	122.4778
F^{22}_{3a3a4a}	-69.0556
F^{22}_{3a4a4a}	-12.5166
F^{22}_{3a3b3b}	-252.3968
F^{22}_{3a3b4b}	63.1066
F^{22}_{3a4b4b}	-8.7954
F^{22}_{4a4a4a}	53.4129
F^{22}_{4a3b3b}	65.0896
F^{22}_{4a3b4b}	-19.4515
F^{22}_{4a4b4b}	-48.1806
F^{11}_{1111}	35.6892
F^{11}_{113a3a}	55.8481

Continued

Table 6.2: Continued

F^{11}_{113a4a}	-17.9412
F^{11}_{114a4a}	6.0808
F^{11}_{113b3b}	55.8481
F^{11}_{113b4b}	-17.9412
F^{11}_{114b4b}	6.0808
$F^{11}_{13a3a3a}$	66.7379
$F^{11}_{13a3a4a}$	-6.5272
$F^{11}_{13a4a4a}$	4.845
$F^{11}_{13a3b3b}$	-66.7379
$F^{11}_{13a3b3b}$	6.5272
$F^{11}_{13a4b4b}$	-4.845
$F^{11}_{14a4a4a}$	3.9756
$F^{11}_{14a3b3b}$	6.5272
$F^{11}_{14a3b3b}$	-4.845
$F^{11}_{14a4b4b}$	-3.9756
$F^{11}_{3a3a3a3a}$	162.1884
$F^{11}_{3a3a3a4a}$	-53.276
$F^{11}_{3a3a4a4a}$	4.5618
$F^{11}_{3a3a3b3b}$	54.0628
$F^{11}_{3a3a3b3b}$	-17.7586
$F^{11}_{3a3a4b4b}$	-25.2104
$F^{11}_{3a4a4a4a}$	-2.5531
$F^{11}_{3a4a3b3b}$	-17.7586
$F^{11}_{3a4a3b3b}$	14.8861
$F^{11}_{3a4a4b4b}$	-0.851
$F^{11}_{4a4a4a4a}$	3.1411
$F^{11}_{4a4a3b3b}$	-25.2104

Continued

Table 6.2: Continued

$F^{11}_{4a4a3b3b}$	-0.851
$F^{11}_{4a4a4b4b}$	1.047
$F^{11}_{3b3b3b3b}$	162.1884
$F^{11}_{3b3b3b4b}$	-53.276
$F^{11}_{3b3b4b4b}$	4.5618
$F^{11}_{3b4b4b4b}$	-2.5531
$F^{11}_{4b4b4b4b}$	3.1411
F^{22}_{1111}	35.6892
F^{22}_{113a3a}	55.8481
F^{22}_{113a4a}	-17.9412
F^{22}_{114a4a}	6.0808
F^{22}_{113b3b}	55.8481
F^{22}_{113b4b}	-17.9412
F^{22}_{114b4b}	6.0808
$F^{22}_{13a3a3a}$	66.7379
$F^{22}_{13a3a4a}$	-6.5272
$F^{22}_{13a4a4a}$	4.845
$F^{22}_{13a3b3b}$	-66.7379
$F^{22}_{13a3b3b}$	6.5272
$F^{22}_{13a4b4b}$	-4.845
$F^{22}_{14a4a4a}$	3.9756
$F^{22}_{14a3b3b}$	6.5272
$F^{22}_{14a3b3b}$	-4.845
$F^{22}_{14a4b4b}$	-3.9756
$F^{22}_{3a3a3a3a}$	162.1884
$F^{22}_{3a3a3a4a}$	-53.276
$F^{22}_{3a3a4a4a}$	4.5618

Continued

Table 6.2: Continued

$F^{22}_{3a3a3b3b}$	54.0628
$F^{22}_{3a3a3b3b}$	-17.7586
$F^{22}_{3a3a4b4b}$	-25.2104
$F^{22}_{3a4a4a4a}$	-2.5531
$F^{22}_{3a4a3b3b}$	-17.7586
$F^{22}_{3a4a3b3b}$	14.8861
$F^{22}_{3a4a4b4b}$	-0.851
$F^{22}_{4a4a4a4a}$	3.1411
$F^{22}_{4a4a3b3b}$	-25.2104
$F^{22}_{4a4a3b3b}$	-0.851
$F^{22}_{4a4a4b4b}$	1.047
$F^{22}_{3b3b3b3b}$	162.1884
$F^{22}_{3b3b3b4b}$	-53.276
$F^{22}_{3b3b4b4b}$	4.5618
$F^{22}_{3b4b4b4b}$	-2.5531
$F^{22}_{4b4b4b4b}$	3.1411

A look at all these plots together seem to indicate that there is some sort of "rebounding" effect occurring at a scaling factor of roughly 0.7 corresponding to a dramatic change in some of the parameters or a complete reversal of the trend up to that point. In particular, a large change occurs for D_4, B_{14}, and C_{34}. However, parameters such as ω_1, D_3, K_3, and ω_4 change from rapidly increasing (or decreasing) to decreasing (or increasing).

The RMS of the fit rises rapidly to 10.191 cm^{-1}. This is surprising as the fit of the experimental spectrum had an error of only 5.52 cm^{-1}. However, a better fit was obtained at 5.683 $cm^{-1}$for the scaling factor of 0.99. This is more similar to the experimental fit error and points out one of the difficulties of conducting this analysis. The fit converges to an RMS

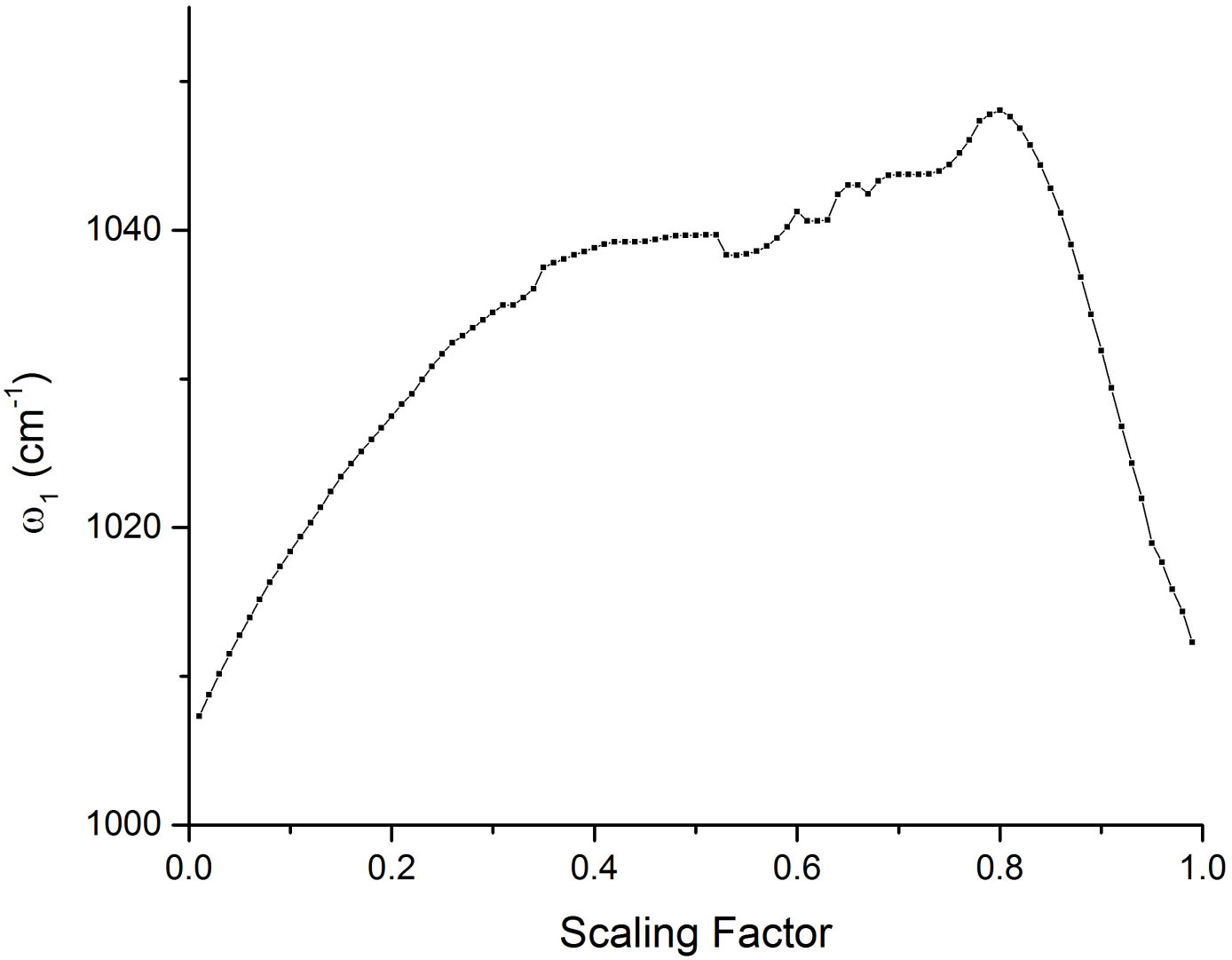

(a) NO_3 True Coupling fit values for ω_1.

Figure 6.2: Scaling fits for the NO_3 True Coupling potential.

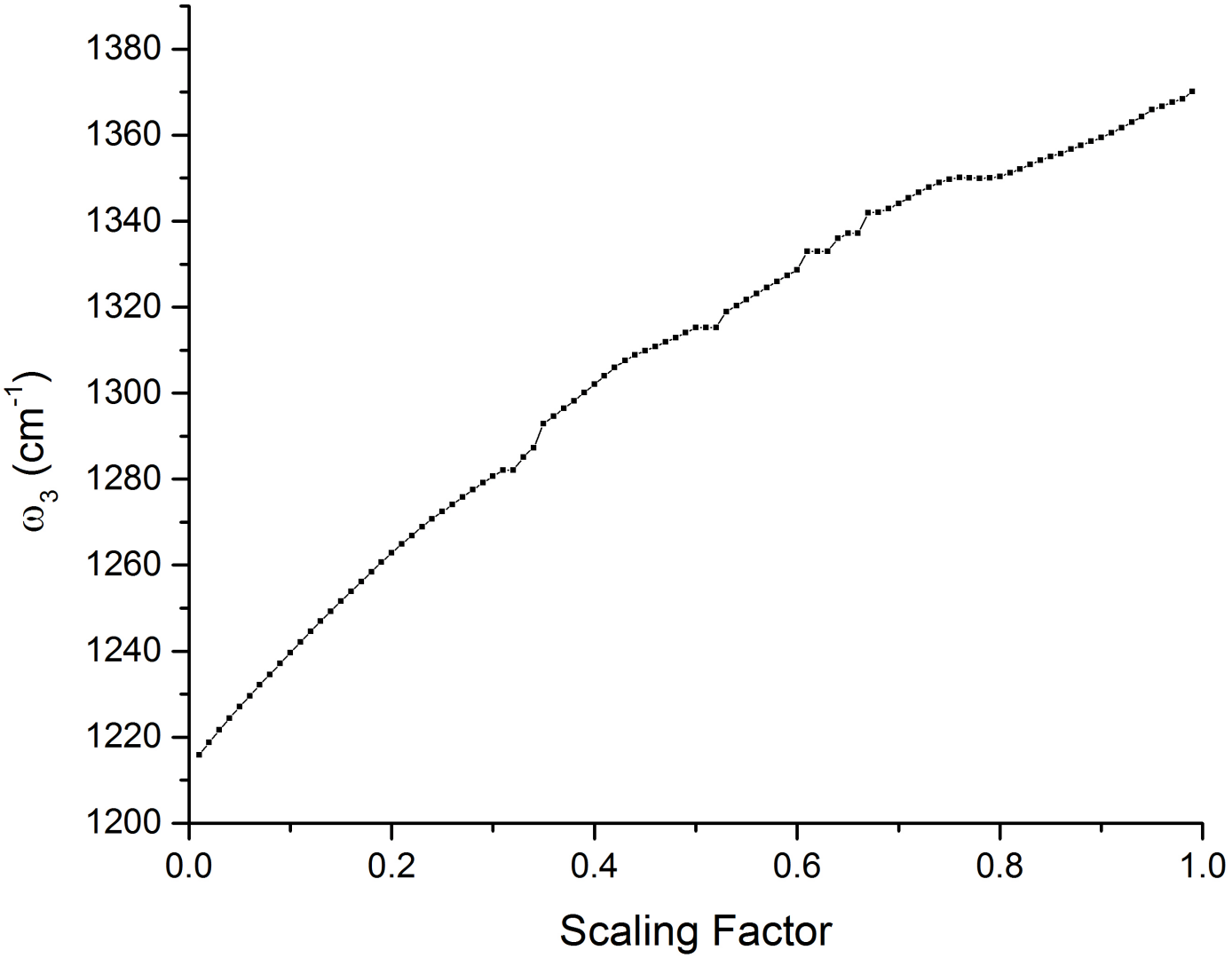

(b) NO_3 True Coupling fit values for ω_3.

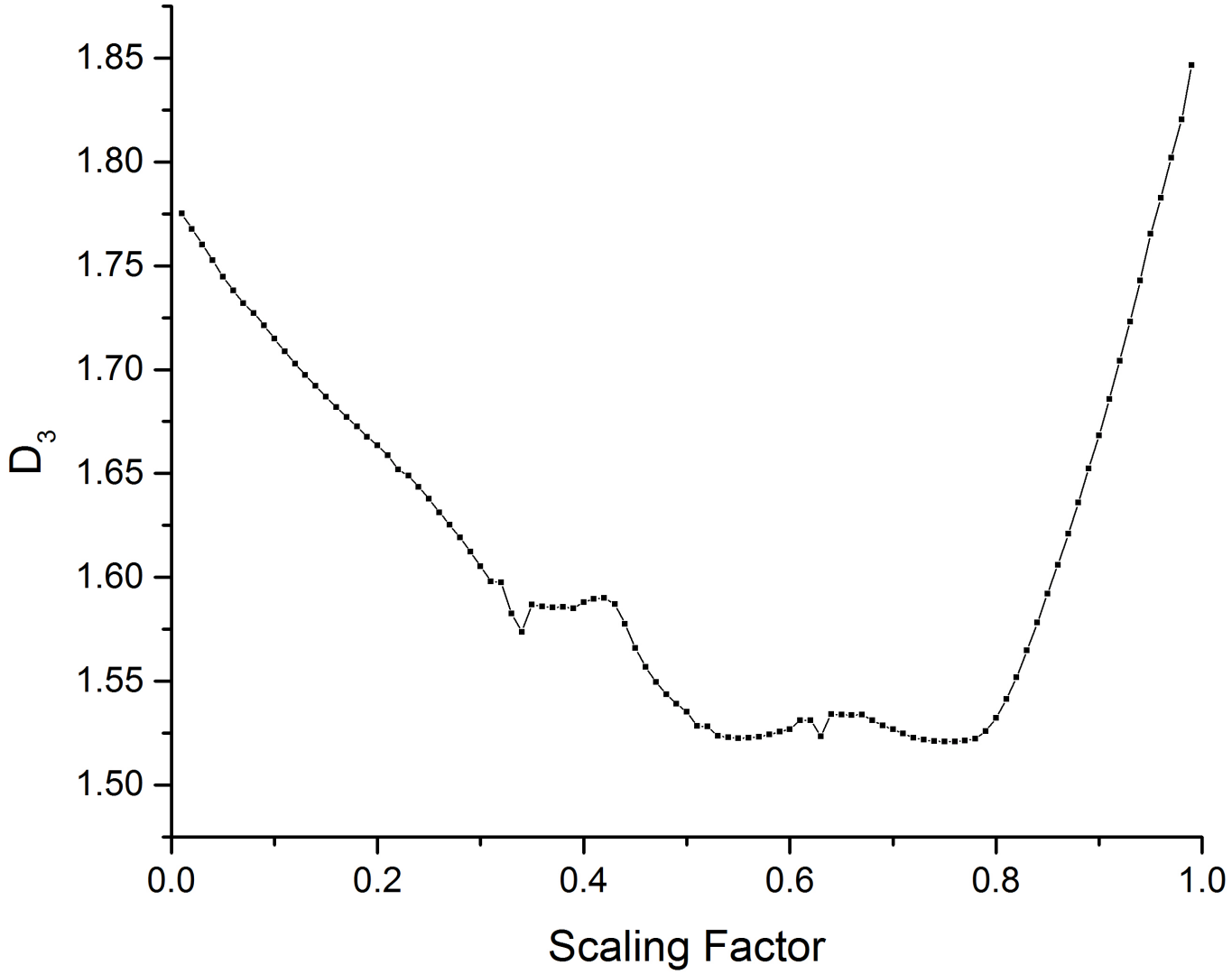

(c) NO_3 True Coupling fit values for D_3.

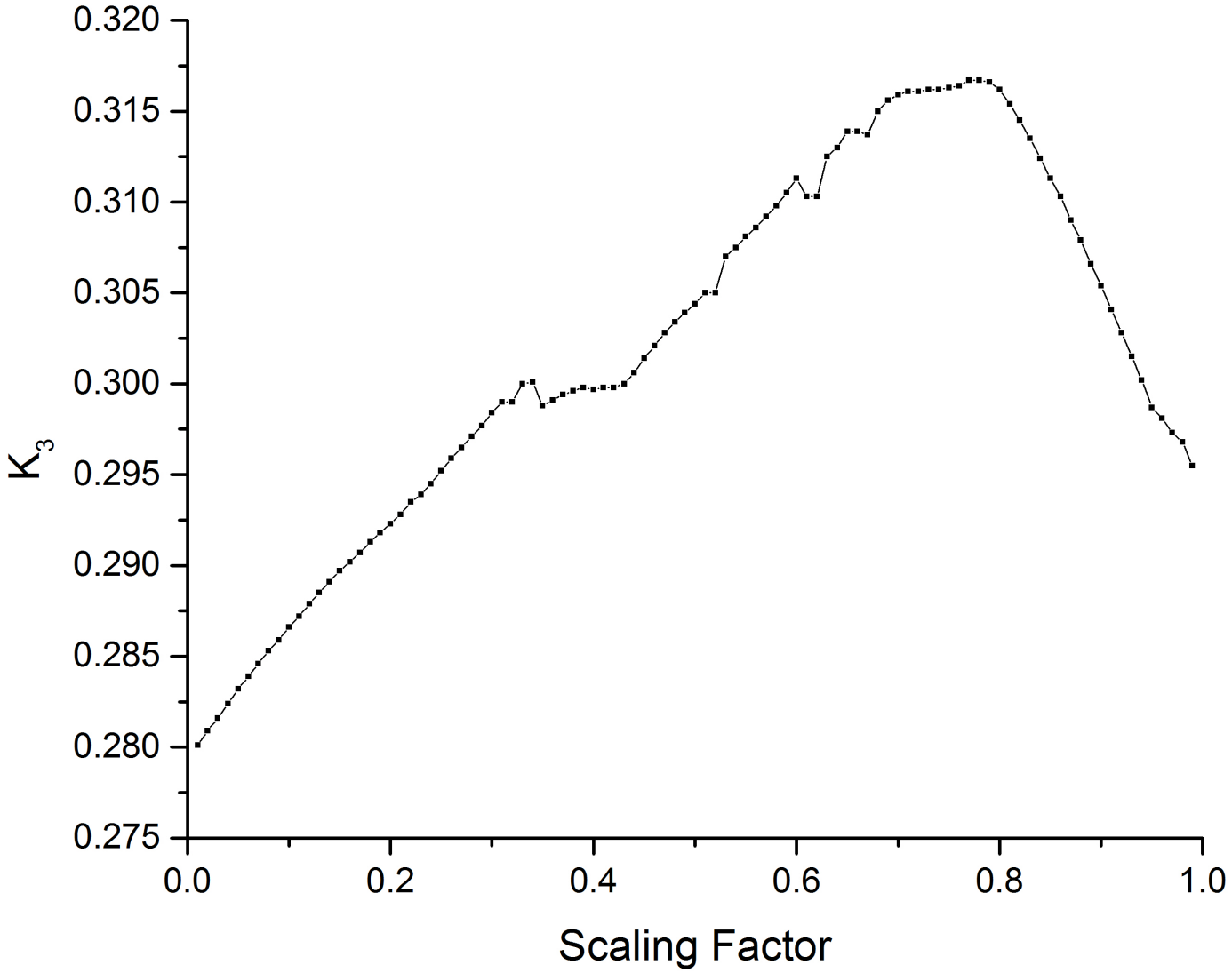

(d) NO_3 True Coupling fit values for K_3.

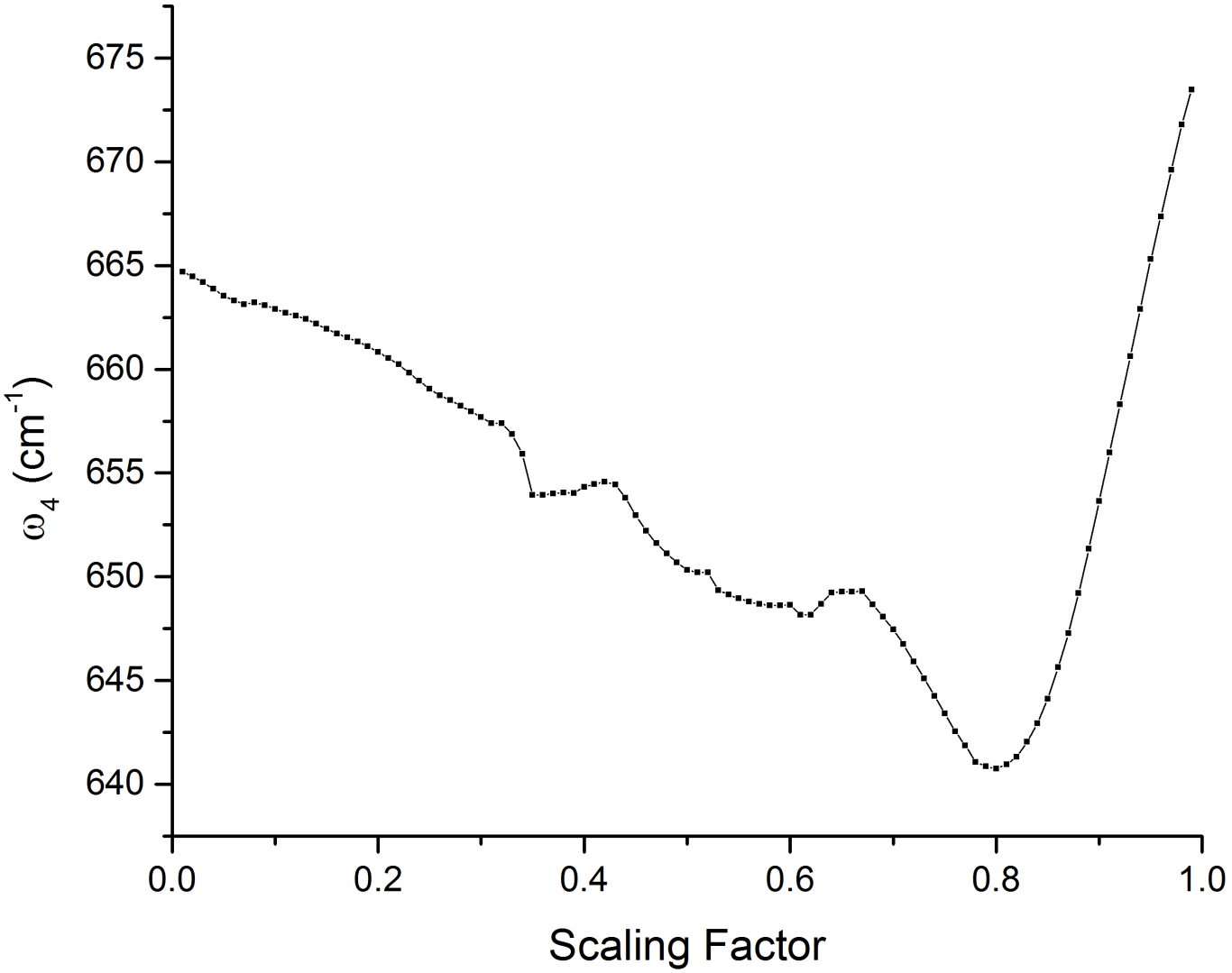

(e) NO_3 True Coupling fit values for ω_4.

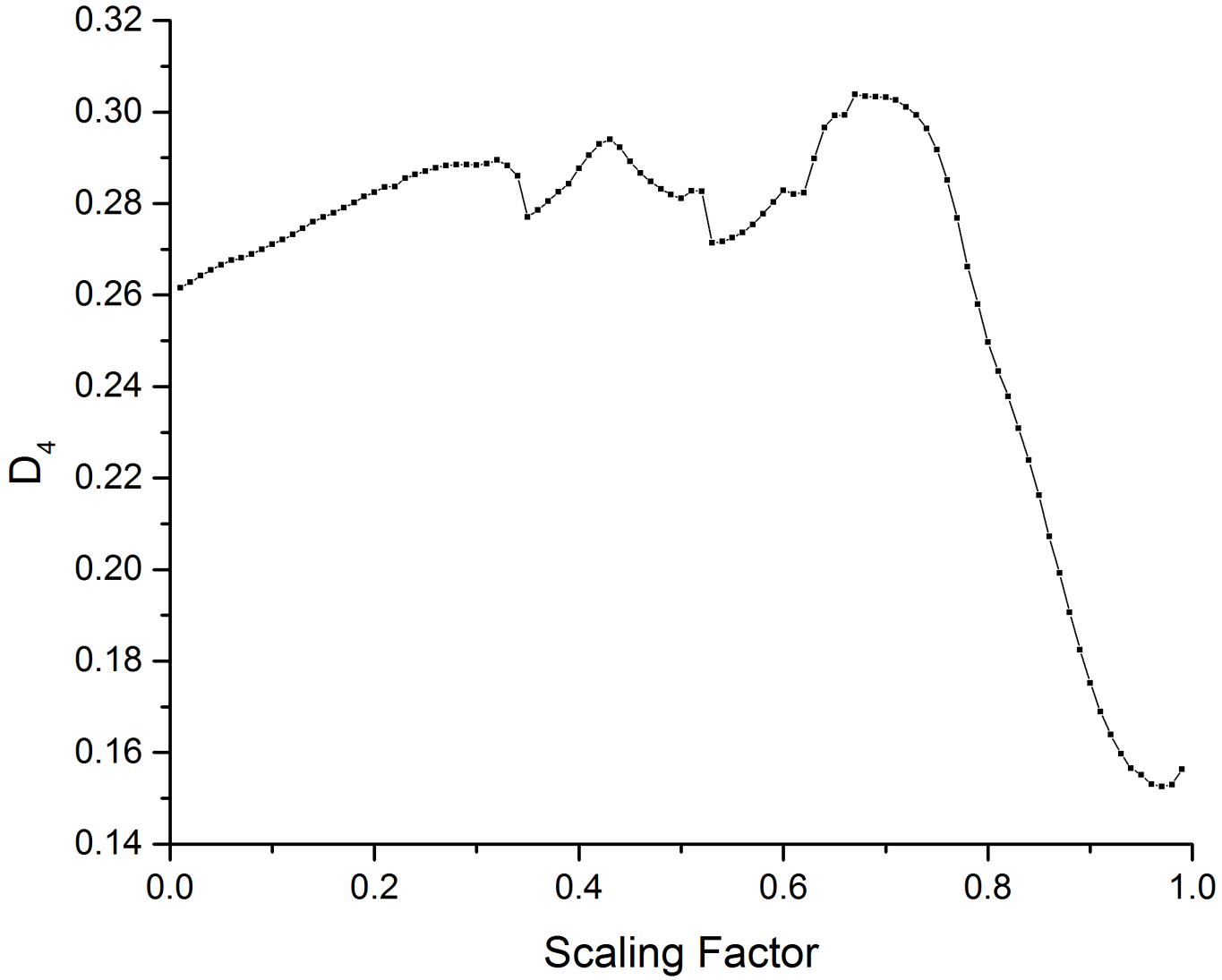

(f) NO_3 True Coupling fit values for D_4.

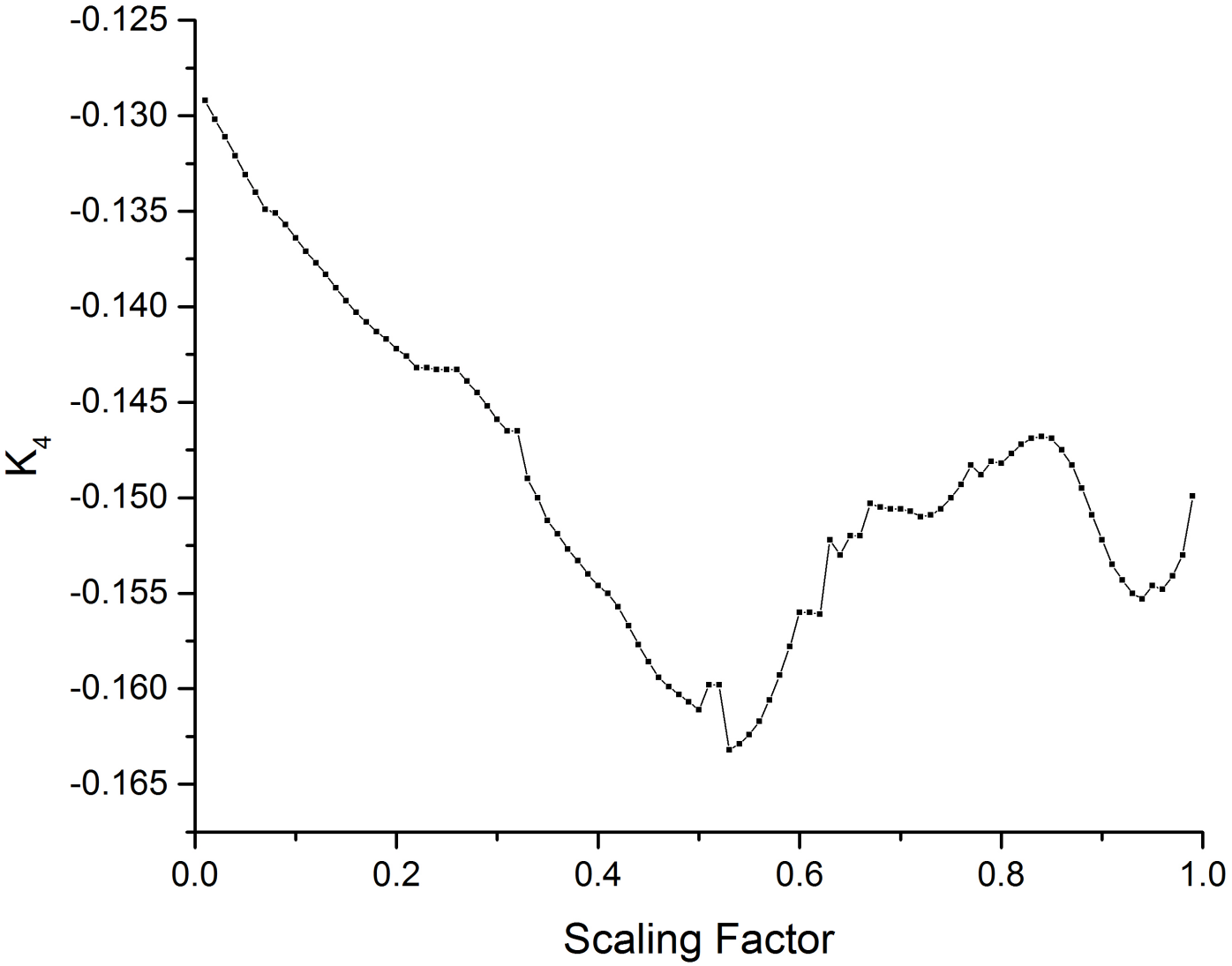

(g) NO_3 True Coupling fit values for K_4.

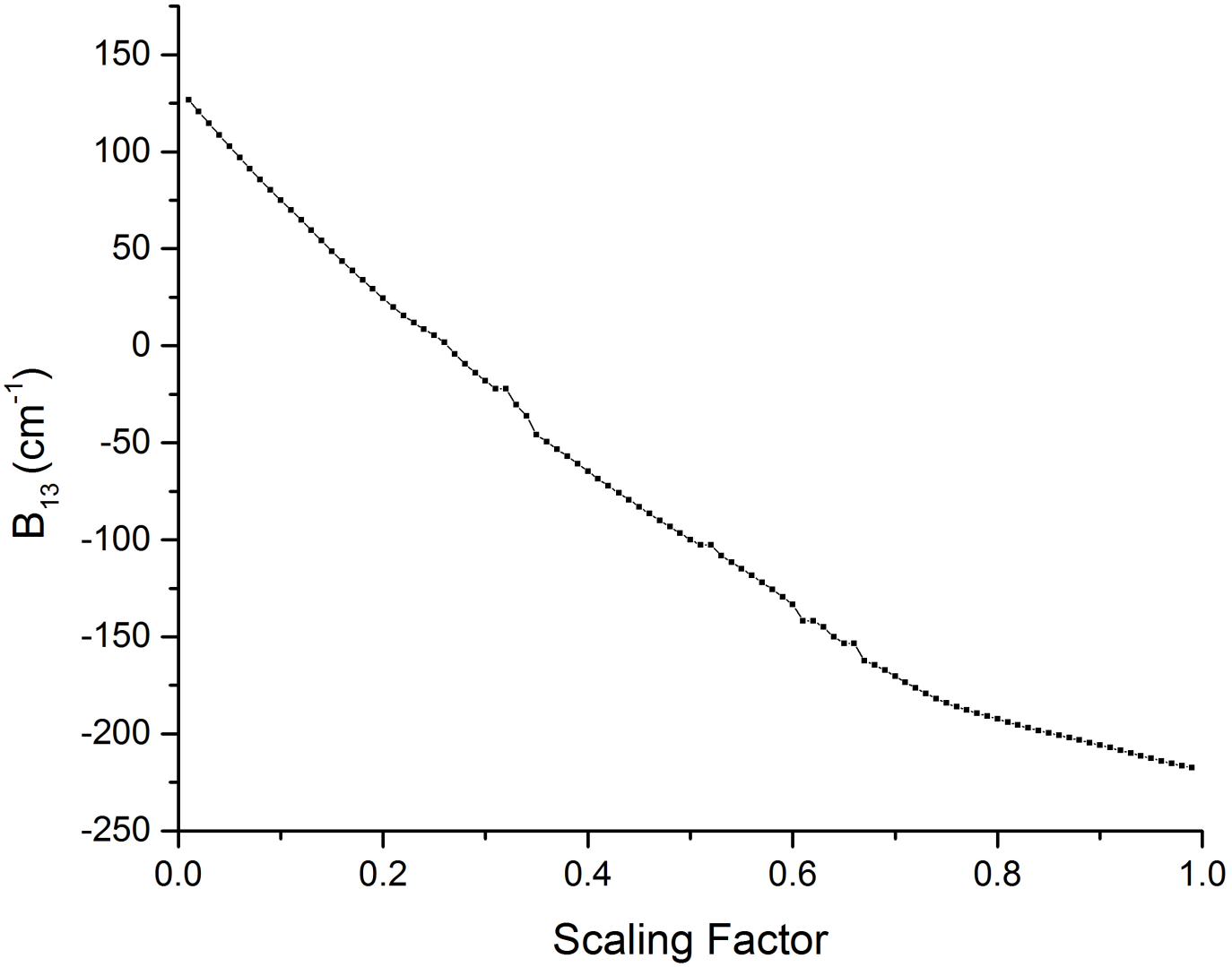

(h) NO_3 True Coupling fit values for B_{13}.

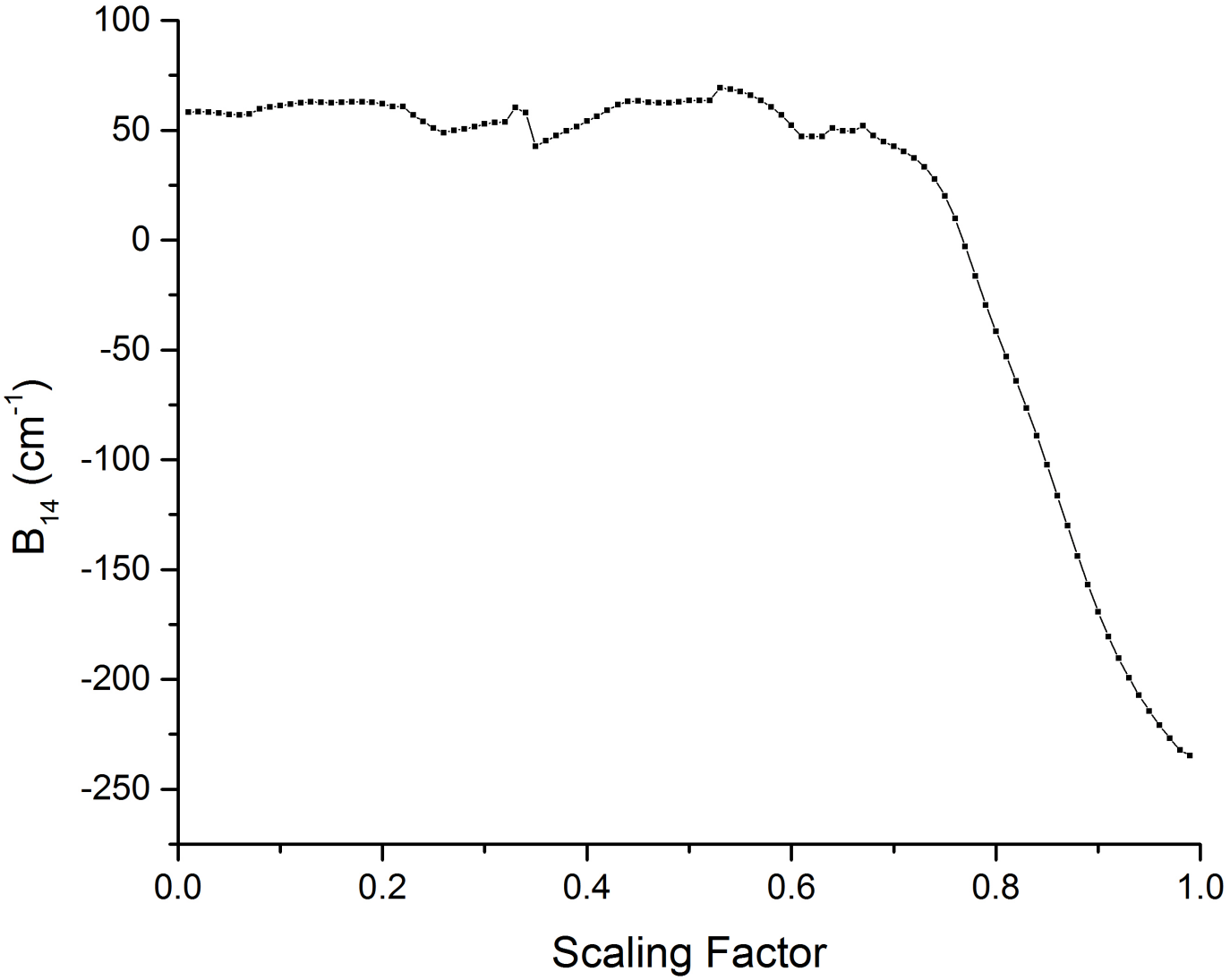

(i) NO_3 True Coupling fit values for B_{14}.

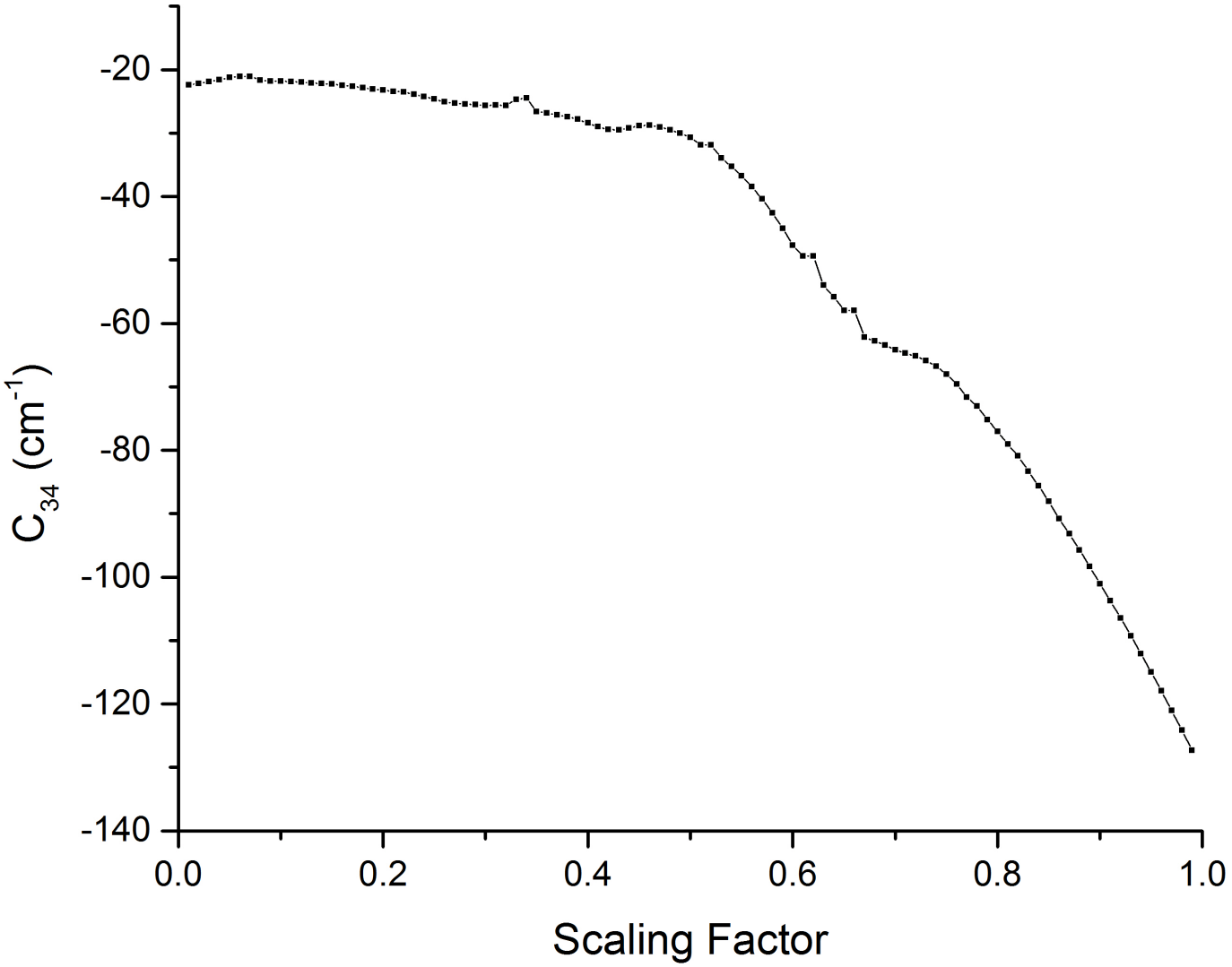

(j) NO_3 True Coupling fit values for C_{34}.

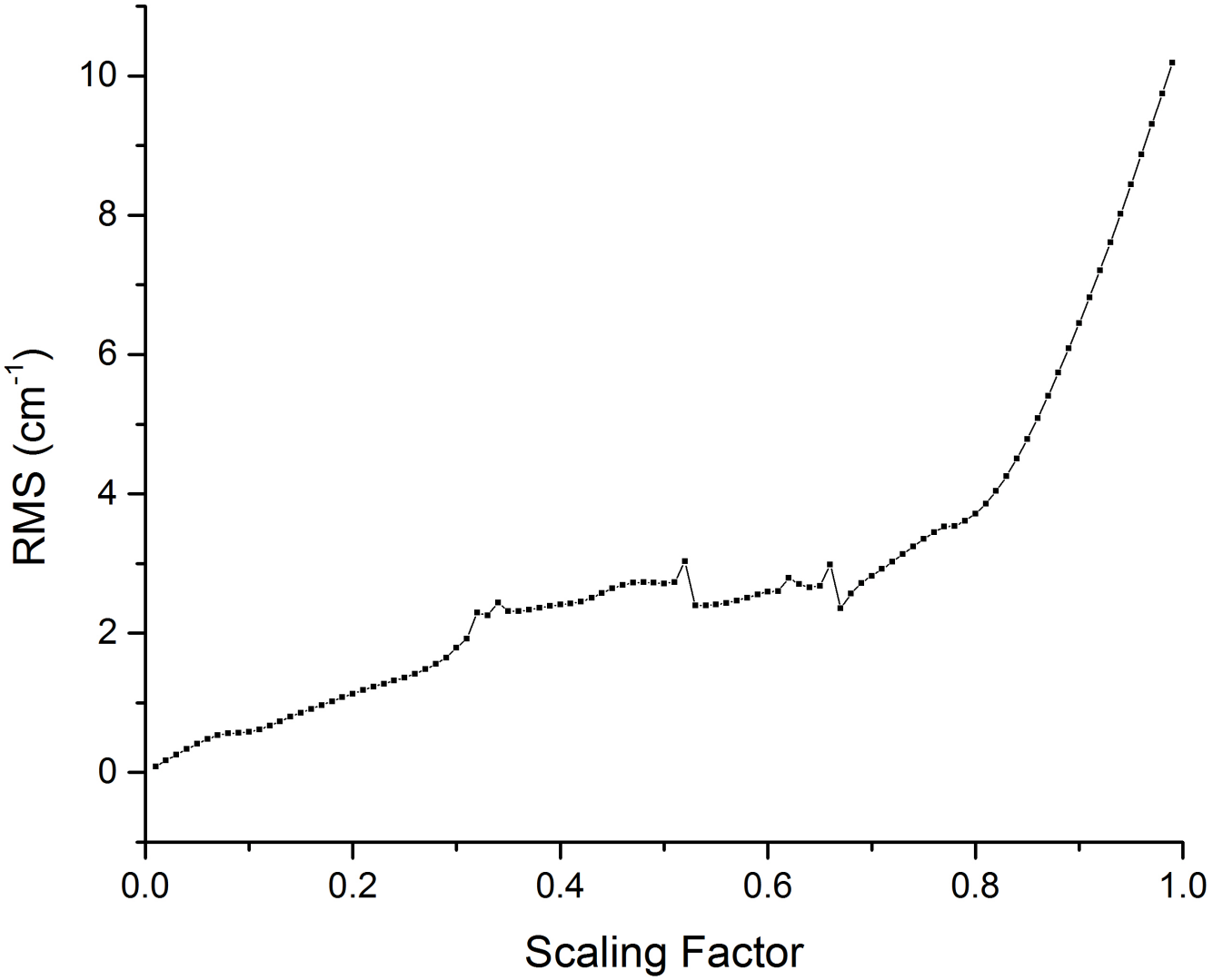

(k) NO_3 True Coupling fit values for RMS.

Table 6.3: Normal modes of Li_3.

Mode	Symmetry	Description
ν_1	a_1'	sym. bend
ν_2	e'	asym. stretch

minimum in parameter space. It is reasonable to expect that there are multiple minimum and different starting parameters will converge to different minimum. The purpose of the scanning fits is thus to trace out the same minimum. A potential candidate of the global minimum is traced out for values of scaling factors from 0.80 to 0.99 and the fit values for D_3 and D_4 and RMS for the original fit and the new fit starting from the set of parameters that gave the 5.683 cm^{-1} RMS are plotted together in Figure 6.3. It is seen that the parameters fit for this second "RMS surface" crosses discontinuously with the original "surface." Hence, there is reason to believe that although a lower RMS value exists, it exists on an RMS surface different than the original. This adds a dimension of complexity to these types of fits. A pictorial representation of this problem is shown in Figure 6.4. The message of this figure is that as scaling factor increases, the minimum RMS can change, and there may be multiple minimum based on different assignments for example. As scaling factor increases, the RMS of these minimum change. The blue shapes indicate starting parameters and the green shapes indicate where the fit converges. Depending on different starting points, the point that the fit converges to may be different, and even better than the original surface.

6.3 The Li_3 Potential

Li_3 is typically considered the canonical case of the Jahn-Teller effect, exhibiting a ground electronic state with E' symmetry and two vibrational modes of a_1' and e' symmetry (all in the D_{3h} representation). ν_2 is the Jahn-Teller active vibrational mode and can couple with ν_2. This is summarized in Table 6.3. Li_3 serves as an ideal model to analyze limitations of the quadratic Hamiltonian. Moreover, literature of Li_3 came to a halt in the 1990s, and hopefully this analysis will revive discussions.

We first present the previous experimental analysis by Wöste.[45] Because Li_3 only has

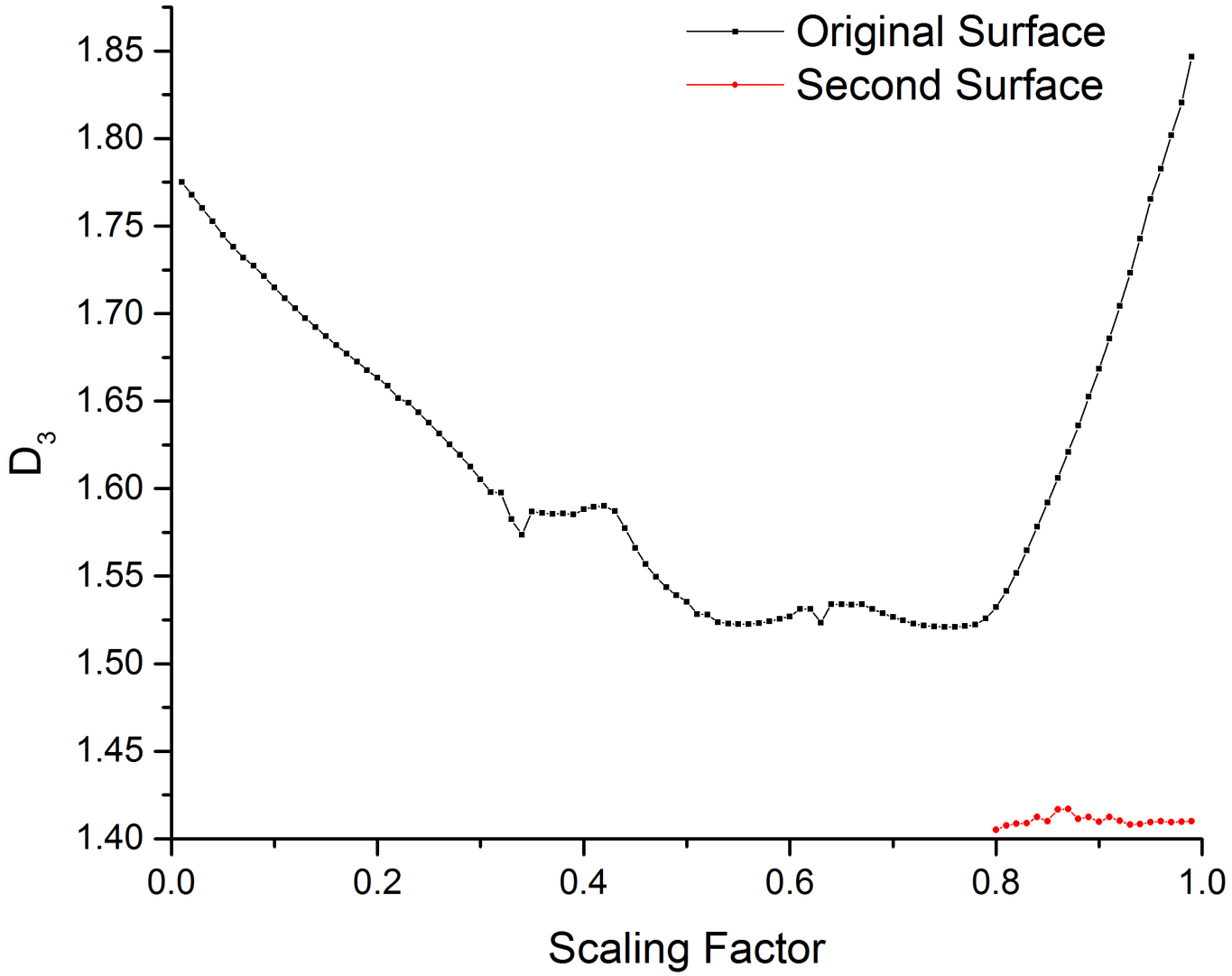

(a) Different converged parameter values for D_3 where the difference is in starting parameters.

Figure 6.3: Scans of different RMS minimums in the NO_3 True Coupling set.

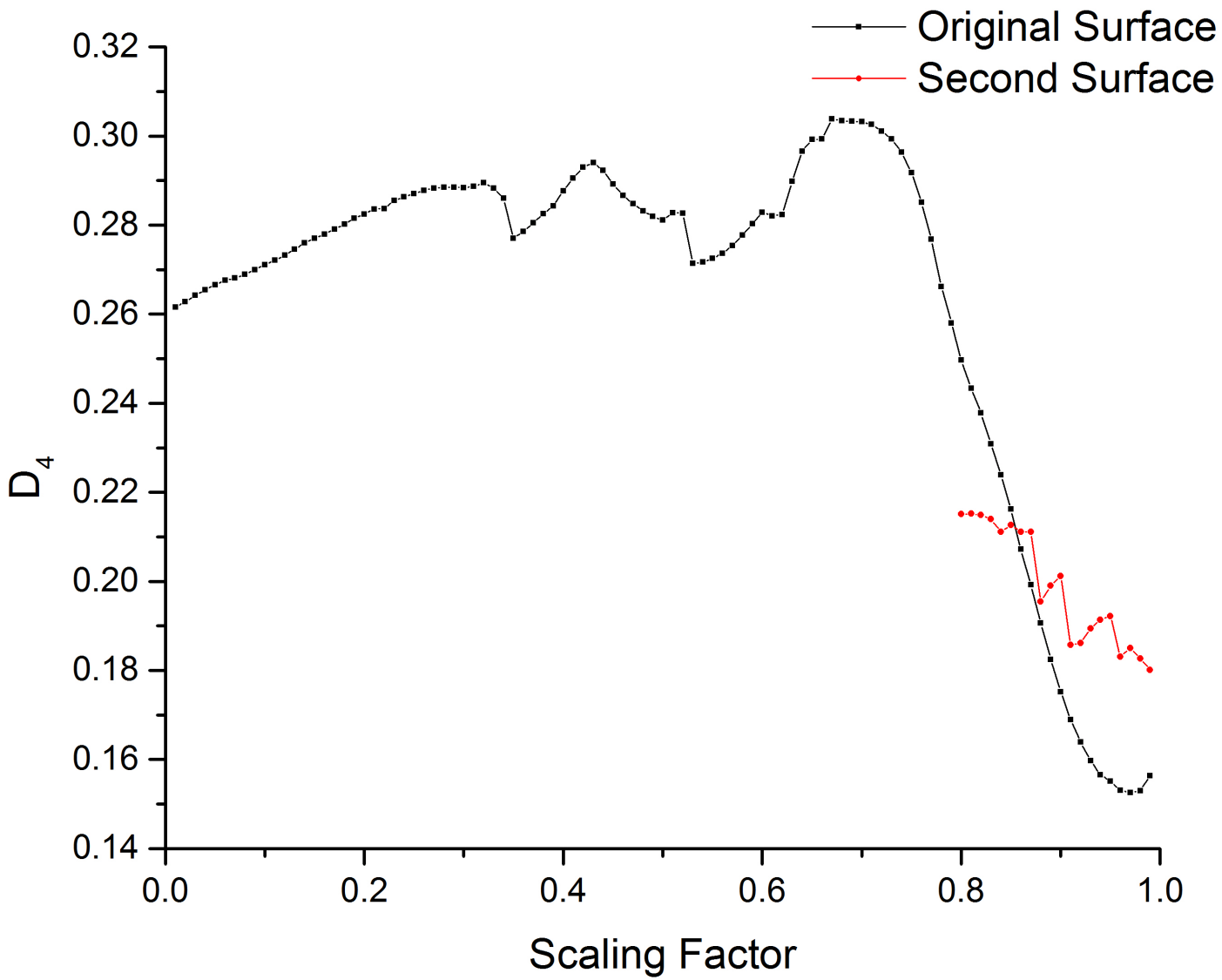

(b) Different converged parameter values for D_4 where the difference is in starting parameters.

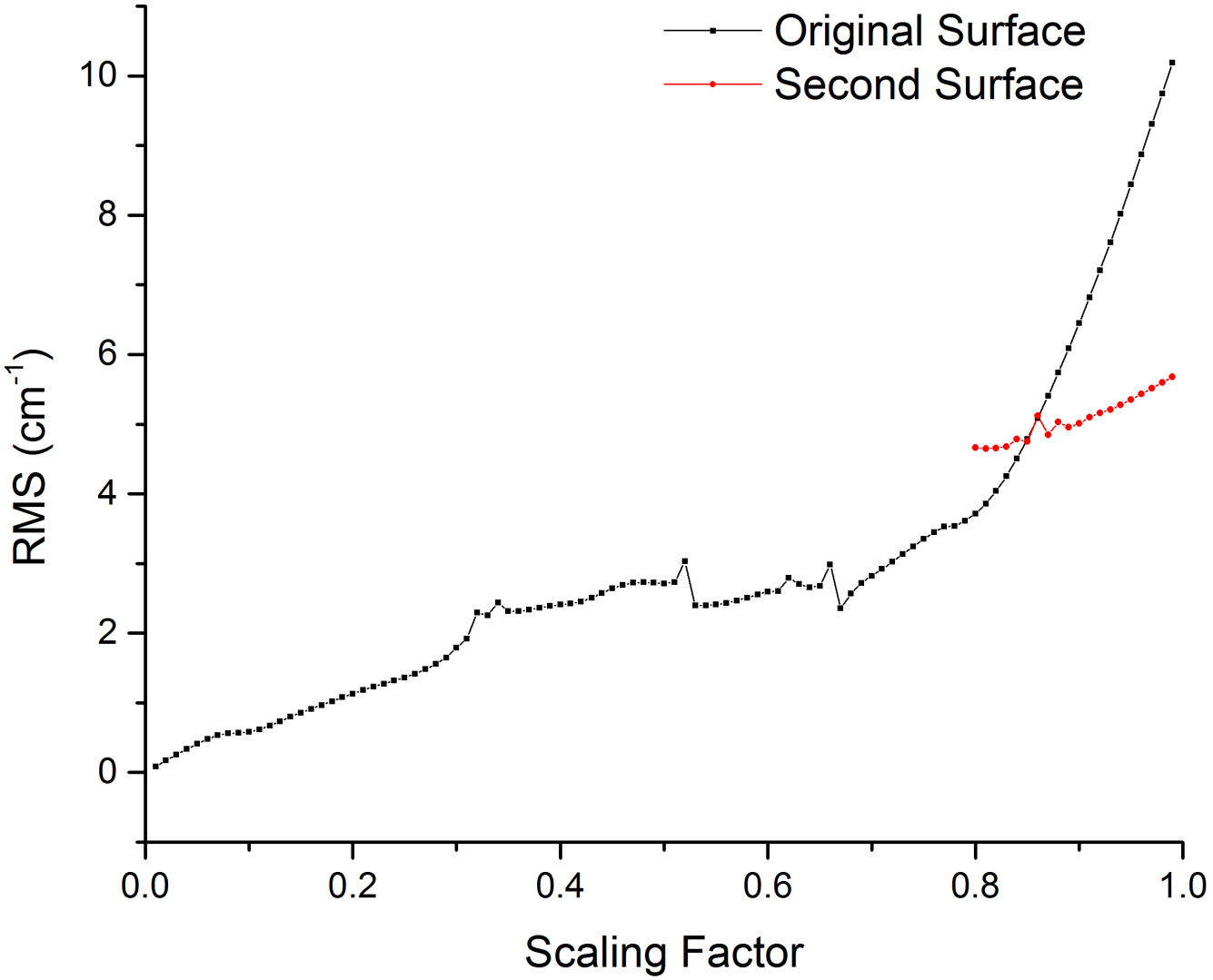

(c) Different RMS of fits where the difference is in starting parameters.

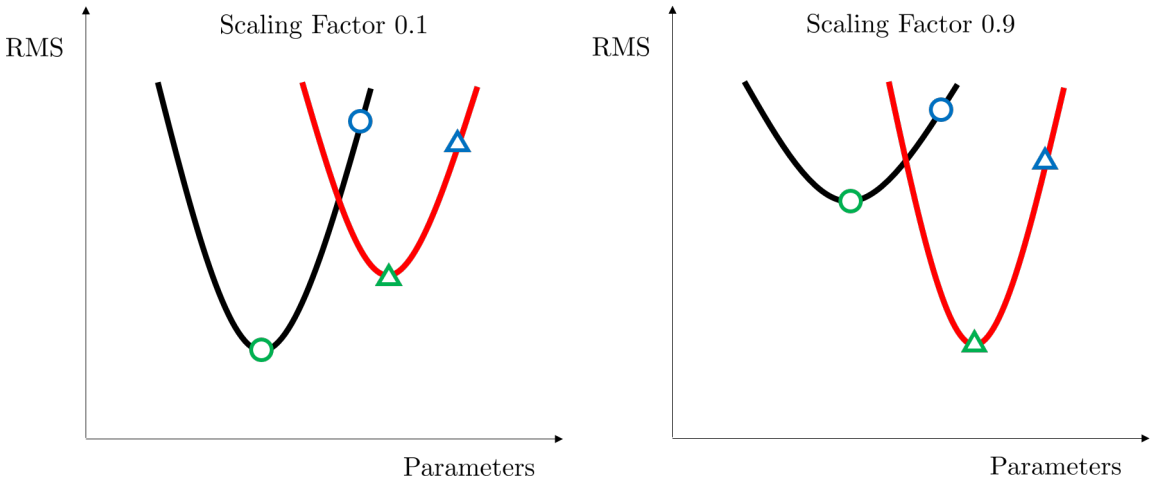

Figure 6.4: Pictorial representation of multiple RMS minimum. As scaling factor changes, the RMS of the fit changes and multiple potential minimum may be present for differences in assignments as an example. Blue shapes indicate starting parameters and green shapes represent converged parameters. Note that a different minimum, and in some cases a better minimum than the original RMS surface, can be obtained by different starting parameters.

two vibrational modes involved in Jahn-Teller coupling, as opposed to the three of NO_3, our calculations converge much faster and this allows use to experiment with the number of levels fit. We will first truncate the levels fit at different energies, changing the number of levels that are fit. One may initially expect that since the quadratic model is fundamentally correct, fitting more levels will unmask the insufficiency of the quadratic model. It will be shown that this is not the case.

In each of the following analyses, the potential is the same and the coupling is calculated using EOMIP with an ROOS/AN0-DZ basis. The coupling values are presented in Table 6.4.

6.3.1 Previous Analysis

The ground state of Li_3 has been analyzed using a quadratic Hamiltonian by Woerste. An *ab-initio* analysis was perfect on Li_3 using ROOS/AN0-DZ and the results are compared to the experimental fit.

The results of the experimental fit by Wöste is listed in Table 6.4.[45] The assignments

Table 6.4: Parameters for the $\tilde{X}$ state of Li_3 based on Wöste's analysis and *ab-initio* calculations.

Parameter	Wöste	*ab-initio*
ω_1 (cm^{-1})	301	314.575
ω_2 (cm^{-1})	150	244.437
D_2	1.782	1.8761
K_2	0.2794	0.04857

used in this analysis are also specified in Table 6.6. The results of the *ab-initio* analysis are listed alongside the experimental fit in the same table, with assignments specified. The quadratic parameters obtained from the fit and the *ab-initio* calculation are listed in Table 6.4. The complete set of *ab-initio* parameters are listed in Table 6.5.

Table 6.5: Parameters for the Li_3 potential. All units are cm^{-1}.

ω_1	314.5757
ω_2	244.4367
F_{2a}^{11}	-473.4924
F_{2b}^{12}	-473.4924
F_{2a}^{22}	473.4924
F_{12a}^{11}	-11.5894
F_{2a2a}^{11}	232.5129
F_{2b2b}^{11}	256.3604
F_{12b}^{12}	-11.5894
F_{2a2b}^{12}	11.9237
F_{12a}^{22}	11.5894
F_{2a2a}^{22}	256.3604
F_{2b3b}^{22}	232.5129
F_{111}^{11}	85.9739
F_{112a}^{11}	-0.8209

Continued

Table 6.5: Continued

F^{11}_{12a2a}	49.9472
F^{11}_{12b2b}	56.3025
F^{11}_{2a2a2a}	55.692
F^{11}_{2a2b2b}	-46.4393
F^{12}_{112b}	-0.8209
F^{12}_{12a2b}	3.1776
F^{12}_{2a2a2b}	2.3131
F^{12}_{2b2b2b}	6.9395
F^{22}_{111}	85.9739
F^{22}_{112a}	0.8209
F^{22}_{12a2a}	56.3025
F^{22}_{12b2b}	49.9472
F^{22}_{2a2a2a}	41.8129
F^{22}_{2a2b2b}	-51.0656
F^{11}_{1111}	19.4109
F^{11}_{1112a}	-0.089
F^{11}_{112a2a}	7.0757
F^{11}_{112b2b}	10.9193
$F^{11}_{12a2a2a}$	13.8875
$F^{11}_{12a2b2b}$	-12.2873
$F^{11}_{2a2a2a2a}$	6.0571
$F^{11}_{2a2a2b2b}$	2.019
$F^{11}_{2b2b2b2b}$	6.0571
F^{12}_{1112b}	-0.089
F^{12}_{112a2b}	1.9218
$F^{12}_{12a2a2b}$	0.4
$F^{12}_{12b2b2b}$	1.2001

Continued

Table 6.6: Experimental and *ab-initio* assignments of the Li_3 ground state vibrational levels.

Experimental (cm^{-1})	Wöste (cm^{-1})	Vibronic Symmetry	*ab-initio* (cm^{-1})	Vibronic Symmetry
37	38	a_2	35	a_2
66	60	a_1	—	—
115	117	e	114	a_1
164	164	e	155	e
205	201	e	—	—
227	220	a_2	225	e
245	246	a_1	247	a_2
290	287	a_2	300	e
303	—	—	345	a_1
313	310	e	355	e
339	344	e	356	a_2
372	381	e	370	e
410	408	e	—	—

Table 6.5: Continued

F^{22}_{1111}	19.4109
F^{22}_{1112a}	0.089
F^{22}_{112a2a}	10.9193
F^{22}_{112b2b}	7.0757
$F^{22}_{12a2a2a}$	11.4872
$F^{22}_{12a2b2b}$	-13.0874
$F^{22}_{2a2a2a2a}$	6.0571
$F^{22}_{2a2a2b2b}$	2.019
$F^{22}_{2b2b2b2b}$	6.0571

Of immediate interest and following the motivation for this analysis, we see that the quadratic Hamiltonian provides levels with an RMS of 4.0156 cm^{-1}. This is low and to many spectroscopists, would be considered characteristic of a good fit. However, the results clearly disagree quantitatively with the quartic analysis. This serves as another example where the quadratic Hamiltonian produces surprising reasonable levels that masks a large, fundamental limitation of the analysis.

6.3.2 Fit of the Li_3 Potential

The values of the cubic and quartic contributions in Table 6.4 were scaled from 0 to 1 in steps of 0.01. Only levels below 1200 cm^{-1} were included in the fit. Each step was fit using the quadratic Hamiltonian. The parameter results are collected and plotted with respect to scaling factor and the plots are pictured in 6.5.

One concern that arises from this analysis is the sign and magnitude of the K_2 term. In Figure 6.6, the a_1'' and a_2'' levels are plotted with respect to scaling factor. We see that the a_1'' and a_2'' levels switch in these graphs at a scaling factor of about 0.3. We emphasize that this effect is due to the inclusion of cubic and quartic terms. In Figure 6.7, the a_1'' and a_2'' levels are plotted against K_2 in the quadratic Hamiltonian. We see that the a_1'' and a_2'' levels are symmetric about a change in sign in K_2. A different sign of K_2 effectively switches the identity of a_1'' and a_2''. This has led to the peculiar effect seen in graph of K_2 in Figure 6.5d. The a_1'' and a_2'' levels switch as a result of the cubic and quartic contributions. However, since the quadratic model cannot capture this effect, the model instead manifests this change as the result of the quadratic K_2 parameter. In reality, K_2 should not change, but it changes both sign and magnitude throughout the scaling. The final value of K_2 has a greater magnitude and different sign than the true value. This leads to a difference in calculated Jahn-Teller stabilization energy.

This is a pattern that was also seen in the NO_3 vibronic analysis, and is one case where we should expect an overestimation of the Jahn-Teller effect in the experimental fit. The issue brought to light by this analysis is not only that the quadratic Hamiltonian is incorrect, but that the RMS of the fit remains excellent. The RMS of the fit at a scaling factor of 0.99 is pictured in the RMS plot for Figure 6.5f and was determined to be 5.629 cm^{-1}. This is similar to the RMS of the fit obtained in the latest NO_3 vibronic analysis[1] of 5.52 cm^{-1}. While it is concerning that radically different results are obtained from the quadratic Hamiltonian and the quartic Hamiltonian, the issue is magnified by the fact that even when this large of an error is present, the RMS of the fit masks the numerical inaccuracy of the fit. In fitting spectra using a quadratic model, even if significant contributions from cubic

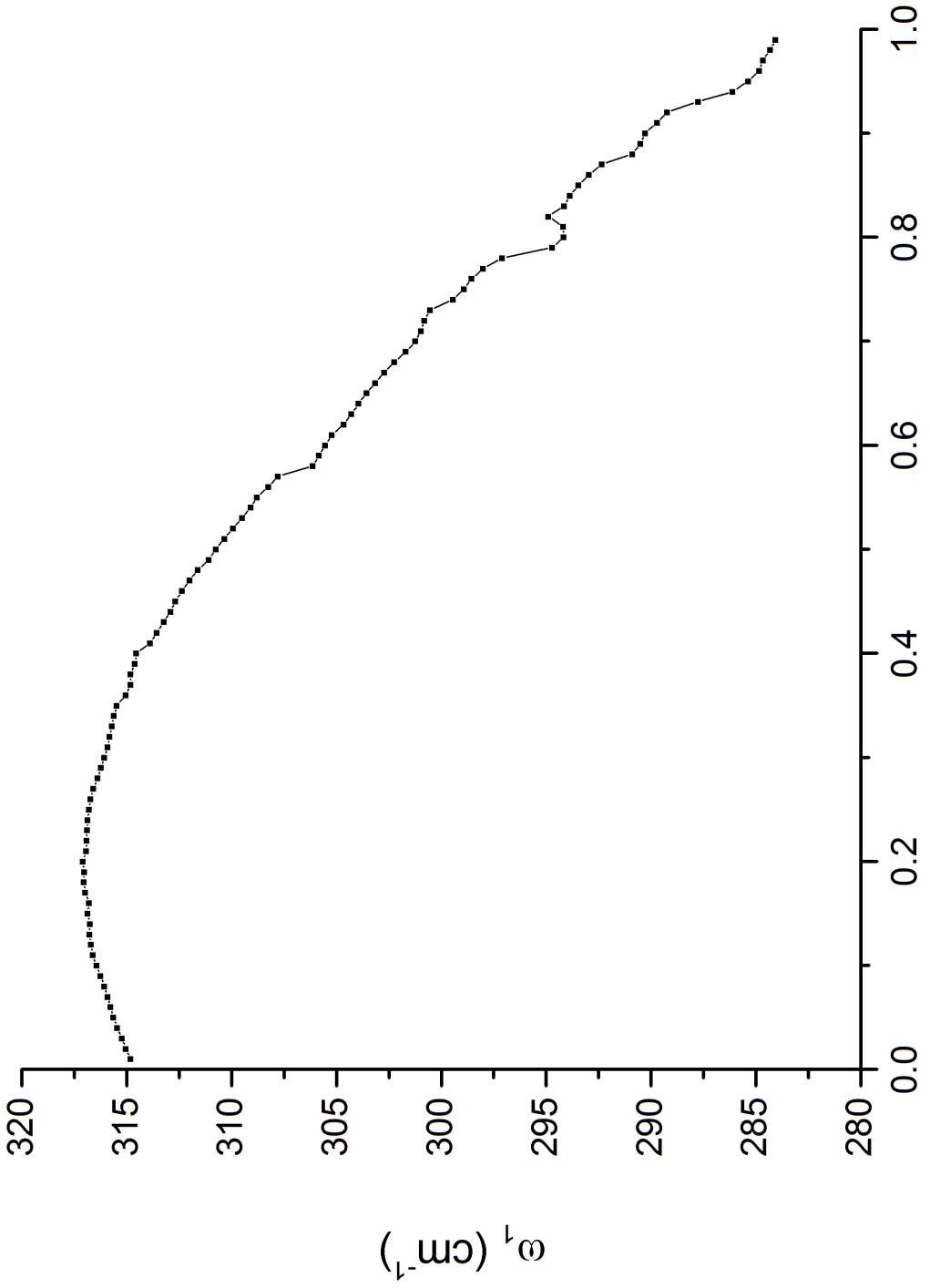

(a) Li_3 fit values for ω_1.

Figure 6.5: Scaling fits for the Li_3 potential.

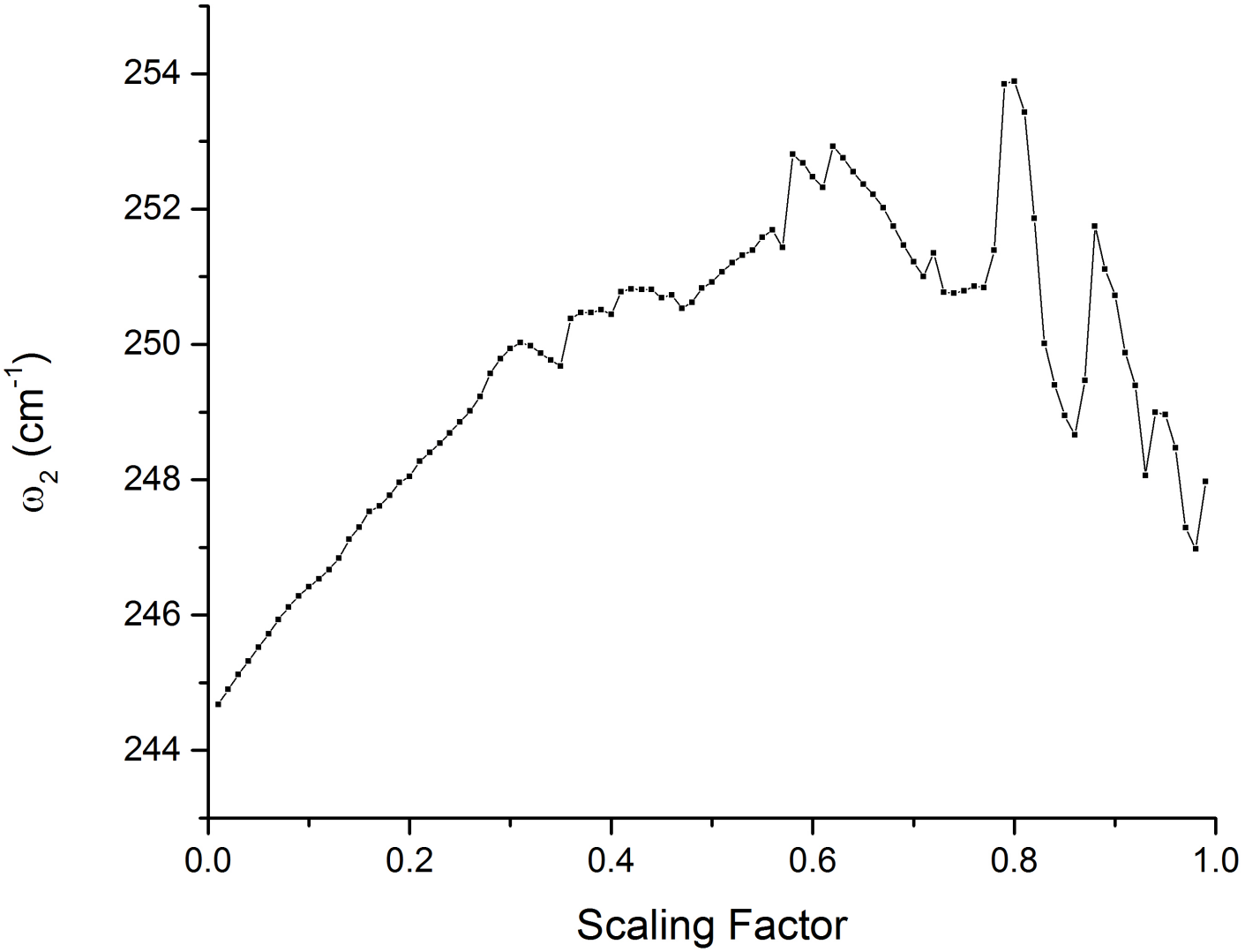

(b) Li_3 fit values for ω_2.

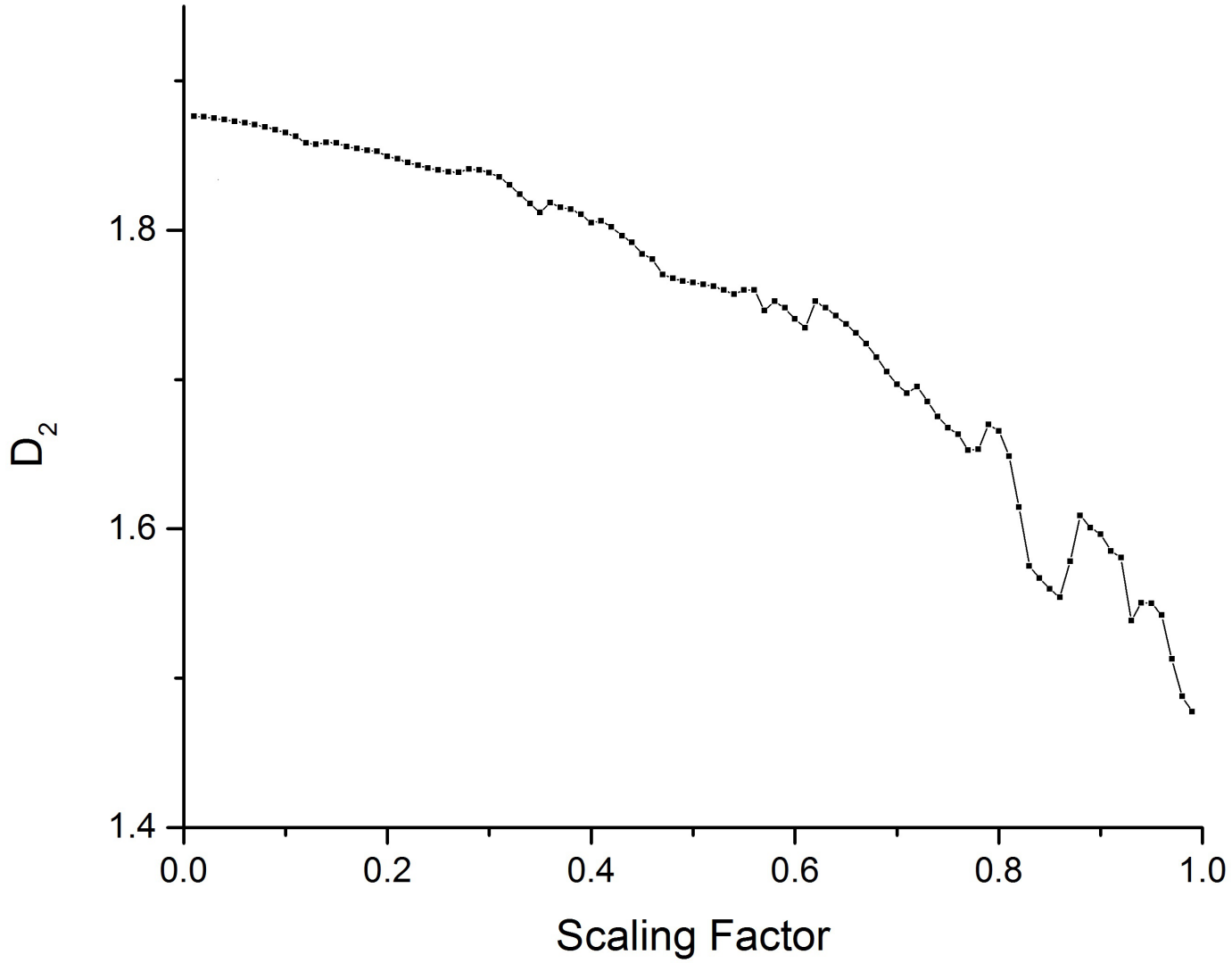

(c) Li_3 fit values for D_2.

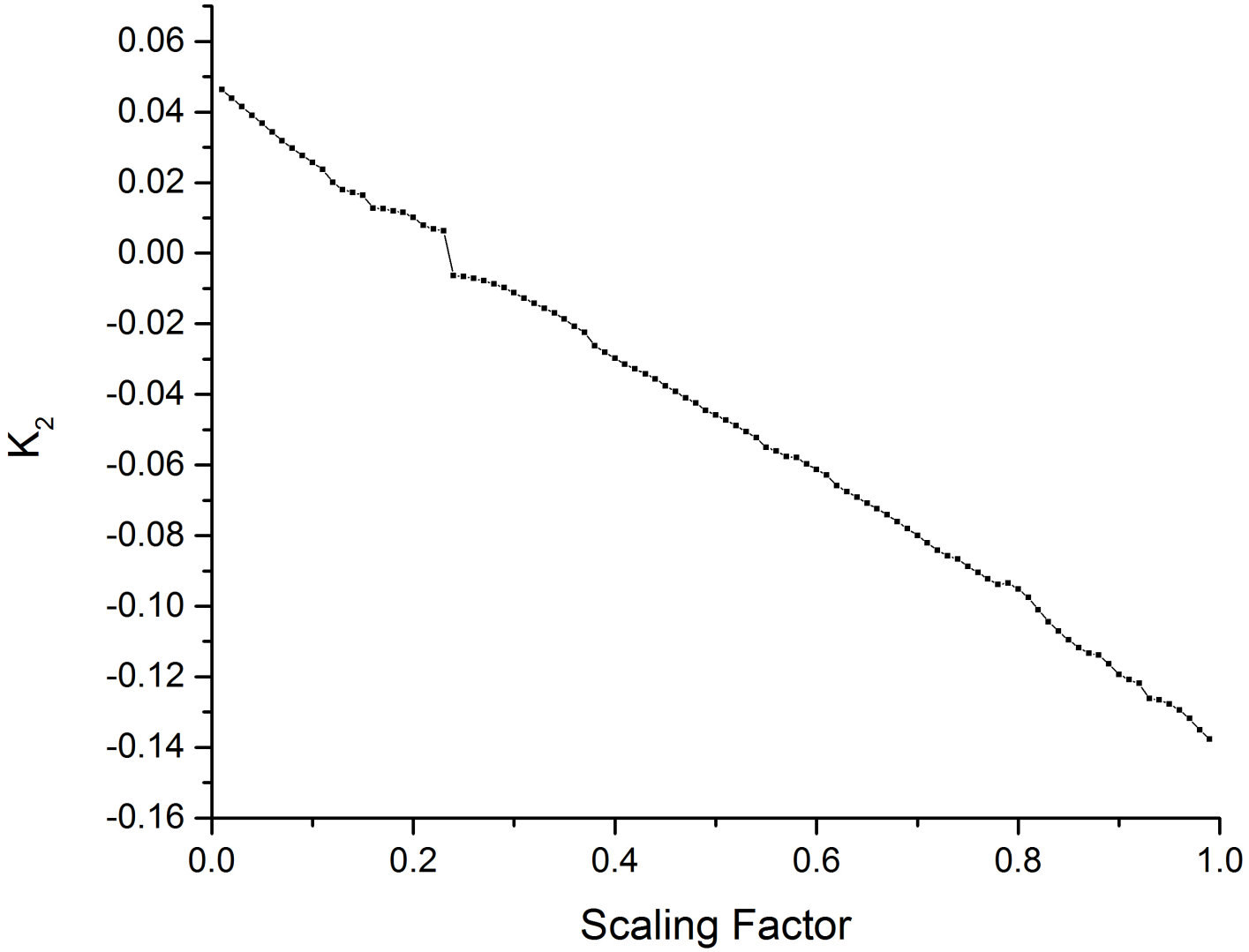

(d) Li_3 fit values for K_2.

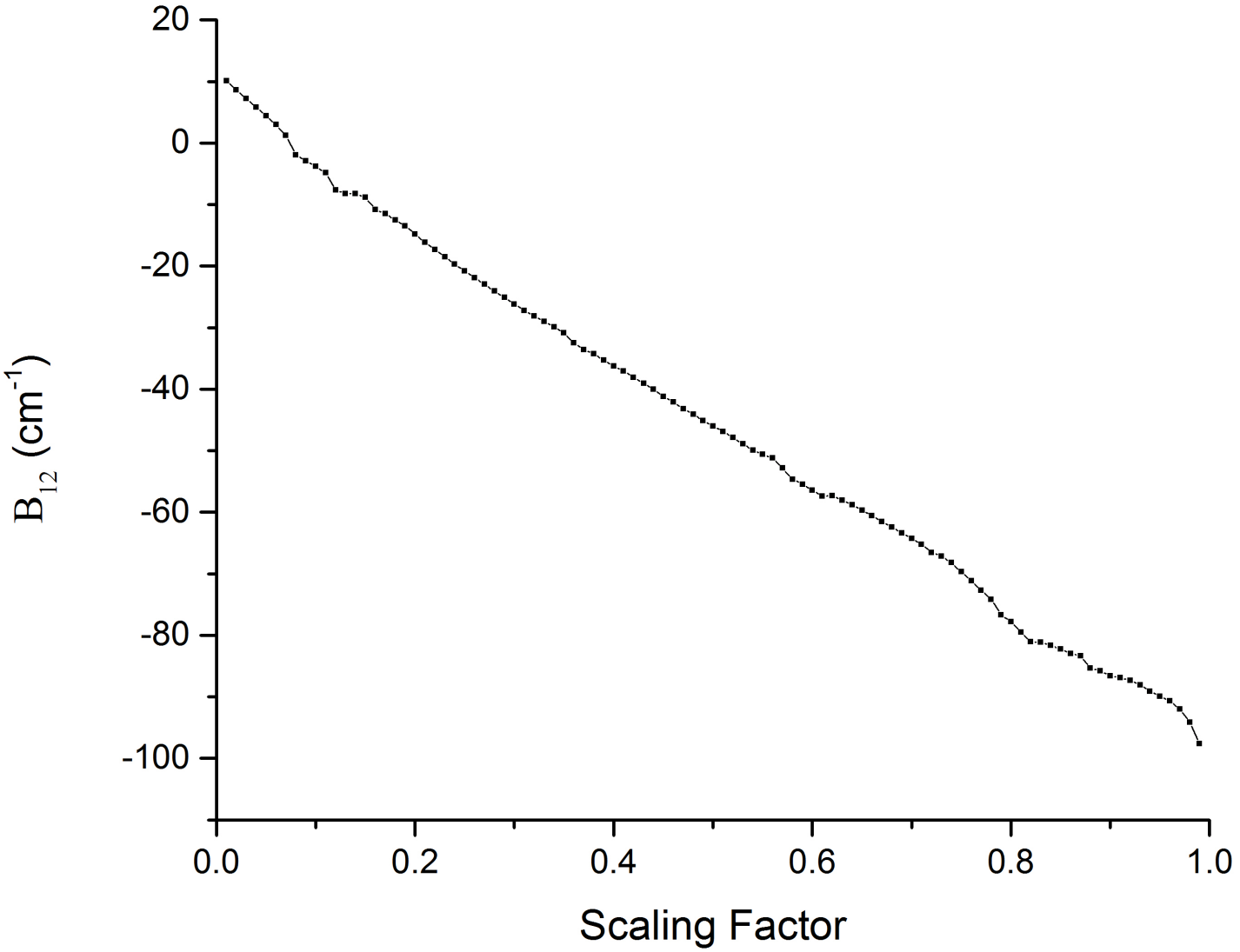

(e) Li_3 fit values for B_{12}.

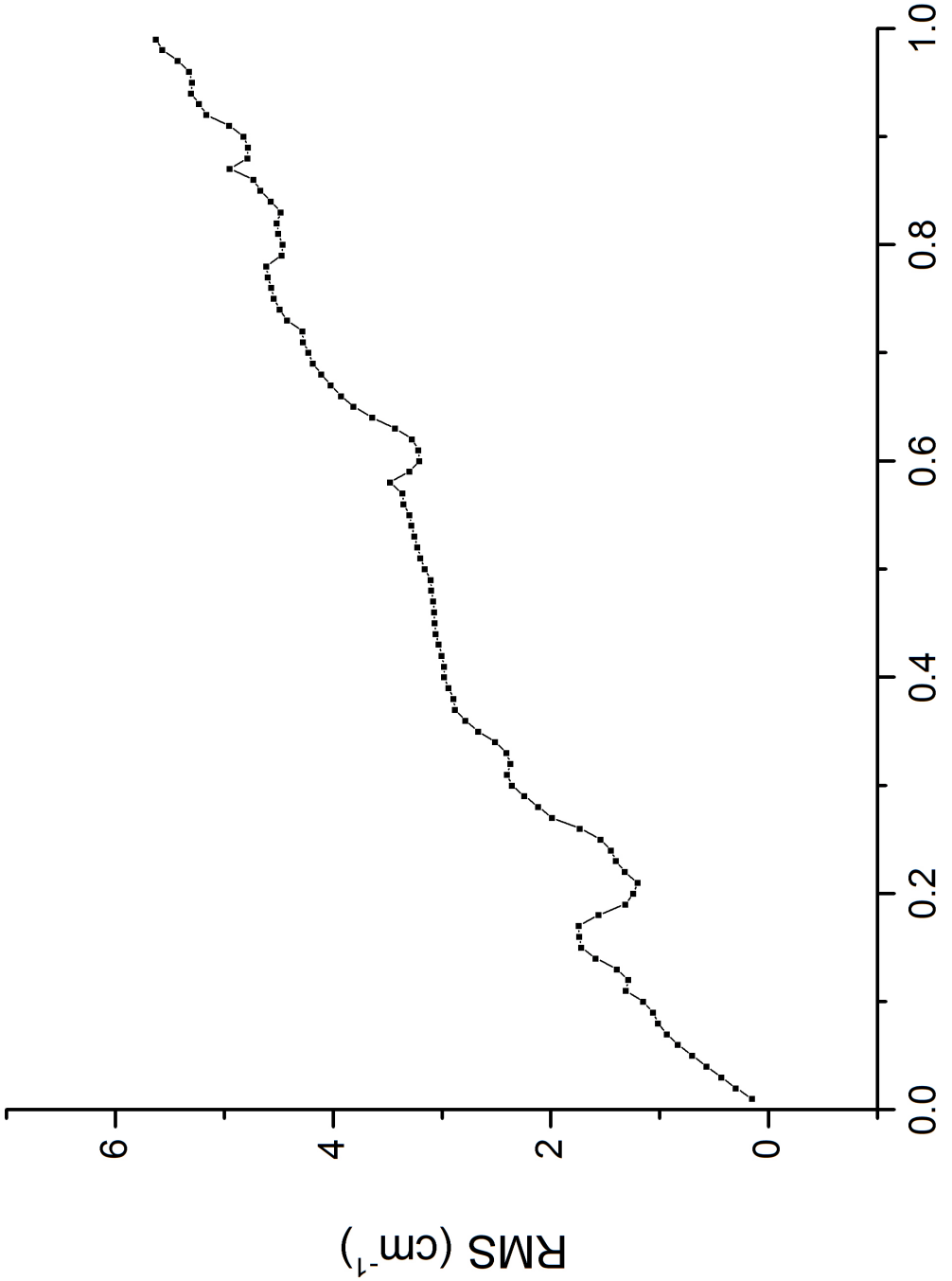

(f) Li_3 RMS values of fits.

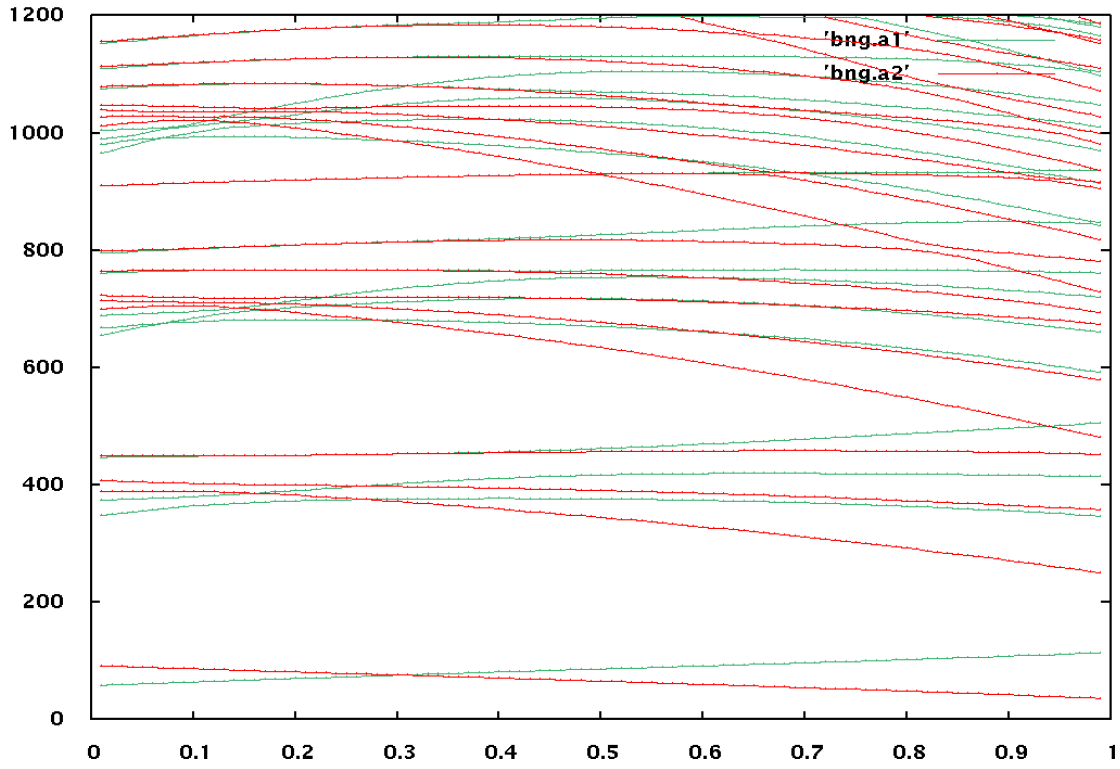

Figure 6.6: a_1'' levels in red are plotted with a_2'' levels in green with respect to scaling factor calculated from quartic Hamiltonian. Notice the crossing of these two types of levels.

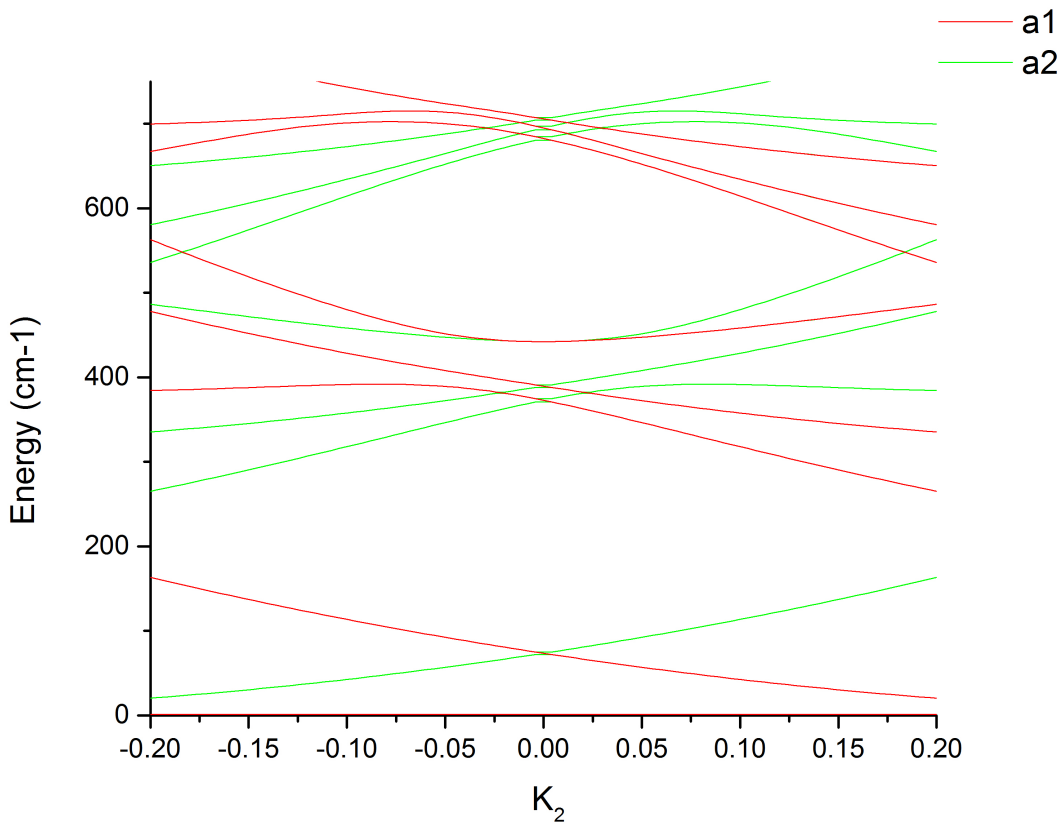

Figure 6.7: a_1'' levels in red are plotted with a_2'' levels in green calculated with respect to K_2 from quadratic Hamiltonian. Notice the symmetry about $K_2 = 0$

and quartic terms exist, a radical change in the quadratic parameters can still produce relatively good fits with poor numerical results as was the case here. Good fits are more deceptive than one might expect.

6.3.3 Increasing Levels used in the Fit

One of the mentioned flaws in the experimental analysis is the inability to fit higher order terms because of lack of experimental levels to fit. By fitting fewer levels, one may also expect to obtain reasonable parameters using a fundamentally flawed model, simply because there are not enough levels exhibiting up to fourth order coupling and the fundamental deficiency in fitting the first few levels can be masked by radical changes in the fit parameters.

To investigate this possibility, three different sets of scaled artificial spectra are produced. The first truncates at 400 cm^{-1}, the second at 800 cm^{-1}, and the third at 1200 cm^{-1}. These levels are fit and the parameters and RMS are plotted against the scaling factor. We are interested in how parameters respond to a higher number of levels, which are again fundamentally unreproducible by the quadratic Hamiltonian, and also in how the RMS changes between the two sets. The plots of these parameters and RMS versus scaling factor are presented in Figure 6.8.

A surprising conclusion from this fit is that fitting more levels does not significantly affect the RMS of the fit. Particularly, between the 400 cm^{-1} and 800 cm^{-1} sets, the RMS remain relatively close, and in some cases, the 800 cm^{-1} set even produces a better RMS. Moving to the 1200 cm^{-1} set, we see that the RMS increases, but not substantially. The last point on the RMS plot for the 400 cm^{-1} set is 5.444 cm^{-1} whereas the 1200 cm^{-1} set is only 5.629 cm^{-1}, not much higher. This illuminates another dimension to the deceptiveness of the quadratic Hamiltonian. We determined that the quadratic Hamiltonian can obtain good fits even potentials with significant contributions from up to fourth order coupling terms in Section 6.2. Even with increasing levels that are fundamentally inaccurate in terms of a quadratic model, the spectrum can be fit well even with a number of levels unreasonable for experimental observation. It seems that increasing the range of experimental observation

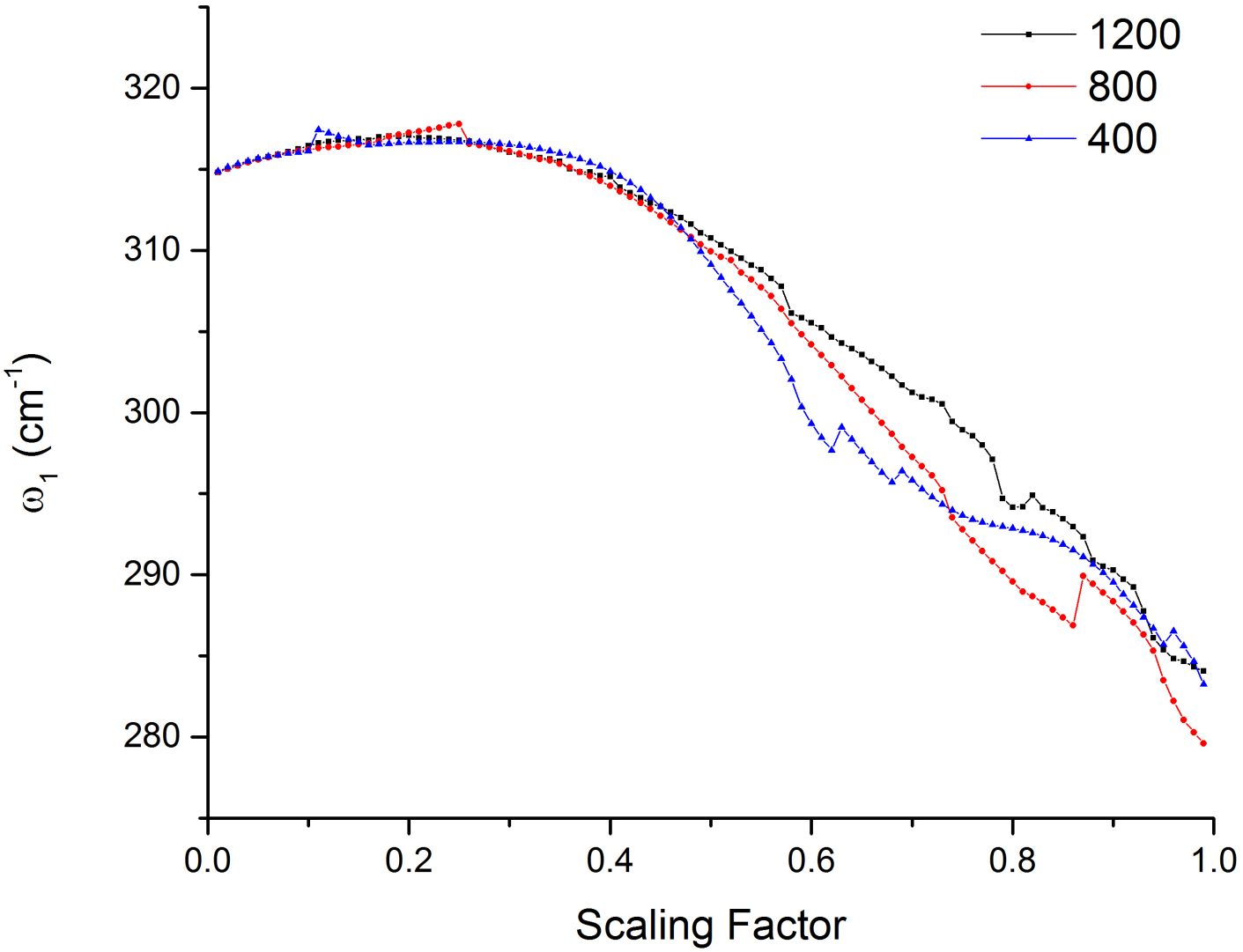

(a) Li_3 fit values for ω_1.

Figure 6.8: Scaling fits for the Li_3 potential. Levels used in the fit are truncated at 400, 800, and 1200 cm^{-1}.

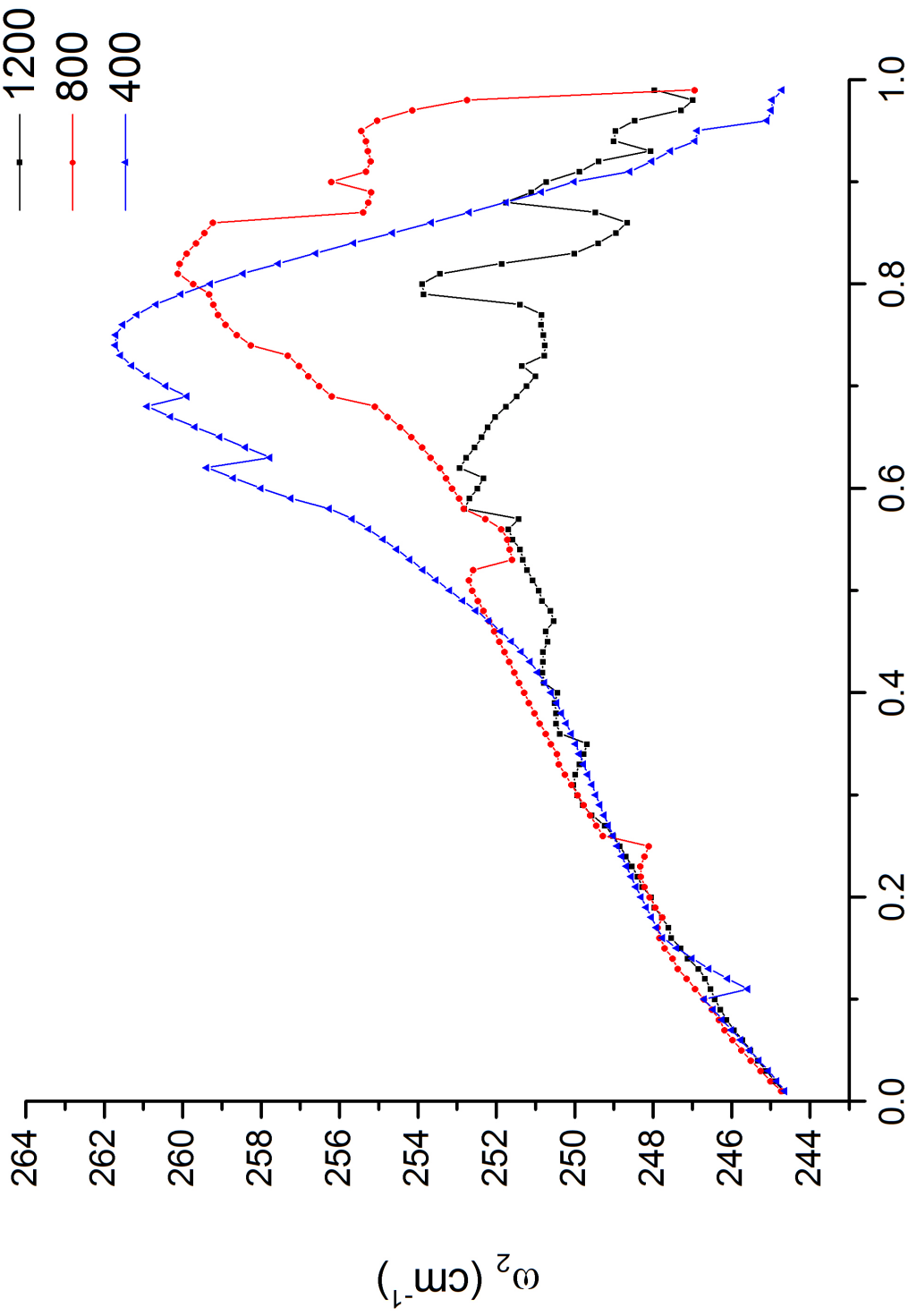

(b) Li_3 fit values for ω_2.

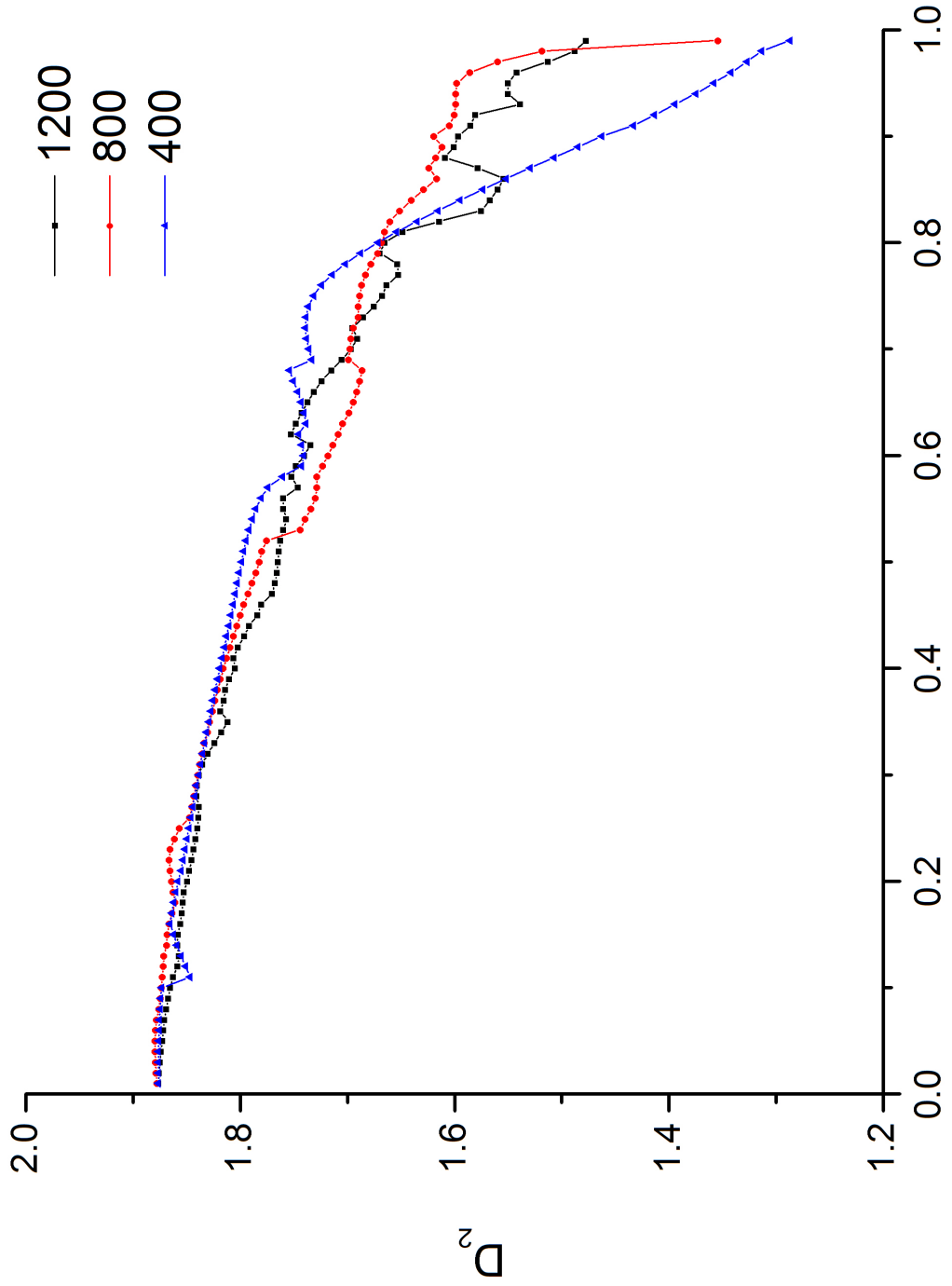

(c) Li_3 fit values for D_2.

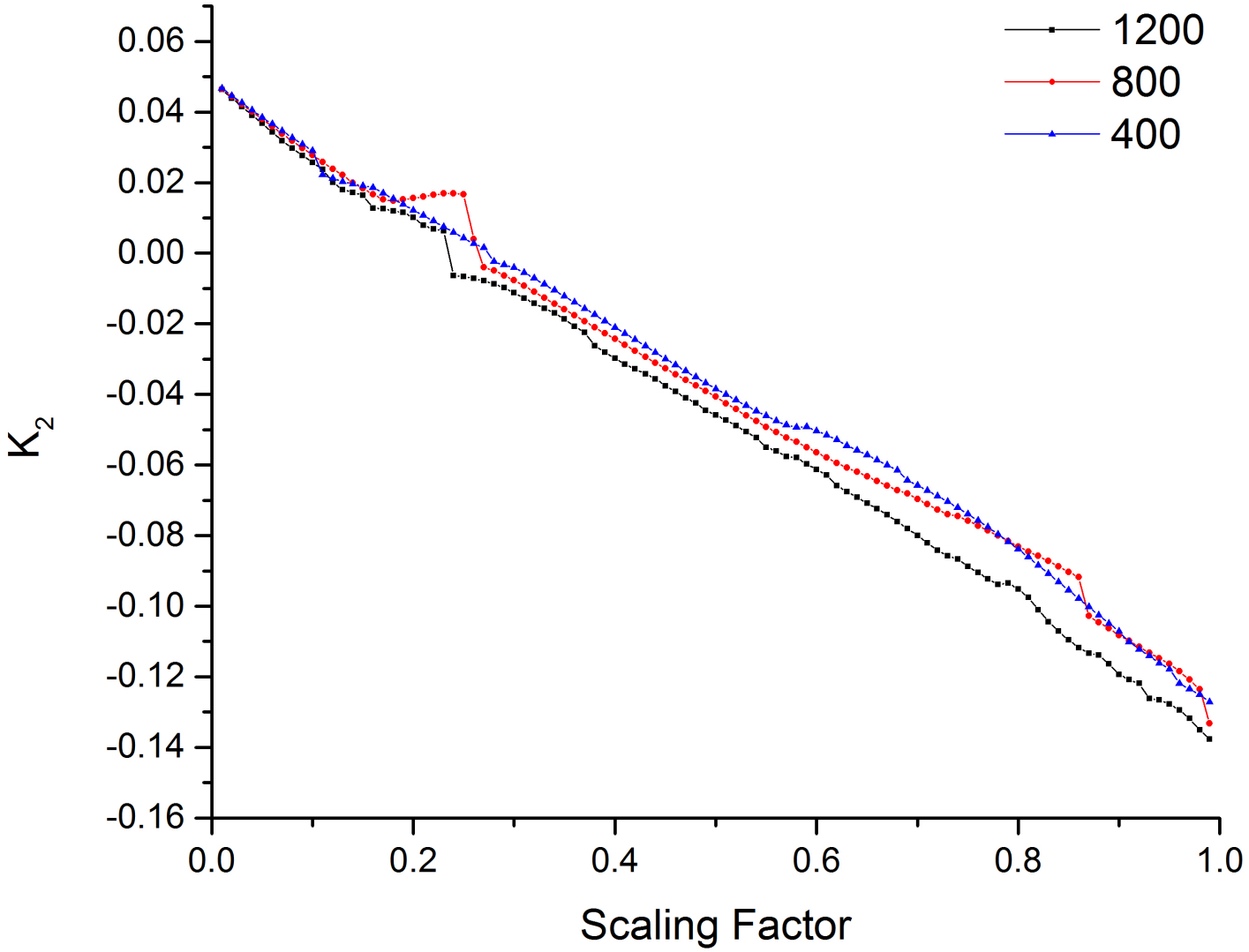

(d) Li_3 fit values for K_2.

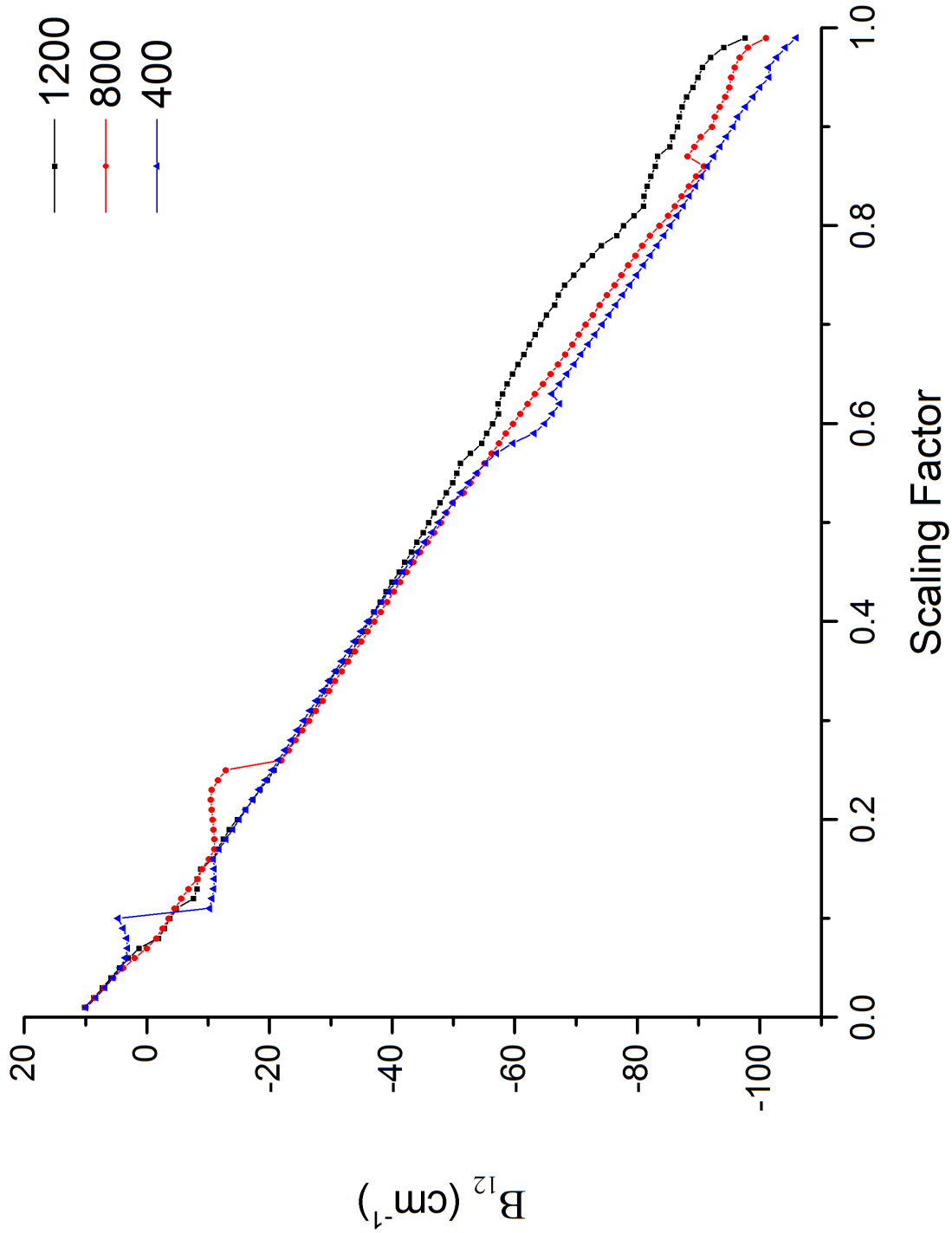

(e) Li_3 fit values for B_{12}.

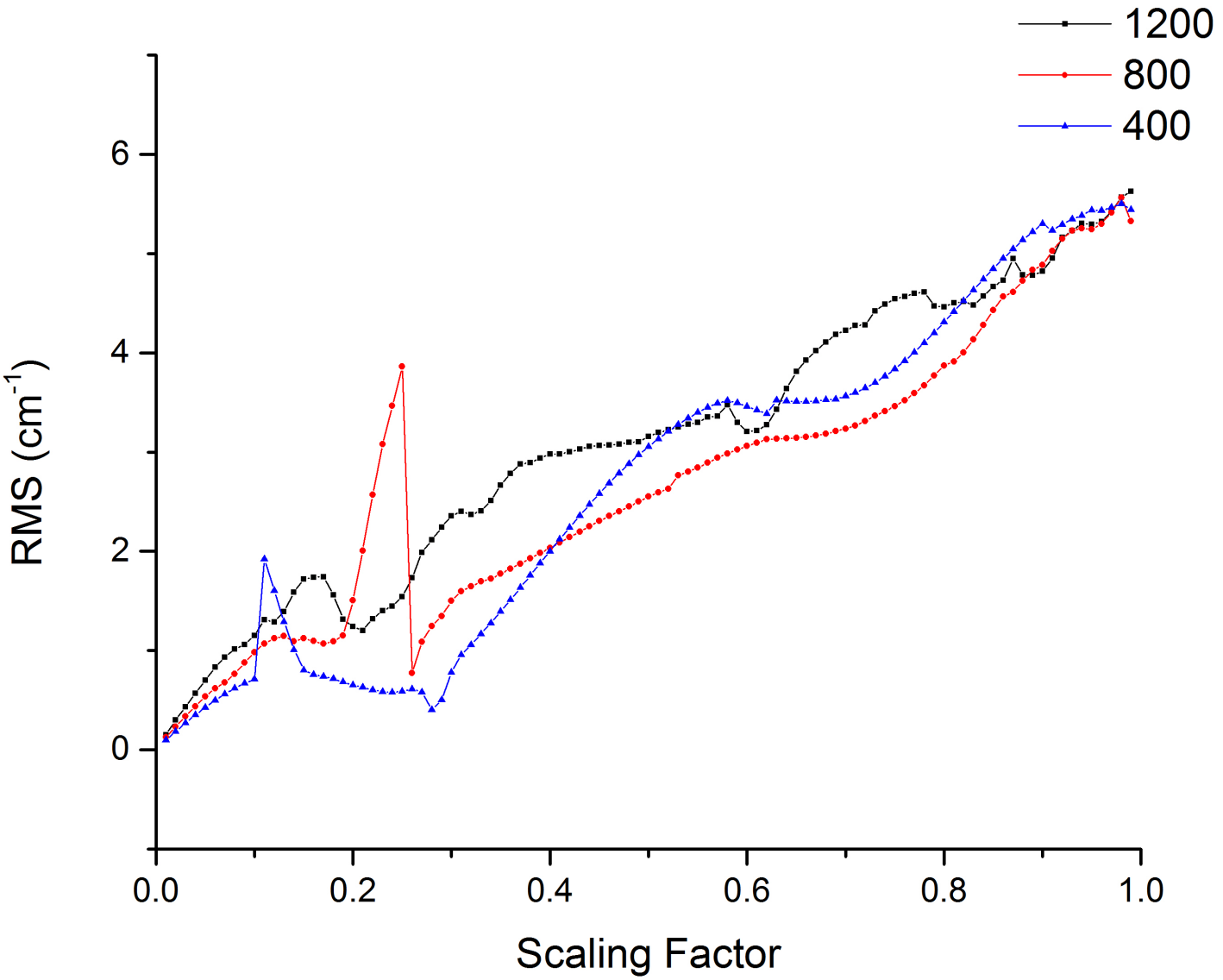

(f) Li_3 RMS values of fits.

would do little in identifying the inability of the quadratic Hamiltonian to describe the data. Instead, fits that would be deemed good would be obtained and wrong parameters would be reported without notice.

A closer look at the parameters demonstrates that although there is some difference in the fit parameters, noticeably in ω_2, the parameters are still very similar across all three cases. If a fit of the 400 cm^{-1} case and the 1200 cm^{-1} case yielded different parameters, then the quality of the model would be suspect. However, the parameters are so similar that one would believe that the 1200 cm^{-1} set has converged a bit better to the true values. Hence, it is very easy to believe that an insufficient model is accurate even looking outside the RMS of the fit. In summary, the fit parameters of the quadratic Hamiltonian are surprisingly stable with respect to the number of levels used in the fit.

6.4 Simulating Experimental Error

A complementary issue regarding experimental fit lies in the inherent experimental error in the data. For instance, we can imagine that even if the true vibronic structure of a molecule is quadratic and should be fit perfectly using a quadratic model, experimental error would prevent a perfect match. In order to understand the accuracy of experimental fits, we must investigate magnitude of error introduced by experimental error in the spectrum. It is important to understand qualitatively the resolution that gives reasonable well-determined parameters by least-squares fitting, and quantitatively how much variance one should expect in parameter values as experimental error changes. Such an understanding will allow us to understand how much error we can attribute to experimental error, rather than an incorrect model.

In order to investigate this possibility, we start with a spectrum using only terms up to second order in the potential. The value of these parameters are listed in Table 6.7. For each level μ_i in the spectrum, independent random variables X_i were generated distributed as a normal random variable with mean μ_i and variance σ^2. A new level is produced from

Table 6.7: Simulating experimental error with a standard deviation of 2 cm^{-1} and fitting only a_1'' levels. True values from which the error is based are also listed.

	True Value	Mean	Standard Deviation
ω_1 (cm^{-1})	750	752.00334	18.29143
ω_3 (cm^{-1})	1417.695	1417.46277	15.65713
D_3	2.2673	2.25971	0.20907
K_3	0.2143	0.21433	0.00677
ω_4 (cm^{-1})	514.907	514.64907	5.59629
D_4	0.0195	0.0273	0.02818
K_4	0.2	0.19739	0.02238
B_{13} (cm^{-1})	-300	-303.00645	31.47329
B_{14} (cm^{-1})	187.8	189.52567	22.94265
C_{34} (cm^{-1})	100	99.84854	8.67084
RMS (cm^{-1})	–	1.02556	1.23561

this random variable, x_i and the set of x_i are fit instead.

$$\begin{aligned} \mu_1 \rightarrow X_1 \sim N(\mu_1, \sigma^2) \rightarrow x_1 \\ \vdots \\ \mu_n \rightarrow X_n \sim N(\mu_n, \sigma^2) \rightarrow x_n \end{aligned} \tag{6.1}$$

This is done 1000 times for each case studied.

6.4.1 Inclusion of e'' Vibronic Levels in the Fit

The first effect studied is the improvement in the fit gained by fitting e'' levels. In the vibronic analysis, e levels were inferred from combination differences and fit as well. To systematically study the effect of fitting e'' levels, two cases were conducted using the above procedure. In all of these cases, the standard deviation used to randomize each level was set to 2 cm^{-1}. In the first case, only a_1'' levels were randomized and fit. In the second case, both a_1'' and e'' levels were randomized and fit. The distribution of the fit parameters and the RMS for both cases are graphically compared in Figure 6.9. The statistical results of all the fits are summarized in Table 6.7 and 6.8.

The mean values obtained from the fit matches well with the true values. Of interest is that the variance distribution of the parameters improves by a factor of about four. However,

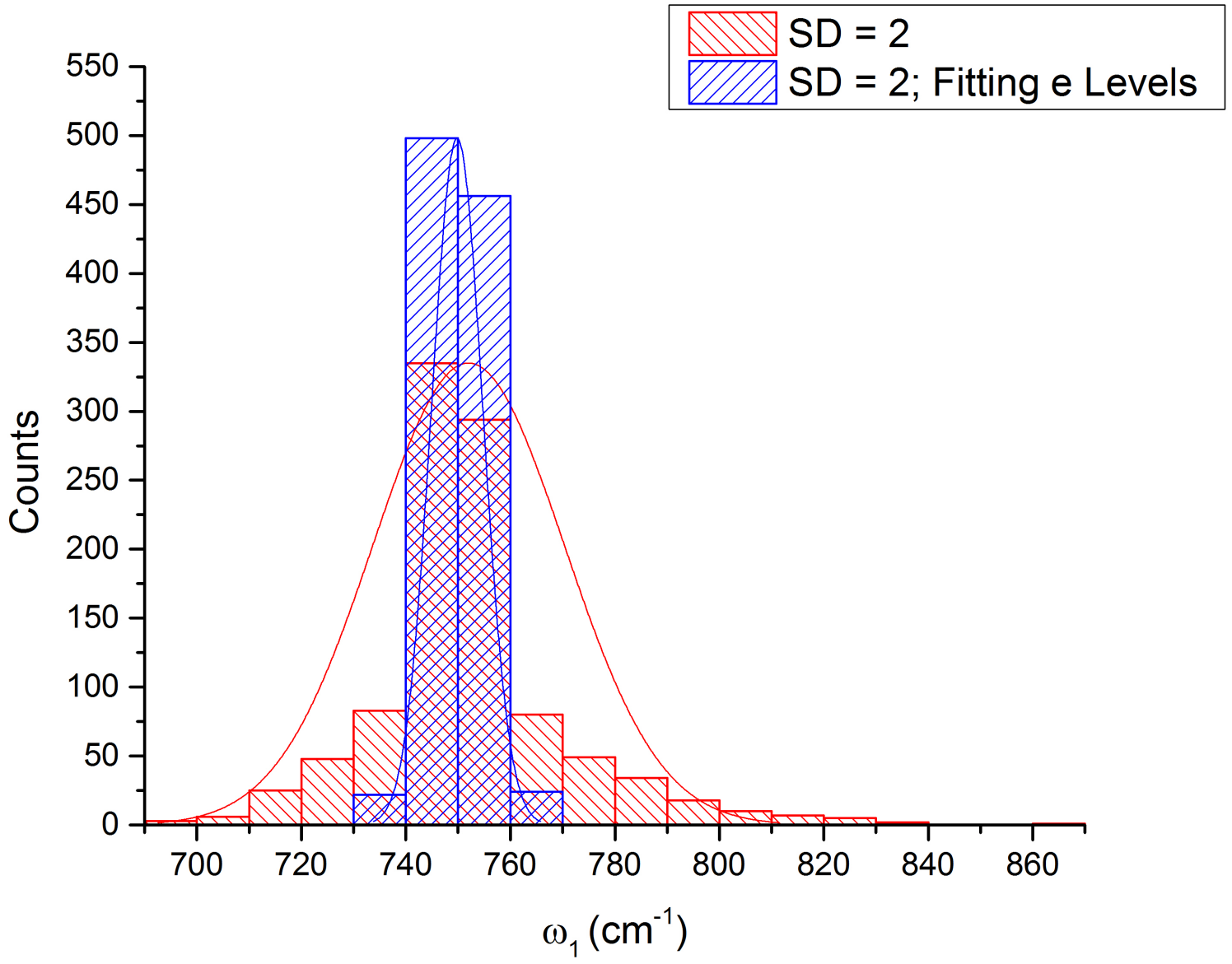

(a) Distribution of ω_1.

Figure 6.9: Distribution of fit parameters for experimental error simulation of standard deviation 2 cm^{-1}. Different number of levels fit.

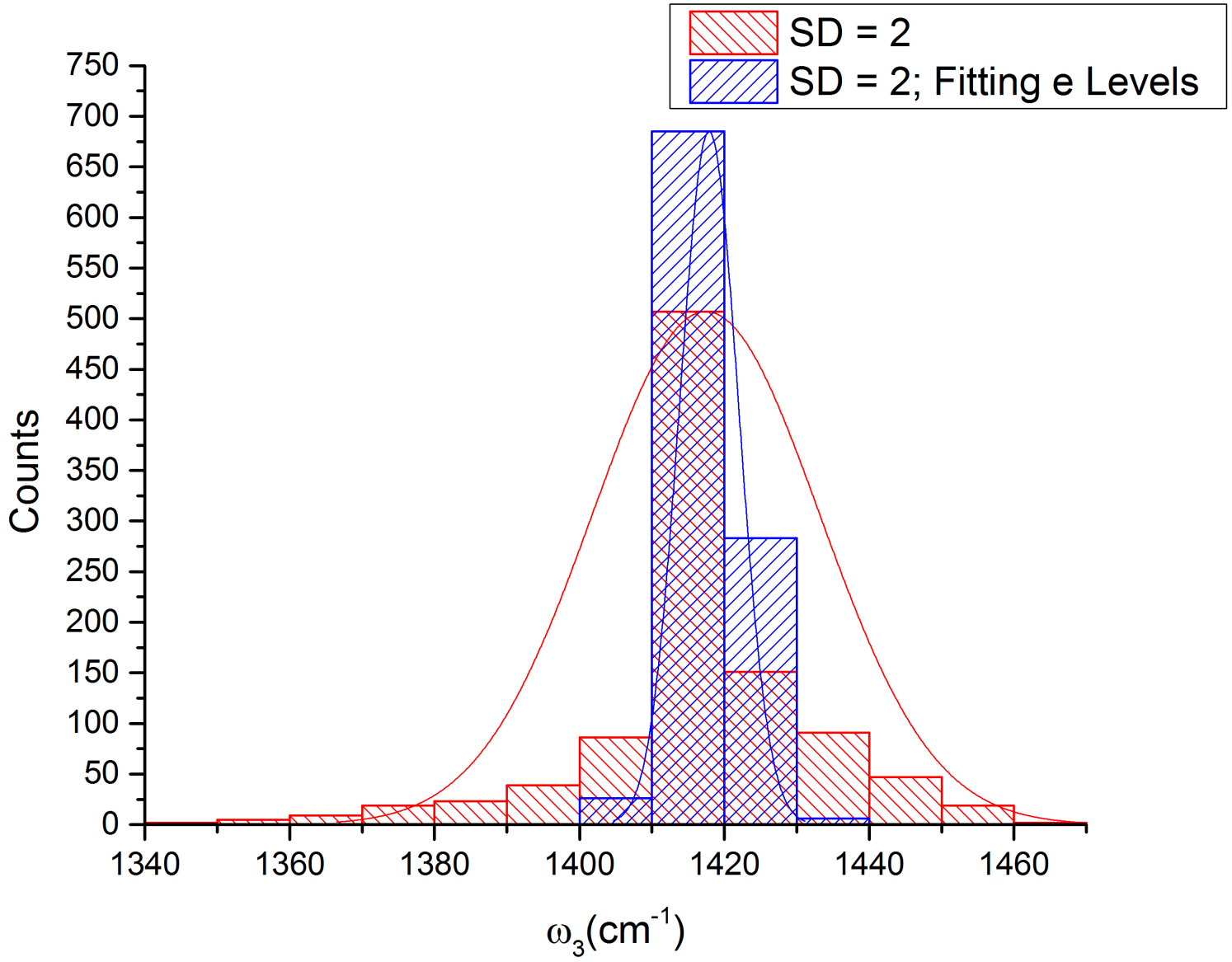

(b) Distribution of ω_3.

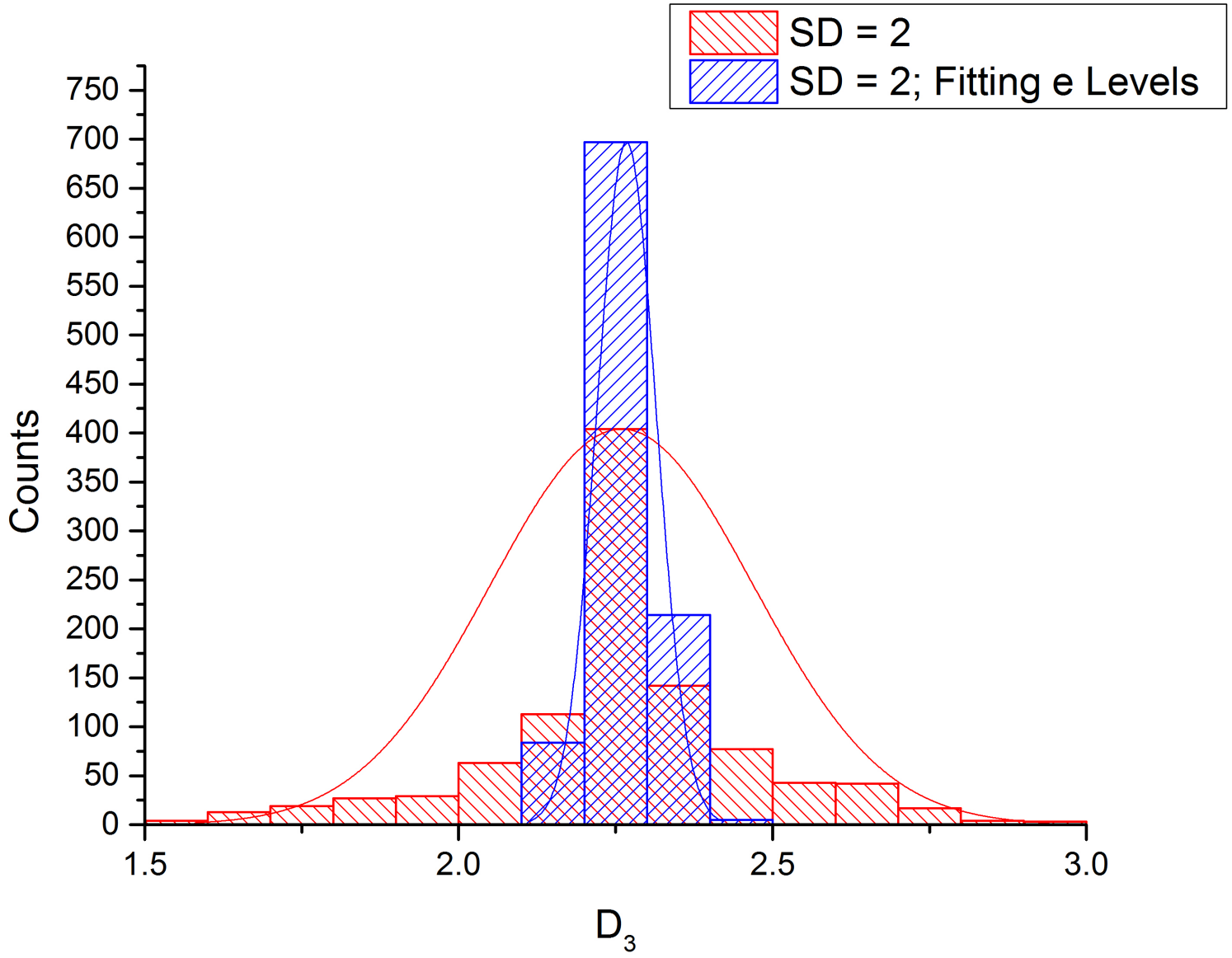

(c) Distribution of D_3.

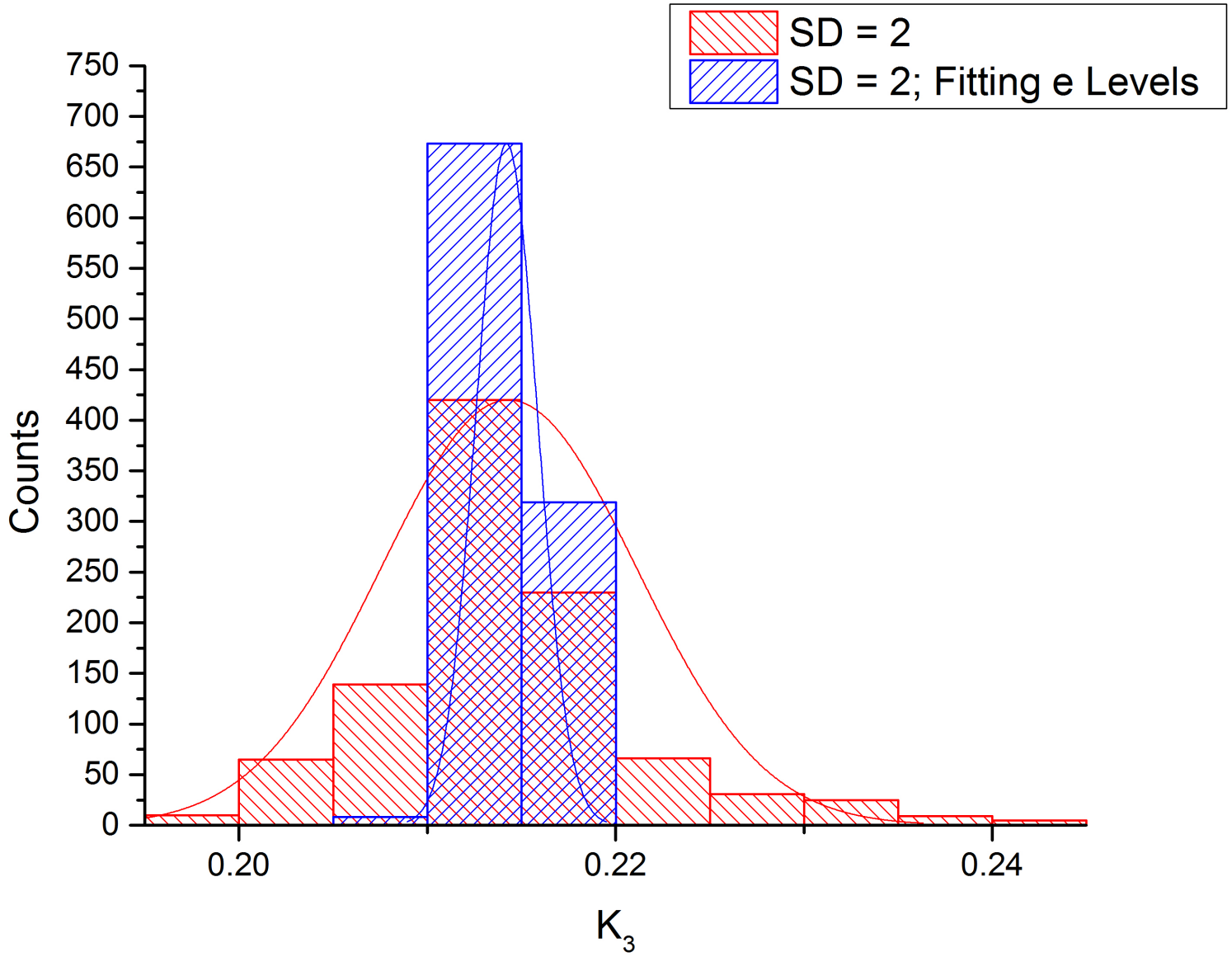

(d) Distribution of K_3.

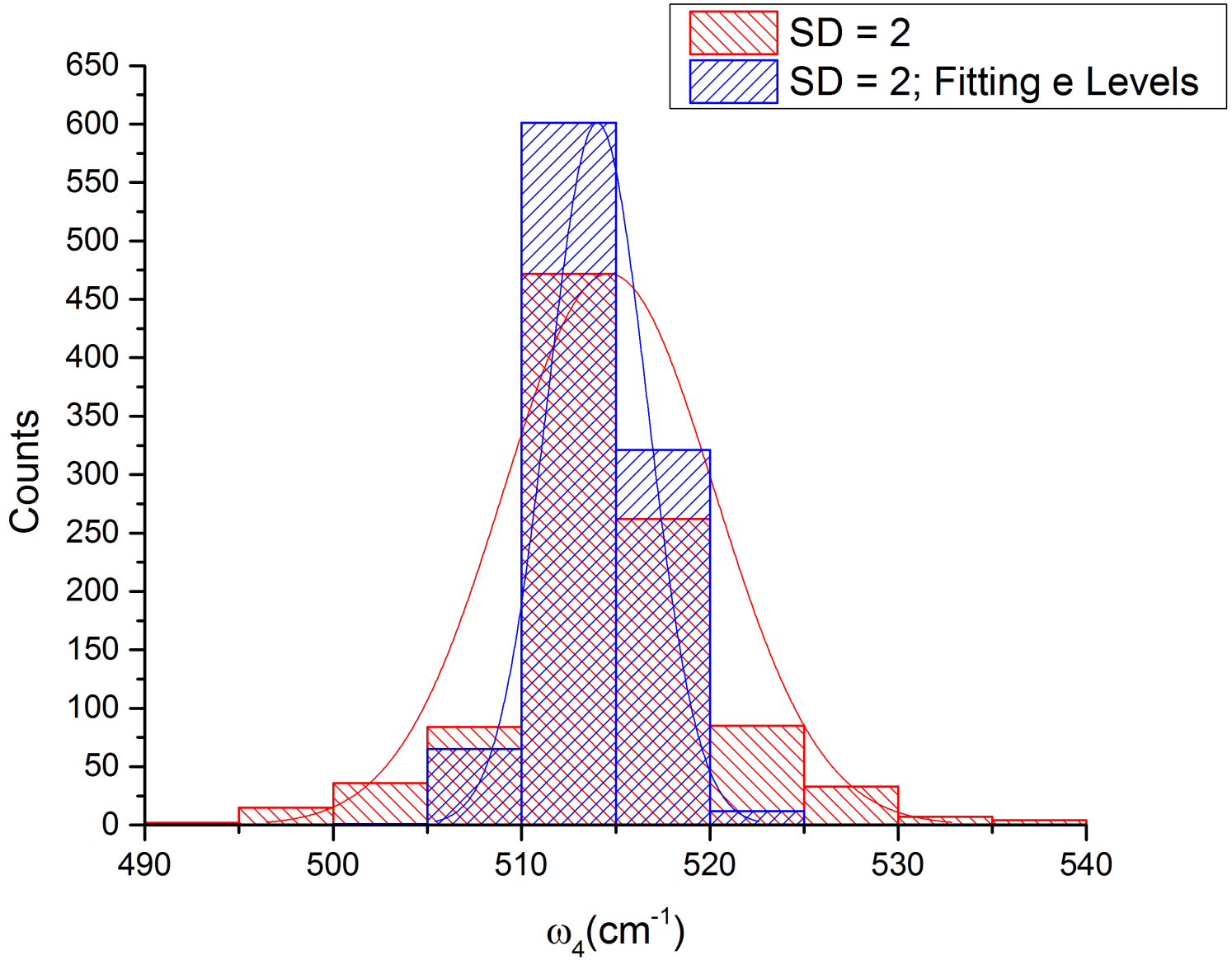

(e) Distribution of ω_4.

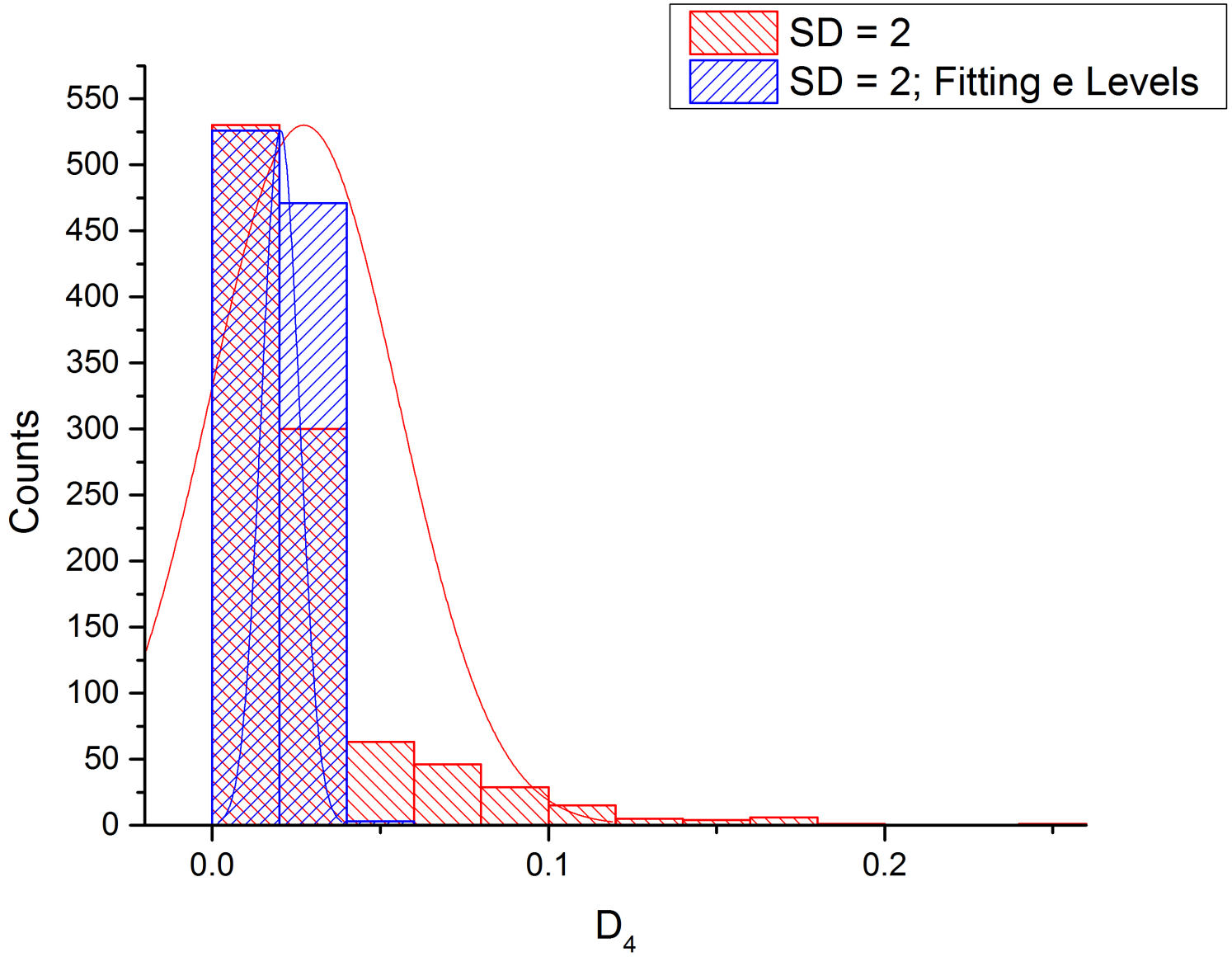

(f) Distribution of D_4.

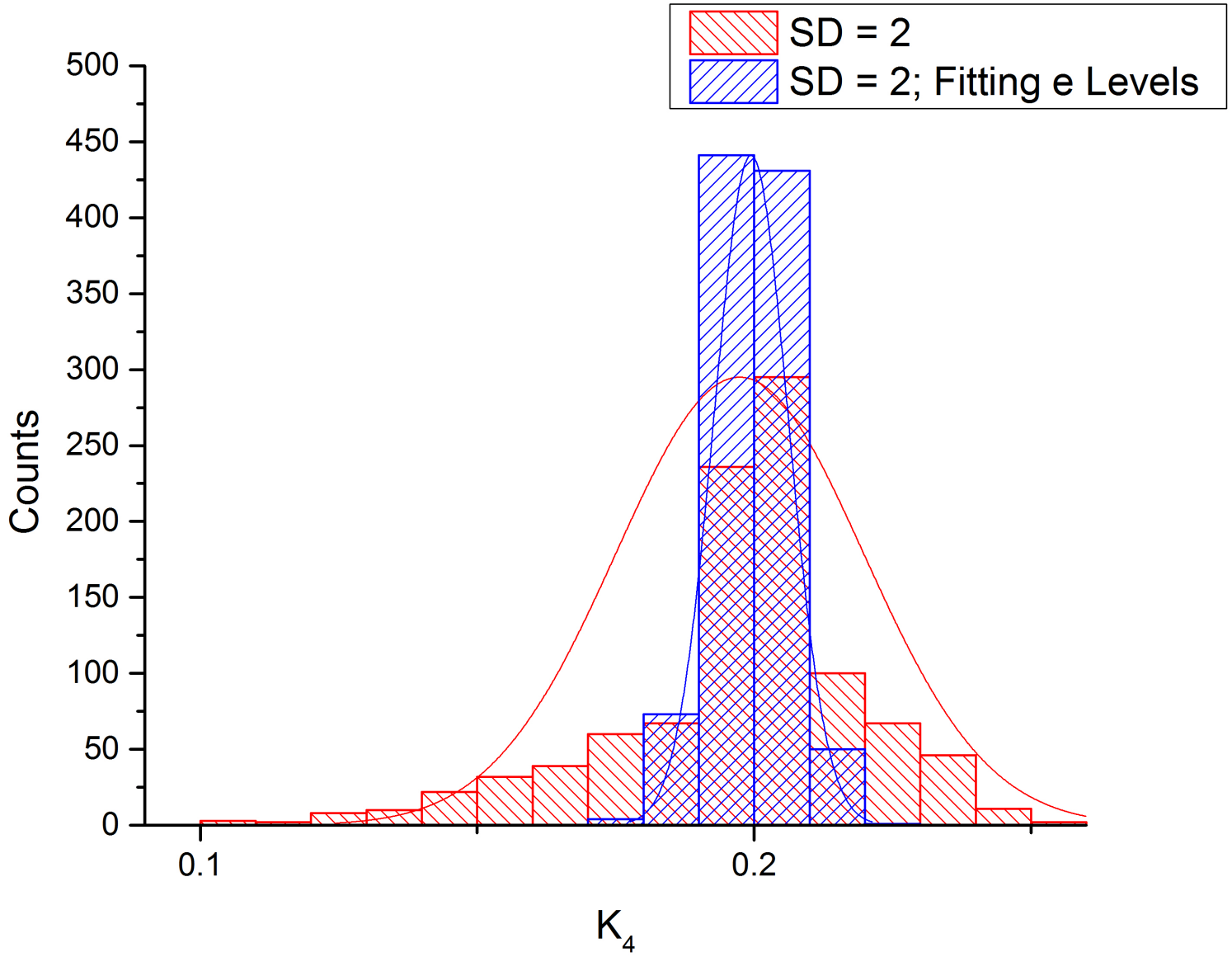

(g) Distribution of K_4.

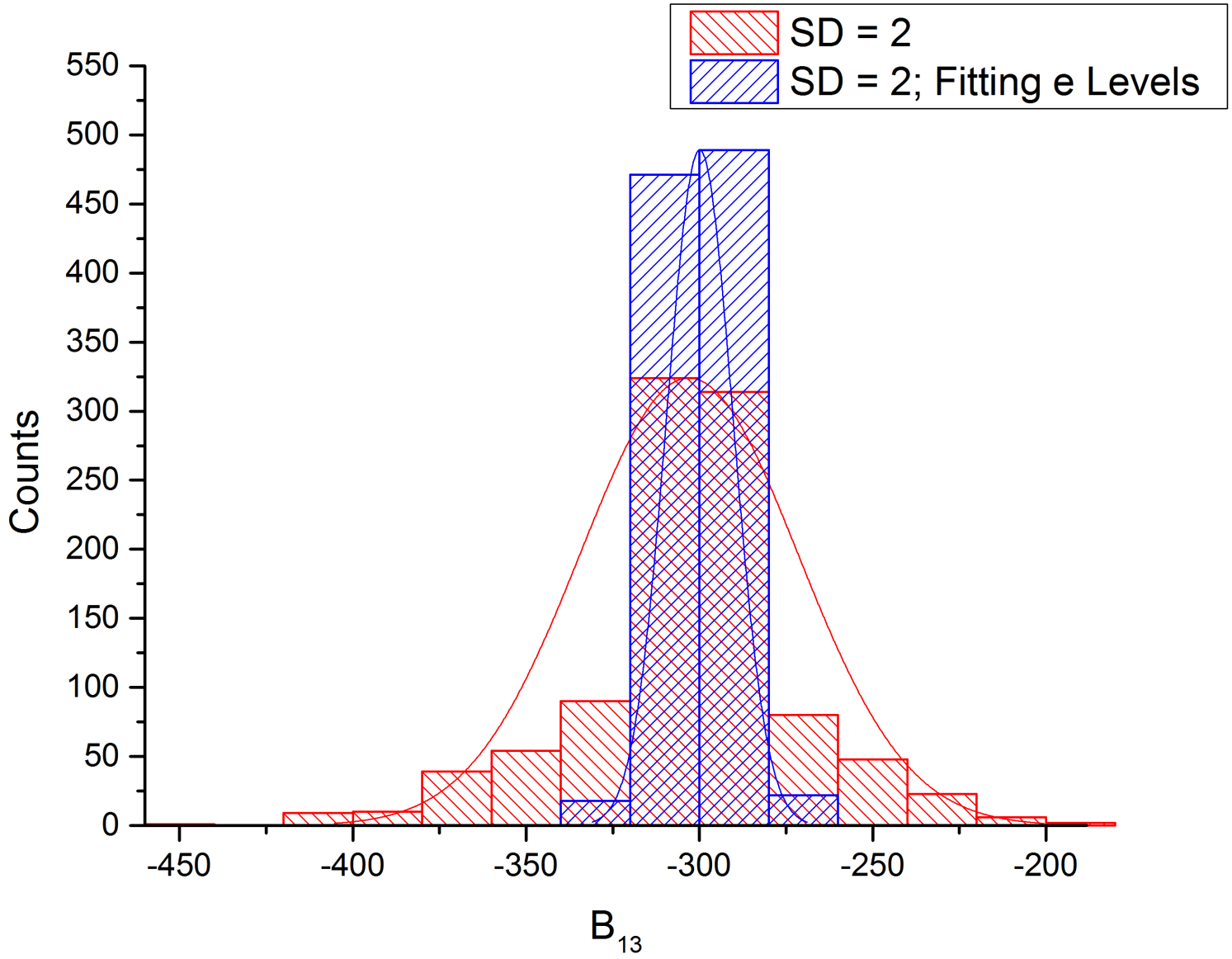

(h) Distribution of B_{13}.

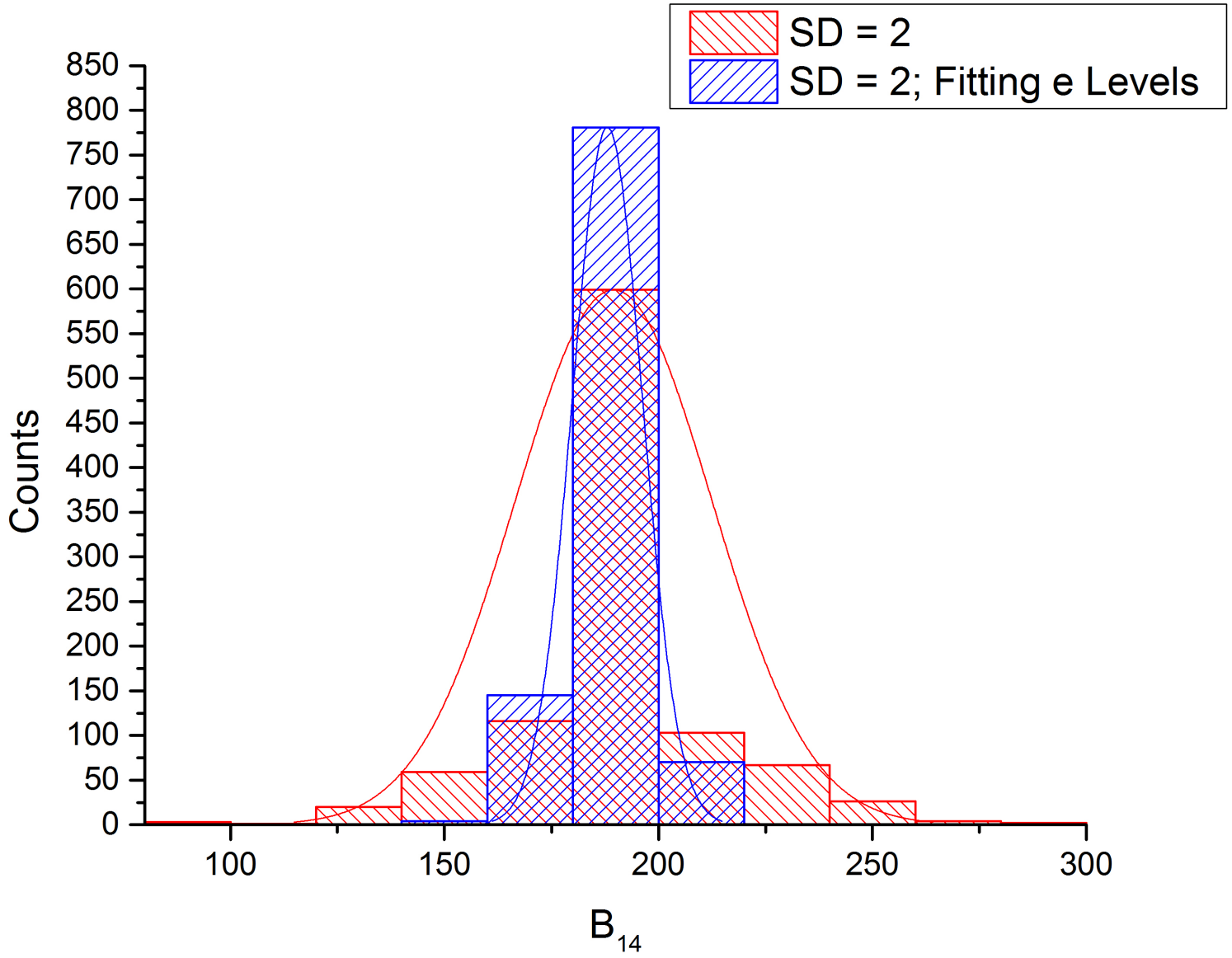

(i) Distribution of B_{14}.

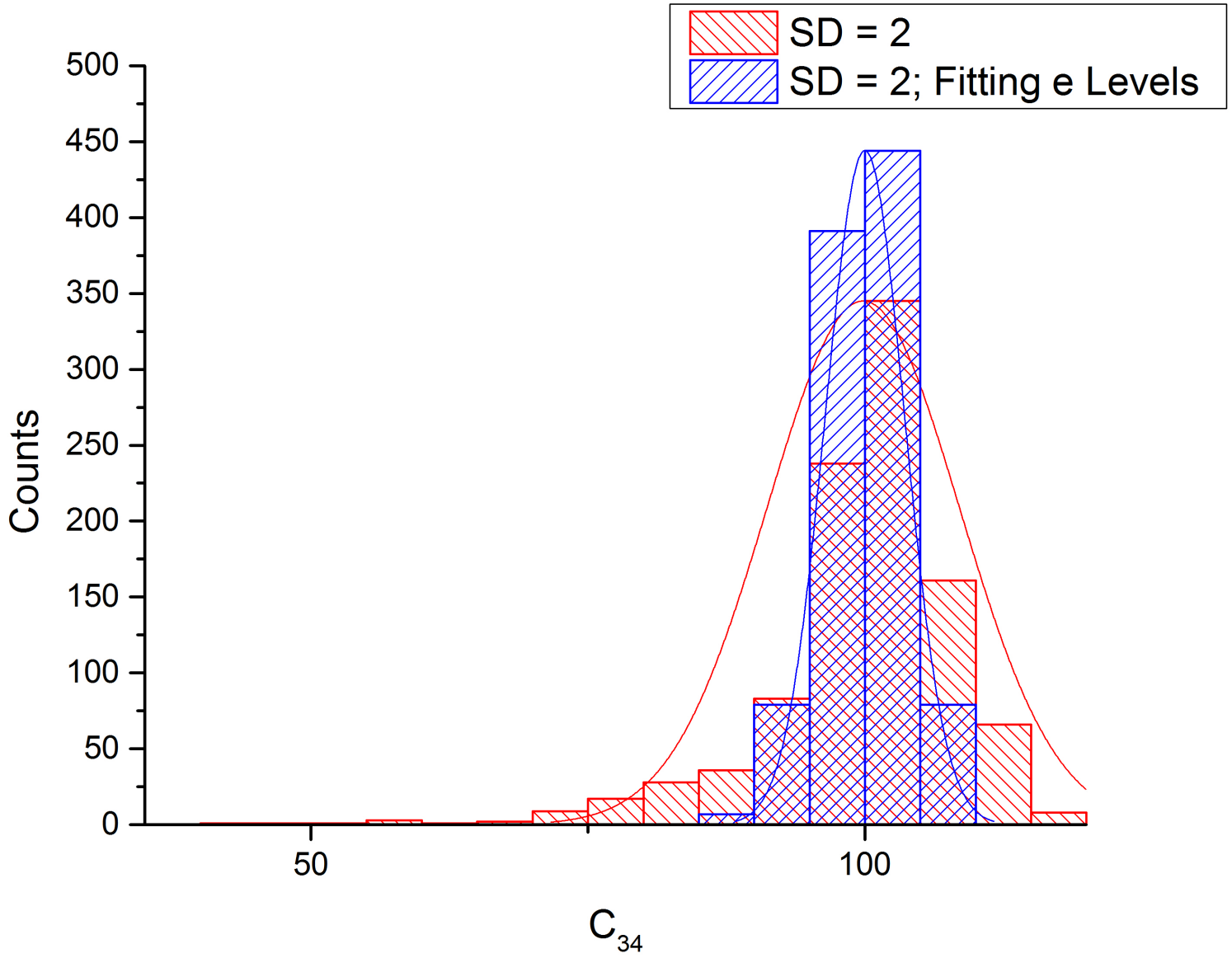

(j) Distribution of C_{34}.

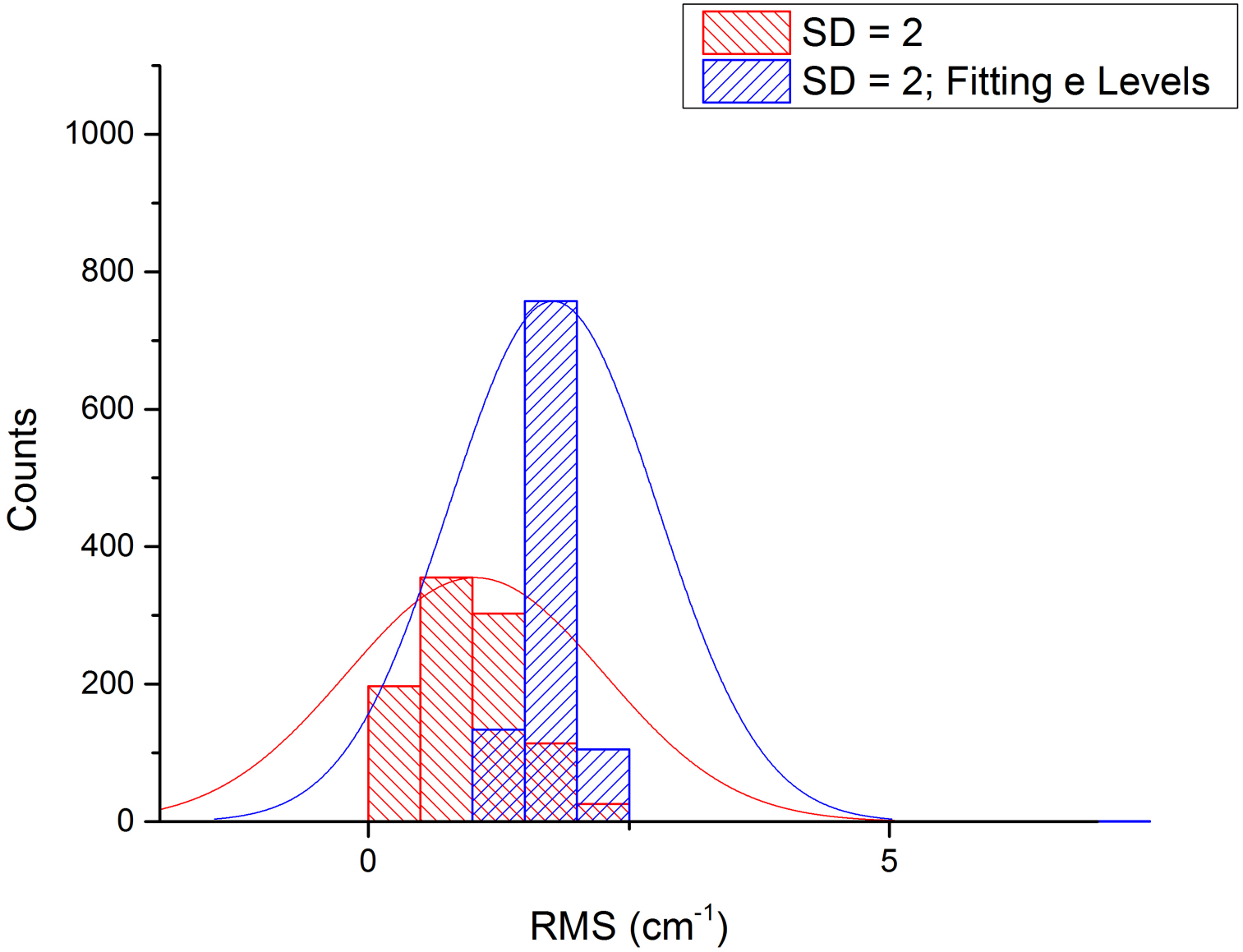

(k) Distribution of RMS.

Table 6.8: Simulating experimental error with a standard deviation of 2 cm^{-1} and fitting both a_1'' and e'' levels.

	True Value	Mean	Standard Deviation
ω_1 (cm^{-1})	750	749.81626	4.92998
ω_3 (cm^{-1})	1417.695	1417.87802	4.07409
D_3	2.2673	2.26706	0.04738
K_3	0.2143	0.21422	0.00163
ω_4 (cm^{-1})	514.907	514.01818	2.641
D_4	0.0195	0.02031	0.00564
K_4	0.2	0.19943	0.00674
B_{13} (cm^{-1})	-300	-299.91604	9.56356
B_{14} (cm^{-1})	187.8	188.03326	8.26419
C_{34} (cm^{-1})	100	99.99587	3.5876
RMS (cm^{-1})	–	1.77305	0.99944

RMS nearly doubles. This is likely because the introduction of more levels increases the amount of levels that deviate from the calculation, and thus increases the RMS. However, it is clear that there is a significant improvement in the precision by fitting these extra levels.

6.4.2 Experimental Error Dependence of Fit Error

The second effect studied is how increasing error in the experimental spectrum manifests as error in the parameter fits and error in the total fit. Three cases were compared. In all these cases, only a_1'' levels were randomized and fit. The first case has a standard deviation of 2 cm^{-1}, the second case has a standard deviation of 4 cm^{-1}. The distribution of fit parameters and RMS of the fits for all cases are graphically compared in Figure 6.10. The statistical values of all the fits with a standard deviation of 4 cm^{-1} are summarized in Table 6.9.

Again, the mean values are similar to the true values. This time, the standard deviation of each parameter's distribution increases by a factor of about 1.2. The RMS appropriately doubles. However, the distribution of the parameters is still quite similar between both cases, and the parameter determination is not significantly improved moving from SD = 4 cm^{-1} to SD = 2 cm^{-1}.

For future work in this direction, larger standard deviations will be tested. A functional

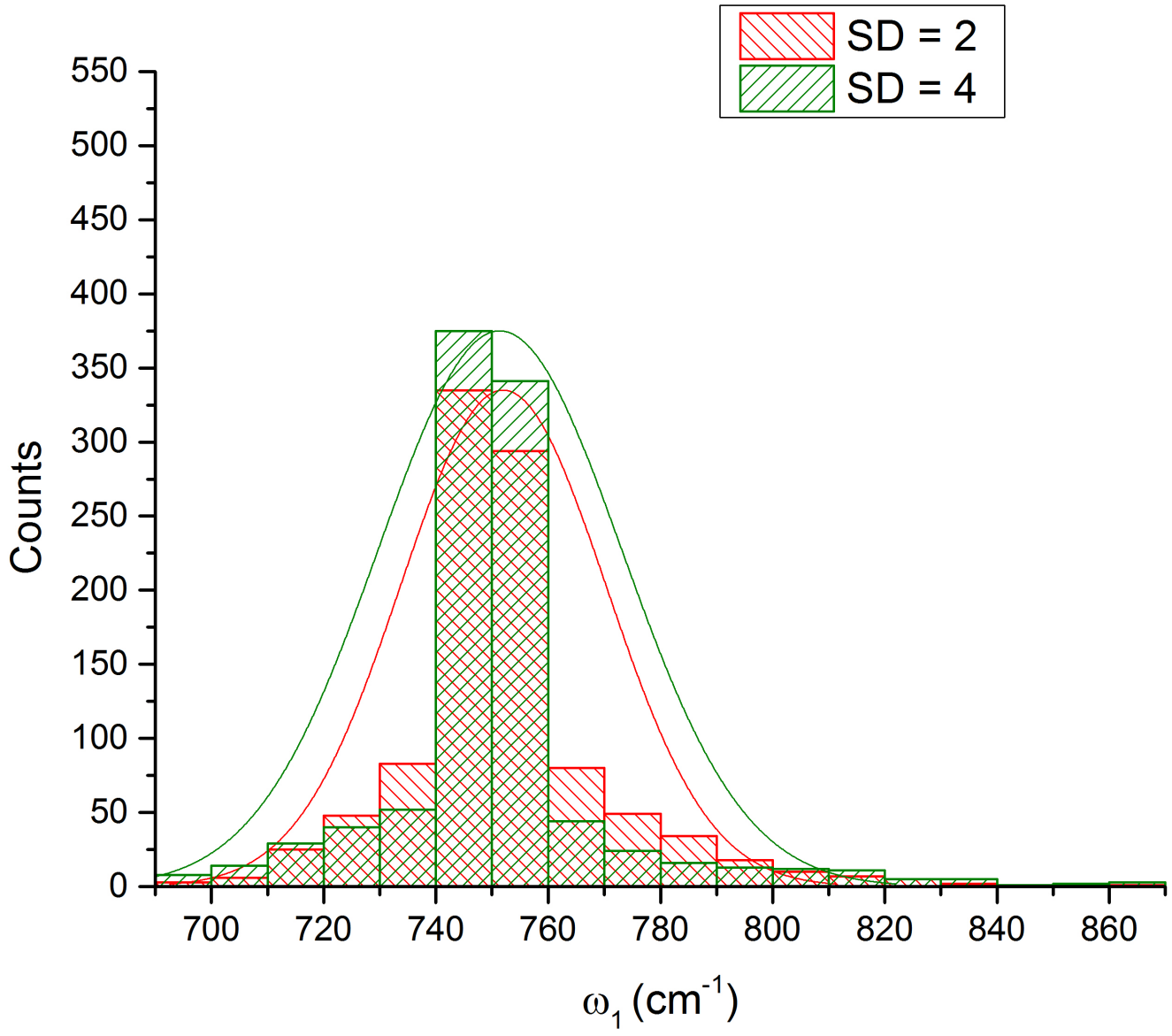

(a) Distribution of ω_1.

Figure 6.10: Distribution of fit parameters for experimental error simulation. Different standard deviations applied to obtain fitted levels.

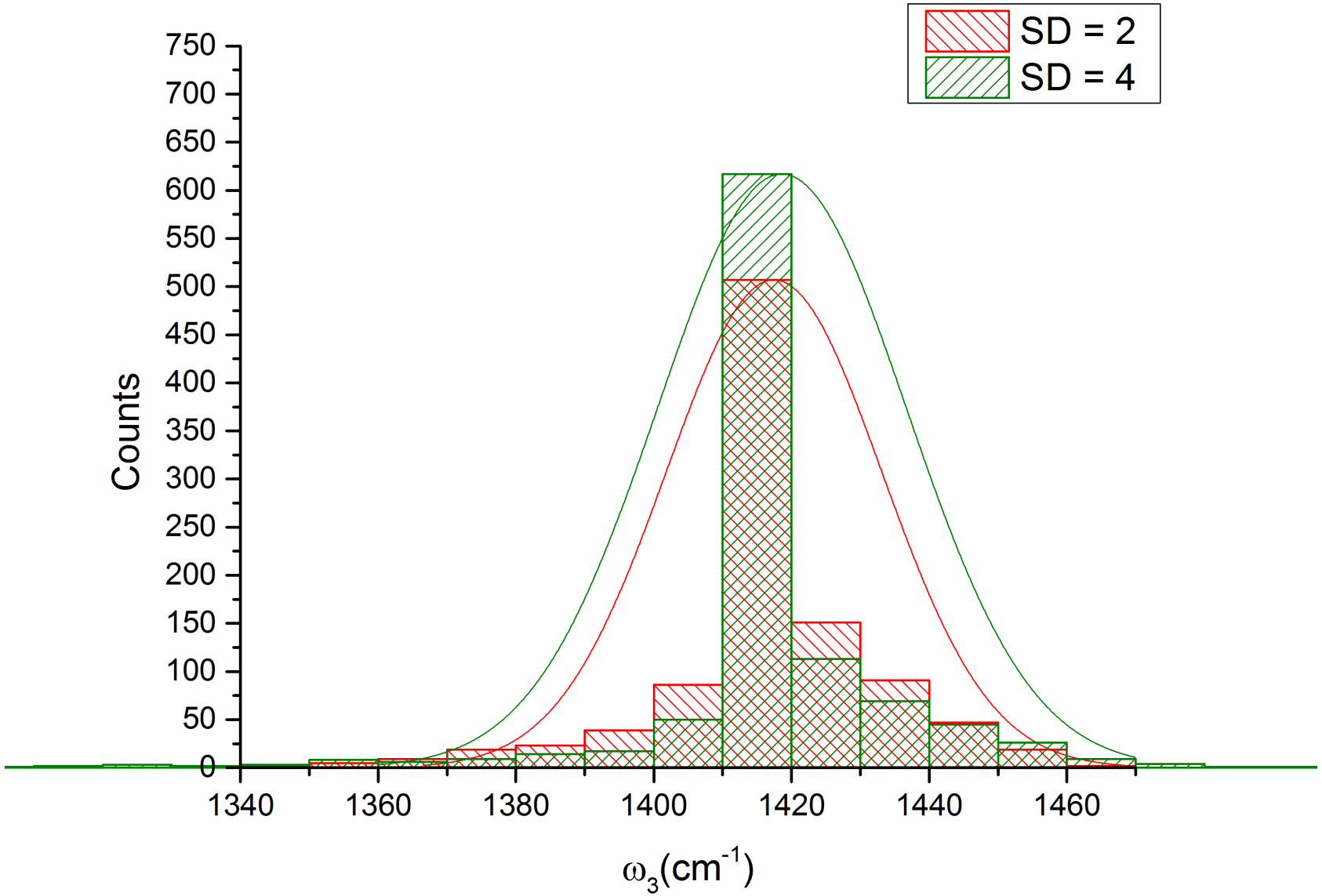

(b) Distribution of ω_3.

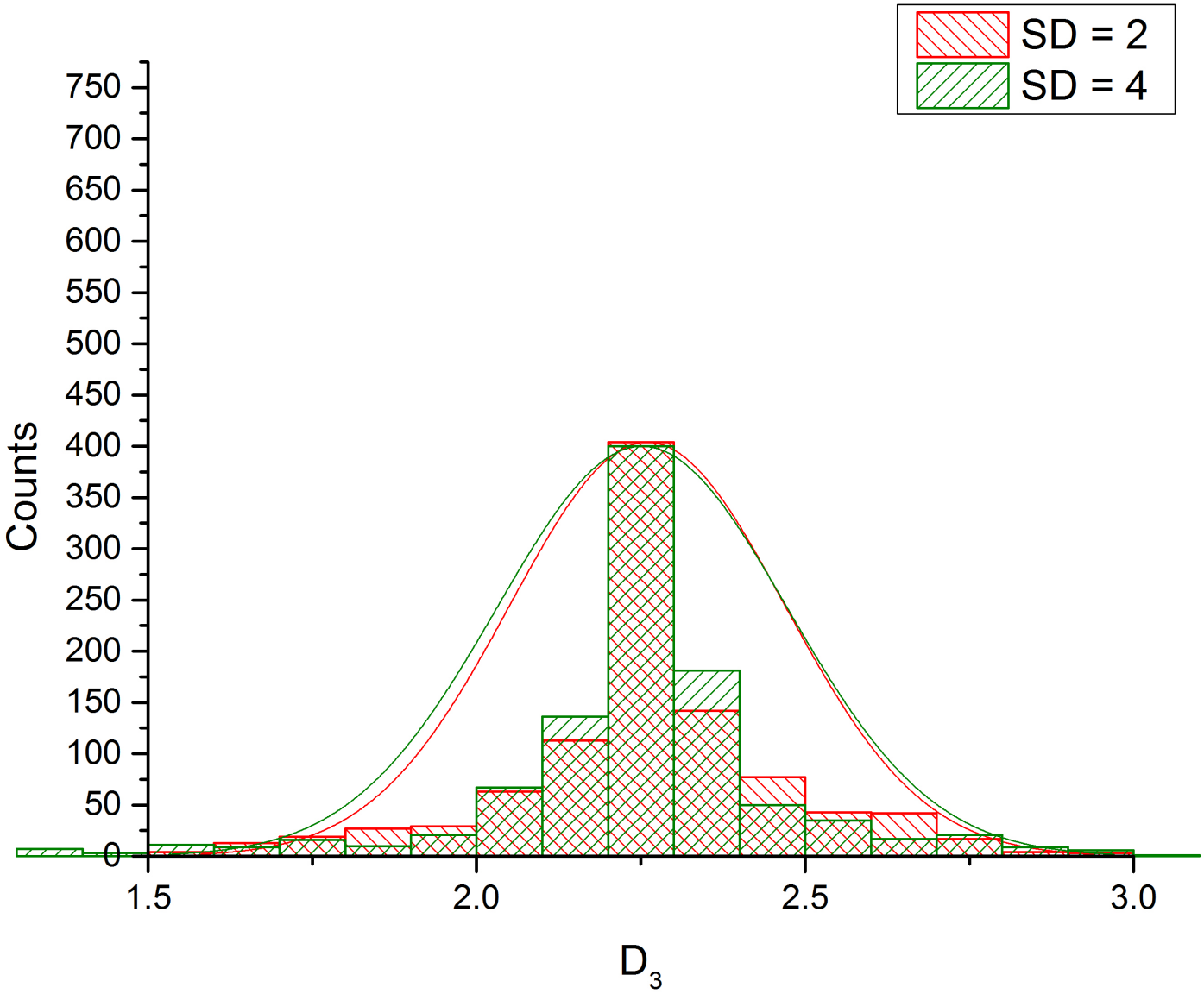

(c) Distribution of D_3.

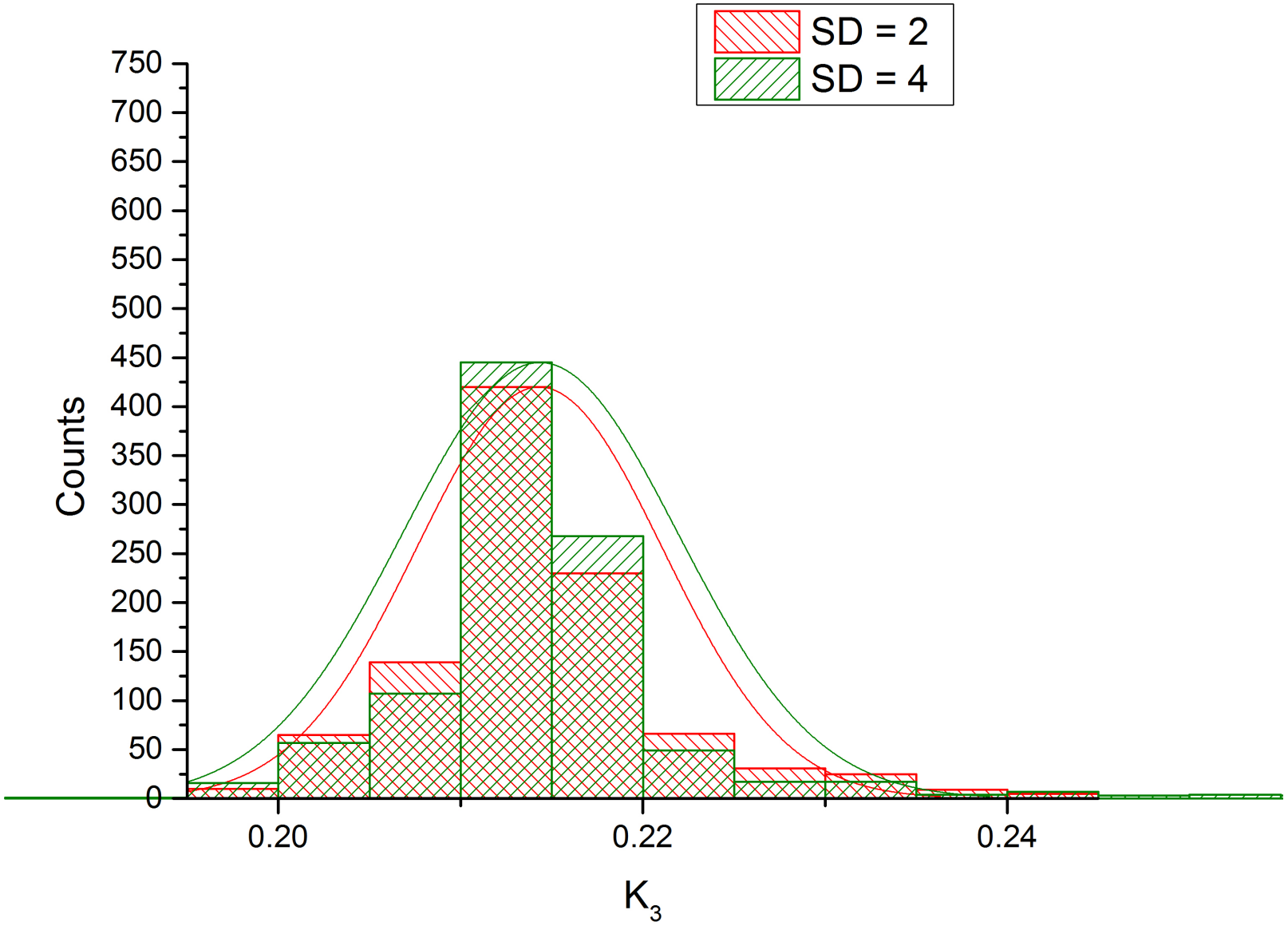

(d) Distribution of K_3.

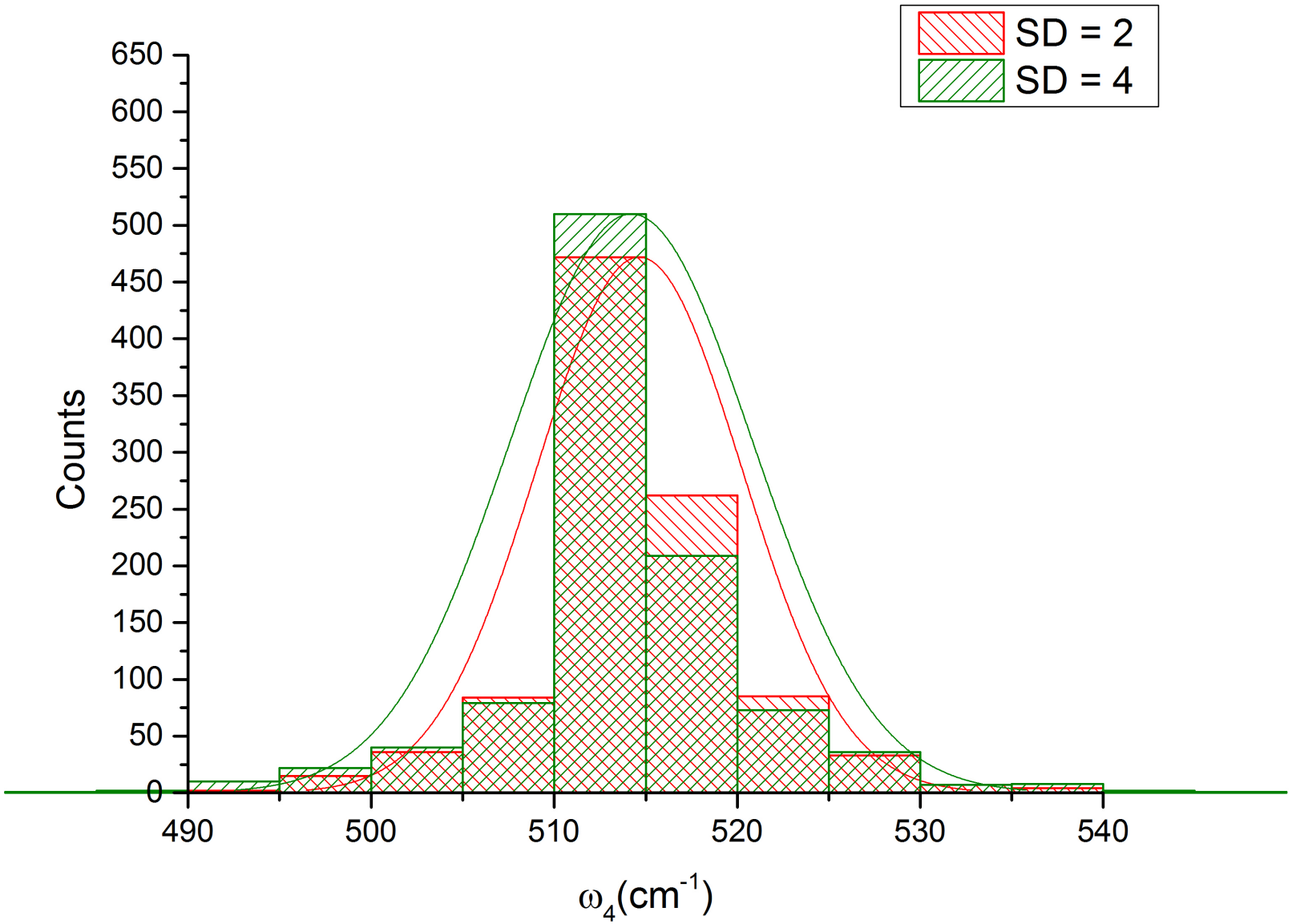

(e) Distribution of ω_4.

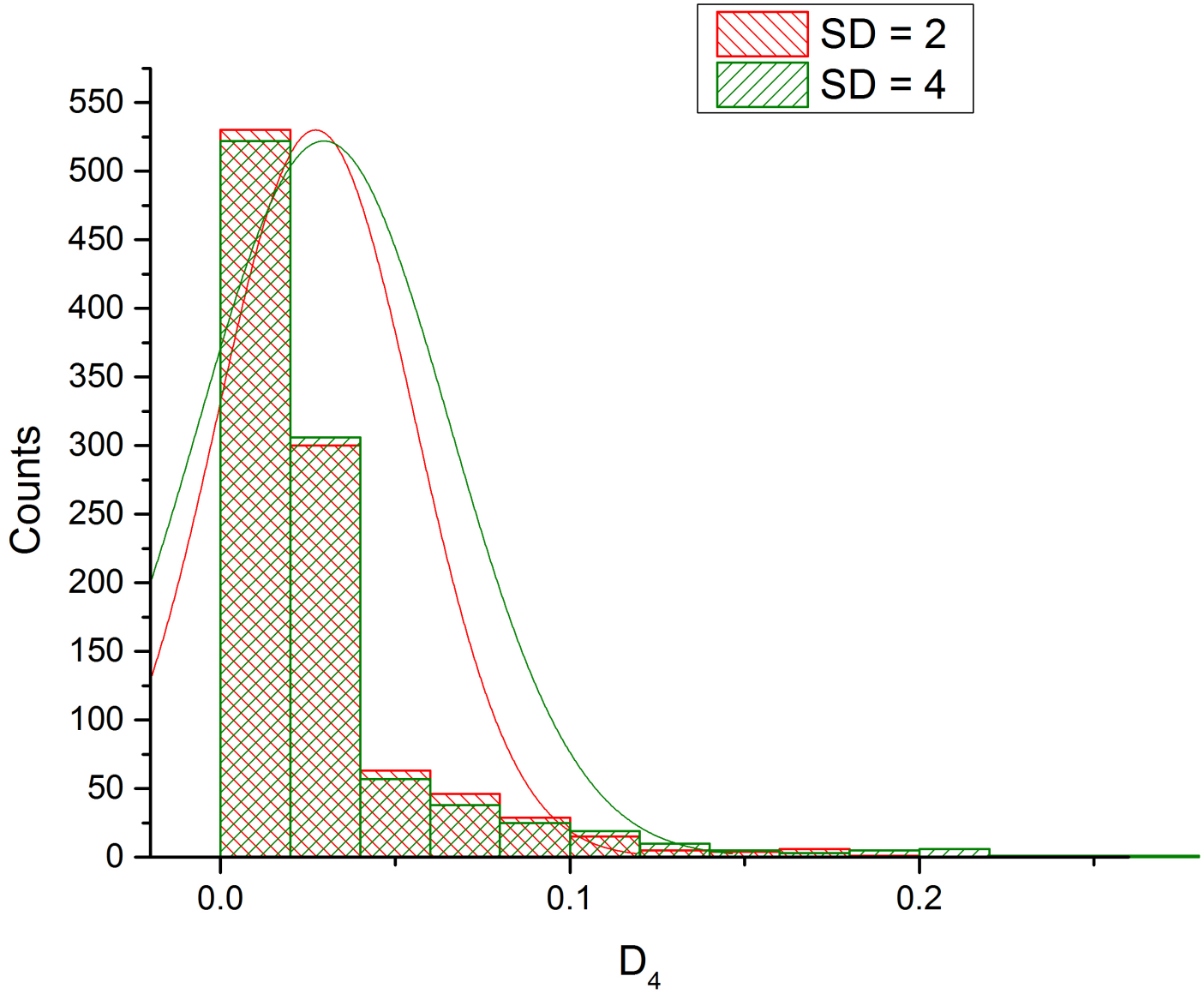

(f) Distribution of D_4.

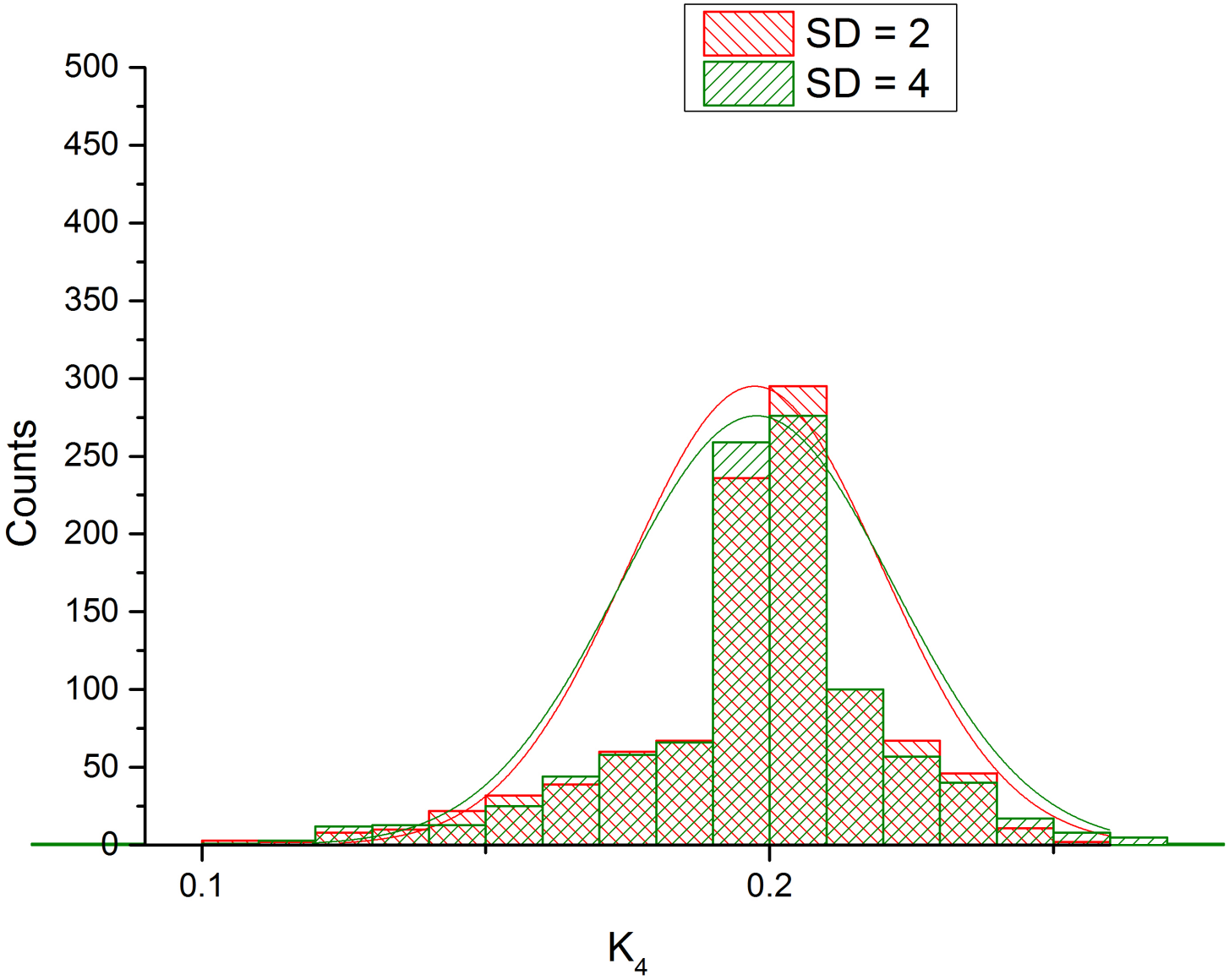

(g) Distribution of K_4.

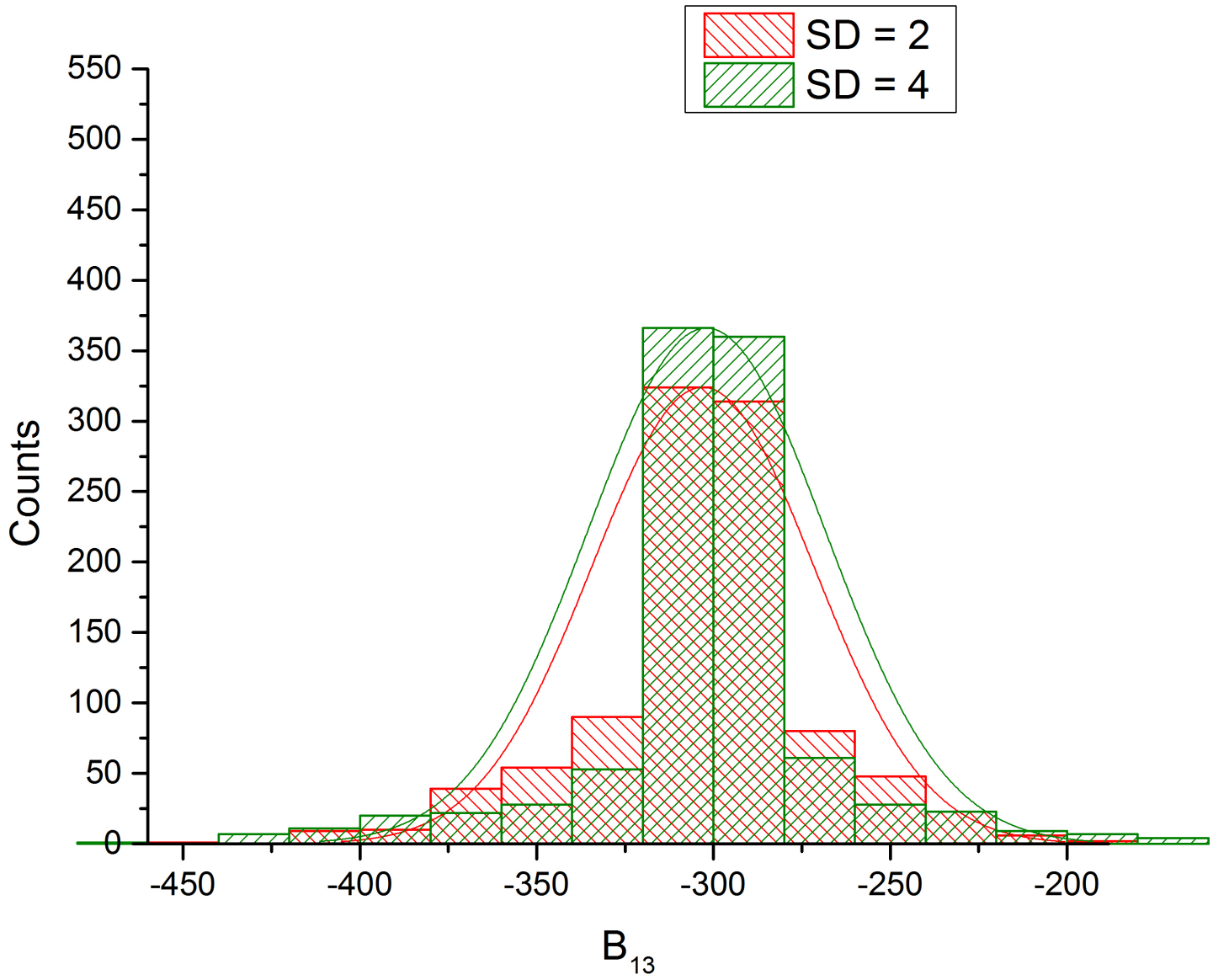

(h) Distribution of B_{13}.

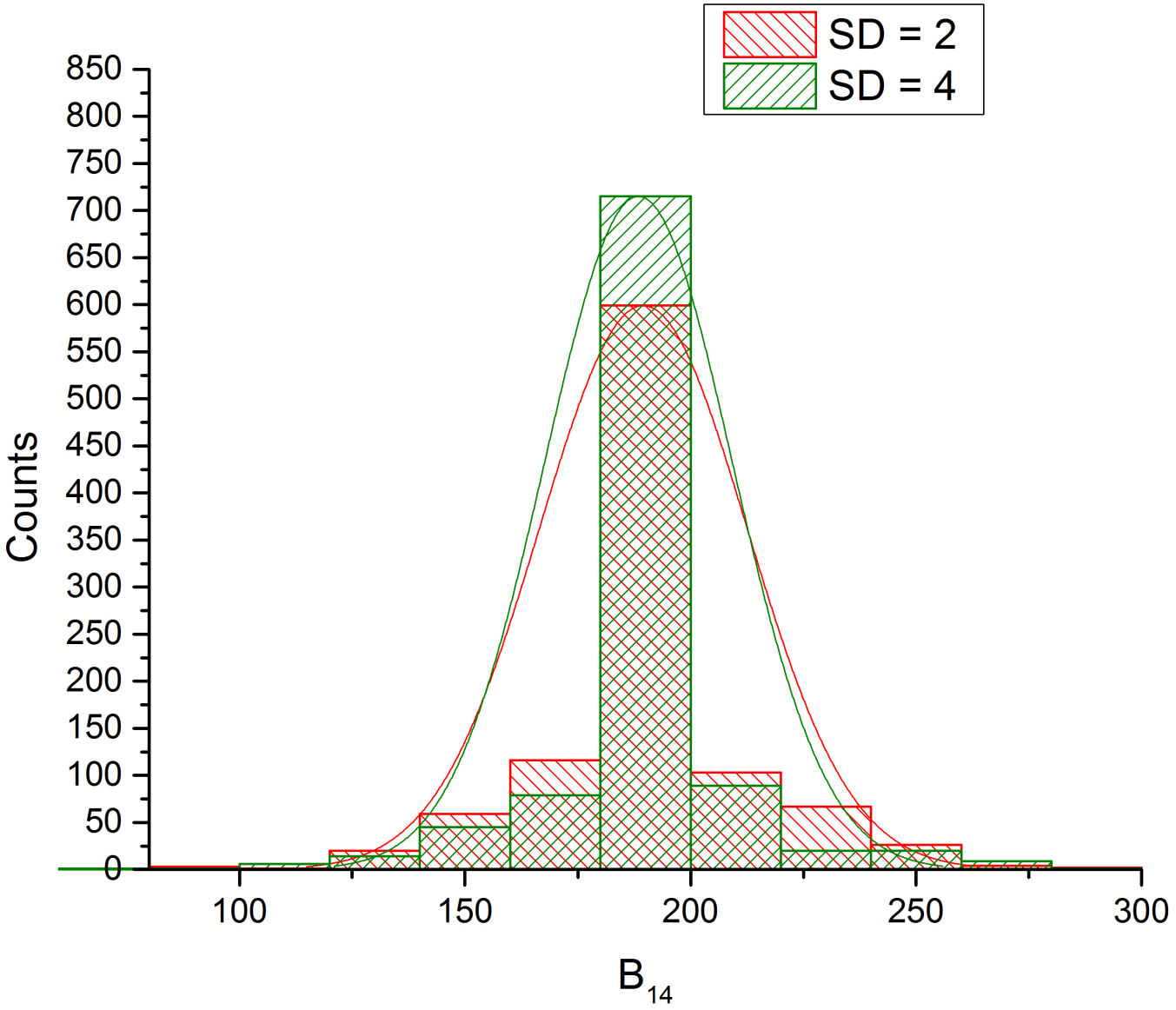

(i) Distribution of B_{14}.

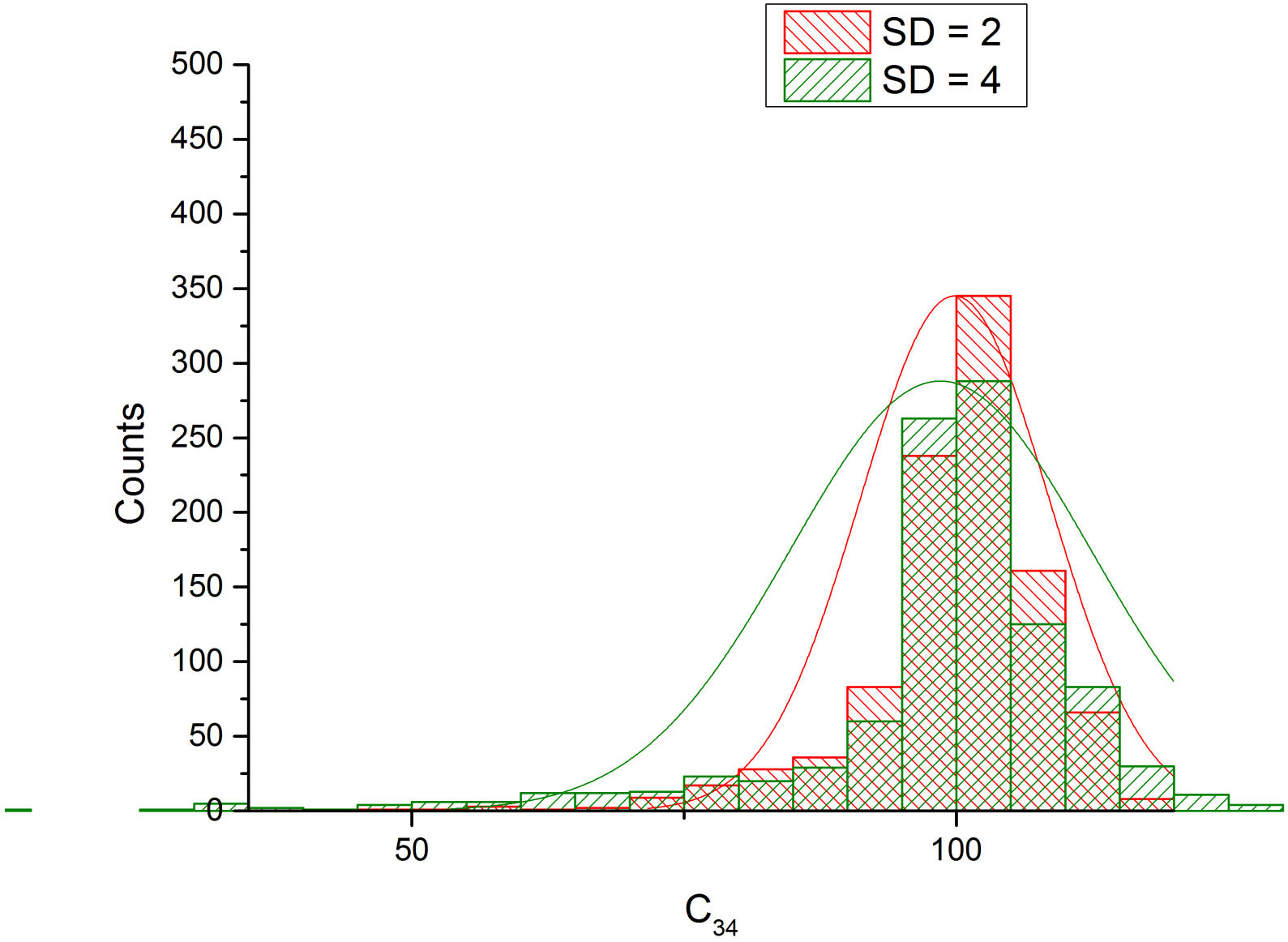

(j) Distribution of C_{34}.

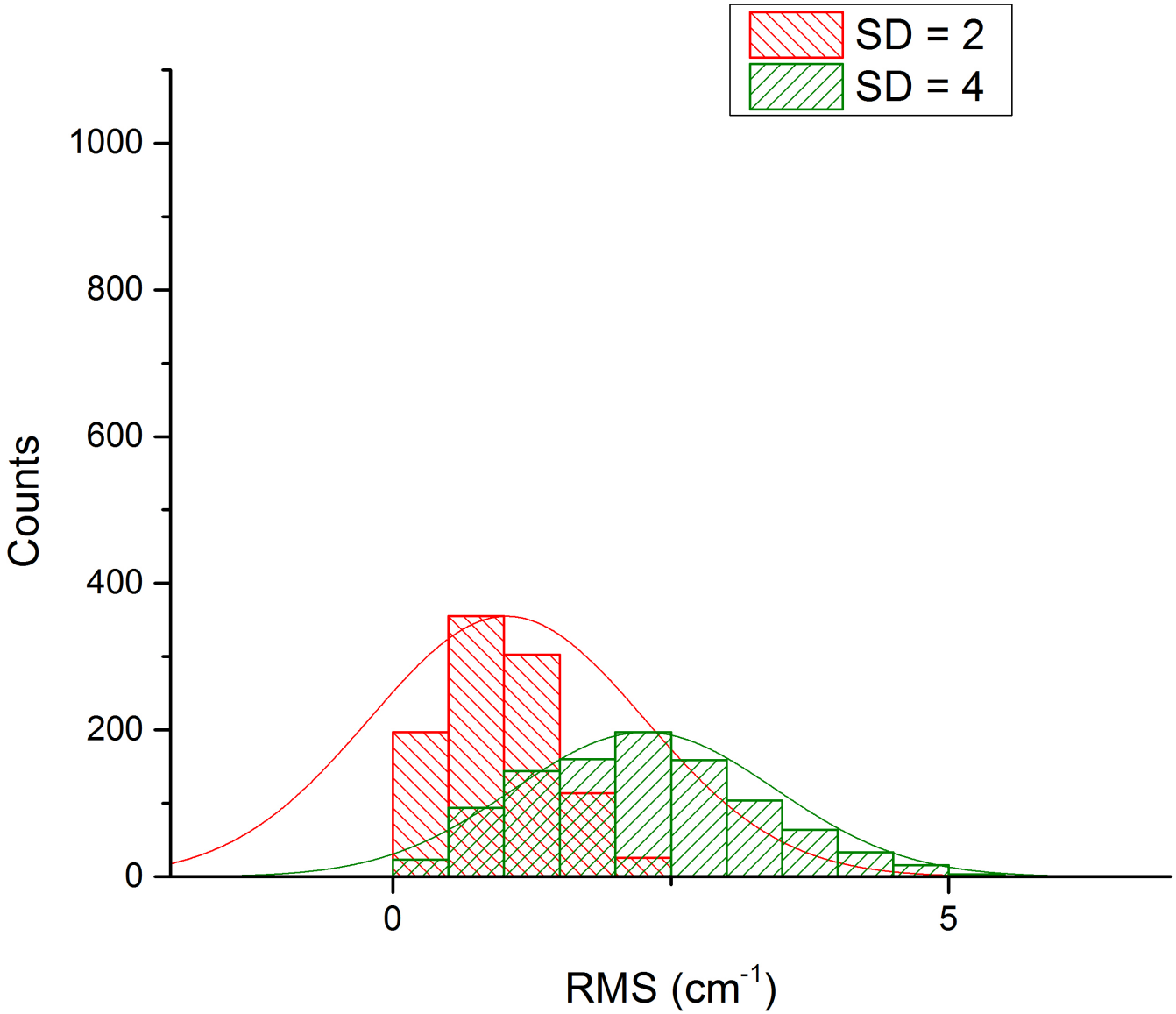

(k) Distribution of RMS.

Table 6.9: Simulating experimental error with a standard deviation of 4 cm^{-1} and fitting only a_1'' levels.

	True Value	Mean	Standard Deviation
ω_1 (cm^{-1})	750	751.4038	21.68573
ω_3 (cm^{-1})	1417.695	1418.61155	18.05201
D_3	2.2673	2.25178	0.22069
K_3	0.2143	0.21437	0.00758
ω_4 (cm^{-1})	514.907	514.21947	6.6262
D_4	0.0195	0.02966	0.03588
K_4	0.2	0.19771	0.02407
B_{13} (cm^{-1})	-300	-301.96909	33.63893
B_{14} (cm^{-1})	187.8	188.45865	20.73405
C_{34} (cm^{-1})	100	98.54662	13.83339
RMS (cm^{-1})	–	2.26547	1.17611

dependence of fit RMS on experimental error will be enlightening. Further projects in this type of analysis is also planned for rotational spectra.

Chapter 7
Conclusion

The high resolution, rotationally resolved spectra of the $\widetilde{A}^2E'' \leftarrow \widetilde{X}^2A_2'$ electronic transition of NO_3 have been rotationally analyzed. The results were obtained from a newly developed Jahn-Teller rotational Hamiltonian. Furthermore, the previous vibronic analysis of the $\widetilde{A}^2E'' \leftarrow \widetilde{X}^2A_2'$ electronic transition was expanded through quantification of the effect of quartic Jahn-Teller coupling terms on fits using a quadratic Jahn-Teller Hamiltonian.

To analyze the rovibronic spectra of NO_3, a new rotational Hamiltonian was derived by explicitly including the effects of vibronic and spin angular momentum. From this, terms corresponding to coriolis coupling, Jahn-Teller distortions, and spin-orbit coupling were derived. These terms allowed the new Hamiltonian to describe the rotational structure of any D_{3h} molecule exhibiting the Jahn-Teller effect. This new, modified rotational Hamiltonian was implemented as a model in SPECVIEW.

The modified rotational Hamiltonian demonstrated success in analyzing the rotational structure of the 2_0^1 and $2_0^1 4_0^2$ vibronic bands in the $\widetilde{A}^2E'' \leftarrow \widetilde{X}^2A_2'$ spectrum. Generally, good agreement was found between experiment and simulation. From the fit parameters, the new model indicated significant coriolis coupling and spin-orbit coupling. The simulation also indicated that the rotational structure exhibits negligible Jahn-Teller effect, in contrary to the current vibronic analysis. Explaining the cause of this discrepancy is still ongoing. However, with this analysis, a large sample of both the parallel and perpendicular bands have been rotationally analyzed. All of these analyses agreed that there is weak to no observable Jahn-Teller coupling in the rotational structure of the $\widetilde{A}^2E''$ state. Evidence

was also found for perturbations in the $\widetilde{A}^2E''$ state rotational levels. Further analysis of the remaining bands and interpretation of the data is still underway.

A further discrepancy lies in the disagreement between *ab-initio* and experimental analyses of the $\widetilde{A}^2E'' \leftarrow \widetilde{X}^2A_2'$ spectrum, particularly regarding the vibronic structure. Since the *ab-initio* model used a model with a higher-order approximation, this was a suspect for the discrepancy. This possibility was quantified by using the experimental fit model to fit artificial spectra from the higher-order quartic Hamiltonian to analyze the effect of higher order terms on the quadratic terms used in the fit. Initially, large fluctuations were seen for higher magnitudes of quartic coupling, and some of these fluctuations may have supported the possibility of overestimation of the Jahn-Teller effect from experimental analyses. However, multiple minimum in the fit were found, complicating the analysis and further data analysis is required to draw firm conclusions. This analysis was extended to the Li_3 system with interesting results regarding the phase of coupling terms, as well as the invariance of fit RMS with respect to number of levels fit. The effect of experimental error was also explored by observing the variance in fit parameters when levels are allowed to vary. Further cases are necessary to obtain useful quantitative estimates on the effect of experimental error on the fit parameters.

Bibliography

[1] T. Codd, M.-W. Chen, M. Roudjane, J.F. Stanton, and T.A. Miller. Jet cooled cavity ringdown spectroscopy of the $\widetilde{A}^2E'' \leftarrow \widetilde{X}^2A_2'$transition of the NO_3 radical. *J. Phys. Chem.*, 142:184305, 2015.

[2] M. Mayer and L. S. Cederbaum. Molecular rotations in vibronically coupled systems. *J. Chem. Phys.*, 105:4938–4963, 1996.

[3] Philip R. Bunker and Per Jensen. *Molecular Symmetry and Spectroscopy.* NRC Research Press, 2 edition, 2006.

[4] K. Kawaguchi, R. Fujimori, J. Tang, and T. Ishiwata. Ftir spectroscopy of no_3: Perturbation analysis of the $\nu_3 + \nu_4$ state. *J. Chem. Phys.*, 117:13732–13742, 2013.

[5] R. P. Wayne, I. Barnes, P. Biggs, J. P. Burrows, C. E. Canosa-Mas, J. Hjorth, G. Le Bras, G. K. Moortgat, D. Perner, G. Poulet, G. Restelli, and H. Sidebottom. The nitrate radical: Physics, chemistry, and the atmosphere. *Atmospheric Environment*, 25:1–203, 1991.

[6] I. Barnes, V. Bastian, K. H. Becker, and Z. Tong. Kinetics and products of the reactions of nitrate radical with monoalkenes, dialkenes, and monoterpenes. *J. Phys. Chem.*, 94:2413–2419, 1990.

[7] Paul S. Monks. Gas-phase radical chemistry in the troposphere. *Chem. Soc. Rev.*, 34:376–395, 2005.

[8] J. H. Kroll and J. H. Seinfeld. Chemistry of secondary organic aerosol: Formation and evolution of low-volatility organics in the atmosphere. *Atomospheric Environment*, 42:35933624, 2008.

[9] A. D. Walsh. The electronic orbitals, shapes, and specra of polyatomic molecules. part v. tetratomic, non-hydride molecules, ab_3. *J. Chem. Soc.*, page 2301, 1953.

[10] W. J. Marinelli, D. M. Swanson, and H. S. Johnston. Absorption cross sections and line shape for the no_3(0-0) band. *J. Chem. Phys.*, 76:2864, 1982.

[11] Stephen M. Ball, Ian M. Povey, Emily G. Norton, and Roderic L. Jones. Broadband cavity ringdown spectroscopy of the no_3 radical. *Chem. Phys. Lett.*, 342:113–120, 2001.

[12] S.S. Brown, H. Stark, and A.R. Ravishankara. Cavity ring-down spectroscopy for atmospheric trace gas detection: application to the nitrate radical (no^3). *Appl. Phys. B*, 75:173–182, 2002.

[13] Eizi Hirota, Kentarou Kawaguchi, Takashi Ishiwata, and Ikuzo Tanaka. Vibronic interactions in the no$_3$ radical. *J. Chem. Phys.*, 95(2):771, July 1991.

[14] T. Ishiwata, I. Tanaka, K. Kawaguchi, and E. Hirota. Infrared diode laser spectroscopy of the no$_3$ ν_3 band. *J. Chem. Phys.*, 82:2196, 1985.

[15] R. R. Friedl and S. P. Sander. Fourier transform infrared spectroscopy of the NO_3 ν_2 and ν_3 bands: Absolute line strength measurements. *J. Phys. Chem.*, 91:2721, 1987.

[16] K. Kawaguchi, E. Hirota, T. Ishiwata, and I. Tanaka. A reinvestigation of the NO_3 1492 cm^{-1} band. *J. Chem. Phys.*, 93:951, 1990.

[17] K. Kawaguchi, T. Ishiwata, I. Tanaka, and E. Hirota. Fourier-transform infrared spectroscopy of the NO_3 radical. *Chem. Phys. Lett.*, 180:436, 1991.

[18] K. Kawaguchi, T. Ishiwata, E. Hirota, and I. Tanaka. Infrared spectroscopy of the NO_3 radical. *Chem. Phys.*, 231:193, 1998.

[19] Takashi Ishiwata, Yukio Nakano, Kentarou Kawaguchi, Eizi Hirota, and Ikuzo Tanaka. Analyses of the infrared bands of ^{15}no$_3$ in the 1850 - 3150 cm^{-1} region. *J. Phys. Chem.*, 114:980–986, 2010.

[20] K. Kawaguchi, T. Ishiwata, I. Tanaka, and E. Hirota. Fourier-transform infrared spectroscopy of the NO_3 radical. *Chem. Phys. Lett.*, 180:436, 1991.

[21] John F. Stanton. On the vibronic level structure in the NO_3 radical: I. the ground electronic state. *J. Chem. Phys.*, 126:134309, 2007.

[22] J. F. Stanton. On the vibronic level in the NO_3 radical: II. adiabatic calculation of the infrared spectrum. *Mol. Phys.*, 107:1059, 2009.

[23] Christopher S. Simmons, Takatoshi Ichino, and John F. Stanton. The ν_3 fundamental in no$_3$ has been seen near 1060 cm^{-1}, albeit some time ago. *J. Phys. Chem. Lett.*, 3:1946–1950, 2012.

[24] Michael P. Grubb, Michelle L. Warter, Hongyan Xiao, Satoshi Maeda, Keiji Morokuma, and Simon W. North. No straight path: Roaming in both ground- and excited-state photolytic channels of no$_3$ $\rightarrow$ NO + o$_2$. *Science*, 335:1075, 2012.

[25] A. Weaver, D. W. Arnold, S. E. Bradforth, and D. M. Neumark. Examination of the $^2a_2'$ and $^2e''$ states of NO_3 by ultraviolet photoelectron spectroscopy of NO_3^-. *J. Chem. Phys.*, 94:1740, 1991.

[26] E. Hirota, T. Ishiwata, K. Kawaguchi, M. Fujitake, N. Ohashi, and I. Tanaka. Near-infrared band of the nitrate radical of NO_3 observed by diode laser spectroscopy. *J. Chem. Phys.*, 107:2829, 1997.

[27] A. Deev, J. Sommar, and M. Okumura. Cavity ringdown spectrum of the forbidden $\widetilde{A}^2\mathrm{e}'' \leftarrow \widetilde{X}^2\mathrm{a}_2$ transition of NO_3: Evidence for static jahn-teller distortion in the $\widetilde{A}$ state. *J. Chem. Phys.*, 122:224305, 2005.

[28] M. E. Jacox and W. E. Thompson. The infrared spectroscopy and photochemistry of NO_3 trapped in solid neon. *J. Chem. Phys.*, 129:204306, 2008.

[29] M. E. Jacox and W. E. Thompson. $\tilde{A}^2\mathrm{e}''$-$\tilde{X}^2\mathrm{a}_2'$ transition of NO_3 trapped in solid neon. *J. Phys. Chem. A*, 114:4712, 2010.

[30] Kana Takematsu, Nathan C. Eddingsaas, David J. Robichaud, and Mitchio Okumura. Spectroscopic studies of the jahn-teller effect in the $\widetilde{A}^2e''$ state of the nitrate radical no_3. *Chem. Phys. Lett.*, 2012.

[31] H. A. Jahn and E. Teller. Stability of polyatomic molecules in degenerate electronic states. i. orbital degeneracy. *Proc. Royal Soc.*, 161, 1937.

[32] Ira Levine. *Quantum Chemistry*. Pearson, 7 edition, 2013.

[33] Timothy A. Barckholtz and Terry A. Miller. Quantitative insights about molecules exhibiting jahn-teller and related effects. *International Reviews in Physical Chemistry*, 17(4):435–524, 1998.

[34] Vadim L. Stakhursky, Ilias Sioutis, György Tarczay, and Terry A. Miller. Computational investigation of the jahn-teller effect in the ground and excited electronic states of the tropyl radical. part i. theoretical calculation of spectroscopically observable parameters. *J. Chem. Phys.*, 128, 2008.

[35] W. Moffitt and W. Thorson. Calcul des fonctions d'onde molèculaires. *Recuil des Memoires*, November 1958. Centre Nationale de la Recherche Scientifique.

[36] R. Meiswinkel and H. Köppel. Impact of totally symmetric vibrations on the e$\bigotimes$e jahn-teller effect. *Chem. Phys.*, 129:463–476, 1989.

[37] Terrance J. Codd. *Spectroscopic Studies of the $\tilde{A}^2E''$ State of NO_3*. PhD thesis, The Ohio State University, 2014.

[38] Ming-Wei Chen. *Laser Spectroscopy Studying Organic and Inorganic Intermediates in The Atmospheric Oxidation Process*. PhD thesis, The Ohio State University, 2011.

[39] J. K. G. Watson. Jahn-teller and l-uncoupling effecs on the rotational energy levels of symmetric and spherical top molecules. *J. Mol. Spec.*, 103:125–146, 1984.

[40] Eizi Hirota. *High-Resolution Spectroscopy of Transient Molecules*. Springer Series, 40 edition, 1985.

[41] J. M. Brown. Rotational energy levels of symmetric top molecules in 2e states. *Mol. Phys.*, 20:817, 1984.

[42] R. N. Zare. *Angular Momentum*. Wiley Interscience, New York, NY, 1988.

[43] D. W. Marquardt, R. G. Bennett, and E. J. Burrell. Least squares analysis of electron paramagnetic resonance spectra. *Journal of Molecular Spectroscopy*, 7:269–279, 1961.

[44] Sergey Bochkanov. Alglib.net.

[45] Ph. Dugoard, J. Chevalere, M. Broyer, J.P. Wolf, and L. Wöste. Vibronic structure of the li_3 ground state. *Chem. Phys. Lett.*, 175:555–560, 1990.

Appendix A
2_0^1 Assignments

Table A.1: 2_0^1 Assignments from the SPECVIEW simulation presented in Chapter 4. All units in cm^{-1}.

$\|J', N', K'\rangle \leftarrow \|J'', N'', K''\rangle$	Sim. frequency	Exp. frequency	Residual ($\times 10^3$)
$\|11/2, 5, 4\rangle \leftarrow \|11/2, 5, 3\rangle$	7737.933191	7737.93463	-1.439
$\|11/2, 5, 4\rangle \leftarrow \|9/2, 4, 3\rangle$	7742.507496	7742.51218	-4.684
$\|9/2, 5, 4\rangle \leftarrow \|9/2, 5, 3\rangle$	7737.886931	7737.88409	2.841
$\|9/2, 5, 4\rangle \leftarrow \|7/2, 4, 3\rangle$	7742.484102	7742.48601	-1.908
$\|21/2, 11, -11\rangle \leftarrow \|23/2, 12, 12\rangle$	7731.483211	7731.47898	4.231
$\|23/2, 11, -11\rangle \leftarrow \|25/2, 12, 12\rangle$	7731.584392	7731.58951	-5.118
$\|13/2, 7, -2\rangle \leftarrow \|15/2, 8, 3\rangle$	7731.979683	7731.97697	2.713
$\|13/2, 7, -2\rangle \leftarrow \|13/2, 7, 3\rangle$	7739.324046	7739.32392	0.126
$\|11/2, 6, 1\rangle \leftarrow \|13/2, 7, 0\rangle$	7732.139545	7732.13036	9.185
$\|11/2, 6, 1\rangle \leftarrow \|9/2, 5, 0\rangle$	7744.075689	7744.06981	5.879
$\|11/2, 6, -2\rangle \leftarrow \|13/2, 7, 3\rangle$	7733.266896	7733.27039	-3.494
$\|11/2, 6, -2\rangle \leftarrow \|11/2, 6, 3\rangle$	7739.695329	7739.70278	-7.451
$\|11/2, 6, -2\rangle \leftarrow \|9/2, 5, 3\rangle$	7745.207927	7745.20733	0.597
$\|15/2, 7, -2\rangle \leftarrow \|17/2, 8, 3\rangle$	7732.247315	7732.24682	0.495
$\|15/2, 7, -2\rangle \leftarrow \|15/2, 7, 3\rangle$	7739.578053	7739.57726	0.793
$\|15/2, 7, -2\rangle \leftarrow \|13/2, 6, 3\rangle$	7745.981628	7745.98054	1.088

Continued

Table A.1: Continued

$\|J', N', K'\rangle \leftarrow \|J'', N'', K''\rangle$	Sim. frequency	Exp. frequency	Residual ($\times 10^3$)
$\|17/2, 8, -5\rangle \leftarrow \|19/2, 9, 6\rangle$	7732.342152	7732.34222	-0.068
$\|17/2, 8, -5\rangle \leftarrow \|17/2, 8, 6\rangle$	7740.582468	7740.57954	2.928
$\|19/2, 9, -8\rangle \leftarrow \|21/2, 10, 9\rangle$	7732.605348	7732.60579	-0.442
$\|19/2, 9, -8\rangle \leftarrow \|19/2, 9, 9\rangle$	7741.760627	7741.7641	-3.473
$\|13/2, 7, -7\rangle \leftarrow \|15/2, 8, 6\rangle$	7733.452363	7733.44831	4.053
$\|13/2, 7, -7\rangle \leftarrow \|13/2, 7, 6\rangle$	7740.801808	7740.80031	1.498
$\|13/2, 6, -2\rangle \leftarrow \|15/2, 7, 3\rangle$	7733.499907	7733.49666	3.247
$\|13/2, 6, -2\rangle \leftarrow \|13/2, 6, 3\rangle$	7739.908714	7739.90738	1.334
$\|13/2, 6, -2\rangle \leftarrow \|11/2, 5, 3\rangle$	7745.400489	7745.40116	-0.671
$\|15/2, 7, -5\rangle \leftarrow \|17/2, 8, 6\rangle$	7733.648439	7733.646	2.439
$\|15/2, 7, -5\rangle \leftarrow \|15/2, 7, 6\rangle$	7740.971591	7740.97122	0.371
$\|15/2, 8, -8\rangle \leftarrow \|17/2, 9, 9\rangle$	7733.856982	7733.85719	-0.208
$\|17/2, 8, -8\rangle \leftarrow \|19/2, 9, 9\rangle$	7733.959673	7733.96003	-0.357
$\|9/2, 5, -2\rangle \leftarrow \|11/2, 6, 3\rangle$	7734.505427	7734.50009	5.337
$\|9/2, 5, -2\rangle \leftarrow \|9/2, 5, 3\rangle$	7740.018025	7740.01716	0.865
$\|9/2, 5, -2\rangle \leftarrow \|7/2, 4, 3\rangle$	7744.615196	7744.61245	2.746
$\|13/2, 6, -5\rangle \leftarrow \|15/2, 7, 6\rangle$	7734.902957	7734.91528	-12.323
$\|13/2, 6, -5\rangle \leftarrow \|13/2, 6, 6\rangle$	7741.308353	7741.32037	-12.017
$\|9/2, 4, -2\rangle \leftarrow \|11/2, 5, 3\rangle$	7735.857861	7735.84285	15.011
$\|9/2, 4, -2\rangle \leftarrow \|9/2, 4, 3\rangle$	7740.432166	7740.41961	12.556
$\|9/2, 5, -5\rangle \leftarrow \|11/2, 6, 6\rangle$	7736.002552	7735.99966	2.892
$\|15/2, 8, 7\rangle \leftarrow \|15/2, 8, 6\rangle$	7736.059899	7736.05857	1.329
$\|15/2, 8, 7\rangle \leftarrow \|13/2, 7, 6\rangle$	7743.409344	7743.40596	3.384
$\|17/2, 8, 7\rangle \leftarrow \|17/2, 8, 6\rangle$	7736.10513	7736.09574	9.39
$\|17/2, 8, 7\rangle \leftarrow \|15/2, 7, 6\rangle$	7743.409344	7743.41429	-4.946
$\|15/2, 8, 4\rangle \leftarrow \|15/2, 8, 3\rangle$	7736.689451	7736.69006	-0.609

Continued

Table A.1: Continued

$\|J', N', K'\rangle \leftarrow \|J'', N'', K''\rangle$	Sim. frequency	Exp. frequency	Residual ($\times 10^3$)
$\|15/2, 8, 4\rangle \leftarrow \|13/2, 7, 3\rangle$	7744.033814	7744.03015	3.664
$\|3/2, 2, 1\rangle \leftarrow \|5/2, 3, 0\rangle$	7736.741748	7736.72379	17.958
$\|3/2, 2, 1\rangle \leftarrow \|1/2, 1, 0\rangle$	7741.343461	7741.33039	13.071
$\|5/2, 2, 1\rangle \leftarrow \|7/2, 3, 0\rangle$	7736.800523	7736.80126	-0.737
$\|5/2, 2, 1\rangle \leftarrow \|3/2, 1, 0\rangle$	7741.369396	7741.37055	-1.154
$\|5/2, 3, -2\rangle \leftarrow \|7/2, 4, 3\rangle$	7736.833187	7736.83238	0.807
$\|5/2, 3, -2\rangle \leftarrow \|5/2, 3, 3\rangle$	7740.516136	7740.51665	-0.514
$\|13/2, 7, 1\rangle \leftarrow \|13/2, 7, 0\rangle$	7737.969852	7737.97184	-1.988
$\|5/2, 2, -2\rangle \leftarrow \|7/2, 3, 3\rangle$	7738.01569	7738.01422	1.47
$\|7/2, 3, 3\rangle \leftarrow \|7/2, 3, 3\rangle$	7739.371682	7739.37222	-0.538
$\|3/2, 2, -2\rangle \leftarrow \|1/2, 1, 0\rangle$	7739.578053	7739.57726	0.793
$\|3/2, 1, 1\rangle \leftarrow \|3/2, 1, 0\rangle$	7739.602683	7739.60397	-1.287
$\|1/2, 1, -1\rangle \leftarrow \|1/2, 1, 0\rangle$	7739.62801	7739.63403	-6.02
$\|1/2, 1, -1\rangle \leftarrow \|3/2, 1, 0\rangle$	7739.65264	7739.65913	-6.49
$\|19/2, 9, -5\rangle \leftarrow \|19/2, 9, 6\rangle$	7740.141534	7740.14517	-3.636
$\|23/2, 11, -8\rangle \leftarrow \|23/2, 11, 9\rangle$	7740.725565	7740.7309	-5.335
$\|9/2, 5, -5\rangle \leftarrow \|9/2, 4, 3\rangle$	7738.135556	7738.13068	4.876
$\|9/2, 5, -5\rangle \leftarrow \|7/2, 3, 3\rangle$	7741.760627	7741.78778	-27.153
$\|9/2, 5, 4\rangle \leftarrow \|7/2, 4, 3\rangle$	7742.484102	7742.49581	-11.708
$\|11/2, 5, 4\rangle \leftarrow \|9/2, 4, 3\rangle$	7742.507496	7742.51708	-9.584
$\|11/2, 6, 4\rangle \leftarrow \|9/2, 5, 3\rangle$	7743.054643	7743.05353	1.113

Appendix B
$2_0^1 4_0^2$ Assignments

Table B.1: $2_0^1 4_0^2$ Assignments from the SPECVIEW simulation presented in Chapter 4. All units in cm^{-1}.

$\|J', N', K'\rangle \leftarrow \|J'', N'', K''\rangle$	Sim. frequency	Exp. frequency	Residual ($\times 10^3$)
$\|13/2, 7, -2\rangle \leftarrow \|15/2, 8, 3\rangle$	8803.799568	8803.7979	1.668
$\|13/2, 7, -2\rangle \leftarrow \|13/2, 7, 3\rangle$	8811.143931	8811.14288	1.051
$\|13/2, 7, -2\rangle \leftarrow \|11/2, 6, 3\rangle$	8817.572364	8817.57104	1.324
$\|15/2, 8, -3\rangle \leftarrow \|17/2, 9, 6\rangle$	8804.16084	8804.15775	3.09
$\|13/2, 6, -2\rangle \leftarrow \|15/2, 7, 3\rangle$	8805.314107	8805.3138	0.307
$\|13/2, 6, -2\rangle \leftarrow \|13/2, 6, 3\rangle$	8811.722915	8811.7213	1.615
$\|13/2, 6, -2\rangle \leftarrow \|11/2, 5, 3\rangle$	8817.214689	8817.21177	2.919
$\|13/2, 7, -5\rangle \leftarrow \|15/2, 8, 6\rangle$	8805.539629	8805.53338	6.249
$\|13/2, 7, -5\rangle \leftarrow \|13/2, 7, 6\rangle$	8812.889074	8812.88302	6.054
$\|9/2, 4, 1\rangle \leftarrow \|11/2, 5, 0\rangle$	8806.272034	8806.28736	-15.326
$\|9/2, 4, 1\rangle \leftarrow \|7/2, 3, 0\rangle$	8814.521056	8814.5242	-3.144
$\|17/2, 9, 7\rangle \leftarrow \|17/2, 9, 6\rangle$	8806.334421	8806.32553	8.891
$\|17/2, 9, 7\rangle \leftarrow \|15/2, 8, 6\rangle$	8814.598905	8814.58783	11.075
$\|9/2, 5, -2\rangle \leftarrow \|11/2, 6, 3\rangle$	8806.375314	8806.37381	1.504
$\|9/2, 5, -2\rangle \leftarrow \|9/2, 5, 3\rangle$	8811.887912	8811.88832	-0.408
$\|9/2, 5, -2\rangle \leftarrow \|7/2, 4, 3\rangle$	8816.485083	8816.48817	-3.087

Continued

Table B.1: Continued

$\|J', N', K'\rangle \leftarrow \|J'', N'', K''\rangle$	Sim. frequency	Exp. frequency	Residual ($\times 10^3$)
$\|11/2, 5, -2\rangle \leftarrow \|13/2, 6, 3\rangle$	8806.536467	8806.53489	1.577
$\|11/2, 5, -2\rangle \leftarrow \|11/2, 5, 3\rangle$	8812.028241	8812.02438	3.861
$\|11/2, 5, -2\rangle \leftarrow \|9/2, 4, 3\rangle$	8816.602546	8816.60145	1.096
$\|13/2, 6, -5\rangle \leftarrow \|15/2, 7, 6\rangle$	8806.944859	8806.9405	4.359
$\|13/2, 6, -5\rangle \leftarrow \|13/2, 6, 6\rangle$	8813.350255	8813.34609	4.165
$\|17/2, 8, 7\rangle \leftarrow \|17/2, 8, 6\rangle$	8806.983811	8806.98329	0.521
$\|17/2, 8, 7\rangle \leftarrow \|15/2, 7, 6\rangle$	8814.306963	8814.30685	0.113
$\|13/2, 7, 7\rangle \leftarrow \|13/2, 7, 6\rangle$	8807.327255	8807.32247	4.785
$\|13/2, 7, 7\rangle \leftarrow \|11/2, 6, 6\rangle$	8813.762098	8813.76017	1.928
$\|9/2, 4, -2\rangle \leftarrow \|11/2, 5, 3\rangle$	8807.704466	8807.71323	-8.764
$\|9/2, 4, -2\rangle \leftarrow \|9/2, 4, 3\rangle$	8812.27877	8812.2876	-8.83
$\|17/2, 8, 4\rangle \leftarrow \|17/2, 8, 3\rangle$	8808.110588	8808.10492	5.668
$\|17/2, 8, 4\rangle \leftarrow \|15/2, 7, 3\rangle$	8815.436093	8815.42937	6.723
$\|3/2, 2, 1\rangle \leftarrow \|5/2, 3, 0\rangle$	8808.326429	8808.3221	4.329
$\|3/2, 2, 1\rangle \leftarrow \|1/2, 1, 0\rangle$	8812.928142	8812.91925	8.892
$\|5/2, 2, 1\rangle \leftarrow \|7/2, 3, 0\rangle$	8808.424622	8808.4206	4.022
$\|5/2, 2, 1\rangle \leftarrow \|3/2, 1, 0\rangle$	8812.993495	8812.9904	3.095
$\|5/2, 3, -2\rangle \leftarrow \|7/2, 4, 3\rangle$	8808.743947	8808.75595	-12.003
$\|5/2, 3, -2\rangle \leftarrow \|5/2, 3, 3\rangle$	8812.426897	8812.43855	-11.653
$\|11/2, 6, 4\rangle \leftarrow \|11/2, 6, 3\rangle$	8808.751777	8808.75595	-4.173
$\|11/2, 6, 4\rangle \leftarrow \|9/2, 5, 3\rangle$	8814.264375	8814.26673	-2.355
$\|19/2, 9, 1\rangle \leftarrow \|19/2, 9, 0\rangle$	8808.77841	8808.78598	-7.57
$\|7/2, 3, -2\rangle \leftarrow \|9/2, 4, 3\rangle$	8808.817177	8808.81704	0.137
$\|7/2, 3, -2\rangle \leftarrow \|7/2, 3, 3\rangle$	8812.473319	8812.47007	3.249
$\|7/2, 4, 4\rangle \leftarrow \|7/2, 4, 3\rangle$	8809.407208	8809.40905	-1.842
$\|7/2, 4, 4\rangle \leftarrow \|5/2, 3, 3\rangle$	8813.090157	8813.09212	-1.963

Continued

Table B.1: Continued

$\|J', N', K'\rangle \leftarrow \|J'', N'', K''\rangle$	Sim. frequency	Exp. frequency	Residual ($\times 10^3$)
$\|9/2, 4, 4\rangle \leftarrow \|9/2, 4, 3\rangle$	8809.473323	8809.46945	3.873
$\|9/2, 4, 4\rangle \leftarrow \|7/2, 3, 3\rangle$	8813.129465	8813.12547	3.995
$\|15/2, 7, 1\rangle \leftarrow \|15/2, 7, 0\rangle$	8809.755657	8809.75607	-0.413
$\|11/2, 5, 1\rangle \leftarrow \|11/2, 5, 0\rangle$	8810.489504	8810.50009	-10.586
$\|17/2, 8, -2\rangle \leftarrow \|17/2, 8, 3\rangle$	8810.950846	8810.9478	3.046
$\|7/2, 3, 1\rangle \leftarrow \|7/2, 3, 0\rangle$	8810.984263	8810.97579	8.473
$\|1/2, 1, 1\rangle \leftarrow \|1/2, 1, 0\rangle$	8811.196343	8811.20583	-9.487
$\|3/2, 1, 1\rangle \leftarrow \|3/2, 1, 0\rangle$	8811.242617	8811.23057	12.047
$\|13/2, 6, -2\rangle \leftarrow \|13/2, 6, 3\rangle$	8811.722915	8811.7213	1.615
$\|17/2, 8, -5\rangle \leftarrow \|19/2, 9, 6\rangle$	8804.341742	8804.3432	-1.458
$\|17/2, 8, -5\rangle \leftarrow \|17/2, 8, 6\rangle$	8812.582058	8812.58456	-2.502
$\|3/2, 1, 1\rangle \leftarrow \|3/2, 1, 0\rangle$	8812.952772	8812.94413	8.642
$\|19/2, 9, 7\rangle \leftarrow \|19/2, 9, 6\rangle$	8806.510107	8806.51975	-9.643
$\|19/2, 9, 7\rangle \leftarrow \|17/2, 8, 6\rangle$	8814.750423	8814.75865	-8.227
$\|13/2, 7, 4\rangle \leftarrow \|13/2, 7, 3\rangle$	8808.340041	8808.35829	-18.249
$\|13/2, 7, 4\rangle \leftarrow \|11/2, 6, 3\rangle$	8814.768473	8814.78556	-17.087
$\|25/2, 12, 10\rangle \leftarrow \|23/2, 11, 9\rangle$	8814.799988	8814.81078	-10.792
$\|21/2, 10, 7\rangle \leftarrow \|19/2, 6, 3\rangle$	8815.131716	8815.13306	-1.344
$\|15/2, 8, 1\rangle \leftarrow \|13/2, 7, 0\rangle$	8816.650926	8816.65607	-5.144